Author:
Roberts, Ian

Title:
Analysis of non-linear aeroelastic systems using numerical continuation

Analysis of Non-Linear Aeroelastic Systems using Numerical Continuation

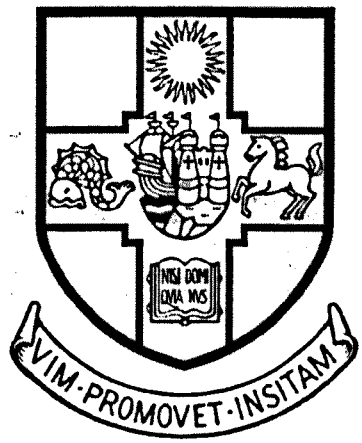

Ian Roberts

Advisor : Prof. N.A.J. Lieven

A dissertation to the University of Bristol in accordance with the requirements of the Degree of Doctor of Philosophy in the Department of Aerospace Engineering in the Faculty of Engineering.

Number of words 41,474

Dedication and Acknowledgements

I would like to acknowledge the guidance provided by Prof. Lieven, the advice of Prof. Champneys in the field of continuation and the assistance of Dr. di Bernardo in the analysis of piecewise linear systems. My biggest thanks go to Drs. Jones and Gaitonde for providing the transonic aerodynamic models and the benefit of their experience in the field.

My thanks also go to the other members of the Zoo and the rest of the Aerospace Engineering Department for an enjoyable three years.

Finally, thank you to Liz and all my family for their support throughout my studies and write up.

Abstract

Non-linearities within structures often present difficulties when developing algorithms to analyse their dynamic properties. Developing a combined aerodynamic and structural - aeroelastic - code is an example where non-linearities can induce particular characteristics as the presence of aerodynamic non-linearities can compound the complexity of the analysis. Furthermore, when non-linearities occur within actuation devices the impact of coupling control systems with the aeroelastic algorithms - aeroservoelastic - must also be considered.

In this work, new methods of analysing aero(servo)elastic systems containing various structural non-linearities are studied. The first technique is used to analyse piecewise linear systems. In this method, aeroelastic equations are recast in a form where the independent variable is the time at which the system reaches a discontinuity, sets of these equations are then combined to form an algebraic set of equations describing a Limit-Cycle Oscillation (LCO). The second technique is applied to more general non-linearities by approximating any discrete non-linearities with trigonometric functions, creating a set of continuous Ordinary Differential Equations (ODEs). For both methods, computational efficiency is achieved by applying numerical continuation to track solution branches.

The models analysed in this work are two and three degree-of-freedom aerofoil sections containing non-linearities in their heave, pitch and/or flap freedoms. Four different aerodynamic representations are used, two incompressible codes establish the accuracy of the new methods. The other codes are used to study transonic flows and show good agreement with work based on aeroelastic systems with both linear and non-linear structures.

Three different control laws - fixed gain, optimal and adaptive - are also investigated to assess their ability to delay flutter onset and suppress LCOs. Optimal control showed the best overall ability to achieve these aims, although it was found that care must be taken not to destabilise areas below the flutter boundary.

Finally, a method of analysing fatigue due to structural non-linearities is investigated. The analysis combines the numerical continuation techniques with the Rainflow method to quantify damage due to simple acceleration-deceleration profiles.

Author's Declaration

I declare that the work in this dissertation was carried out in accordance with the Regulations of the University of Bristol. The work is original except where indicated by special reference in the text and no part of the dissertation has been submitted for any other degree.

Any views expressed in this dissertation are those of the author and in no way represent those of the University of Bristol.

The dissertation has not been presented to any other University for examination either in the United Kingdom or overseas.

Signed _____ **Date** 30/04/04

Erratum Sheet

Contents

Nomenclature

$\mathbf{A, B, C, D}$	general state-space system matrices
b	semi-chord
$\mathbf{B}$	damping matrix
$\mathbf{B_{nc}}$	aerodynamic equivalent damping matrix
$\mathbf{B_s}$	structural damping matrix
C_{ij}	approximate flux integral at i,jth cell
$c_{h/\alpha/\beta}$	non-dimensional damping in heave/pitch/flap freedom
$\hat{c}_l$	perturbed lift
$\hat{c}_m$	perturbed moment about the elastic axis
$\hat{c}_n$	perturbed moment about hinge line
$\boldsymbol{c}^T$	vector transpose [0,0,...,1,...,0]
C_β	distance of hinge line aft of aerofoil mid-chord
$C(\bar{s})$	generalised Theodorsen function
$\overline{\mathbf{C}}$	manipulated stiffness matrix
$\boldsymbol{DE}$	disspipative (frictional) energy
e	total specific energy
$\mathbf{e^A}$	$= Ve^RV^{-1}$
$\mathbf{e^R}$	matrix with exponentials of the eigenvalues of A on leading diagonal
$\boldsymbol{f}_a$	vector of lifts and moments
$f(\alpha_1)$	magnitude of step function to the left of the step
$f(\alpha_2)$	magnitude of step function to the right of the step
F	amplitude of sinusoidal input forces
$\boldsymbol{F}$	vector of input forces
$\boldsymbol{F}$	convective flux terms in x (section 2.2.3 only)
$F(\eta, \zeta, t)$	vector transform from computational to physical domain
G_0	preloaded stiffness
G_{01}	magnitude of preloads for positive pitch rate
G_{02}	magnitude of preloads for negative pitch rate
G_f	inner stiffness in bilinear system
$G(u)$	system pre-load
$G(\alpha)$	non-linear stiffness in pitch
$\boldsymbol{G}$	convective flux terms in y (section 2.2.3 only)
h	dimensional heave
h_a	heave, positive upwards (non-dimensional with respect to chord)
h_j	magnitude of tangent vector to manifold

$\tilde{H}$	matrix containing responses to an impulse in each degree-of-freedom
$\mathbf{H_{rs}}$	Hankel matrix
i	iteration step number
$I_{0,1}$	modified Bessel function of the second kind
I_α	mass moment of inertia
J	cost function
J	Jacobian of the state equations (Chapter 3)
k	linear system stiffness
$k_{h/\alpha/\beta}$	stiffness in heave/pitch/flap freedom
K	blending parameter (section 2.2.3 only)
K_i	control system gains
$\mathbf{K}$	stiffness matrix
$\mathbf{K_s}$	structural stiffness matrix
$\mathbf{K_{nc}}$	equivalent aerodynamic stiffness matrix
$\overline{\mathbf{K}}$	manipulated stiffness matrices
$K_{0,1}$	modified Bessel function of the first kind
$\overline{\mathbf{K}}_s$	manipulated structural stiffness matrix
KE	kinetic energy
l_m	length of side m
L	total lift force
L_1	lift due to circulation
L_2	lift due to apparent mass times acceleration
L_3	centrifugal lift
L_{nc}	non-circulatory lift
L_{nr}	rational component of circulatory lift
L_r	non-rational component of circulatory lift
m	aerofoil mass
M	total moment about elastic axis
M	system manifold, unique curve of solutions
M_a	apparent moment of inertia times angular acceleration
$M(h)$	non-linear stiffness in heave
$\mathbf{M}$	mass matrix
$\mathbf{M}$	monodromy matrix (Chapter 3)
$\mathbf{M_{nc}}$	aerodynamic equivalent mass matrix
$\mathbf{M_s}$	structural mass matrix
$M(y)$	spring restoring force
M_∞	freestream Mach number
m	pseudo time level

n	discrete time interval
N_j	number of corrector steps
N_{opt}	optimal number of corrector steps
$N(\beta)$	non-linear flap stiffness
p	pressure
$P(t)$	external force in heave
$\boldsymbol{PE}$	potential (elastic) energy
q_i	generalised co-ordinates
$\boldsymbol{q}$	vector of structural states
Q	cost function based on system states
$\boldsymbol{Q}$	vector of conserved variables (section 2.2.3 only)
$Q(t)$	external moment about hinge axis
$Q_{aero}(s)$	Theodorsen's vector equivalent of aerodynamic loads
$\mathbf{Q}$	matrix of penalty functions on state variables
$r(t)$	reference signal
r_α	radius of gyration about elastic axis
r_β	radius of gyration about hinge axis
R	cost function based on control motion
R_{ij}	$= C_{ij} - D_{ij}$
$R(t)$	external moment about elastic axis
$\boldsymbol{R}$	vector of eigenvalues of $\mathbf{A}$
$\mathbf{R}$	matrix of penalty functions on controller variables
$s = (\sigma + i\omega)$	Laplace transform variable
$\bar{s}$	$= sb/U$
s	arclength, distance along solution curve (Chapter 3)
t	time
t_i	time at which time integration reaches a boundary of a linear domain
t_+	time when transients have damped out
T	period of oscillation
u	x component of velocity
$\boldsymbol{u}$	state vector
u_g	grid velocity in x direction
U	contravariant velocity
U	freestream velocity
$\boldsymbol{U}$	vector of states and state rates
$\boldsymbol{U}_1$	vector of structural displacements
$\boldsymbol{U}_2$	vector of structural velocities
U_l	flutter velocity of linear system

$U^\star$	non-dimensional velocity or speed index
v	y component of velocity
v_g	grid velocity in y direction
$\boldsymbol{v}_j$	vector tangential to manifold
$\mathbf{V}$	eigenvectors of state space matrix
V	contravariant velocity
w	downwash
$w_{1,2,3,4}$	additional states describing integral
$\boldsymbol{W}$	virtual external energy
Δx_m	x component of length of side m
x_p	augmented states
$\boldsymbol{x}$	vector of required simultaneous equation solutions
$\boldsymbol{x}$	$= \begin{Bmatrix} \boldsymbol{u} \\ \boldsymbol{z} \end{Bmatrix}$
x_α	distance of CG aft of elastic axis (fraction of semi-chord)
$\boldsymbol{X}$	vector of aerodynamic perturbed state variables (section 2.2.4 only)
y	system state
$\tilde{y}$	predicted system states
Δy_m	y component of length of side m
$y(0)$	initial system state
$\boldsymbol{y}^s$	system states at a stationary solution
$\boldsymbol{Y}$	output vector
$\boldsymbol{z}$	vector of state rates
$\boldsymbol{z}^\star$	initial conditions of states and continuation parameter
α	pitch angle
$\overline{\alpha}$	time integration stability and accuracy parameter
α_f	lower end of the freeplay zone
α_j^i	blending functions
α_j	real component of jth eigenvalue
α_l	lower boundary of freeplay region
α_u	upper boundary of freeplay region
α_s	position of step
α_{l-}	lower boundary of freeplay for negative pitch rate
α_{u-}	upper boundary of freeplay for negative pitch rate
α_{l+}	lower boundary of freeplay for positive pitch rate
α_{u+}	upper boundary of freeplay for positive pitch rate
α_{MCS}	arbitrary MCS controller constant

α_R	required pitch rotation
β	flap angle relative to main surface
β_c	control surface position
β_j	imaginary component of the jth eigenvalue
β_R	required control surface rotation
β_{MCS}	arbitrary MCS controller constant
χ	intermediate co-ordinate system
δ	extent of bilinear/freeplay region
$\overline{\delta}$	time integration stability and accuracy parameter
$\hat{\delta}_i(n)$	impulse function (section 2.2.4 only)
ϵ	scaling parameter
ϵ_R	required heave displacement
γ	ratio of specific heats
η	parametric grid co-ordinates
ρ	freestream air density
λ	continuation parameter
Λ	intermediate co-ordinate system
$\tilde{\lambda}$	predicted continuation parameter
μ	aerofoil mass air ratio
μ	floquet multipliers, eigenvalues of the monodromy matrix (Chapter 3)
τ	non-dimensional time
τ_0	initial non-dimensional time
ω	frequency
$\overline{\omega}$	$= \omega_\epsilon/\omega_\alpha$
ω_α	natural (uncoupled) natural frequency in pitch
ω_β	natural (uncoupled) natural frequency in control surface rotation
ω_ϵ	natural (uncoupled) natural frequency in heave
ξ	heave, positive downwards (non-dimensional with respect to b)
ϕ_τ	Wagner's function
ζ	parametric grid co-ordinates (section 2.2.3 only)
ψ_i	multiplier coefficient for ith order of polynomial
ψ_3	multiple of cubic stiffness coefficient

List of Figures

Chapter 1

Introduction

This chapter provides a brief introduction to the field of aeroelasticity. The fundamental interactions that are involved are explained along with their application within industry. Specific issues, that are the object of recent research are highlighted along with a brief description of the phenomena involved. An outline of project aims is then presented highlighting the specific areas of detailed research.

1.1 Aeroelasticity

Research within the aerospace field was, for many years, based on the forces that act on an aircraft in flight as defined by Collar's triangle (see figure 1.1[8])

Collar's definition of these major forces neatly defines major research areas concerned with aircraft flight as well as the focused disciplines represented by the intersections. As such, the research fields were defined as:

- stability and control (flight mechanics): the interaction of inertial and aerodynamic forces;
- structural vibration: the interaction of elastic and inertial forces;
- static aeroelasticity: the interaction of aerodynamic and elastic forces; and
- (non-static) aeroelasticity: the interaction of aerodynamic, elastic and inertial forces.

Collar's triangle therefore defined dynamic aeroelasticity as a unique discipline which in-

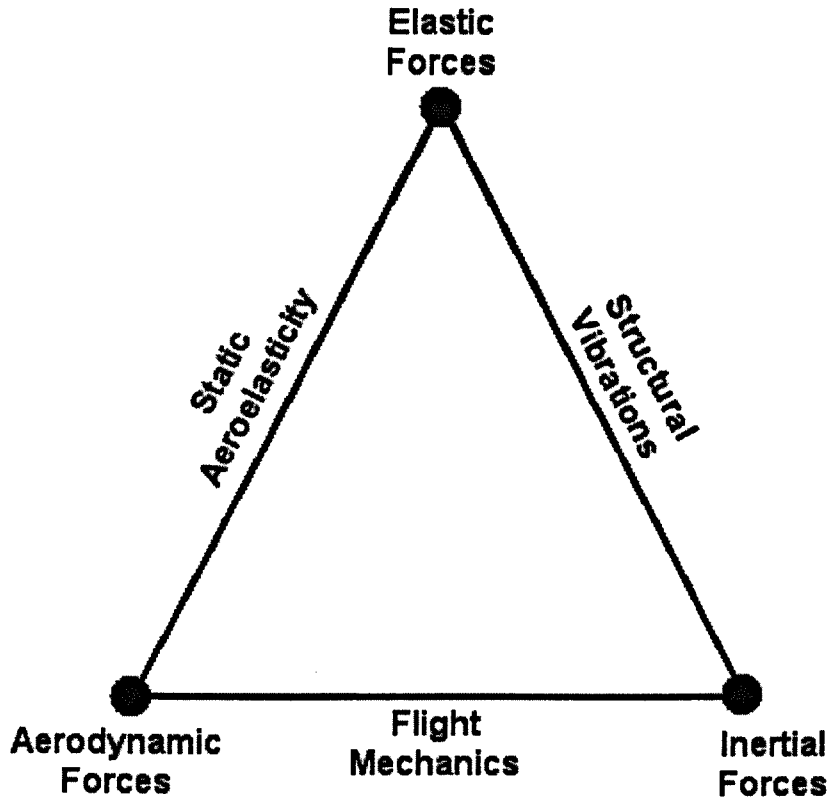

Fig 1.1: Collar's Triangle of Aeroelastic Forces

volved the mutual interaction between all three core forces. Latterly, the disciplines within the aerospace field have become refined, allowing aeroelastics to encompass the fields of control and thermal interaction resulting in the disciplines called aeroservoelasticity and aerothermoelasticity respectively. However, the extensions to the field do not extend the disciplines as first defined by Collar because the forces created by these extended fields can still be encompassed within the basic disciplines, e.g. the aerothermoelastic forces are due to aerodynamic heating and the control forces are other elastic and inertial forces.

The subject of aeroelasticity impinges on many industries and incorporates the fields of aeronautical, civil and mechanical engineering. For example the motions of bridge decks [9] and galloping of transmission wires [10, 11] within civil engineering and the vibrations of pipes due to fluid flow within mechanical engineering. As a result of its wide reach, modern aeroelasticity has been developed from focused research within a wide range of fields and is incorporated into many modern design procedures. However, the overriding view of aeroelastic phenomena is that they are undesirable as the motions compromise system performance and induce fatigue problems within the structure. However recently, the development of compos-

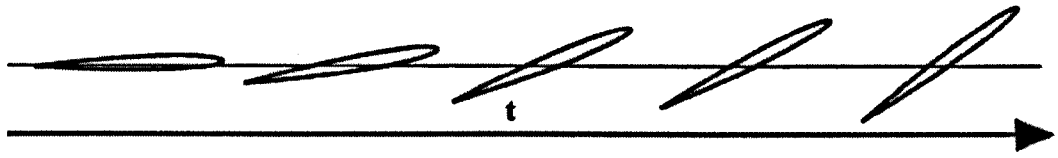

Fig 1.2: Divergent Instability: Snapshots of Aerofoil Motion

ite technologies has allowed static aeroelastic phenomena such as optimised wing twist to be exploited by using novel fibre lay-ups [12].

1.2 Aeroelastic Phenomena

1.2.1 Static Aeroelasticity

Static aeroelasticity is concerned with the analysis of aerodynamic-structure interaction whilst ignoring the inertial forces on the system i.e. the mass terms do not affect the motion.

$$g(q) = F \tag{1.1}$$

where $g(q)$ is a vector dependant on the structural displacement and F are external or aerodynamic forces. A commonly studied aerospace example of such a phenomenon is the divergent aerofoil as illustrated in figure 1.2. Such a system undergoes a divergent loss of stability, as opposed to an oscillatory loss of stability in the case of dynamic cases (see figure 1.3). As the divergent nature of the system is independent of the velocity and acceleration of the structure, the motion results from the static aerodynamic forces acting on the structure being too high for it to maintain it's integrity. The divergence phenomenon has been observed in wings e.g. S.P. Langley Aerodrome, and is a design driver for pylon mounted stores where the aerodynamic centre can have a large eccentricity from the elastic axis. Divergent failure was a particular problem for aircraft with aerodynamically beneficial swept-forward wings until the utilisation of carbon-fibre based composites allowed tailored structures to be developed with minimal weight penalty [12].

Control surface reversal is a further example of static aeroelasticity where the deflection of a control surface causes a pitching angle of the main surface contrary to the conventional definition. This motion occurs because it is more energetically advantageous for the main

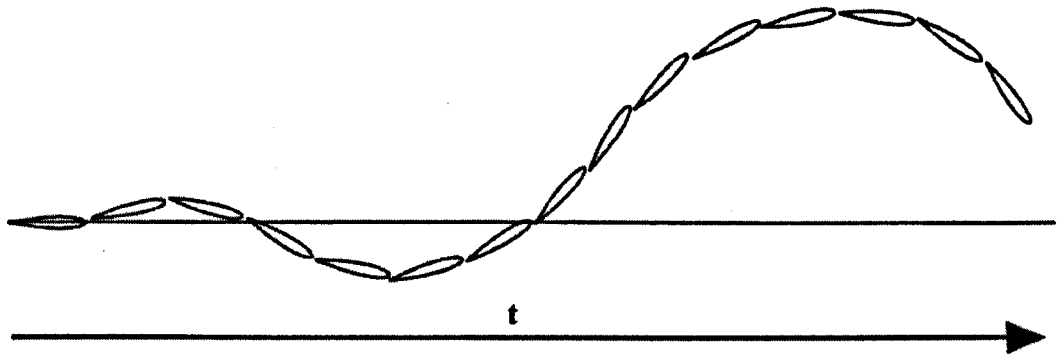

Fig 1.3: Oscillatory Instability: Snapshots of Aerofoil Motion

surface to rotate as opposed to the control surface itself. This phenomenon occurs in systems where there are very large wing loadings and hindered supersonic flight during early studies. The twist and bending of a wing in cruise flight is another static phenomenon which is of particular interest to the civil aircraft industry. The deflection of wings during cruise flight is important in modern aircraft design because of its contribution to overall aircraft drag and, consequently, fuel efficiency. Additionally, in the military field the same phenomena can lead to reductions in combat effectiveness and compromise radar cross section.

Other examples of static aeroelastics include the rolling of a wing in steady conditions where the control surface deflects causing wing bending to occur at steady rates. As the motion is a steady state, their is no acceleration and therefore no inertial contribution. The elastic deflection of control surfaces is also an example of static phenomena, where the airloads on the control surface cause it to deflect. This deflection is in addition to any control surface deflection and thus changes the effectiveness of the controller. The elastic deflection of components within pipes containing flowing fluids e.g. oil pipelines and jet engines, often alters how efficiently they operate and further highlight the importance of considering static aeroelasticity in any design.

1.2.2 Dynamic Aeroelasticity

Dynamic aeroelasticity covers a wide range of phenomena and differs from the static form in that the inertial terms are now included within the analysis. The inertial terms are included to take into account the oscillatory nature of the systems, see figure 1.3. All the studies of aeroelastic phenomena can be described by the basic formula,

$$\mathbf{M}\ddot{\boldsymbol{q}} + \mathbf{B}\dot{\boldsymbol{q}} + \mathbf{K}\boldsymbol{q} = \boldsymbol{F} \tag{1.2}$$

where M, K and B are the mass, stiffness and damping matrices respectively, $\boldsymbol{q}$ is the displacement of the system and $\boldsymbol{F}$ is a vector of aerodynamic forces. The problem therefore reduces to equating the forces generated within the structure with the forces generated in the local airflow.

Using the above formulation, the most commonly cited undesirable form of dynamic aeroelastic phenomenon, flutter, can be explained. Conventional flutter phenomenon occurs when the aerodynamic forcing put in to the structure is fed back to the air as a large motion that creates a larger force, resulting in an oscillatory divergent motion. In effect, the energy extracted from the flow is greater than the energy dissipated within the structure. This energy transfer results in catastrophic failure as the material performance limits are exceeded. Such aircraft flutter has been widely studied and forms a core part of the aircraft industries analysi procedure as it can severley restrict an aircraft's operating flight envelope. The location of conventional flutter boundaries is usually performed by forming a flutter model, as described by equation 1.2. This is done in a three step process; firstly, the finite element structural model is constructed and a normal modes analysis performed, secondly an aerodynamic panel or doublet lattice method is used to generates aerodynamic influence coefficients dependant on the mode shape and, finally, the aerodynamic and modal models are combined to form a flutter model. Once the aerodynamic and structural models are combined a frequency domain analysis is performed that monitors both the frequencies and damping of the various modes as a parameter such as air speed or density is varied. The flutter boundary is thus located by either frequency coalescense or, more usually, negative damping, of one or more modes.

In reality, various other forms of flutter exist, these include stall and shock-stall. Stall flutter occurs when the flow separates at high angles-of-attack and does not re-attach until a much lower angle is reached [13]. Shock-stall differs from stall flutter in that the separation is caused due to shock motion and strength [14]. Shock-stall and stall flutter in-turn differ from the conventional flutter form in that they arise from non-linearities within the aerodynamic flow that generate the oscillatory forcing. Non-linear flutter phenomena occur, not only on aircraft components, but also on transmission lines (galloping) [10, 11] and on bridges, e.g. the Tacoma Narrows bridge [9]. Such flutter is not always catastrophic, but can result in large amplitude oscillations that create fatigue problems. The oscillations due to non-linearities are frequently referred to as Limit-Cycle Oscillations or LCOs as they have a finite amplitude repeatable motion. Often the oscillations that occur due to structural non-linearities are small and therefore

do not effect the flutter boundary. However, when oscillations occur in the transonic regime the motions can be quite large; thus the flutter boundary is redefined as the point at which the onset of oscillations occur and not when actual divergent oscillations - flutter - occurs. In solving the above problems the equations themselves are essentially just the form of the aerodynamics or structure changes.

Control surface buzz is an aeroelastic phenomenon that occurs in transonic flow and is due to the motion of a shockwave over the main surface/control surface interface [13]. The motion that is induced by buzz can be very high frequency as large changes of moments about the aileron hinge position result from small shock motions. The motion that occurs is a simple limit-cycle oscillation (LCO) but can be catastrophic due to rapidly accumulated fatigue damage.

In supersonic flow, panel flutter can occur when there is a pressure difference across a plate whose edges are rigidly supported [15]. The flutter motion is self-exciting and is dependent on the mass, geometry and the forces exerted on the panel due to the structural attachments. The panel oscillations are only observed in supersonic flow as the differential thermal effects can result in large compressive loads being applied to the skin. An analogy to such a motion is the buckling of a beam, as shown in figure 1.4 which is enhanced when a lateral force (c.f. differential pressure) is applied. When a panel buckles inwards the resulting drop in pressure over the panel causes an opposing force such that the panel buckles outwards. As such the motion has two stable buckled solutions between which the plate oscillates due to the pressure field variation with deflected positions.

Finally, non-linearities within structures, control systems and aerodynamics can often result in oscillatory behaviour below the predicted flutter boundary. Such motions are often of low amplitude but cause a reduction in component life due to fatigue.

1.3 Technical Challenges

In the field of aeroelasticity, the general challenge is to generate models that better predict the dynamic behaviour of an onject in an airflow e.g. an aircraft in flight. With this requirement, both the structural and aerodynamic models must better represent the actual structural properties and air forces respectively.

In aeroelasticity, structural models tend to fall in to two major categories; reduced beam models that represent the fundamental structure of the aircraft, and full stressing models. Beam models

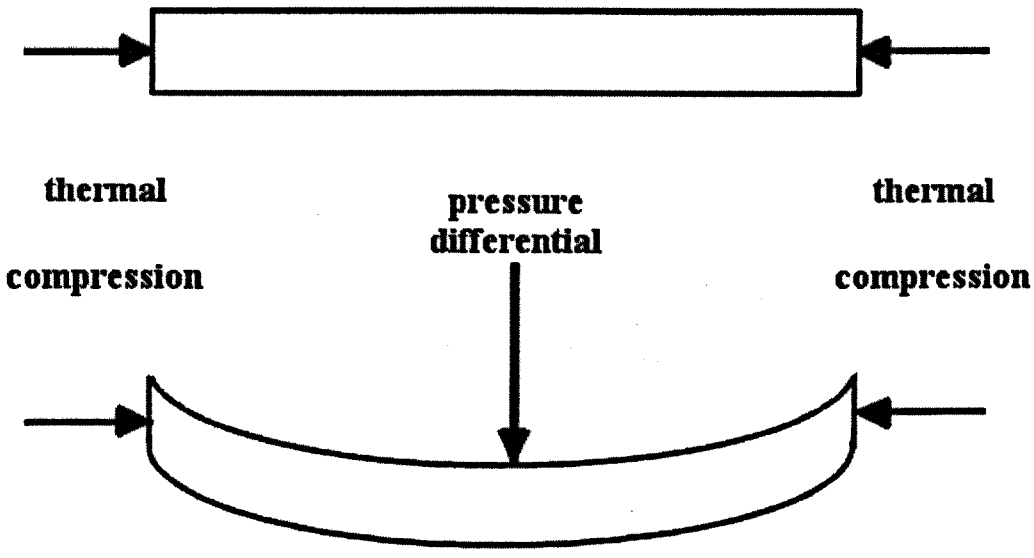

Fig 1.4: Beam Buckling Analogy of Panel Flutter

are constructed from a number of beam, point and shell elements that are designed to represent the general behaviour of the major components of an aircraft. As such, beam models are often simple but can miss out some of the more detailed phenomenon that modern analysis require including. Conversley, full stessing models contain much structural and mass data but are designed to perform stressing on, therefore they are prone to generating "tent pole" modes which occur when the constraints, imposed by the stress department, are not sufficient for dynamic modelling resulting in unrealistic modal displacement shapes for the aircraft. The usual method of validating structural models is through ground resonance testing. This then introduces another challenge, the ability to update the structural model to correlate with the test data. This process must be performed in such a way as to not overly change any one individual parameter whilst making sure that all of the modes created are close to the desired shape and frequency. This has lead to research in to model correlating where software is designed to alter the structural model so that it matches the measured models. Such software, is however, not fully developed and usually requires an engineer to alter the model to be close to the desired results before it can start its analysis. In this way, the beam model is often easier to update as the number of parameters to be modified is smaller. More generally, in structural dynamics, much of the effort has concentrated on the accuracy of local effect modelling, as many of the techniques currently practised are rapid but only applicable to linear systems. The modelling of non-linear factors, such as damping, stiffening and joint motion, have remained problematic as many of the non-linearities cannot be measured directly but must be applied generically over the whole system. Furthermore, when structural non-linearities are included within models the

method of analysis requires changing as most of the modal methods rely on the assumption of linearity.

Conventional aerodynamic modelling, when applied to aeroelastic problems, has long relied upon the use on doublet lattice and panel codes that often utilise simple thin body inviscid theory with arbitrary factors that compensate for flow features such as shocks and boundary layers. In these codes, the aerodynamics of stores and even fuselages are sometimes not simulated. There is therefore a need to improve the prediction of aerodynamic forces so as to to allow a more realistic prediction of the aeroelastic behaviour. As a result of the inadequacies of many of the conventional aerodynamic codes much effort has been devoted to improving unsteady aerodynamic predictions. Over the past decades, the advent of CFD has resulted in huge step forwards in the detailed simulation of dynamic airflows around complex bodies. These methods allow the capture of complex phenomena such as shock waves and even boundary layers. Such simulations are often slow, therefore to allow the tools to be used for prediction purposes, data is often drawn from the models and combined with wind tunnel data, to allow updating of the traditional panel methods e.g. shock positions are located and added to models. More recently, the advent of Reduced Order aerodynamic Models (discussed later) has created an effcient way by which the important aerodynamic phenomena can be taken from the model and utilised in a much more efficient manner. The application of aeroelasticity within turbomachinery, such as jet engines, has also presented many non-linear problems and resulted in aerothermoelastic problems becoming the subject of recent studies with the interaction of flows from moving parts on downstream components and the effect of parasitic flows being of particular interest [16].

The full coupling of Finite Element (FE) structural models with Computational Fluid Dynamics (CFD) models has had much effort devoted to it over recent years with mixed success. The current state of the art is constrained by computational expense of modelling such techniques. This expense is due to incorporating a moving grid CFD code for the flow around complex moving structures, the iterative nature of the time solution process and communication between CFD anf FE models. The CFD solution itself is the most costly aspect as it relies on five sets of equations being solved at hundreds of thousands of grid points, for a whole or half aircraft. The communication problem is the transfer of loads from the fine CFD grids on to an often sparse structural grid and, conversley, the transfer of deflections from a sparse structural model on to a fine CFD grid. This particular problem can often be seen at interfaces between different parts of the structure where relative motions can cause CFD grids to collapse. As a result of the computational cost and inability to use modal solutions, work has been driven forward in the field of Reduced Order aerodynamic Modelling (ROM) [6, 17, 18, 19] where

the full CFD codes are reduced to a low-dimensional equivalent formulation that captures the essential flow properties. However, even with the advent of Reduced Order Modelling, the full coupling work still requires advancing as any developments in reduced model generation require validation with full codes which, in turn, must be validated against experimental and full-scale results. Many of the problems described above are concerned with the aerodynamic drive toward more rapid tools for the analysis of aeroelastic problems. This marks a shift away from many CFD conventional techniques that are aiming to improve the accuracy in the simulation of various types of phenomena such as stall, to systems that allow the more general whole aircraft phenomena to be predicted better.

Over recent years the inclusion of control within the aeroelastic field has led to the rapid development of aeroservoelastic design tools [20, 21, 22, 23, 24, 25]. These advances are being pushed by both the commercial aircraft industry, which requires an aircraft that can fly closer to the flutter boundary, and the military aircraft manufacturers who have ambitions to fly aircraft through the flutter boundary. Both sectors require the extension of the flight envelope to allow more efficient performance but are limited by certification issues over control systems. The less stringent certification levels in the military sector have allowed for more rapid development within all fields of aerospace along with the drive toward Unmanned Air Vehicles (UAVs) meaning that certification limits can be altered as risk to life is significantly reduced. The design of control systems that can react quickly to the instabilities that can occur in dynamic aeroelastic systems means, however, that tolerances, such as dead-bands, must be refined. As most aeroelastic phenomena occur rapidly it means such poor tolerances are not acceptable within the industry. Additionally, the requirement for flight through the flutter boundary is a driver for the afore mentioned aerodynamic and structural developments, as oscillatory motion that could be benign below the flutter boundary could lead to rapid fatigue above this limit. Fatigue itself is a major driver in the aeroelastic field as the in-service costs of aircraft can become prohibitive if component lives are too short due to non-linear aeroelastic phenomena.

1.4 Scope of Thesis

The main focus of the work described here is the study of aeroelastic systems with non-linearities. The work has four distinct objectives:

- the implementation of a mathematical method for rapid identification of limit-cycle os-

cillations within non-linear aeroelastic systems. The non-linearities must be permitted to be as arbitrary as possible, such that any non-linearity in any system state could be analysed by the method;

- the development of a method for the analysis of the behaviour of transonic aeroelastic systems containing non-linearities. The transonic regime is a particular problem due to non-linearity present within the airflow. At present, such systems are restricted to being analysed by finite volume, time integration schemes, or panel methods with wind-tunnel or CFD correction factors applied. Any method that is designed to analyse such systems must not greatly compromise the system accuracy;

- the design of a control system that is capable of suppressing flutter beyond the uncontrolled or open loop flutter boundary. The control system must demonstrate a good level of extension upon the linear flutter boundary without compromising stability elsewhere within the flight envelope. A range of control systems must be examined to assess the best overall system for the task. Considerations must be made of basic control systems as well as more modern active and adaptive systems; and

- the development of a control system that allow the attenuation of oscillations due to structural non-linearities within the control circuit. This analysis must examine the level of attenuation that can be achieved whilst also considering the control effort that is required in such a system. Additionally, the implementation of controllers designed for linear aeroelastic systems within the non-linear aeroelastic system are to be considered to assess their validity. The controllers must be demonstrated on a control system containing backlash. It is deemed that such a system provides the best test of the system as - over certain ranges - the controller should have no effect on the system response.

The first and second objectives are the main drivers for the work undertaken as current techniques for the analysis of non-linear aeroelastic systems particularly, and non-linear dynamic systems more generally, are limited to techniques that adequately solve for very specific forms of non-linearity. The application of control laws to the non-linear aeroelastic problem has two main drivers. The first driver is to assess if it is possible to apply control laws to systems where the non-linearity is part of the control circuit. The second driver is to assess if controllers designed for flutter suppression of linear systems have a negative or positive impact on the amplitude of the oscillations present within non-linear aeroelastic structures.

The analyses are concentrated on two and three degree-of-freedom systems in two dimensional flow. This restriction is applied because firstly, there are a number of testcases presented for

such systems which allows good comparison and validation to be made and, secondly, the two-dimensional system affords the author and reader a more thorough insight in to the problem both physically and mathematically.

Chapter 2

Aeroelasticity

This chapter presents a review of the field of non-linear aeroelasticity due to structural non-linearities and the techniques currently applied to such problems. The basic form of structures and the associated non-linearities is presented first followed by the aerodynamic models that are to be applied to the problems. The way in which the aerodynamic and structural models are combined and solved is then described. A brief description of Ground Vibration Tests (GVT) is then made along with an explanation of how they can be modelled in a similar manner to the aeroelastic equations.

2.1 Structures

2.1.1 Overview

In the aircraft industry the assumption of structural linearity is often made in both the design and analysis of components. From these models the flutter/divergence boundaries and characteristics are determined. Using data from both ground vibration and flight tests the validity of the structural models are determined and then updated by modifying the stiffness and damping matrices. The costs of implementing such test procedures are large and incorrect prediction of the flutter envelope at these late stages in the design and production phase of an aircraft leads to large financial and/or performance penalties. As a result, there has been a drive by both the aircraft industry and heavy industry in general to develop structural models that are more representative of a true structure. In order to generate an accurate dynamic model of a structure, research has been focused on the areas of damping modelling, joint analysis and concentrated

non-linearity analysis. The latter topic is the main focus of this research but some aspects of the work are applicable to the field of joint analysis.

2.1.2 Structural Non-Linearities

The analysis of linear dynamic systems is now a comparatively trivial task with the advent of modal analysis techniques and high-speed computer processing. The most significant problem that is encountered with such techniques is the quantification of structural damping. The addition of damping to systems is a somewhat black-art with experience being the major engineering tool. However, the inclusion of damping within a model makes little difference to the boundary of operation of an aircraft, as much of the damping is provided by the aerodynamics and, in many instances, the gradients of the velocity versus damping curves are high. In areas where non-linearities in either aerodynamics or structure cause "small" amplitude oscillations, the inclusion of accurate damping can remove or greatly attenuate some of the periodic motions.

Oscillatory phenomena within aircraft systems due to structural non-linearity, was largely ignored in the early years of the aircraft industry as techniques for the prediction of simple linear phenomena were the primary focus of research. However, in the early 1950s Woolston et al. [26, 27] and later Shen [28, 29] devoted much effort to the definition of the concentrated non-linearities and the modelling of such systems. These authors work used analogue computation, basic numerical techniques and wind tunnel models to perform fundamental modelling on the concentrated non-linearities as defined in [26]. The distinction between concentrated and distributed non-linearity can be seen in the effects that they cause. Concentrated non-linearities result in oscillations restricted to a small locality whereas distributed non-linearities act over the whole structure and essentially fit into the area of joint modelling [30, 31] e.g. riveted and bolted sections. Common areas in which concentrated non-linearities exist are within control system assemblies and engine/pylon/store attachments.

Breitbach [31, 32] was the next author to contribute significantly to the non-linear aeroelastic field some 17 years later, with a further review of non-linearities and the introduction of modified modal analysis tools to analyse the aeroelastic phenomena. More recently the field of research has expanded markedly, driven by an industry desire for more accurate component modelling and the requirement of aircraft to push the flight envelope up to and beyond the flutter boundary. With the requirement to extend the flight envelope, the loads that an aircraft experiences have resulted in the once inconsequential oscillations resulting from non-linearities

becoming areas of concern. These oscillation have consequences on the aircraft in terms of both handling quality, vibration and, perhaps more importantly, fatigue (the ramifications of structural non-linearities upon fatigue aspects is discussed briefly in the results section). Additionally, for aircraft performance improvement to be possible and practically applied within industry the predictive tools used to analyse these non-linear systems must generate results in times comparable to the modal techniques currently used.

In the following sections a review of the basic models identified by Woolston et al. [26] is made which is supplemented by some comments on the combination of such non-linearities. Research relevant to each of the various forms of non-linearity is reviewed within the appropriate sections.

2.1.3 Cubic Non-linearities

2.1.3.1 Overview

A cubic non-linearity, as its name suggests, can be expressed in terms of a cubic polynomial equation of the form,

$$M(y) = k(y + \psi_3 y^3) \tag{2.1}$$

where $M(y)$ is the system restoring force in the y degree-of-freedom, k is the linear system stiffness and ψ_3 is a scalar number that determines the "strength" of the non-linearity.

Cubic non-linearities take two basic forms, either softening or stiffening, as shown in the force-displacement curve in figure 2.1. A softening type non-linearity occurs when the value of ψ_3 is negative. The softening non-linearity is defined as being when the system becomes less stiff, when compared to the linearly stiff system, as the displacement increases. In practical situations such softening is quite rare and highly undesirable and is usually only observed when individual aircraft panels flutter after some form of plastic deformation has occurred to the material. The softening non-linearities results in system limit-cycles below the flutter boundary calculated using a linear model i.e. $\psi_3 = 0$ (referred to as sub-critical LCOs).

Cubic stiffening non-linearities commonly occur in components such as thin wings or, more prominently, pylon intersections [30, 33]. For a cubic stiffening non-linearity the magnitude of the stiffness increases with increasing displacement (relative to the linear stiffening). Cubic

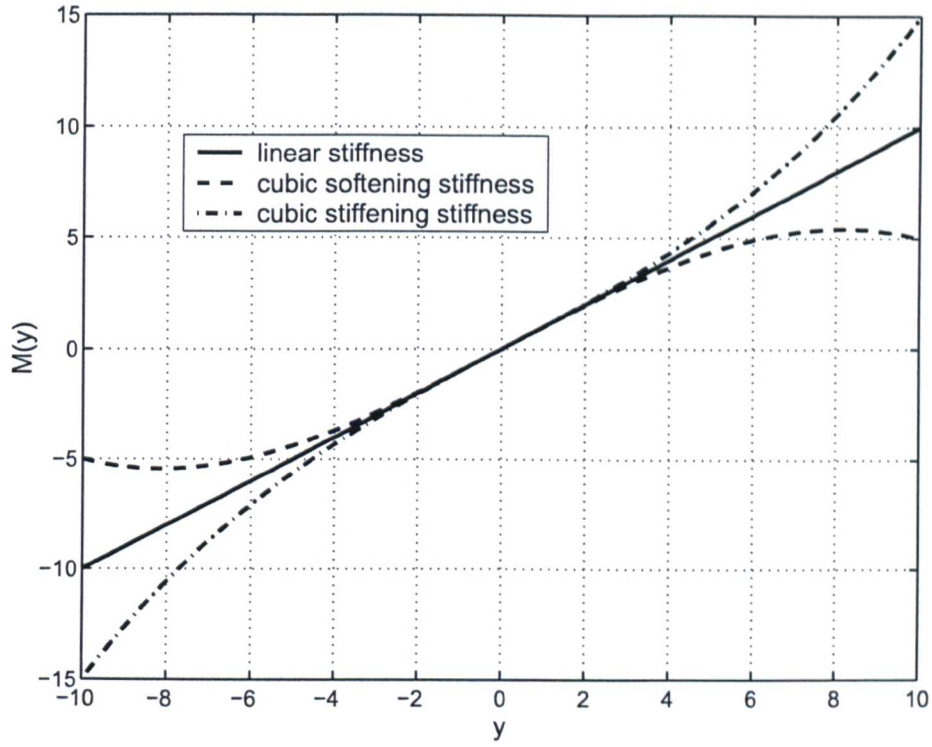

Fig 2.1: Force-Displacement Curve for Cubic Non-Linearities

stiffening occurs in most structures but is most noticeable when the oscillatory motions are large. For large displacements the different components tend to lock together, stiffening the system.

The basic phenomenon of cubic stiffening has been studied widely, not only in the aerospace field, but also as general mechanical and electrical occurrence. A fundamental cubic non-linearity testcase used by both mathematicians [34] and engineers [35] is the Duffing Oscillator which is a single degree of freedom system represented (in terms of displacement, y) by the equation,

$$\ddot{y} + c\dot{y} + k(y + \psi_3 y^3) = F sin(\omega t) \tag{2.2}$$

This simple testcase demonstrates phenomena that can be observed in experimental modal analysis where there is a sinusoidal input of various magnitudes and frequencies. Figure 2.2 shows the response of the stiffening system for a sinusoidal input force, frequency ω and magnitude F in the same degree-of-freedom. In Figure 2.2 the dark dots represent stable limit-cycle oscillations (LCOs) whereas the empty dots are unstable LCOs. A fundamental problem with non-linear systems is shown in this figure, in that, for a given frequency, there are two different stable LCOs on to which the system could be attracted (as well as an unsta-

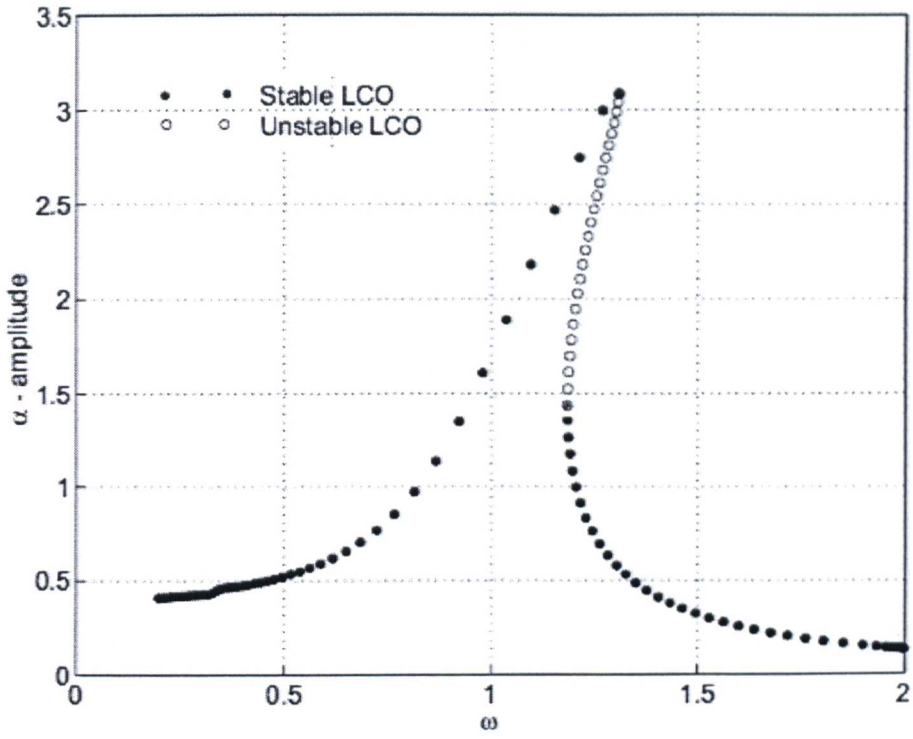

Fig 2.2: Amplitude of Cubic System to a Sinusoidal Forcing

ble cycle). An additional problem with such non-linearities is the "jump" phenomenon [35], which is when a system "jumps" from a solution on one stable branch on to another branch at an often indeterminate point. In general, however, the jumps occur in a form similar to that shown in figure 2.3, creating a type of hysteresis effect. Such hysteresis has been observed by authors studying aeroelastic systems where limit-cycles appear and disappear at different velocities depending on whether the velocity is slowly increasing through the range or slowly decreasing through the range [36]. A softening system response shows the same peak "bending" phenomenon as the stiffening system, but the peak deflects towards lower frequencies. The direction in which a peak bends, gives a good indication as to whether the system is stiffening or softening when performing standard modal tests. Finally, the limitations of linearised analysis are found in such systems as, for a given forcing frequency, the amplitude of the oscillation does not vary linearly with the magnitude of the input force e.g. doubling the force does not double the response. The analysis of multi-dimensional systems containing multiple cubic stiffening non-linearities has been shown to result in much more complicated response curves, [35].

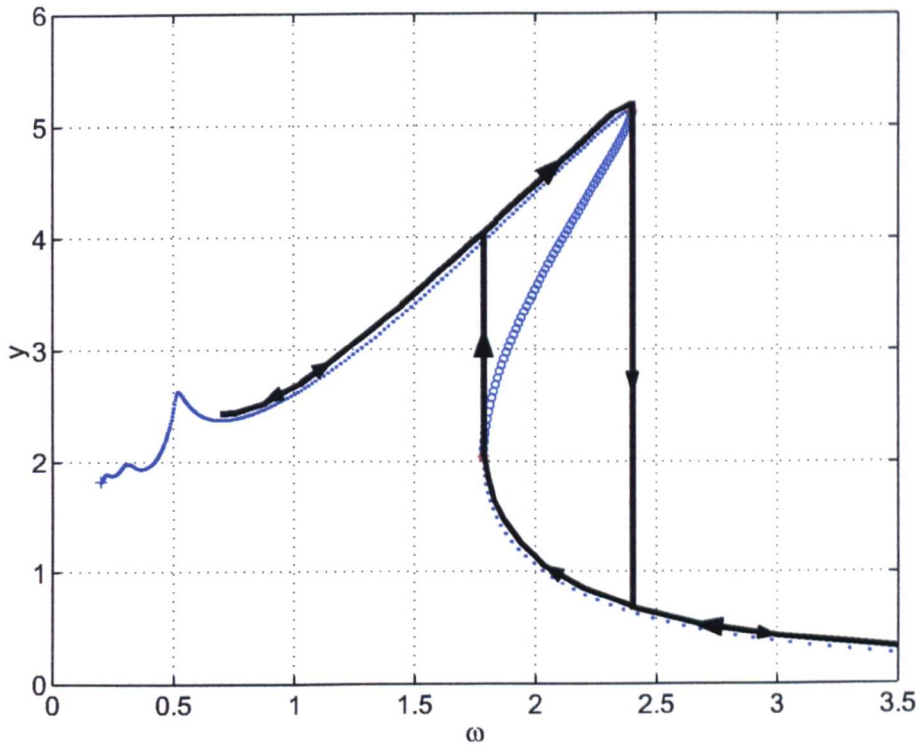

Fig 2.3: Jump Phenomena within Cubic Stiffening

2.1.3.2 Analysis Techniques

Analogue computing methods were the first techniques employed in the analysis of cubic non-linearities by Woolston et al. [26, 27]. This technique involved the use of electrical components such as resistors, capacitors and inductors to represent mass, damping and stiffness. They suffered from poor accuracy, as is inherent in such analysis techniques, and the method additionally restricted the authors to the analysis of weak non-linearities i.e. systems where the degree of non-linearity is minor compared to a linear system. Shen [29] expanded on this work, by applying the harmonic balance technique that allowed the weak non-linearity restriction to be removed. During the mid 1980s Lee et al. [37] analysed a basic pitch-plunge aeroelastic model with varying amounts of cubic stiffening/softening. In the studies a low-speed aerodynamic model, after Fung [1], was used to model the flow. A Runge-Kutta time integration was used to track the system response with time, allowing a graph of LCO amplitude versus velocity to be plotted for the various cases.

In an attempt to introduce a more rapid technique Zhao and Yang [38] used an equivalent stiffness analysis approach - similar to that used by Dowell [15] to analyse plate buckling - to study the effect of cubic stiffening non-linearities. Zhao and Yang classified periodic motions for various positions of the elastic axis and then validated their results against time integration

analyses. The large static deflections, particularly, and the periodic motions, more generally, were seen to exist at very large angles-of-attack where the very basic linear aerodynamics used by the authors is not applicable.

In the late 1990s a collection of authors from Canada published several papers relating to the field of non-linear aeroelastics. Studies of cubic non-linearities by these authors started with a paper by Lee, Gong and Wong [35], in which the basic properties of cubic non-linearities, as discussed at the beginning of this section, were founded. The work built the aerodynamics previously derived by Fung [1] with an additional inclusion of four terms representing the integral terms that allowed the expression of the system in a state-space form. The results were obtained for both aeronautical and mathematical examples. Slowly varying motions and the fact that the systems settled in to an LCO so that transient terms could be neglected was assumed. The results showed the bending tendencies previously described but were observed as being less pronounced in the aerospace applications as the linear aerodynamics approximation restricted the system to low-amplitude oscillations. The system showed that, for low velocities, a second resonant peak was observed within the amplitude responses but disappeared at higher velocities. This phenomenon was possibly due to the coalescence of resonant peaks. The paper also derived a simple relationship between pitch and plunge amplitude and forcing frequency, but due to the assumption of slow variation with time, lacked the ability to observe higher harmonics.

Liu [39] and Wong and Lee [7] applied the centre manifold theory to the same cubic non-linearity problem as described in the previous paragraph [35]. The application of the centre manifold technique is, at the time of publication, limited to the analysis of first harmonic solutions although viable extensions to the technique were proposed to overcome this restriction. The methodology used enables the original eighth order system to be reduced to a simple relationship between the two structural degrees-of-freedom, heave and pitch. As with the paper in the previous paragraph it is assumed that the system coefficients are slowly varying with respect to non-dimensional time. The crucial step in this analysis is that the centre manifold is approximated by a low-order polynomial. The full details of the work are beyond the scope of this section but may be found in [39, 7]. The results obtained by this method compared favourably to those generated by conventional Runge-Kutta time integration methodologies.

A major review on the subject of non-linear aeroelastic systems was also performed by Lee et al. [30], in which non-linearities in both structure and aerodynamics were studied. The review included an amalgamation of much of the work concerned with structural non-linearities including cubic non-linearities. Many of the papers covered in the previous paragraphs were

reviewed and included interesting observations on the chaotic motions of cubic systems. It was observed that, from the work of Lee and LeBlanc [37] and Lee et al. [40], the weaker the cubic non-linearity with respect to the linear stiffness, the lower the level of chaos.

In the United Kingdom work has been performed on aeroelastic systems with cubic non-linearities at Manchester University [41, 42]. This work is an extension of the work performed in Canada [39, 7] with the inclusion of averaging methods that allowed the consideration of both autonomous and non-autonomous systems. The results obtained by this method were, like those of Liu et al. [39] and Wong et al. [7], highly accurate in comparison with time integration techniques.

Recent work performed by Sheta et al. [33] analysed systems with polynomial non-linearities both experimentally and using a Navier-Stokes computational aerodynamics code. The non-linearity studied is a quartic polynomial in pitch and is included within this section as it shows the same tendencies as cubic stiffening, although it is noted that for small angles the stiffness curve resembles a softening type system. The experimental model studied was a constant, unswept chord wing with a NACA-0015 aerofoil section, represented by a two-dimensional section for the computational analysis. Results showed excellent correlation between physical and computational experiments for pitch with good results also obtained for heave. Comparisons were also made between different aerodynamic models including linear aerodynamic modelling and the inviscid Euler equations. The results show that the use of Euler aerodynamics is sufficient for such analyses, with differences between these results and those of the Navier-Stokes equations being acceptably small. The analysis of computational expense for the different techniques, which would have aided the assessment of industrial applicability, was not made in this paper. The authors additionally highlighted the importance of modelling both aerodynamic and structural non-linearities when accurate analyses are required.

2.1.4 Bilinear Stiffness and Backlash/Freeplay Non-linearities

2.1.4.1 Overview

Many authors in the aeroelastics field have highlighted systems with bilinear stiffness properties, as shown in figure 2.4, as particularly problematic [26, 27, 43, 44]. Bilinear systems are characterised by three distinctive zones, two outer zones with the equivalent of a linear stiffness and a small central area with either a larger or, more usually, lower stiffness. A special form of bilinear stiffness occurs when the central zone has zero stiffness. This is called a backlash

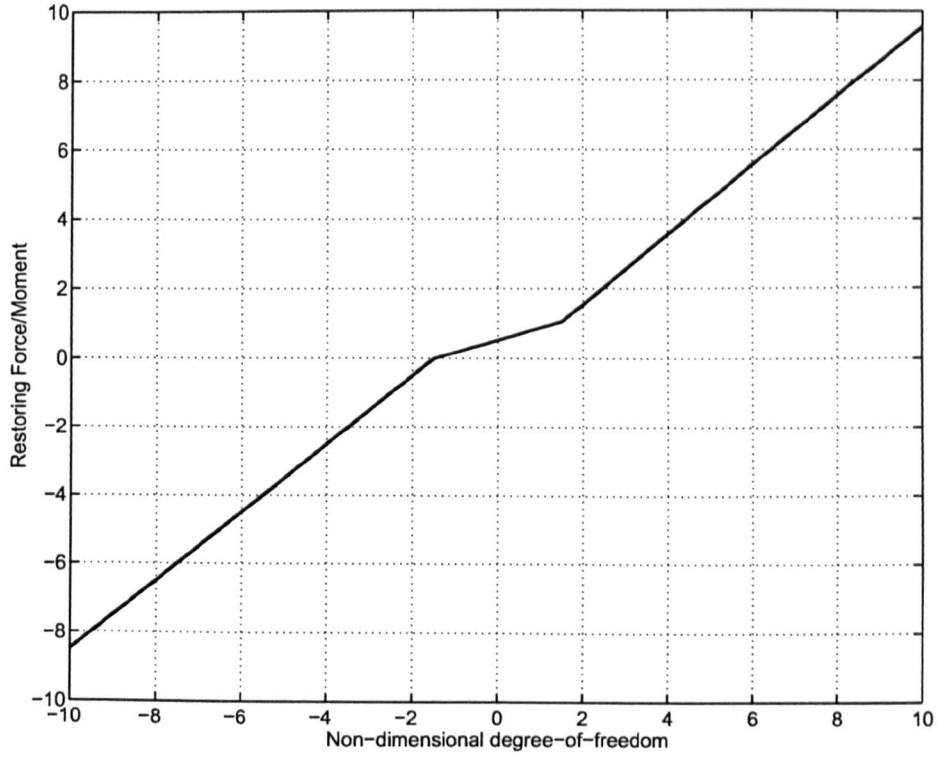

Fig 2.4: A General Bilinear Non-Linearity Curve

or freeplay non-linearity as shown in figure 2.5. Both the bilinear and backlash non-linearities are found within structural joints and bearing assemblies attached to control surfaces. These forms of piecewise-linear systems are observed not to affect the flutter velocity as, near the flutter boundary, amplitudes become large and the effect of the small freeplay region is negligible. Freeplay is of particular concern within control systems as the motion is uncontrollable within the freeplay region. As a result the effectiveness of normal control methodologies is unknown [23, 25]. With softening bilinear (central region is of lower stiffness) and freeplaying stiffnesses, fatigue is a considerable problem because limit-cycle oscillations (LCOs) can be observed at levels far below the calculated flutter velocity (sub critical LCOs)

A common extension to the study of non-linear aeroelastic is the addition of preload to the system which results in a force-displacement curve as shown in figure 2.6. This form of freeplay or backlash appears when the static position lies offset from the central region due to the steady forces, such as static masses/inertias and steady aerodynamic forces, acting on the system [26, 27, 45].

The major limitations to the efficient analysis of piecewise linear systems - such a systems containing bilinear and freeplay non-linearities - are that motions are initial condition dependent and the capture of switching points - points that separate the linear zones - is required to gain accurate solutions [44]. The initial condition dependence can also lead to a jumping

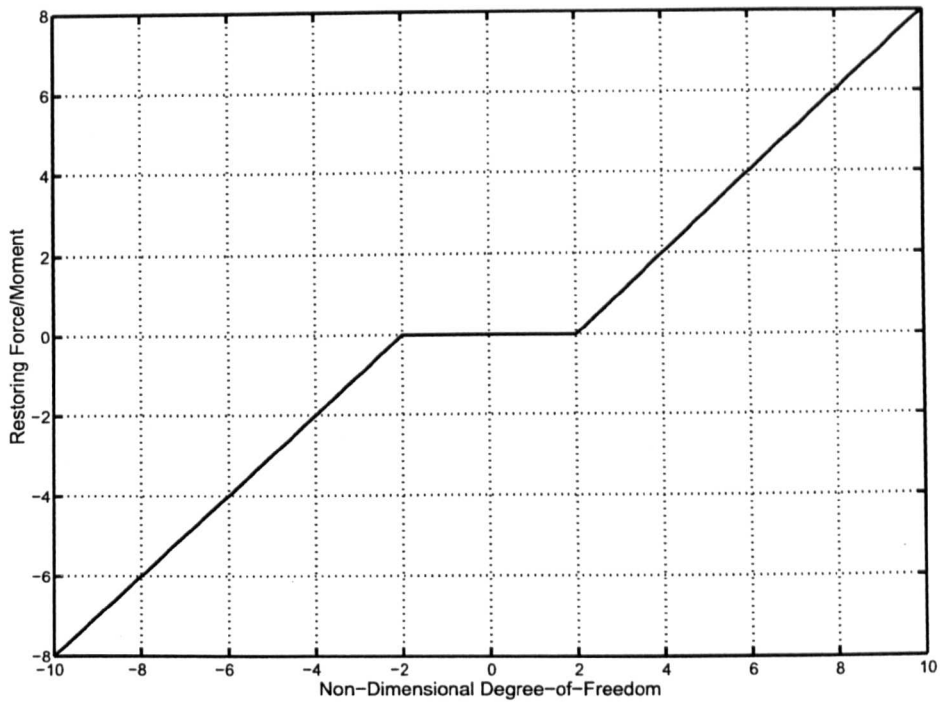

Fig 2.5: A General Backlash Non-Linearitiy Curve

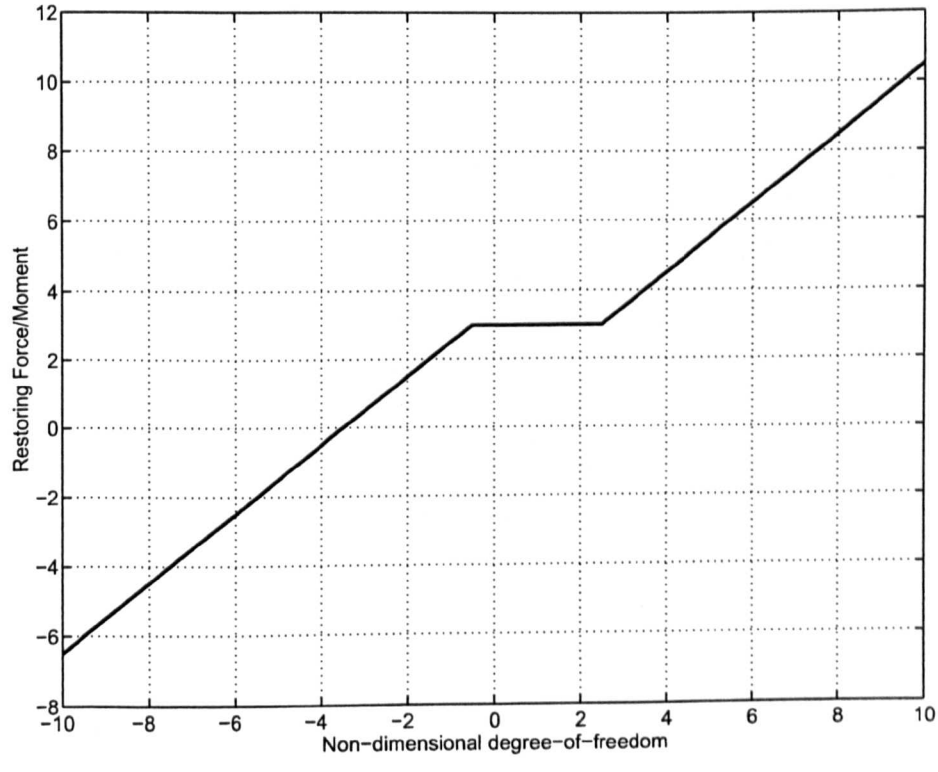

Fig 2.6: A General Backlash Non-Linearitiy Curve with Preload

phenomenon between different stable LCOs depending on the perturbation applied.

2.1.4.2 Analysis Techniques

The first study of bilinear stiffnesses was, as with the cubic stiffening non-linearities (section 2.1.3), performed by Woolston et al. [26, 27]. Analogue computing techniques and wind tunnel models were used to analyse a system free to pitch and plunge with a freeplay in the pitch degree-of-freedom. The major traits of the freeplay system were derived in this work: firstly the freeplay system does not affect the position of the flutter boundary compared to a system with the linear stiffness of the outer regions; secondly the limit-cycles that result from systems with freeplay are dependent on the initial conditions of the system states; thirdly, the system exhibits LCOs well below the linear flutter boundary. For large amounts of freeplay it was observed that the system effectively acted as a softening spring therefore showing traits similar to that of a softening cubic spring. Shen [28] extended this work through the use of the harmonic balance technique and established that the stability boundaries are significantly different depending on the amount of preload applied to the system. However, the use of the harmonic balance only allowed the analysis of super-harmonics of the fundamental frequencies, and as a result the sub-harmonics were not captured. The super- and sub-harmonics are defined as being oscillations that are of greater and lower amplitude than the fundamental respectively.

In 1977 Breitbach [32] revisited the field of structural non-linearities. The work studied freeplay non-linearities on a three degree-of-freedom (pitch, plunge and non-linear flap rotation) structural model with comparisons being made against wind tunnel results. The numerical analysis used harmonic balance techniques that replaced the original non-linear stiffness with an equivalent stiffness coefficient coupled with a damping loss angle. The comparative results were shown to match well for the limited number of cases illustrated.

Yang and Zhao [46] presented results for a two degree-of-freedom aerofoil section with a bilinear non-linearity in pitch. The results presented were from wind tunnel tests, harmonic balance and digital analyses. The digital analysis converted frequency domain methods into the time domain by using the feedback control theory representation of the system [47]. As the aerodynamics used included cumulative functions (as derived by Theodorsen [48]), lag functions were used as a method of feeding back the history terms. The authors concluded that the digital system provided exact solutions to the non-linear problem, unlike the harmonic balance technique, but was impractical as all possible initial conditions had to be simulated in order to capture all phenomena. As a further note, they also commented that the harmonic

balance was a more practically applied method as, for normal levels of structural damping, the sub-harmonic motions that are neglected in the technique are usually strongly filtered from the system. This point was further verified in that the harmonic balance results were, in general, closer to the experimental results than the digital results were. The ability to use the harmonic balance method to detect two or more stable and/or unstable LCOs for a given set of input parameters was also shown, i.e. initial condition dependency.

Price, Lee and Alighanbari [45] analysed a two degree-of-freedom system using Houbolts finite difference method applied to the aerodynamic equations from Fung [1]. Their studies looked at freeplaying systems both with and without preload, and for different initial conditions. In the study several methods of analysing the results were used, including time integration results, domain mapping, power spectral density (PSD) plots, phase plane plots and Poincaré sections. These thorough studies provided a good understanding of the system and highlighted inherent problems when analysing such systems. The domain mapping and time integrations showed the initial condition dependency observed by many authors, additionally it was noted that in order to map the complete domain it would require, for the test case used, a five dimensional graph. The PSD plots enabled the principal frequencies, including sub- and super-harmonics, to be identified with a largely broadband response seen for chaotic motions. The PSD results became easily visualised by the use of phase plane plots and Poincaré sections, with the dominant cycles being easily seen as loops and point clustering on the respective figures. Phase plane plots depict state versus state rate and allow oscillations to be seen as closed cycles. In the plots the sub harmonics are observed as small loops within the major loops and superharmonics clearly seen as large loops. The Poincaré section is a plane in multi-dimensional space where points are plotted as time simulations pass through it. Thus, these sections show clustering points as the motion tends towards a point on an LCO. The authors study of chaotic regions showed dependency on the relative mass of the aerofoil but damping was seen not to affect the chaotic region.

The work of Price et al. [45], described above, was extended in 1996 by Alighanbari and Price [49], who applied the principle of numerical continuation to the freeplay problem. The technique involved reworking of the basic aerodynamics described in [1] into a state-space form with a third-order rational approximation to the freeplay non-linearity. Using the AUTO software [50] the resultant systems of equations were studied, and both stable and unstable LCOs were rapidly identified. The continuation software uses a predictor/corrector method to track static and oscillatory solutions, with stability being assessed through the use of eigenvalues for stable solutions and Floquet multipliers for oscillatory solutions. The results from this methodology showed good correlation to the results previously generated using time-integration tech-

niques [45]. The methodology used, however, showed some weaknesses as no stable solutions were obtained over a range of velocities, this was attributed to chaotic motion but was later contradicted [7]. A second weakness was also observed as LCOs were seen to exist entirely within the freeplay region. This phenomenon cannot occur as the freeplay region is entirely linear, but is attributed to the rational approximation smoothing the discrete non-linearity.

The importance of accurate switching point identification was illustrated in a technical note by Conner et al. [51]. The paper showed that the solutions with and without boundary identification could show radically different forms, as often the sub-harmonics are not detected. The technique implemented follows from a paper by Henón [52] who developed a single step-back method to identify the boundary exactly, without requiring the iterative procedures that are often used to obtain accurate boundary capturing. Henóns method was then applied by Conner et al. [44] to a three degree-of-freedom testcase with freeplay in the flap. The work used the aerodynamics model derived by Edwards [2] to create a state-space model of the system with a wind tunnel test also being performed to validate the theoretical models results. Damping was incorporated within the model by performing wind off resonant frequency test on the wind tunnel model without the non-linearity. This technique allowed good results to be generated throughout the test range. The analysis of the experimental system with the harmonic balance was seen to be impossible as sub-harmonics were observed that cannot be captured using such techniques. As the harmonic balance technique would fail for such cases the authors decision to use time integration methods was validated. The experimental model showed some of the fatigue and wear properties associated with LCOs as the damping measured before and after the test differed by up to 12.5%. Later work by Tang et al. [53] used a reduced-order aerodynamic model derived from Peters [54] finite state model for two-dimensional flow on the testcase outlined above. The new aerodynamics showed slight improvement in correlation with experimental results.

Luber [43] presented one of the few analyses of in-service aircraft. The paper examined the amount of backlash and hysteresis measured in the rudder and taileron of the Tornado aircraft and then analysed the system using the harmonic balance method as used by Breitbach [31]. No overall conclusions were drawn in the paper except to say that the general methodology is in agreement with much of the previously performed analyses. The paper provided useful abbreviated information on the US military aeroelastic specifications for aircraft as outlined in the MIL-SPEC [55] (similarly for UK military aircraft the DEF-STAN [56]). The important specifications are defined as:

1. There shall be a fifteen percent equivalent airspeed margin on the applicable design limit

speed envelope, both at constant altitude and constant Mach number.

2. The damping coefficient, g (structural damping), for any critical flutter mode or for any significant dynamic response mode shall be at least three percent for all altitudes on flight speeds up to the design limit speed.

The wear limits defined in the specifications for control surfaces and tabs are defined in terms of freeplay and must be maintained throughout the aircraft's life, not just at the time of production. The specifications of freeplay vary between components, depending on how much control power the surfaces have on the rigid body dynamics. The limits are:

1. For a trailing edge control surface which extends outboard of the 75 percent span station of the main surface, the total freeplay shall not exceed 0.13^o or 0.0022 radians.

2. For an all-movable control surface, the total freeplay shall not exceed 0.034^o or 0.0006 radians.

3. For wing fold, the total freeplay shall not exceed 0.25^o or 0.0044 radians.

It can be seen that these specifications are very stringent and the definitions particularly emphasise the fatigue aspect of the problem. The tests performed by Luber on several aircraft rarely detected exceedence of their freeplay specifications for taileron motion and no exceedence for the rudder. Little information was given in the report relating to the correlation between model and actual aircraft results restricting the conclusions that could be drawn from the work.

Dimitriadis and Cooper [57] recently investigated the possibility of controlling a freeplaying system after performing simple energy analyses of the time histories. The work used a quasi-steady aerodynamics strip theory to analyse a three degree-of-freedom system with freeplay in control surface motion. The analysis made in the work acknowledged the occurrence of different limit-cycles depending on initial conditions but concentrated on the stability of these motions. By analysing the system's energy and the position of the control system when the energy was at its maximum, the relative stability of the stable LCOs could be derived. The work showed that by the application of chirp signals to the system it was possible to switch from the low amplitude to the high amplitude oscillatory system. The control implemented used a simple control surface rate feedback with gains calculated as the ratio of the maximum pitch rate to maximum pitch. The inclusion of this control system resulted in a rapid damping of the motion. However, the freeplay problem was constrained in this paper as the authors kept the freeplay position fixed whilst control surface actuation occurred. Such an assumption, although convenient, does not strictly represent the real system as the freeplay range is

a function of the control surface position and as a result is a much more complex system to analyse.

Clark et al. [23] developed a control system based on the model developed by Conner et al. [51]. This work acknowledged that conventional linear control methodologies can effectively attenuate most LCOs resulting from freeplay by converting the high amplitude low frequency oscillations in to low amplitude high frequency oscillations in the pitch and plunge degrees-of-freedom. This conclusion is related to the results drawn previously in the energy analyses of Dimitriadis and Cooper [57]. In this work it was noted that the flap amplitude of the controlled system was hardly affected whilst the frequency of oscillation was much larger than that of the uncontrolled system. This result is expected as control power over the freeplaying surface is lost whilst in the freeplay region. This means the flap motion must be quicker in order to compensate. Additionally, emphasis was also placed on minimisation of pitch rotation further amplifying this motion. The derivation of the control system used H_2-synthesis which generated the gains applied to the system via the minimisation of a cost function.

Tang et al. [58] analysed the response of three degree-of-freedom, freeplaying systems to gust excitation. The work compared results generated using a rotated slotted cylinder gust generator within a wind tunnel facility and theoretical models using the Peters finite state airload model [54] as used previously by the same authors [53]. The work concentrated on the system response to single harmonic and continuous frequency gusts (mimicking random gusts). A reasonable correlation was seen to occur between the wind tunnel and analytical results with the dominant frequency being identified accurately in most of the tests. Discrepancies in the system are thought to be attributed to the higher dominant frequencies where little correlation between theory and test is found.

Trickey, Virgin and Dowell [59] introduced a wide range of techniques for analysing results from both experimental tests and numerical analyses. Their paper gives a good overview of methods of analysis including bifurcation analysis, time responses and spectrograms. The latter technique is a form of power spectral density (PSD) diagram plotted against airspeed with the peaks in the PSD response being represented by colour intensities. For experimental models the authors introduced a penetration index scheme that allowed a linear map of the system to be created. This system is based on the Poincaré section - these results were also plotted in the paper - which is the equivalent of a fixed plane in multi-dimensional space with trajectories providing discrete points on the plane as the states pass through the plane during a time simulation. This technique leaves clusters of points from which information about the LCOs can be taken. The Poincaré section allows stability to be assessed by observing the

grouping of points that shows basins of attraction. The penetration index scheme proposed by Trickey et al. [59] takes the equivalent of several Poincaré sections and plots the dominant attractors against the penetration index. This allowed correlation between successive intervals to be made and a linear map generated. The paper also examined the nature of instabilities by examining the Floquet multipliers of the system and the way in which the eigenvalues left the stable unit radius circle. The results presented in the paper were very generalised but provide a good foundation for future development of experimental analytical techniques including online monitoring of experimental systems.

Wong et al. [7] presented a new method for the analysis of piecewise linear aeroelastic systems by the use of the point transformation method. This is similar to a method developed separately in this work. The method exactly captures the switching point between different linear regimes, an essential criterion identified by Conner et al. [44]. This scheme assumed that the aerodynamic models used are linear for the range of interest and therefore there exists a unique solution to the state-space formulation of the equations of motion for the separate linear regions. Using this fact it becomes possible to solve the equations in order to satisfy the switching point conditions. As a result, a time simulation can be performed by stepping from one switching point to the next switching point. The drawbacks to such a methodology is the requirement that a numerical, iterative method must be used in order to capture the switching point precisely as multiple solutions are possible, and the further problem of initial condition dependency problem is not solved. Such a method, however, is a large step towards a more rapid system analysis methodology as described later in this work. Further details of this technique can also be found in [60, 61].

Alighanbari and Lee [62] performed research into experimental analysis of freeplaying systems. Their work recognised that non-linear phenomena in flight-test data can often be overlooked as the chaotic and small amplitude LCOs characteristics, associated with non-linear structures, can be falsely attributed to noise within the signal analysis. The method introduced in their paper reconstructs phase plane diagrams from the mutual information function and analysis of the false neighbours. Their worked showed that the data could be successfully extracted given sufficiently accurate data measurements.

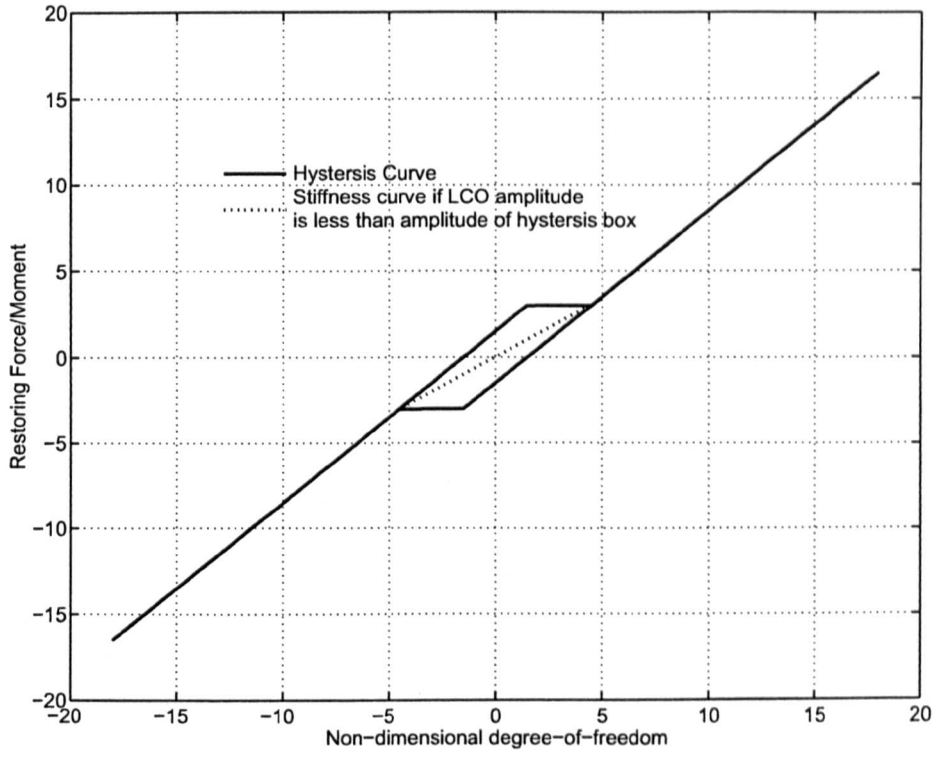

Fig 2.7: A Hysteresis Non-Linearitiy Curve

2.1.5 Hysteresis Non-Linearities

2.1.5.1 Overview

An hysteresis form of non-linearity, as shown in figure 2.7, occurs in systems with general non-linear stiffness coupled with solid friction type damping. Hysteresis characteristics are linear variations of displacement with applied force until a jump in displacement occurs for a small increase in force. If the force is further increased the displacement again varies linearly. When the force is gradually removed the phenomenon repeats itself except that the point at which the jump occurs is at a lower value. This type of motion is analogous to a freeplay non-linearity with preload, except for the change in jumping point, therefore, the characteristics observed in such systems are similar. Analysis of hysteretic motions has received relatively little attention as its form does not lend itself to simple analysis. When the amplitude of the motion is low it is usually assumed that the force-displacement curve is linear and bisects the hysteresis loop, as shown in figure 2.7.

Hysteresis non-linearities occur at low levels in most systems but can become significant in the yaw pivot of variable wing sweep aircraft. Examples of such non-linearities have been observed in both the F-111 [30] and Tornado [43] aircraft. As with many forms of non-linearities the dependency of the system initial conditions means thorough analysis must be performed

in order to ensure all possible LCOs are captured.

2.1.5.2 Analysis Techniques

The first work on hysteresis type non-linearities, as with the previous two sections, was performed by Woolston et al. [26, 27]. The work looked at hysteresis type non-linearities that occurred in aircraft wings due to rivet slip (such non-linearities are rarer today due to modern manufacturing techniques and materials). This work was based on analogue computing and showed the trend of variable amplitude of the motion depending on damping. The variable damping is expected because, for small amplitudes, the system is linear and the stiffness curve passes through the hysteresis loop, and for large amplitude oscillations the small range over which hysteresis occurs hardly affects the motion. The effects of hysteresis are only seen fully for intermediate levels of oscillation in which the system spends a large proportion of its time going around the hysteresis loop. The hysteresis, like the freeplay non-linearity, was shown to have little affect on the flutter velocity as the amount of hysteresis is negligible in comparison to the amplitude of the oscillations near flutter.

Breitbach [32] presented an example of an hysteresis non-linearity which developed on a glider aircraft aileron hinge, when a typical backlash type non-linearity was placed under preload. The general tendencies of the system are observed to be similar to an offset cubic curve. A further realistic system was presented for the same aircraft's rudder which showed a much more frictional tendency with very high ratios between the various bilinear stiffness regions. In the presentation of the results the assumption of linear stiffness within the hysteresis box is seen to be invalid as the hysteresis curves were seen to simply scale downwards (e.g. see figure 2.8, note that in practical situations rounding of the intersections between the vertical and horizontal sections was observed). Hysteretic systems therefore act much like a classical backlash non-linearity where change in velocity coincides with freeplay position. The case studied concentrated on a linear representation of the hysteresis non-linearity, as shown in figure 2.7, and a case with offset bilinear stiffness curves. The tendencies observed by the authors were, again, similar to those observed in the freeplay cases studied. The technique employed was the harmonic balance method which restricted the isolation of oscillations to super harmonics of the fundamental frequencies.

Ferrari et al. [63] and Luber [43] presented work on the backlash present in Tornado aircraft in both the yawing pivots and the store pivots. Both motions showed the basic hysteresis tendencies although, as with the work of Breitbach [32], the cubic stiffening effects were also

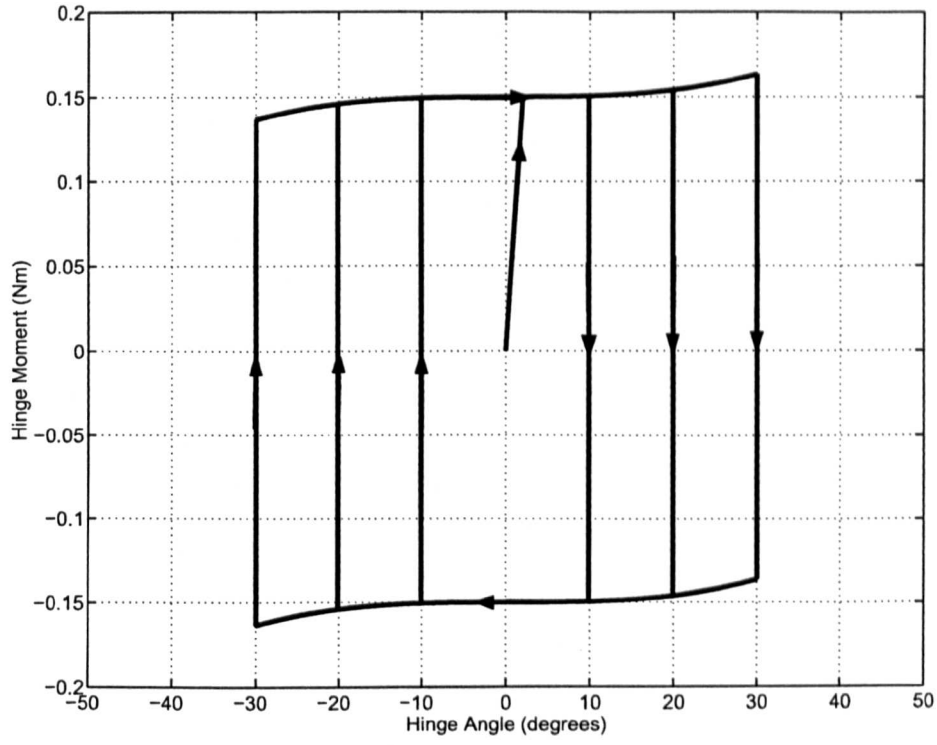

Fig 2.8: Displacement within the Hysteresis Loop

observed. The authors of both papers utilised the harmonic balance technique in order to analyse the tendencies of the structure and compared their results with flight data. Ferrari et al. [63] showed reasonable correlation when comparing store damping values for both analyses, although the flight test data showed different tendencies depending on the form of excitation (either longitudinal or lateral). From their work, Ferrari et al. [63] concluded that the inclusion of non-linearities was not important when calculating aircraft flutter boundaries but presented some fatigue issues. Additionally it was thought that the oscillatory tendencies below the flutter boundary were not significant enough to effect aircraft handling qualities. The results generated by Luber [43] were again reasonable when compared to flight test data but could be further improved. Overall both Luber [43] and Ferrari et al. [63] concluded that the basic trends could be observed in their analysis but more accurate modelling of both aerodynamics and structure were required.

In the work of Chan [64] and the later review by Lee et al. [30] results of time simulations of two degree-of-freedom aeroelastic systems in low-speed flow were presented. A time integration method was used, with the aerodynamics being based on those derived by Lee et al. [35]. This work showed the advantage of time simulations over harmonic balance techniques with more detail of the limit-cycle oscillations being captured than is possible with harmonic balance techniques. However, the authors did comment that the use of higher order approximations such as those used by Johnson [65] give much closer results. The techniques applied

by the author are seen to be very time consuming with a large number of time-integration runs having to be performed in order to map the whole domain of possible solutions. The authors also observed a lowering of the flutter boundary depending on the initial displacement applied to the system. The tendency to lower the flutter boundary seems to the author to be an incomplete assumption as factors such as mass and ratio of heave and pitch frequencies were changed simultaneously. As these factors are known to alter the flutter boundaries independently the conclusions cannot be clearly drawn. It was also observed that the amounts of freeplay within the system were above realistic system levels ($\pm 2.5^o$ c.f. $\pm 0.25^o$ for operational aircraft).

Wong et al. [7] and Liu et al. [61] used a point transformation technique to identify limit-cycles within piecewise linear aeroelastic systems. This technique uses the linear nature of the hysteresis in the various sections to solve the aeroelastic equations of motion exactly at the system boundaries. The result of this system leads to a highly accurate method for capturing limit-cycles but, although faster than time integration techniques, still requires integration techniques to be applied and does not overcome the dependency of resultant motion on initial conditions

2.1.6 Combined Non-Linearities

The combination of the non-linearities as outlined in the previous sections has, as far as the author is aware, had no coverage. Non-linearities that feature freeplay, bilinear softening or hysteresis coupled with cubic stiffening have not been researched, although many papers [26, 27, 31, 43, 63] show realistic systems with the effects of these types of non-linearities. Figures 2.9 and 2.10 show some of the combined effects. The effect of these non-linearities is thought to include both pre- and post-flutter trends as, below the linear flutter velocity, the freeplaying motion causes oscillation whilst, above the linear flutter velocity, the cubic stiffening effect delays the flutter onset.

The limitations on the study of combining such non-linearities has been highlighted over the previous section. These are that, with the exception of time integration techniques, the techniques are usually aimed at smooth systems such as cubic non-linearities or at piecewise linear non-linearities. The methods outlined in the previous sections are mutually exclusive and therefore the application to piecewise non-linear systems is not possible.

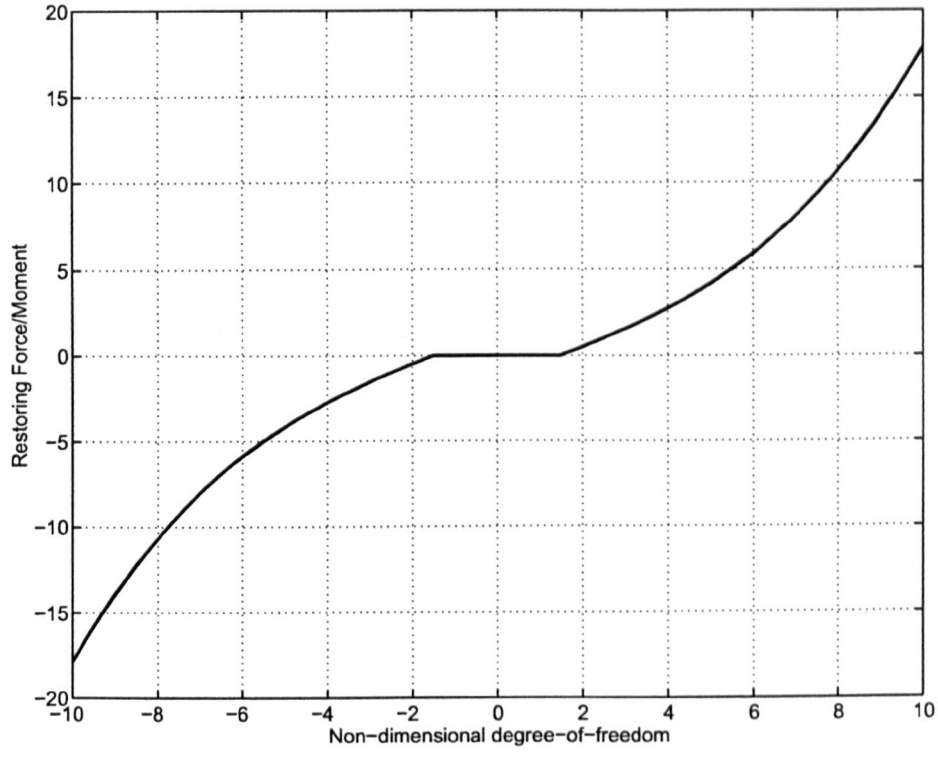

Fig 2.9: A Combined Backlash and Cubic Non-Linearitiy Curve

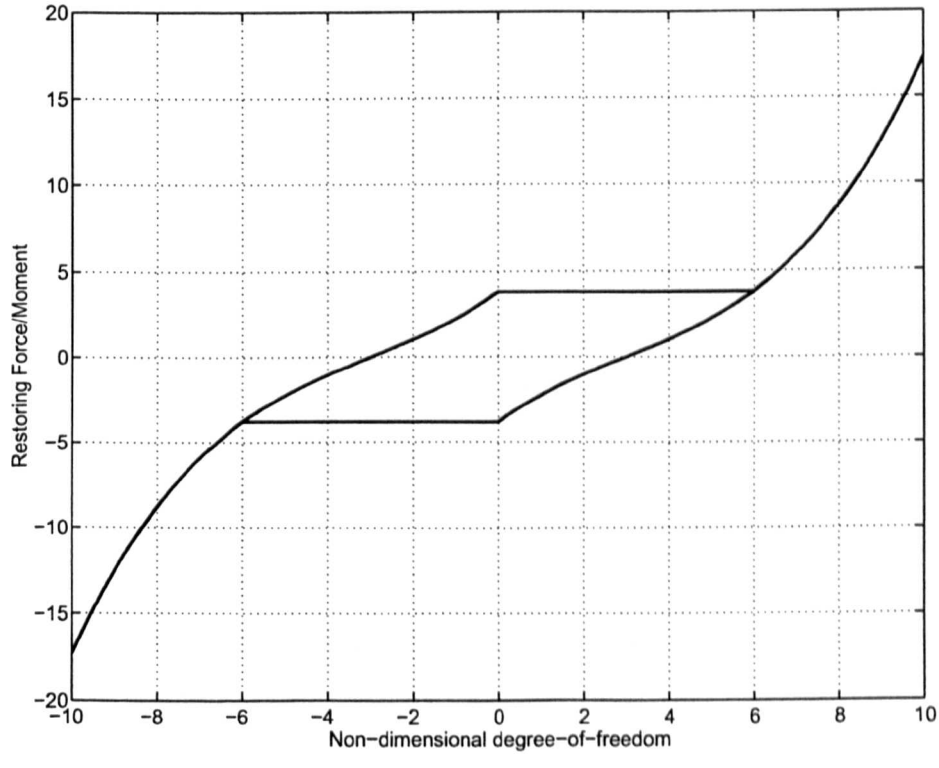

Fig 2.10: A Combined Hysteresis and Cubic Non-Linearitiy Curve

2.1.7 Structural Equations of Motion

The equations of motion for any dynamic system are based upon Lagrange's equation. This equates the externally applied virtual work (aerodynamic work) with the internally dissipated energy (kinetic, potential and frictional energy). Lagrange's equation is therefore given by,

$$\frac{d}{dt}\left(\frac{\partial(\boldsymbol{KE})}{\partial \dot{q}_i}\right) - \frac{\partial(\boldsymbol{KE})}{\partial q_i} + \frac{\partial(\boldsymbol{PE})}{\partial q_i} + \frac{\partial(\boldsymbol{DE})}{\partial \dot{q}_i} = \frac{\partial \boldsymbol{W}}{\partial q_i} \tag{2.3}$$

where

q_i =General Coordinates

$\boldsymbol{KE}$=Kinetic Energy

$\boldsymbol{PE}$=Potential (Elastic) Energy

$\boldsymbol{DE}$=Dissipative (Frictional) Energy

∂q_i =Virtual Displacement of q_i

$\partial \boldsymbol{W}$=Virtual External Energy

For a general n-dimensional aeroelastic system the various forms of energy are,

$$\boldsymbol{KE} = \frac{1}{2}\mathrm{M}\dot{q}_i^2 \tag{2.4}$$

$$\boldsymbol{PE} = \frac{1}{2}\mathrm{K}q_i^2 \tag{2.5}$$

$$\boldsymbol{DE} = \frac{1}{2}\mathrm{B}\dot{q}_i^2 \tag{2.6}$$

$$\partial \boldsymbol{W} = \boldsymbol{F}\partial q_i \tag{2.7}$$

where M, K and B are the mass, stiffness and damping matrices respectively and $\boldsymbol{F}$ is a vector of input forces. In multi degree-of-freedom systems the damping and stiffness matrices are largely diagonal, i.e. there is no cross coupling between the equations of the various degrees-of-freedom, but the mass terms involve full coupling as there are off diagonal terms involved. Occasionally, some of the off diagonal terms may be neglected when they are small relative to the on diagonal terms.

Applying Lagrange's equation to the energy representations results in the fundamental dynamic equation of motion,

$$\mathrm{M}\ddot{\boldsymbol{q}} + \mathrm{B}\dot{\boldsymbol{q}} + \mathrm{K}\boldsymbol{q} = \boldsymbol{F} \tag{2.8}$$

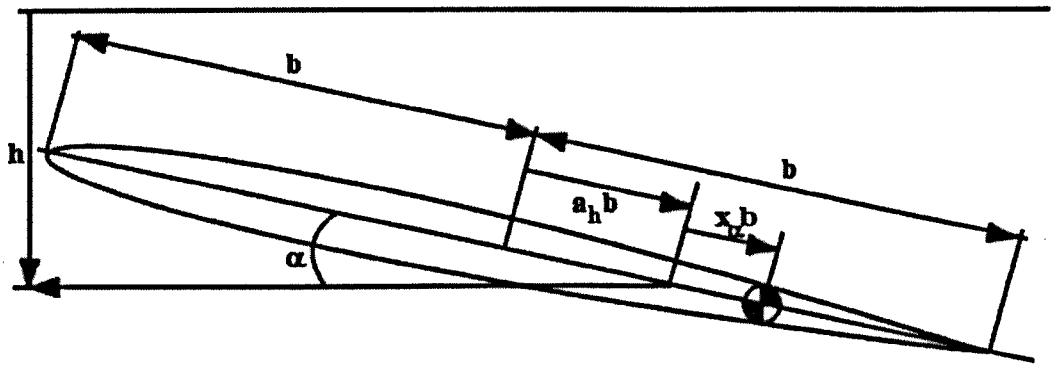

Fig 2.11: Two Degree-of-Freedom Aerofoil Testcase

2.1.8 Test Cases - Two and Three Degree-of-Freedom Aerofoil Sections

2.1.8.1 Linear Equations

The first form of testcase used in this work is based upon a simple two degree-of-freedom aerofoil model, as shown in figure 2.11 whose equations of motion are,

$$\begin{aligned} m\ddot{h}(t) + mx_\alpha b\ddot{\alpha}(t) + c_h\dot{h}(t) + k_h h(t) &= P(t) \\ mx_\alpha b\ddot{h}(t) + mr_\alpha^2 b^2\ddot{\alpha}(t) + c_\alpha\dot{\alpha}(t) + k_\alpha\alpha(t) &= R(t) \end{aligned} \tag{2.9}$$

m	aerofoil mass
r_α	aerofoil radius of gyration
$x_\alpha b$	distance of centre-of-gravity, aft of elastic axis
$c_{h/\alpha}$	damping in heave/pitch
$k_{h/\alpha}$	stiffness in heave/pitch
$P(t)$	external force applied vertically
$R(t)$	external moment applied around the elastic axis

Using this formulation it becomes possible to apply various aerodynamic models by replacing $P(t)$ and $R(t)$ by the calculated lift (strictly negative lift as heave is positive downwards) and moment.

The second testcase is a three degree-of-freedom aerofoil section with a control surface, as shown in figure 2.12. This testcase extends the equation of motions for the two degree-of-freedom system to,

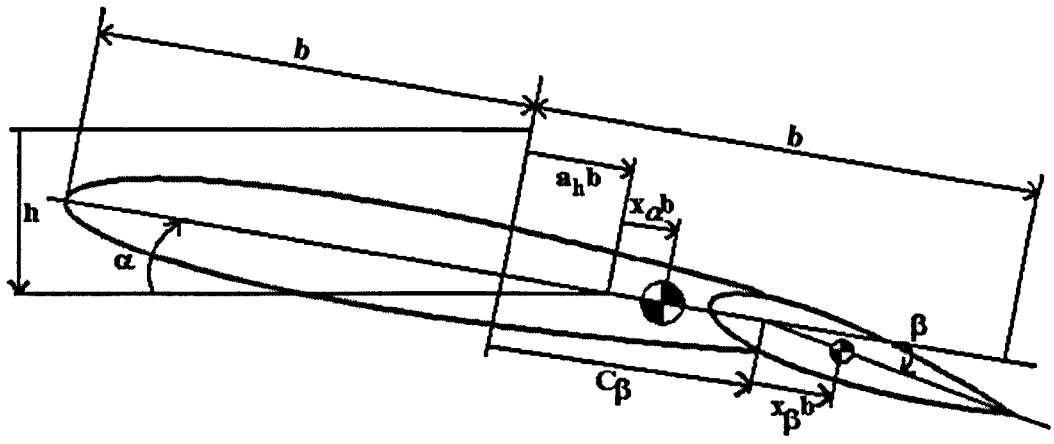

Fig 2.12: Three Degree-of-Freedom Aerofoil Testcase

$$
\begin{aligned}
m\ddot{h}(t) + mx_\alpha b\ddot{\alpha}(t) + mx_\beta b\ddot{\beta}(t) + c_h\dot{h}(t) + k_h h(t) &= P(t) \\
mx_\alpha b\ddot{h}(t) + mr_\alpha^2 b^2\ddot{\alpha}(t) + [(C_\beta - a_h)mx_\beta b^2 + mr_\beta^2 b^2]\ddot{\beta}(t) + c_\alpha\dot{\alpha}(t) + k_\alpha\alpha(t) &= R(t) \\
mx_\beta b\ddot{h}(t) + [(C_\beta - a_h)mx_\beta b^2 + mr_\beta^2 b^2]\ddot{\alpha}(t) + mr_\beta^2 b^2\ddot{\beta}(t) + c_\beta\dot{\beta}(t) + k_\beta\beta(t) &= Q(t)
\end{aligned}
\tag{2.10}
$$

r_β	control surface radius of gyration about hinge line
$C_\beta b$	distance of hinge line aft of aerofoil mid chord
c_β	damping in control surface rotation
k_β	rotational stiffness about hinge
$Q(t)$	external moment applied about the hinge

2.1.8.2 Non-Linear Equations

When non-linear stiffnesses are present within the system the terms defined as $k_h h$, $k_\alpha \alpha$ and $k_\beta \beta$ must be replaced with their equivalent non-linear representations $M(h)$, $G(\alpha)$ and $N(\beta)$. The systems may contain non-linearities in more than one of these degrees-of-freedom, but the general tendencies are that the non-linearities occur in the α and/or β degrees-of-freedom. When non-linearities occur in both of the rotational states this would simulate an all-moving tailplane with a control tab, which could both contain the same or different forms of non-linearities in their control systems.

The equations for the non-linearities outlined in the previous sections are described below

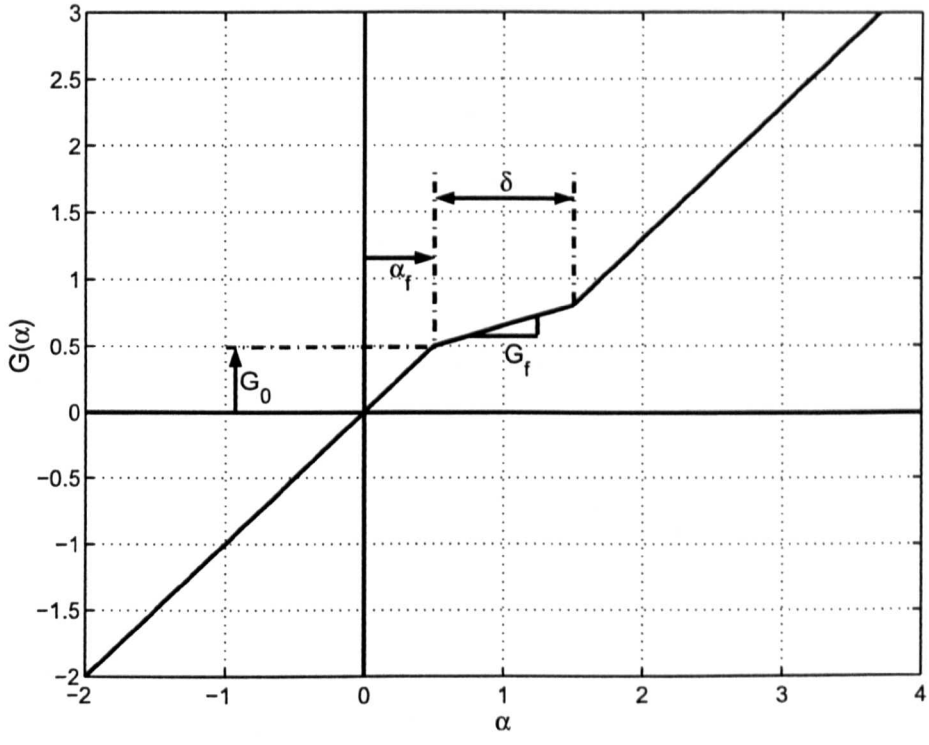

Fig 2.13: Bilinear Stiffness Non-Linearity

for the α state in terms of $G(\alpha)$ but are equally applicable to the other states by replacing α with h or β and $G(\alpha)$ with $M(h)$ or $N(\beta)$. For a polynomial spring, of which cubic stiffening/softening is a subset, the formulation is,

$$G(\alpha) = \sum_{i=1}^{N} \psi_i \alpha^i \tag{2.11}$$

where N is the order of the polynomial and ψ_i are constants defining the degree of non-linearity. For a bilinear spring,

$$G(\alpha) = \begin{cases} G_0 + \alpha - \alpha_f & \text{for} \quad \alpha < \alpha_f \\ G_0 + G_f(\alpha - \alpha_f) & \text{for} \quad \alpha_f \leq \alpha \leq \alpha_f + \delta \\ G_0 + \alpha - \alpha_f + \delta(G_f - 1) & \text{for} \quad \alpha > \alpha_f + \delta \end{cases} \tag{2.12}$$

where G_0, G_f, α_f and δ are constants shown in figure 2.13. For the hysteretic spring, shown

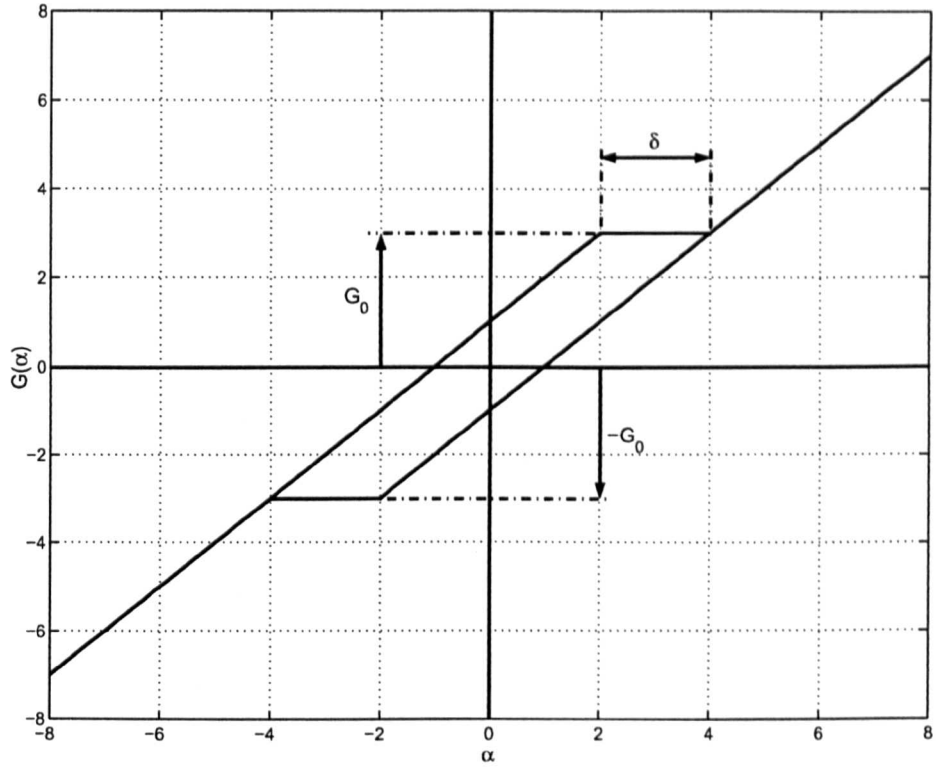

Fig 2.14: Hysteresis Stiffness Non-Linearity

in figure 2.14, the restoring force is described as,

$$G(\alpha) = \begin{cases} \alpha - \alpha_f + G_0 & \text{for } \alpha < \alpha_f \text{ and } \dot{\alpha} > 0 \\ \alpha + \alpha_f - G_0 & \text{for } \alpha > -\alpha_f \text{ and } \dot{\alpha} < 0 \\ G_0 & \text{for } \alpha_f \leq \alpha \leq \alpha_f + \delta \text{ and } \dot{\alpha} > 0 \\ -G_0 & \text{for } -\alpha_f - \delta \leq \alpha \leq \alpha_f \text{ and } \dot{\alpha} < 0 \\ \alpha - \alpha_f - \delta + G_0 & \text{for } \alpha > \alpha_f + \delta \text{ and } \dot{\alpha} > 0 \\ \alpha + \alpha_f + \delta - G_0 & \text{for } \alpha < -\alpha_f - \delta \text{ and } \dot{\alpha} < 0 \end{cases} \tag{2.13}$$

where G_0, G_f, α_f and δ are constants. For a combined cubic and bilinear non-linearity as shown in figure 2.15, the equations become,

$$G(\alpha) = \begin{cases} G_0 + (\alpha - \alpha_f)(1 + \psi_3(\alpha - \alpha_f)^2) & \text{for } \alpha < \alpha_f \\ G_0 + G_f(\alpha - \alpha_f) & \text{for } \alpha_f \leq \alpha \leq \alpha + \delta \\ G_0 + \delta G_f + [\alpha - (\alpha_f + \delta)](1 + \psi_3[\alpha - (\alpha_f + \delta)]^2) & \text{for } \alpha > \alpha_f + \delta \end{cases} \tag{2.14}$$

where ψ_3 is the weighting term of the cubic.

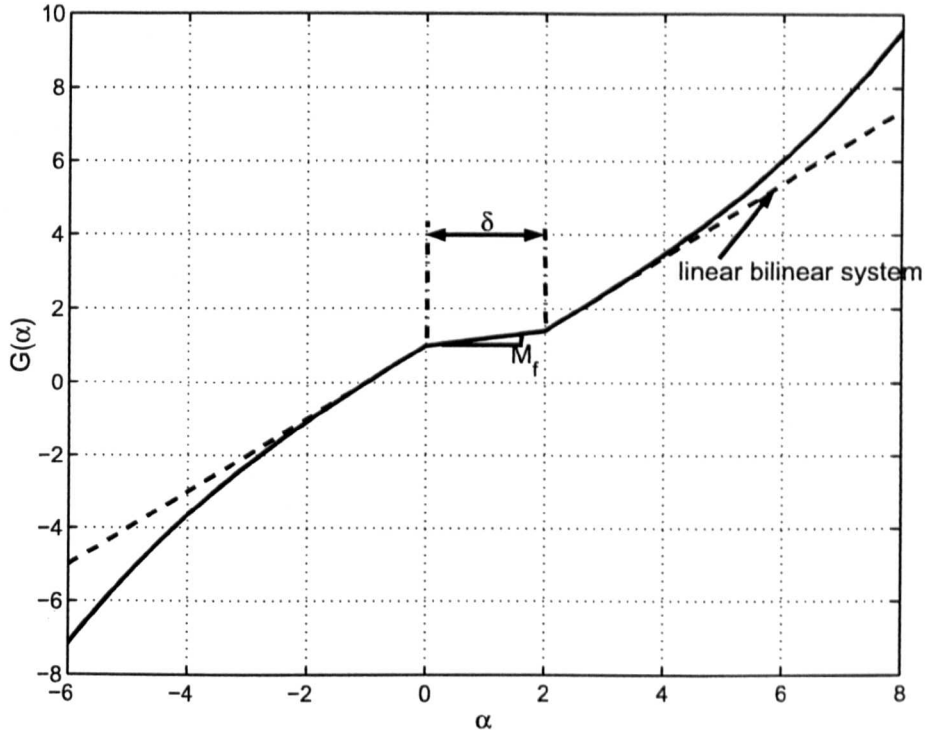

Fig 2.15: Combined Bilinear and Cubic Stiffness Non-Linearity

For all the equations outlined above, the non-linear systems are non-dimensionalised to give a slope (stiffness) of unity for the outer linear portions of the hysteresis and bilinear non-linearities and for $\psi_3 = 0$ for cubic systems. These systems can, however, be scaled by multiplying by a factor k_α that is the equivalent linear system stiffness (similarly k_h and k_β for non-linearities in heave and flap rotation).

2.2 Aerodynamics

2.2.1 Introduction

In the work described in this thesis four basic aerodynamics models have been used. The first two are derived from the same low-speed incompressible flow model and are therefore only applicable for freestream Mach numbers below approximately 0.2 (note the second model can be extended to supersonic flows). The third model is a time accurate finite-volume code based on the non-linear Euler equations that can be applied to subsonic, transonic and supersonic flows. Finally, the fourth model is a Reduced Order Model (or ROM) derived from the non-linear Euler code and has the same range of applicability. The purpose of a ROM is to give low

cost solutions which are close approximations to those generated using the full Euler equations. The low-speed models were chosen as they are well established and testcases are available for comparative purposes. The third and fourth models were used for flows in the transonic region as this is where many of the structural non-linearities become problematic because of high surface loads. The method for obtaining ROMs has only recently been developed and they are particularly useful as they allow techniques usually used for low-speed analysis to be applied to transonic problems. The following sections provide brief mathematical descriptions of the models along with some comments on their applicability for various testcases.

2.2.2 Incompressible Flow Modelling

2.2.2.1 Fung's Method [1]: Incompressible Model for Two Dimensional, Two Degree-of-Freedom Aerofoil Sections

The first model to be used is described by Fung [1] and is based on the unsteady aerodynamic forces acting on a thin aerofoil in a two-dimensional incompressible fluid. The derivation of Fung's model is based on the equations derived by Wagner, Küssner, von Kármán, Sears and many other authors [66, 67, 68, 48]. The formulations presented are derived for a two degree-of-freedom aerofoil section only and applicability is limited to velocities below, approximately, Mach 0.2.

The aerodynamic model assumes that the aerofoil is "thin" and that its angle to the flow is small, therefore the approximation $sin\alpha = \alpha$ is valid. As the motion starts impulsively from rest, with a forward velocity of U, the "downwash" on the aerofoil is, $w = U\alpha$. Combining this with the practical assumption that the flow leaves the trailing edge with a finite velocity, the lift due to circulation is

$$L_1 = 2\pi b\rho U w \Phi(\tau), \tag{2.15}$$

where b is the length of the semi-chord, ρ is the air density and τ is the non-dimensional time.

$$\tau = Ut/b \tag{2.16}$$

$\Phi(\tau)$ is called Wagner's function and is illustrated in figure 2.16. In this work Jones' approximation to the function is used

$$\Phi(\tau) = 1 - 0.165e^{-0.0455\tau} - 0.335e^{-0.300\tau} \tag{2.17}$$

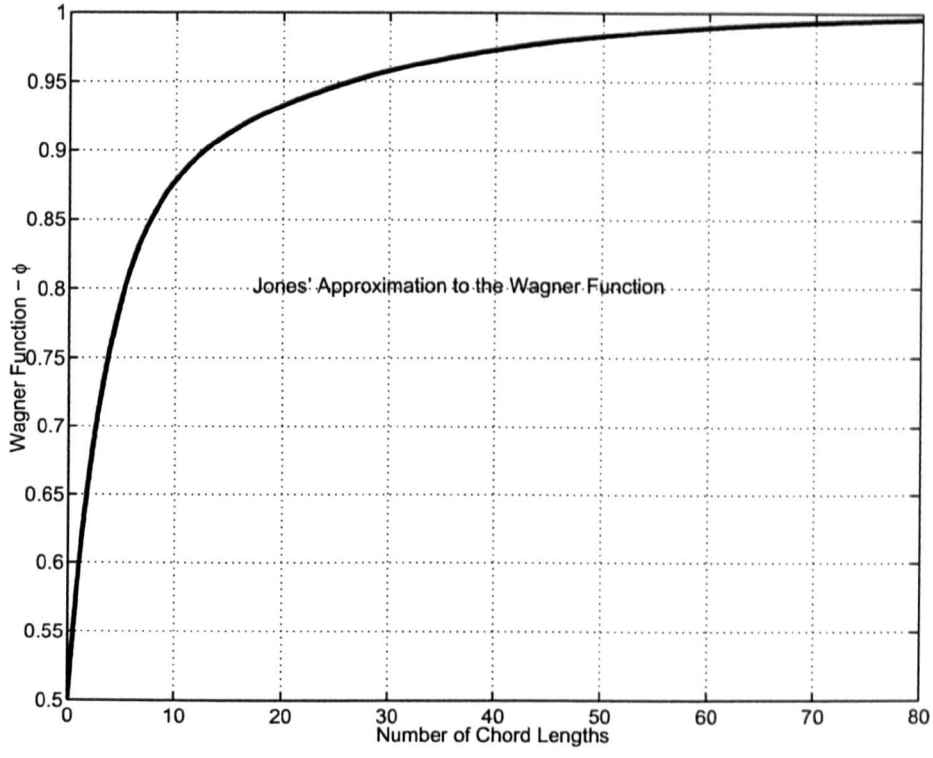

Fig 2.16: The Wagner Function

The methods of analysis, to be described later, require the combined aero-structural equations be formulated into sets of Ordinary Differnetial Equations (ODEs). To convert the equations in to the ODE form it is necessary to define four new states to replace the integral terms. These were proposed by Lee et al. [35] and are given by

$$\begin{aligned} w_1 &= \int_0^\tau e^{-0.0455(\tau-\tau_0)}\alpha(\tau_0)d\tau_0 \\ w_2 &= \int_0^\tau e^{-0.300(\tau-\tau_0)}\alpha(\tau_0)d\tau_0 \\ w_3 &= \int_0^\tau e^{-0.0455(\tau-\tau_0)}\xi(\tau_0)d\tau_0 \\ w_4 &= \int_0^\tau e^{-0.300(\tau-\tau_0)}\xi(\tau_0)d\tau_0 \end{aligned} \tag{2.18}$$

where α is the pitch of the aerofoil and ξ is its heave (positive downwards) non-dimensionalised with respect to semi-chord ($\xi = h/b$). In order to calculate the lift due to circulation, the downwash w is replaced by the increment of downwash at the $3/4$-chord point. The downwash comprises of three components; a downwash due to the pitch angle ($w = U\alpha$ assuming small angles), a downwash due to vertical translation ($w = \frac{U}{b}h'$ where a prime $'$ denotes a differentiation with respect to non-dimensional time, τ) and a non-uniform downwash due to pitch rate, $\dot{\alpha}$ ($w = \left(\frac{1}{2} - a_h\right)U\alpha'$). Note that differentiation with respect to physical time is represented by an overdot. In this equation $a_h b$ is the distance of the elastic axis aft of the

semi-chord. Summing the values of the downwash the circulation becomes,

$$w(\tau) = U\alpha(\tau) + \frac{U}{b}h'(\tau) + (\frac{1}{2} - a_h)U\alpha' \tag{2.19}$$

The increment in the downwash at the 3/4-chord at a given time τ_0 can be calculated and, from this, the lift due to circulation is,

$$L_1(\tau) = 2\pi b\rho U^2 \int_{-\infty}^{\tau} \Phi(\tau - \tau_0) \left[\alpha'(\tau_0) + \frac{1}{b}h''(\tau_0) + \left(\frac{1}{2} - a_h\right)\alpha''(\tau_0)\right] d\tau_0 \tag{2.20}$$

In addition to the circulatory lift, there is a lift force at the mid-chord equivalent to the apparent mass, $\rho\pi b^2$, times the vertical acceleration at the mid-chord. This lift is given by

$$L_2 = \rho\pi U^2(h'' - a_h b\alpha'') \tag{2.21}$$

Also a lift force exists at the 3/4-chord point, which accounts for the force that balances the apparent mass times the outward acceleration on the aerofoil. This is calculated as,

$$L_3 = \rho\pi b U^2\alpha' \tag{2.22}$$

From these results the moment is calculated as,

$$M = (\frac{1}{2} + a_h)bL_1 + a_h bL_2 - (\frac{1}{2} - a_h)bL_3 + M_a \tag{2.23}$$

where M_a is a couple equivalent to the apparent moment of inertia times the angular acceleration,

$$M_a = -\frac{\rho\pi b^2 U^2}{8}\alpha'' \tag{2.24}$$

From these equations the resultant lift and moment coefficients about the elastic axis are,

$$\begin{aligned} C_L(\tau) &= \pi(\xi'' - a_h\alpha'' + \alpha') + 2\pi\{\alpha(0) + \xi'(0) + (\frac{1}{2} - a_h)\alpha'(0)\}\phi(\tau) \\ &\quad + 2\pi\int_0^{\tau} \phi(\tau - \tau_0)(\alpha'(\tau_0) + \xi''(\tau_0) + (\frac{1}{2} - a_h)\alpha''(\tau_0))d\tau_0 \end{aligned} \tag{2.25}$$

$$\begin{aligned} C_M(\tau) &= \pi(\frac{1}{2} + a_h)\{\alpha(0) + \xi' + (\frac{1}{2} - a_h)\alpha'(0)\}\phi(\tau) \\ &\quad + \pi(\frac{1}{2} + a_h)\int_0^{\tau} \phi(\tau - \tau_0)(\alpha'(\tau_0) + \xi''(\tau_0) + (\frac{1}{2} - a_h)\alpha''(\tau_0))d\tau_0 \\ &\quad + \frac{\pi}{2}a_h(\xi'' - a_h\alpha'') - (\frac{1}{2} - a_h)\frac{\pi}{2}\alpha' - \frac{\pi}{16}\alpha'' \end{aligned} \tag{2.26}$$

Using the augmented states given in equation 2.18, Lee et al. [35] constructed a set of equations that define the lift and moment for arbitrary motions in heave and pitch,

$$c_0\xi'' + c_1\alpha'' + c_2\xi' + c_3\alpha' + c_4\xi + c_5\alpha + c_6 w_1 + c_7 w_2 + c_8 w_3 + c_9 w_4 = f(\tau) \tag{2.27}$$

$$d_0\xi'' + d_1\alpha'' + d_2\xi' + d_3\alpha' + d_4\xi + d_5\alpha + d_6 w_1 + d_7 w_2 + d_8 w_3 + d_9 w_4 = g(\tau) \tag{2.28}$$

The coefficients $c_0, \cdots, c_9, d_0, \cdots, d_9$ and $f(\tau), g(\tau)$ are given in Appendix A. In these equations $f(\tau)$ and $g(\tau)$ are functions dependent on initial conditions and Wagner's function. These can be neglected for large values of τ as any transients would be damped out.

These equations are to be coupled with the structural equations in section 2.1.8 to allow a state-space model of the complete aeroelastic system to be created including any non-linearities that may be present within the structure. As the terms $f(\tau)$ and $g(\tau)$ contain initial condition dependency terms, care has to be taken when implementing control analyses. For simplicity, it is assumed that the system has either been in motion for a long time and therefore the transients have decayed or the initial displacements must be set to zero and any initiating impulses applied in the velocity terms. Using this technique, generality is not lost, model construction is simplified and the advantages of state-space modelling can be embraced.

2.2.2.2 Edwards' Method [2]: Incompressible Model for Two-Dimensional Three Degree-of-Freedom Aerofoil Sections

The method derived by Edwards et al. [2] is based on the same theory as that presented by Fung [1] and derived in the previous section. By using the Padé approximations to the simple harmonic loads, Edwards et al. [2] was able to represent the rational components of the circulatory lift by two additional ordinary differential equations and two augmented states. As for the previous model, the system derived allows a state-space model of the aeroelastic system to be constructed. The model derived by this method is for a three degree-of-freedom aerofoil section with the freedoms in heave, pitch and flap rotation. This technique is only applicable to low-speed incompressible fluid flows (below approximately Mach 0.2), but the author also presented a methodology that is applicable to compressible supersonic flow (for further details see [69]).

The Laplace domain representation of equations 2.20, 2.21 and 2.22 are,

$$L_{nc} = \pi\rho b^2 \left[\ddot{h} + U\dot{\alpha} - a_h b\ddot{\alpha}\right] \tag{2.29}$$

$$L_r = 2\pi\rho bU \left[\dot{h} + U\alpha + b(\frac{1}{2} - a_h)\dot{\alpha} - \sum_{i=1}^{n} Res\phi(\bar{s})Q(s)e^{st}|_{s=s_i}\right] \tag{2.30}$$

$$L_{nr} = 2\pi\rho bU \int_0^\infty \frac{Q(re^{i\pi})e^{-rt}}{\bar{r}[(K_0 - K_1)^2 + \pi^2(I_0 + I_1)^2]} dr \tag{2.31}$$

where L_{nc} is the non-circulatory lift of equations 2.21 and 2.22 and L_r and L_{nr} are the rational and non-rational components of the circulatory lift respectively. In this formulation s is the Laplace Transform variable, $s = \sigma + \imath\omega$, $\bar{s} = sb/U$, $\phi(\bar{s}) = 1 - C(\bar{s})$ where $C(\bar{s})$ is the

generalised Theodorsen function (related to Wagner's function) and,

$$Q(s) = sh(s) + U\alpha(s) + (\frac{1}{2} - a_h)bs\alpha(s) \tag{2.32}$$

K_0, K_1 and I_0, I_1 are modified Bessel functions of the first and second kinds respectively.

Following the work of Theodorsen [48] the aerodynamic loads in heave, pitch and flap rotation can be represented by $Q_{aero}(s)$ as,

$$Q_{aero}(s) = \frac{1}{\pi\mu}\left(\frac{U}{b}\right)^2 [M_{nc}\bar{s}^2 + B_{nc}\bar{s} + K_{nc} + C(\bar{s})R[S_2\bar{s} + S_1]] \tag{2.33}$$

where the matrices in equation 2.33 are given in Appendix B. It can be seen that the representation is in the form of an aerodynamic equivalence to a mass, damping and stiffness matrix, except for the final term that includes $C(\bar{s})$. Performing a Laplace transformation on Jones' [70] exponential approximation of Wagner's function, given in 2.17, gives an approximation to $C(\bar{s})$ as,

$$C(\bar{s}) \cong \frac{0.5\bar{s}^2 + 0.2808\bar{s} + 0.01365}{\bar{s}^2 + 0.3455\bar{s} + 0.01365} \tag{2.34}$$

Converting this system of equations into the time domain results in a state-space representation of the aerodynamics as,

$$\begin{bmatrix} \mathbf{I} & \mathbf{0} & \mathbf{0} \\ \mathbf{0} & -\eta\mathbf{M_{nc}} & \mathbf{0} \\ \mathbf{0} & \mathbf{0} & \mathbf{I} \end{bmatrix} \begin{Bmatrix} \dot{\boldsymbol{x}} \\ \ddot{\boldsymbol{x}} \\ \dot{\boldsymbol{x}}_p \end{Bmatrix} =$$

$$\begin{bmatrix} \mathbf{0} & \mathbf{I} & \mathbf{0} \\ \eta(U/b)^2[\mathbf{K_{nc}} + 0.5\boldsymbol{RS_1}] & \eta(U/b)[\mathbf{B_{nc}} + 0.5\boldsymbol{RS_2}] & \eta(U/b)[\boldsymbol{RN}] \\ (U/b)\begin{bmatrix} 0 \\ \boldsymbol{S_1} \end{bmatrix} & \begin{bmatrix} 0 \\ \boldsymbol{S_2} \end{bmatrix} & \mathbf{F_p} \end{bmatrix} \begin{Bmatrix} \boldsymbol{x} \\ \dot{\boldsymbol{x}} \\ \boldsymbol{x}_p \end{Bmatrix} \tag{2.35}$$

where,

$$\eta = \frac{1}{\pi\mu} \qquad \boldsymbol{x} = \begin{Bmatrix} h \\ \alpha \\ \beta \end{Bmatrix}$$

x_p is a vector of the two augmented states required to represent 2.34. The matrices in equation 2.35 can be found in Appendix B.

Using the above technique Edwards achieved a good representation of the eigenvalues of the system. In particular around the ω axis, the roots of $\bar{s}$ are found to correlate exactly with the values from 2.17.

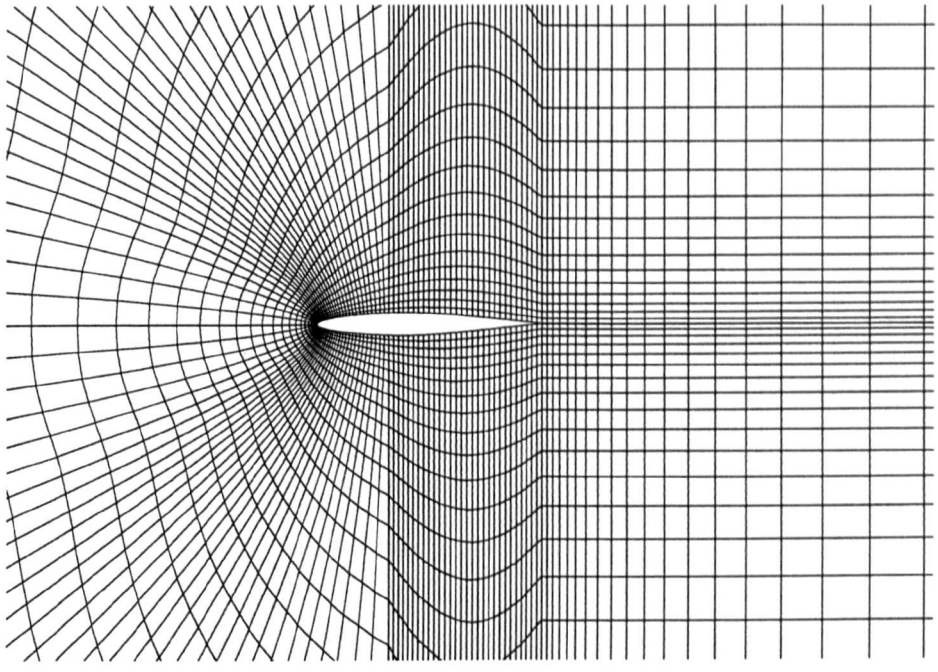

Fig 2.17: Finite Volume Discretisation of a Flow Field around an Aerofoil Section (C-grid)

2.2.3 Finite Volume Method: Full Euler Simulations

The fundamental equations governing fluid dynamics were derived by Euler for inviscid flow, and later extended to give the Navier-Stokes equations for viscous flows. The analytic solution of these equations is not generally possible and a numerical procedure must be performed using finite volume, element or difference representations. In the finite volume representation the fluid is broken down into a number of cells, as shown in figure 2.17, and the equations solved at the cell-centres or vertices. The fundamental equations are based on conservation of mass, momentum and energy. The Euler equations, neglect the frictional and thermal conduction terms, therefore factors such as separated flow and boundary layers are not simulated directly. The Euler scheme is most applicable to high Reynolds Number flows where the boundary layer is thin and so for aircraft surfaces Mach numbers roughly between 0.3 and 1.2 is reasonable. The details of the derivation of the fundamental equations of fluid flow can be found in many books on the subject and so is not essential for inclusion in this work. The aerodynamic code to be described here is based on Jameson's original cell centred scheme as implemented by Gaitonde [71] for unsteady flows on moving meshes.

2.2.3.1 Moving Grid Euler Equations [3]

Inviscid, compressible, two-dimensional flow can be represented by the Euler equations that are written in integral form on a moving mesh as

$$\frac{\partial}{\partial t}\int\int_A \boldsymbol{Q}dA + \int_{\partial A}(\boldsymbol{F}dy - \boldsymbol{G}dx) = 0 \tag{2.37}$$

where $\boldsymbol{Q}$ represents the vector of conserved variables, $\boldsymbol{F}$ and $\boldsymbol{G}$ are the convective flux terms in the x and y directions respectively, A is the area of the domain over which the integration takes place and ∂A is the boundary of the area A. The vectors $\boldsymbol{Q}$, $\boldsymbol{F}$ and $\boldsymbol{G}$ are,

$$Q = \begin{Bmatrix} \rho \\ \rho u \\ \rho v \\ \rho e \end{Bmatrix} \tag{2.38}$$

$$F = \begin{Bmatrix} \rho U \\ \rho u U + p \\ \rho v U \\ \rho e U + p u \end{Bmatrix} \tag{2.39}$$

$$G = \begin{Bmatrix} \rho V \\ \rho u V \\ \rho v V + p \\ \rho e V + p v \end{Bmatrix} \tag{2.40}$$

where p, ρ, u, v and e are the pressure, density, x- and y-components of velocity and total specific energy. The contravariant velocities U and V are expressed as,

$$U = u - u_g \qquad V = v - v_g \tag{2.41}$$

where u_g and v_g are the grid speeds in the x and y directions respectively. The pressure, p, is obtained via the perfect gas relation,

$$p = (\gamma - 1)\left[\rho e - \frac{\rho(u^2 + v^2)}{2}\right] \tag{2.42}$$

where γ is the ratio of specific heats (1.403 for standard air).

2.2.3.2 Solution Procedure

The Euler equations 2.37 are applied to each cell of the grid. Following Jameson et al. [72] the time and spatial terms in the equations can be decoupled and for the ijth cell of the grid

the following equation is obtained,

$$\frac{d}{dt}(A_{ij}\boldsymbol{Q}_{ij}) + \boldsymbol{C}_{ij} = 0 \tag{2.43}$$

where $\boldsymbol{Q}_{ij}$ is a cell-average value of $\boldsymbol{Q}$ assumed to be located at the cell-centre. A_{ij} is the area of the cell and $\boldsymbol{C}_{ij}$ approximates the flux integral component of 2.37 and is given by

$$\boldsymbol{C}_{ij} = \sum_{m=1}^{4}(\boldsymbol{F}_m\Delta y_m - \boldsymbol{G}_m\Delta x_m) \tag{2.44}$$

where the flux vectors, $\boldsymbol{F}_m$ and $\boldsymbol{G}_m$, are calculated on the cell sides which have lengths of Δx_m and Δy_m as their x and y components. The conserved variables on each side are taken as the average of the values at the cell-centres adjacent to the given side. The grid speeds on the cell side are taken as the average of the speeds at the vertices of the side.

In order to prevent oscillatory solutions near shocks and odd/even point decoupling, equation 2.43 is augmented with an artificial dissipation term,

$$\frac{d}{dt}(A_{ij}\boldsymbol{Q}_{ij}) + \boldsymbol{C}_{ij} - \boldsymbol{D}_{ij} = 0 \tag{2.45}$$

which is given by Jameson et al. [72] and depends on the local pressure gradient.

Following Jameson [73], an implicit algorithm is obtained by approximating 2.45 at time level $(n+1)$ by,

$$\frac{d}{dt}(A_{ij}^{n+1}\boldsymbol{Q}_{ij}^{n+1}) + \boldsymbol{R}_{ij}^{n+1} = 0 \tag{2.46}$$

where

$$\boldsymbol{R}_{ij} = \boldsymbol{C}_{ij} - \boldsymbol{D}_{ij} \tag{2.47}$$

and the superscript $(n+1)$ denotes the time level $(n+1)\Delta t$.

The time derivative is approximated by an implicit finite difference approximation. Using a second order time discretisation equation 2.46 becomes,

$$\boldsymbol{R}^{*}(\boldsymbol{Q}_{ij}^{n+1}) = \frac{3A_{ij}^{n+1}\boldsymbol{Q}_{ij}^{n+1} - 4A_{ij}^{n}\boldsymbol{Q}_{ij}^{n} + A_{ij}^{n-1}\boldsymbol{Q}_{ij}^{n-1}}{2\Delta t} + \boldsymbol{R}(\boldsymbol{Q}_{ij}^{n+1}) = 0 \tag{2.48}$$

This is then solved via a dual-time scheme. A derivative with respect to a fictitious pseudo time, τ, is added to equation 2.48,

$$A_{ij}^{n+1}\frac{d\boldsymbol{Q}_{ij}^{n+1}}{d\tau} + \boldsymbol{R}^{*}(\boldsymbol{Q}_{ij}^{n+1}) = 0 \tag{2.49}$$

The solution of 2.48 is then equivalent to marching equation 2.49 to a steady state in pseudo time. Note that the area in 2.49 is calculated via a geometric conservation law in order to ensure that the scheme could capture the freestream,

$$\frac{d}{dt}\int\int_{A} dxdy + \int_{\partial A}(u_g dy - v_g dx) = 0 \tag{2.50}$$

This is solved using the same implicit finite difference as used for the physical conservation equations, see [73].

2.2.3.3 Integration in Pseudo Time

The system of equation 2.49 is integrated in pseudo time using an explicit four-stage Runge-Kutta method;

$$\begin{aligned}
Q^{(0)} &= (Q_{ij}^{n+1})^m \\
Q^{(1)} &= Q^{(0)} - \frac{1}{4}\frac{\Delta\tau}{A_{ij}^{n+1}} R^*(Q^{(0)}) \\
Q^{(2)} &= Q^{(0)} - \frac{1}{3}\frac{\Delta\tau}{A_{ij}^{n+1}} R^*(Q^{(1)}) \\
Q^{(3)} &= Q^{(0)} - \frac{1}{2}\frac{\Delta\tau}{A_{ij}^{n+1}} R^*(Q^{(2)}) \\
Q^{(4)} &= Q^{(0)} - \frac{\Delta\tau}{A_{ij}^{n+1}} R^*(Q^{(3)}) \\
(Q_{ij}^{n+1})^{m+1} &= Q^{(4)}
\end{aligned} \tag{2.51}$$

where the superscript m denotes the pseudo time level $m\Delta\tau$ and

$$R^*(Q^{(L)}) = \left[\frac{3A_{ij}^{n+1}Q^{(L)} - 4A_{ij}^{n}Q_{ij}^{n} + A_{ij}^{n-1}Q_{ij}^{n-1}}{2\Delta t} + C_{ij}^{n+1}(Q^{(L)}) - D_{ij}^{n+1}(Q^{(0)}) \right] \tag{2.52}$$

Note that the dissipation is fixed at its first stage value throughout each pseudo time integration step for computational efficiency and restrictions on the pseudo-time step size are applied to guarantee stability.

2.2.3.4 Moving Grid Algorithm

The section above described a form of finite volume solver that is commonly used to solve static problems by setting $u_g = v_g = 0$ and maintaining constant grid areas. In order to solve the equations of the previous section, including the moving body, it is necessary to implement an algorithm that can calculate the position and speed of the grid at any time. The method chosen to calculate these grids is that of Gaitonde and Fiddes [3] and is outlined below.

The solution of the Euler equations on a moving mesh requires a new grid and the corresponding grid speeds at each time step. In view of the potentially large numbers of possible configurations that can occur, any grid generation technique must not be too time consuming.

Algebraic grid generation based on transfinite interpolation (or TFI) was used to rapidly generate a structured moving grid. The grid generation procedure effectively interpolates grid points in the computational domain from prescribed points on the inner boundary (aerofoil surface) and the outer boundary (far-field). An additional benefit of this scheme is that the speeds of the grid points can be found analytically by using the same scheme.

In this work, the motion or deformation of the aerofoil is available from the structural equation such that the surface position is known at a given time, t. At each time-step the transformation from the computational to physical domains is a vector function,

$$\boldsymbol{F}(\eta,\zeta,t) = \begin{Bmatrix} x(\eta,\zeta,t) \\ y(\eta,\zeta,t) \end{Bmatrix} \tag{2.53}$$

where η and ζ are parametric co-ordinates of the grid. Without a loss of generality,

$$0 \leq \eta \leq 1, \qquad 0 \leq \zeta \leq 1 \tag{2.54}$$

This formulation allows the computational domain to be defined in a regular rectangular co-ordinate system as shown in figure 2.18. Using this construction only the position of the boundaries and the direction at which the grid lines leave the boundaries is required, see [74]. In this computational domain definition the aerofoil surface corresponds to $\zeta = 0$ and the far-field boundary corresponds to $\zeta = 1$, with the mapping given by,

$$\boldsymbol{F}(\eta,\zeta,t) = \alpha_1^0(\zeta)\boldsymbol{F}(\eta,0,t) + \alpha_1^1(\zeta)\frac{\partial \boldsymbol{F}}{\partial \zeta}(\zeta,0,t) + \alpha_2^0(\zeta)\boldsymbol{F}(\zeta,1,t) + \alpha_2^1(\zeta)\frac{\partial \boldsymbol{F}}{\partial \zeta}(\zeta,1,t) \tag{2.55}$$

This produces a boundary fitted grid, with specified boundary directions provided the blending functions satisfy certain conditions, see [3].

If grid control at the outer boundary is not enforced then the blending functions, α_j^i, as described by Eriksson [74], can be applied, producing an exponential stretching of the grid from the aerofoil surface to the far-field boundary. The functions are,

$$\begin{aligned} \alpha_1^0(\zeta) &= 1 - \frac{e^{K\zeta} - 1 - K\zeta}{e^K - 1 - K} \\ \alpha_1^1(\zeta) &= \xi - \frac{e^{K\zeta} - 1 - K\zeta}{e^K - 1 - K} \\ \alpha_2^0(\zeta) &= \frac{e^{K\zeta} - 1 - K\zeta}{e^K - 1 - K} \\ \alpha_2^1(\zeta) &= 0 \end{aligned} \tag{2.56}$$

where K is a stretching parameter.

However, these simple blending functions do not always give sufficient control over grid spacing, as discussed in reference [75]. Additional grid control can be obtained by defining an

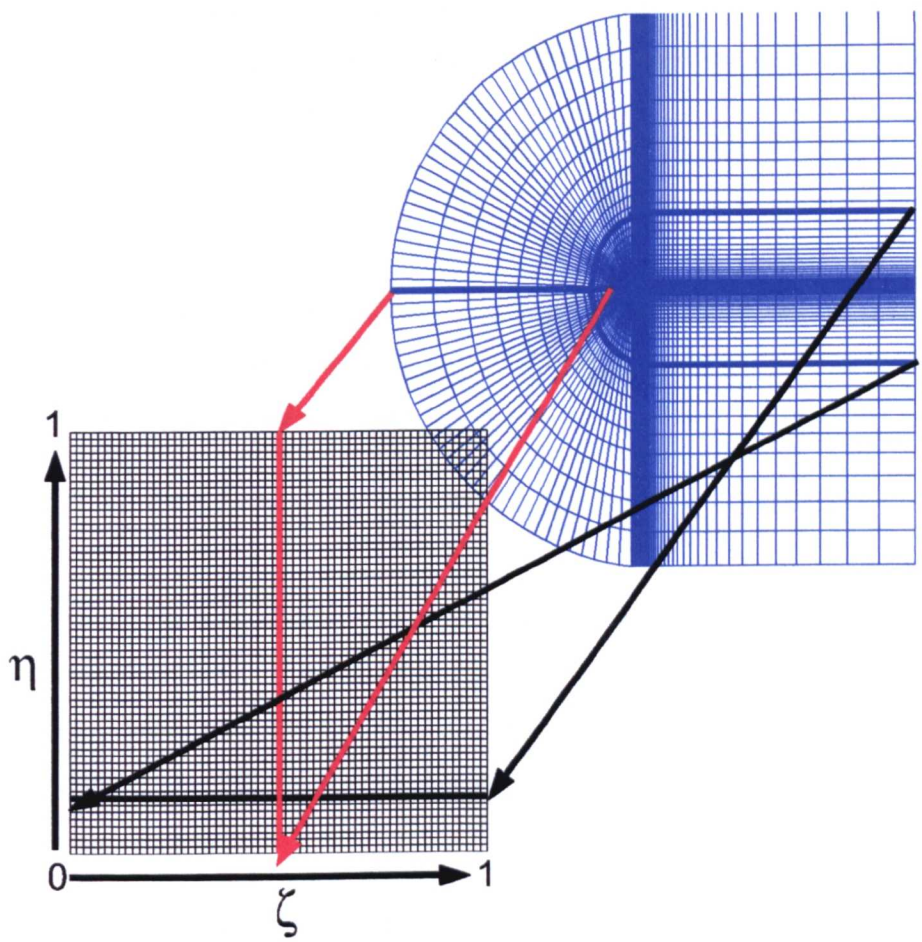

Fig 2.18: Aerodynamic Grid Mapping Characteristics

intermediate set of control variables, where each intermediate co-ordinate is related to a corresponding computational co-ordinate by single-valued functions. For example if the intermediate co-ordinates are χ and ζ then

$$\chi = f(\eta), \qquad \Lambda = g(\zeta) \tag{2.57}$$

where χ and Λ lie in the range zero to one and $f(\eta)$ and $g(\zeta)$ are monotonically increasing in the range, $0 \leq \eta \leq 1$ and $0 \leq \zeta \leq 1$. The uniformly spaced points in the computational domain thus map to rectangular non-uniformly spaced points in the intermediate domain. The blending functions are the rewritten as functions of the intermediate variable, giving

$$\boldsymbol{F}(\eta,\zeta,t) = \alpha_1^0(\Lambda)\boldsymbol{F}(\eta,0,t) + \alpha_1^1(\Lambda)\frac{\partial \boldsymbol{F}}{\partial \Lambda}(\eta,0,t) + \alpha_2^0(\Lambda)\boldsymbol{F}(\eta,1,t) \tag{2.58}$$

assuming $\alpha_2^1(\Lambda) = 0$.

The grid speeds required by the flow solver can then be easily found by differentiating 2.58 with respect to time. As the outer boundary of this calculation is fixed and assuming the blending functions are independent of time

$$\frac{\partial \boldsymbol{F}}{\partial t}(\eta,\zeta,t) = \alpha_1^0(\Lambda)\frac{\partial \boldsymbol{F}}{\partial t}(\eta,0,t) + \alpha_1^1(\Lambda)\frac{\partial}{\partial t}\left(\frac{\partial \boldsymbol{F}}{\partial \Lambda}\right)(\eta,0,t) \tag{2.59}$$

Applying the above method, a technique to generate and then deform a two-dimensional grid systems has been described. The technique has been well established and has been demonstrated to allow "good" grid deformation when suitable account is taken of factors such as required grid density and surface grid point location.

2.2.4 Reduced Order Modelling

2.2.4.1 Introduction

The modelling of the flow about a typical aerodynamic geometry using the full Euler equations in finite volume form yields a very large, non-linear system of ODE's (of the order of 30,000 for a typical two-dimensional cases presented in this work). For unsteady problems this large set of equations must be solved at each real time step. Whilst the dual time scheme of sections 2.2.3.2 and 2.2.3.3 has proved to be computationally efficient compared with alternative unsteady time integration schemes, e.g. explicit, it is still expensive when many parameters need to be investigated. There has therefore been a new focus of research effort into so-called reduced order models (ROMs).

The principle of the ROM technique is to reduce the flow equations with several thousand degrees-of-freedom (5 degrees-of-freedom at each node in two-dimensional flow), to a linear system with only hundreds or even tens of degrees-of-freedom whilst retaining much of the accuracy of the full equation set. There are several techniques available to allow ROMs to be generated [76, 17, 19, 18]. In this work ROMs produced using the approach described by Gaitonde and Jones are used [4, 5, 6] due to their compact formulation and availability to the author. The first step in generating the ROMs used here has been the assumption that the flow equations have been linearised about a non-linear steady state condition. Non-linear phenomena such as shocks and vorticity are therefore captured but their motion is linearised with respect to structural motion.

2.2.4.2 Time-Linearised Euler Equations [4]

The Euler equations given by section 2.2.3 are applicable to full non-linear unsteady inviscid flows with no restriction on the size of the unsteadiness. In many cases the unsteadiness present in the flow is small and flow quantities can therefore be approximated by the sum of the mean base flow value plus a small unsteady perturbation component. A time-linearised set of equations can then be found by substituting into the full equations and linearising.

In the conservation equations 2.45, the following substitutions are made,

$$\begin{aligned}
\rho &= \overline{\rho}(x,y) + \hat{\rho}(x,y,t) \\
u &= \overline{u}(x,y) + \hat{u}(x,y,t) \\
v &= \overline{v}(x,y) + \hat{v}(x,y,t) \\
p &= \overline{p}(x,y) + \hat{p}(x,y,t) \\
x &= \overline{x} + \hat{x}(t) \\
y &= \overline{x} + \hat{y}(t) \\
A &= \overline{A} + \hat{A}(t) \\
\boldsymbol{D} &= \overline{\boldsymbol{D}} + \hat{\boldsymbol{D}}
\end{aligned} \tag{2.60}$$

where an overbar indicates a mean flow quantity and a hat indicates a perturbation.

Assuming that the grid speeds and other perturbations are small, only the linear first-order terms need be retained and the time-linearised Euler equations are obtained.

$$\overline{A}_{ij}\frac{d\hat{\boldsymbol{q}}_{ij}}{dt} + (\mathbf{B^1})^{-1}_{ij}(\boldsymbol{R^1})_{ij} + (\mathbf{B^1})^{-1}_{ij}(\boldsymbol{S^1})_{ij} = 0 \tag{2.61}$$

where,

$$\hat{q} = \begin{Bmatrix} \hat{\rho} \\ \hat{u} \\ \hat{v} \\ \hat{p} \end{Bmatrix} \tag{2.62}$$

The other matrices in equation 2.61 are given in Appendix C along with the perturbation form of the Geometric Conservation Law.

Special consideration needs to be given to the usual Jameson type dissipation as it cannot be simply linearised. This complication arises because the switch used cannot be linearised. In order to obtain a truly linear dissipation a switch based on the mean switch value has been used by other authors. However, these techniques are yet to be fully developed therefore the switch values have been fixed [5].

2.2.4.3 Impulse Response Function [5]

The impulse responses or Markov parameters of a system are "*memory*" functions or temporal representations of the manner in which, and the time over which, a perturbation remains active in the response of the system. Once such responses are available the exact response to an arbitrary input (steady or unsteady) can be predicted because all responses of the system are scaled and shifted superpositions of the "*memory*" functions, see Wylie and Barrett [77] for the continuous theory and Silva [78] for the discrete theory. For example, for a three degree-of-freedom aerofoil section, the response for any input can be constructed via convolution from the impulse responses for heave, pitch and control surface deflections and their respective velocities. In this work solutions are not calculated by reconstruction, rather the impulse responses are used to obtain a ROM via the Eigensystem Realization Algorithm (ERA) [79].

It is worth noting that in many studies where reconstructed systems are analysed, the decoupling of the displacement from its derivative, e.g. heave and heave-rate, has not been made. This is incorrect and causes impulse or step inputs to give rise to infinite values for their derivatives. As a result many authors opted to use smoothed input functions resulting in finite values for the derivatives. However since the displacement and derivative are not decoupled, the frequencies that are excited are a function of the shape of the pulse with high frequencies being excited by narrow pulses and low frequencies excited by wider pulses. Implementing two separate impulses for each mode, one in displacement and one in its derivative, gives an infinite range frequency excitation. From the literature, many of the smooth impulse techniques are perceived to be successful as, with reasonably wide inputs, the low-frequencies that are

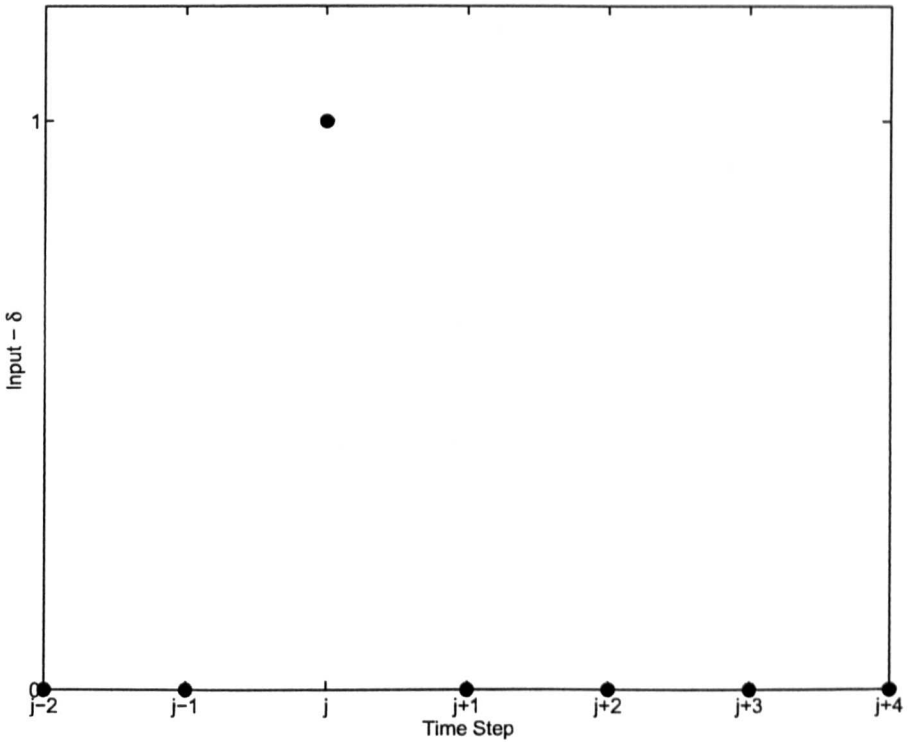

Fig 2.19: Impulse Excitation

dominant in aerodynamic flows are excited and errors due to incorrect derivative definition are small. However, for cases with stronger non-linear responses the separation of the inputs must be made.

To find the sample or discrete pulse response for discrete systems means that in each of the modes an impulse of the form,

$$\delta_i(n) = \begin{cases} 1 & \text{for} \quad n = j \\ 0 & \text{for} \quad n \neq j \end{cases} \tag{2.63}$$

is applied with n being a discrete-time variable and j being a selected time-step, see figure 2.19. Each other mode has a zero input. The system response to any general input can be obtained as a convolution sum of the inputs with the sample responses of the system, see [5].

For the heave degree-of-freedom it is sufficient to implement the impulses in both y and $\dot{y}$ to obtain the heave freedoms Markov parameters. As pitch and flap motions are rotations both x and y and their associated velocities change for points on the aerofoil therefore four impulses are required. However, if the motions are assumed small, the motion can be linearised thus reducing the number of inputs required to two, one for the x and y displacements, which always act together, and a second impulse for their respective rates.

2.2.4.4 Eigenvalue Realisation Algorithm and the Reduced Order Model [6]

The following section gives an overview of the process required to generate the Reduced Order Model (ROM) using the Eigenvalue Realization Algorithm (ERA), full details of the methodology used can be found in reference [6].

The time-linearised Euler equations 2.61 can be written in state-space form for a three degree-of-freedom aeroelastic system as,

$$\begin{aligned} \dot{\boldsymbol{X}}(t) &= \mathbf{A}\boldsymbol{X}(\mathrm{t}) + \mathbf{B}\boldsymbol{U}(\mathrm{t}) \\ \boldsymbol{Y}(t) &= \mathbf{C}\boldsymbol{X}(\mathrm{t}) + \mathbf{D}\boldsymbol{U}(\mathrm{t}) \end{aligned} \tag{2.64}$$

where $\mathbf{A}, \mathbf{B}, \mathbf{C}$ and $\mathbf{D}$ are system matrices. The vectors $\boldsymbol{U}$ and $\boldsymbol{X}$ are,

$$\boldsymbol{U} = \begin{Bmatrix} h \\ \alpha \\ \beta \\ \dot{h} \\ \dot{\alpha} \\ \dot{\beta} \end{Bmatrix}, \qquad \boldsymbol{X} = \begin{Bmatrix} \hat{\rho}_{2,2} \\ \hat{u}_{2,2} \\ \hat{v}_{2,2} \\ \hat{p}_{2,2} \\ \vdots \\ \hat{\rho}_{imax,jmax} \\ \hat{u}_{imax,jmax} \\ \hat{v}_{imax,jmax} \\ \hat{p}_{imax,jmax} \end{Bmatrix} \tag{2.65}$$

where h is the heave displacement, α is the pitch rotation and β is the flap rotation. The terms in the $\boldsymbol{X}$ vector are the perturbations of the density, speeds and pressures from their mean values. As the scheme is cell-centred, the centres are labelled as $i = 2, imax$ and $j = 2, jmax$ in the computational domain.

The vector $\boldsymbol{Y}$ is the output, which can contain any quantities that can be calculated from the data available, but, for aeroelastic systems, it is convenient to set it to,

$$\boldsymbol{Y} = \begin{Bmatrix} \hat{C}_l \\ \hat{C}_m \\ \hat{C}_h \end{Bmatrix} \tag{2.66}$$

where $\hat{C}_l, \hat{C}_m$ and $\hat{C}_h$ are the changes in lift, elastic axis moment and hinge moment coefficients from their mean values.

Using this representation it is possible to realise and reduce the system matrices by constructing the Hankel matrix from the continuous system's Markov parameters or impulse functions

[79]. However, the information required to construct the matrix is not always directly available and therefore, a discrete approximation to the continuous linear system is required instead. The state-space representation of 2.64 is put in discrete form using an implicit approximation to the time derivative which is given by,

$$\frac{\tilde{\boldsymbol{X}}_k - \tilde{\boldsymbol{X}}_{k-1}}{\Delta t} = \mathbf{A}\tilde{\boldsymbol{X}}_\mathbf{k} + \mathbf{B}\tilde{\boldsymbol{U}}_\mathbf{k}$$
$$\tilde{\boldsymbol{Y}}_k = \mathbf{C}\tilde{\boldsymbol{X}}_\mathbf{k} + \mathbf{D}\tilde{\boldsymbol{U}}_\mathbf{k} \tag{2.67}$$

where $\tilde{\boldsymbol{X}}$, $\tilde{\boldsymbol{U}}$ and $\tilde{\boldsymbol{Y}}$ are discrete approximations to $\boldsymbol{X}$, $\boldsymbol{U}$ and $\boldsymbol{Y}$, and the subscript k represents the time level $k\Delta t$. These equations can be rearranged as,

$$\tilde{\boldsymbol{X}}_k = \tilde{\mathbf{A}}\tilde{\boldsymbol{X}}_{\mathbf{k-1}} + \tilde{\mathbf{B}}\tilde{\boldsymbol{U}}_\mathbf{k}$$
$$\tilde{\boldsymbol{Y}}_k = \tilde{\mathbf{C}}\tilde{\boldsymbol{X}}_\mathbf{k} + \tilde{\mathbf{D}}\tilde{\boldsymbol{U}}_\mathbf{k} \tag{2.68}$$

where,

$$\tilde{\mathbf{A}} = (\mathbf{I} - \mathbf{A}\Delta\mathbf{t})^{-1}$$
$$\tilde{\mathbf{B}} = (\mathbf{I} - \mathbf{A}\Delta\mathbf{t})^{-1}\mathbf{B}\Delta\mathbf{t}$$
$$\tilde{\mathbf{C}} = \mathbf{C}$$
$$\tilde{\mathbf{D}} = \mathbf{D} \tag{2.69}$$

This formulation can be solved using the z-transforms [5, 80, 81], resulting in the discrete output equation,

$$\tilde{\boldsymbol{Y}}(k) = \sum_{k=0}^{n} \tilde{\mathbf{H}}(\mathbf{k}-\mathbf{n})\tilde{\boldsymbol{U}}_\mathbf{n} \tag{2.70}$$

The matrix $\tilde{\mathbf{H}}$ is composed of columns which are the outputs for a unit sample input on each input channel separately, i.e. the ith column is the output vector at time k for a unit sample input in the ith component of $\tilde{\boldsymbol{U}}$ with all other entries of $\tilde{\boldsymbol{U}}$ set to zero, see Aplevich [82]. Note that the columns of $\tilde{\mathbf{H}}$ are also called the Markov parameters of the system.

The Eigenvalue Realisation Algorithm is that of Juang and Pappa [79] and can be applied to both continuous and discrete Hankel matrices requiring only a knowledge of the Markov parameters. If the system has p outputs and m inputs then each of the Markov parameters are of size $p \times m$, and the Hankel matrix $\mathbf{H}_{rs}(k)$ is thus of size $rp \times sm$.

The Singular Value Decomposition (SVD) method requires that the Hankel matrix, $\mathbf{H}_{rs}(0)$, can be represented as,

$$\mathbf{H}_{rs}(0) = \mathbf{U}\mathbf{W}\mathbf{V}^\mathbf{T} \tag{2.71}$$

where the matrix $\mathbf{W}$ is diagonal (of order $sm \times sm$) with the elements from top left to bottom right in increasing size order, $\mathbf{U}$ is $rp \times sm$ and $\mathbf{V}$ is $sm \times sm$. The rank of the ROM of

the system is determined by the number of elements of W which are larger than some desired accuracy or by taking into account only the n largest singular values of W. If the Hankel matrix is then partitioned and approximated by,

$$\mathbf{H_{rs}(0) = PFQ^T} \tag{2.72}$$

where the matrices U, W and V have been reduced in size by deleting unnecessary rows and columns as appropriate to give P, F and Q respectively, see [6].

It is then shown in [79] that the matrices can be realised as,

$$\begin{aligned}\tilde{\mathbf{A}} &= \mathbf{F^{-\frac{1}{2}} P^T H_{rs}(1) Q F^{-\frac{1}{2}}} \\ \tilde{\mathbf{B}} &= \mathbf{F^{\frac{1}{2}} Q^T E_m} \\ \tilde{\mathbf{C}} &= \mathbf{E_p^T P F^{\frac{1}{2}}}\end{aligned} \tag{2.73}$$

where

$$\mathbf{E_p = [I_p, 0_p, 0_p, \ldots, 0_p]_{pxrp}} \qquad \mathbf{E_m^T = [I_m, 0_m, 0_m, \ldots, 0_m]_{mxsm}} \tag{2.74}$$

To reconstruct the continuous ROM such that the time-step size can be varied, the inverse of the transformations of the equations 2.69 is performed. However, the terms which have been omitted from the reduced size Hankel matrix may not be exactly the same terms which would have been omitted from the equivalent continuous Hankel matrix. However, it is probable that the dominant terms are correctly predicted.

2.3 Aeroelastic Coupling

The methodology that is adopted for coupling depends upon the formulations of the aerodynamic equations as different non-dimensionalising methods are used. Also consideration has to be given to the formulation of the finite volume Euler equations of section 2.2.3 as they are not in state-space form.

2.3.1 Coupling of Fung's Method [7]

To couple the structural dynamics equations with those of section 2.2.2.1 requires lengths to be non-dimensionalised with respect to the semi-chord, b, mass to be non-dimensionalised with respect to the relative density of the air and time to be non-dimensionalised to the time taken

for the body to move the distance of a semi-chord. The formulation used here is from the methodology used by Wong et al. [7]. In non-dimensional form equations 2.9 become,

$$\begin{aligned}
\xi'' + x_\alpha \alpha'' + 2\zeta_\xi \frac{\varpi}{U^*}\xi' + \left(\frac{\varpi}{U^*}\right)^2 M(\xi) &= -\frac{1}{\pi\mu}C_L(\tau) \\
\frac{x_\alpha}{r_\alpha^2}\xi'' + \alpha'' + 2\zeta_\alpha \frac{1}{U^*}\alpha' + \left(\frac{1}{U^*}\right)^2 G(\alpha) &= \frac{2}{\pi\mu r_\alpha^2}C_M(\tau)
\end{aligned} \tag{2.75}$$

for a two degree-of-freedom test case where,

$$\begin{aligned}
&\mu = \frac{m}{\pi\rho b^2}, \quad r_\alpha^2 = \frac{I_\alpha}{mb^2}, \quad \xi = \frac{h}{b}, \quad \tau = \frac{Ut}{b}, \\
&U^* = \frac{U}{b\omega_\alpha}, c_h = \frac{\zeta_h}{2m\omega_h}, c_\alpha = \frac{\zeta_\alpha}{2I_\alpha\omega_\alpha} \text{ and } \varpi = \frac{\omega_\xi}{\omega_\alpha}
\end{aligned} \tag{2.76}$$

If the aerodynamic equations of 2.27 are combined with the above representation of the structural equations, it results in the state-space form (given by Wong et al. [7]),

$$\begin{Bmatrix} \alpha' \\ \alpha'' \\ \xi' \\ \xi'' \\ w_1' \\ w_2' \\ w_3' \\ w_4' \end{Bmatrix} = \begin{bmatrix} 0 & 1 & 0 & 0 & 0 & 0 & 0 & 0 \\ a_{21} & a_{22} & a_{23} & a_{24} & a_{25} & a_{26} & a_{27} & a_{28} \\ 0 & 0 & 0 & 1 & 0 & 0 & 0 & 0 \\ a_{41} & a_{42} & a_{43} & a_{44} & a_{45} & a_{46} & a_{47} & a_{48} \\ 1 & 0 & 0 & 0 & -\varepsilon_1 & 0 & 0 & 0 \\ 1 & 0 & 0 & 0 & 0 & -\varepsilon_2 & 0 & 0 \\ 0 & 0 & 1 & 0 & 0 & 0 & -\varepsilon_1 & 0 \\ 0 & 0 & 1 & 0 & 0 & 0 & 0 & -\varepsilon_2 \end{bmatrix} \begin{Bmatrix} \alpha \\ \alpha' \\ \xi \\ \xi' \\ w_1 \\ w_2 \\ w_3 \\ w_4 \end{Bmatrix}$$
$$+ \begin{Bmatrix} 0 \\ j(d_0(\frac{\varpi}{U^*})^2 M(\xi) - c_0(\frac{1}{U^*})^2 G(\alpha)) \\ 0 \\ j(-d_1(\frac{\varpi}{U^*})^2 M(\xi) + c_1(\frac{1}{U^*})^2 G(\alpha)) \\ 0 \\ 0 \\ 0 \\ 0 \end{Bmatrix} \tag{2.77}$$

where the terms $j, a_{21}, \ldots, a_{28}$ and $a_{41}, \ldots, a_{48}$ are given in Appendix D.

2.3.2 Coupling of Edwards' Method [2]

The coupling of the aerodynamics of Edwards et al. [2] with the three degree-of-freedom structural equations as defined in equations 2.10 uses the same non-dimensional factors as in

the previous section except that the time remains dimensional, resulting in,

$$\begin{aligned}
\xi'' + x_\alpha\alpha'' + x_\beta\beta'' + 2\zeta_\xi\xi' + \omega_\xi^2 M(\xi) &= -C_L(\tau) \\
x_\alpha\xi'' + r_\alpha^2\alpha'' + [r_\beta^2 + x_\beta(C_\beta - a_h)]\beta'' + 2\zeta_\alpha\alpha' + r_\alpha^2\omega_\alpha^2 G(\alpha) &= 2C_M(\tau) \\
x_\beta\xi'' + [r_\beta^2 + x_\beta(C_\beta - a_h)]\alpha'' + r_\beta^2\beta'' + 2\zeta_\beta\beta' + r_\beta^2\omega_\beta^2 N(\beta) &= 2C_H(\tau)
\end{aligned} \tag{2.78}$$

This formulation is consistent with the form of equation 2.34 and can be easily implemented by replacing the sub matrices with the equivalent structural mass, damping and stiffness terms. This results in,

$$\begin{bmatrix} \mathbf{I} & \mathbf{0} & \mathbf{0} \\ \mathbf{0} & \mathbf{M_s} - \eta\mathbf{M_{nc}} & \mathbf{0} \\ \mathbf{0} & \mathbf{0} & \mathbf{I} \end{bmatrix} \begin{Bmatrix} \dot{\boldsymbol{x}} \\ \ddot{\boldsymbol{x}} \\ \dot{\boldsymbol{x}}_p \end{Bmatrix} =$$

$$\begin{bmatrix} \mathbf{0} & \mathbf{I} & \mathbf{0} \\ \eta(U/b)^2(\mathbf{K_{nc}} + 0.5\boldsymbol{RS_1}) & -\mathbf{B_s} + \eta(\mathbf{U/b})(\mathbf{B_{nc}} + 0.5\boldsymbol{RS_2}) & \eta(U/b)\boldsymbol{RN} \\ (U/b)\begin{bmatrix} \mathbf{0} \\ \boldsymbol{S_1} \end{bmatrix} & \begin{bmatrix} \mathbf{0} \\ \boldsymbol{S_2} \end{bmatrix} & \mathbf{F_p} \end{bmatrix} \begin{Bmatrix} \boldsymbol{x} \\ \dot{\boldsymbol{x}} \\ \boldsymbol{x}_p \end{Bmatrix} +$$

$$\begin{Bmatrix} \mathbf{0} \\ \boldsymbol{K_s} \\ \mathbf{0} \end{Bmatrix} \tag{2.79}$$

where

$$\mathbf{M_s} = \begin{bmatrix} 1 & x_\alpha & x_\beta \\ x_\alpha & r_\alpha^2 & [r_\beta^2 + x_\beta(C_\beta - a_h)] \\ x_\beta & [r_\beta^2 + x_\beta(C_\beta - a_h)] & r_\beta^2 \end{bmatrix} \tag{2.80}$$

$$\mathbf{B_s} = \begin{bmatrix} 2\omega_\xi\zeta_\xi & 0 & 0 \\ 0 & 2\omega_\alpha\zeta_\alpha & 0 \\ 0 & 0 & 2\omega_\beta\zeta_\beta \end{bmatrix} \tag{2.81}$$

$$\boldsymbol{K_s} = \begin{Bmatrix} M(\xi)\omega_\xi^2 \\ G(\alpha)r_\alpha^2\omega_\alpha^2 \\ N(\beta)r_\beta^2\omega_\beta^2 \end{Bmatrix} \tag{2.82}$$

2.3.3 Coupling the Full Euler Code

The direct coupling of the full Euler code with the structural dynamics equations was not made in this study. Instead, a strong coupling scheme as developed by Newmark [83, 84] and used

by Djayapertapa [85] was adopted. Newmark's method is applied to a time integration scheme as,

$$\boldsymbol{q}'^{t+\Delta T} = \boldsymbol{q}'^{t} + \Delta t(1-\overline{\delta})\boldsymbol{q}''^{t} + \Delta t\overline{\delta}\boldsymbol{q}''^{t+\Delta t} \tag{2.83}$$

$$\boldsymbol{q}^{t+\Delta T} = \boldsymbol{q}^{t} + \Delta t\boldsymbol{q}'^{t} + \Delta t^2(\frac{1}{2}-\overline{\alpha})\boldsymbol{q}''^{t} + \Delta t^2\overline{\alpha}\boldsymbol{q}''^{t+\Delta t} \tag{2.84}$$

where $\boldsymbol{q}$ represents the structural states, $'$ is differentiation with respect to non-dimensional time and $\overline{\delta}$ and $\overline{\alpha}$ are parameters chosen to maintain integration accuracy and stability. For the testcases in this work the variables are set to $\overline{\delta} = \frac{1}{2}$ and $\overline{\alpha} = \frac{1}{4}$ which have been proven to give good accuracy [85]. The vector $\boldsymbol{q}$ contains the structural states, ξ, α and β. It is assumed that the value of $\boldsymbol{q}$ from the current time-step, t, is known and so, to predict the information at $t+\Delta t$ only $\boldsymbol{q}''^{t+\Delta t}$ is required. The basic equation 2.8 can be applied at time level $t+\Delta t$ as,

$$\mathbf{M}\boldsymbol{q}''^{t+\Delta t} + \mathbf{B_s}\boldsymbol{q}'^{t+\Delta t} + \mathbf{K}\boldsymbol{q}^{t+\Delta t} = \boldsymbol{f}_{\mathbf{a}}^{t+\Delta t} \tag{2.85}$$

where $\boldsymbol{f}_a^{t+\Delta t}$ is the vector of lift, moment and hinge moment. The mass, damping and stiffness matrices are non-dimensionalised consistently with the aerodynamic non-dimensioning to give,

$$\mathbf{M} = \begin{bmatrix} 1 & x_\alpha & x_\beta \\ x_\alpha & r_\alpha^2 & [r_\beta^2 + x_\beta(C_\beta - a_h)] \\ x_\beta & [r_\beta^2 + x_\beta(C_\beta - a_h)] & r_\beta^2 \end{bmatrix} \tag{2.86}$$

$$\mathbf{B_s} = \frac{2M_\infty\sqrt{\gamma}}{U^*\sqrt{\mu}} \begin{bmatrix} 2\omega_\xi\zeta_\xi & 0 & 0 \\ 0 & 2\omega_\alpha\zeta_\alpha & 0 \\ 0 & 0 & 2\omega_\beta\zeta_\beta \end{bmatrix} \tag{2.87}$$

$$\mathbf{K} = \frac{4M_\infty^2\gamma}{U^{*2}\mu} \begin{bmatrix} (\frac{\omega_h}{\omega_\alpha})^2 & 0 & 0 \\ 0 & r_\alpha^2 & 0 \\ 0 & 0 & r_\beta^2\left(\frac{\omega_\beta}{\omega_\alpha}\right)^2 \end{bmatrix} \tag{2.88}$$

Substituting $\boldsymbol{q}'^{t+\Delta T}$ and $\boldsymbol{q}^{t+\Delta T}$ from equations 2.83 and 2.84 into equation 2.85 gives,

$$\begin{aligned}[\mathbf{M} + \Delta t\overline{\delta}\mathbf{B_s} + \Delta t^2\overline{\alpha}\mathbf{K}]\boldsymbol{q}''^{t+\Delta t} = &\boldsymbol{f}_a^{t+\Delta t} - \mathbf{B_s}\{\boldsymbol{q}'^{t} + \Delta t(1-\overline{\delta})\boldsymbol{q}''^{t}\} - \\ &\mathbf{K}\{\boldsymbol{q}^{t} + \Delta t\boldsymbol{q}' + \Delta t^2(\frac{1}{2}-\overline{\alpha})\boldsymbol{q}''^{t}\}\end{aligned} \tag{2.89}$$

The above formulation allows the calculation of $\boldsymbol{q}''^{t+\Delta T}$ directly and thus both $\boldsymbol{q}'^{t+\Delta T}$ and $\boldsymbol{q}^{t+\Delta T}$ if the aerodynamic forces are known at the time-step $t+\Delta t$.

In order to obtain a fully accurate solution, the equations for the dynamics and aerodynamics must be solved simultaneously for $\boldsymbol{q}$ and $\boldsymbol{f}_a$. The simultaneous solution is only possible if an

iterative procedure is used. In this procedure [85], at a time-step $t + \Delta t$, the aerodynamic and dynamics codes are run several times until,

$$max(|\boldsymbol{f}_a^l - \boldsymbol{f}_a^{l-1}|) < \Gamma \tag{2.90}$$

where l is a number of iterations between the aerodynamic and coupled codes at time level $t+\Delta t$ and Γ is a specified convergence tolerance. This process is started by initially estimating $\boldsymbol{f}_a^{t+\Delta t}$ as,

$$\boldsymbol{f}_a^{t+\Delta t} \approx 3\boldsymbol{f}_a^t - 3\boldsymbol{f}_a^{t-\Delta t} + \boldsymbol{f}_a^{t-2\Delta t} \tag{2.91}$$

then, solving the structural equations 2.89, to give new displacement, $\tilde{\boldsymbol{q}}^{t+\Delta t}$, and velocity, $\tilde{\dot{\boldsymbol{q}}}^{t+\Delta t}$. These values are then returned to the aerodynamics code to give a new value for $\boldsymbol{f}_a^{t+\Delta t}$. The new force value is then substituted into 2.89 and the process repeated until convergence is achieved. Weak coupling schemes - which are not used here - solve for $\boldsymbol{q}$ and $\boldsymbol{f}$ out of step, thus avoiding iteration but introducing an additional error. Strong coupling has many benefits over weak coupling [85], but mainly that for a given convergence rate the number of steps required per cyclic oscillation is much lower. For the cases that are modelled in this work the number of steps per cycle is set at approximately 60. This approach was shown by Djayapertapa [85] to give good accuracy with only a small penalty in terms of computational speed.

When applying this technique to non-linear structural problems such as cubic stiffening and freeplay this formulation is not directly applicable. The equations become non-linear functions of the position vector $\boldsymbol{q}$ and therefore equation 2.85 is not valid. For the case of the simple bilinear and hysteresis this problem can be overcome by using the stiffness in the particular region of interest. For polynomial non-linearities the solution required is complicated, as the system stiffness changes through every time-step. As a result the stiffness at each time-step must be linearised to form an equivalent stiffness matrix $\tilde{\mathbf{K}}$. This has implications upon the time-step that can be utilised. However, it is possible, during the iterative convergence stage, to alter $\tilde{\mathbf{K}}$ to be the average between time-steps t and $t + \Delta t$, so maximising the allowable time-step. Using this method, however, care must be taken at turning points and at switching points if piecewise non-linear systems are implemented as the predicted stiffnesses maybe incorrect. This would result in a requirement for a very small time-step relative to step sizes typically used in linear analysis.

2.3.4 Coupling the Reduced Order Model (ROM)

The ROM can be easily coupled to the structural model to create a state-space model of complicated non-linear systems. The basic formulation of the ROM gives a state space model of the aerodynamics as,

$$\begin{aligned}\dot{\boldsymbol{X}}(t) &= \mathbf{A}\boldsymbol{X}(\mathrm{t}) + \mathbf{B}\boldsymbol{U}(\mathrm{t}) \\ \boldsymbol{Y}(t) &= \mathbf{C}\boldsymbol{X}(\mathrm{t}) + \mathbf{D}\boldsymbol{U}(\mathrm{t})\end{aligned} \tag{2.92}$$

where,

$$\boldsymbol{U} = \begin{Bmatrix} h_a \\ \alpha \\ \beta \\ \dot{h}_a \\ \dot{\alpha} \\ \dot{\beta} \end{Bmatrix}, \qquad \boldsymbol{Y} = \begin{Bmatrix} \hat{C}_L \\ \hat{C}_{M_{ea}} \\ \hat{C}_H \end{Bmatrix} \tag{2.93}$$

where h_a is positive upwards and non-dimensionalised with respect to chord in the aerodynamic formulation so $h_a = -2\xi$. Rearranging the equations of motion into a form consistent with this aerodynamic formulation, the structural equations become,

$$\begin{bmatrix} -2 & x_\alpha & x_\beta \\ -2x_\alpha & r_\alpha^2 & r_\beta^2 + x_\beta(C_\beta - a_h) \\ -2x_\beta & r_\beta^2 + x_\beta(C_\beta - a_h) & r_\beta^2 \end{bmatrix} \begin{Bmatrix} \ddot{h}_a \\ \ddot{\alpha} \\ \beta \end{Bmatrix}$$

$$+ \frac{2M_\infty\sqrt{\gamma}}{U^*\sqrt{\mu}} \begin{bmatrix} 4\omega_\xi\zeta_\xi & 0 & 0 \\ 0 & 2\omega_\alpha\zeta_\alpha & 0 \\ 0 & 0 & 2\omega_\beta\zeta_\beta \end{bmatrix} \begin{Bmatrix} \dot{h}_a \\ \dot{\alpha} \\ \dot{\beta} \end{Bmatrix} + \frac{4M_\infty^2\gamma}{U^{*2}\mu} \begin{bmatrix} -2(\frac{\omega_h}{\omega_a})^2 & 0 & 0 \\ 0 & r_\alpha^2 & 0 \\ 0 & 0 & r_\beta^2\left(\frac{\omega_\beta}{\omega_a}\right)^2 \end{bmatrix} \begin{Bmatrix} h_a \\ \alpha \\ \beta \end{Bmatrix}$$

$$= \frac{4M_\infty^2\gamma}{\pi\mu} \begin{Bmatrix} -(\overline{C_L} + \hat{C_L}) \\ 2(\overline{C_{M_{ea}}} + \hat{C_{M_{ea}}}) \\ 2(\overline{C_H} + \hat{C_H}) \end{Bmatrix} \tag{2.94}$$

which is of the form of the equations of motion 2.8. If the vector $\boldsymbol{U}$ is split into,

$$\boldsymbol{U}_1 = \begin{Bmatrix} h_a \\ \alpha \\ \beta \end{Bmatrix} \qquad \boldsymbol{U}_2 = \begin{Bmatrix} \dot{h}_a \\ \dot{\alpha} \\ \dot{\beta} \end{Bmatrix} \tag{2.95}$$

using the state space formulae 2.92 the equations of motion become,

$$\mathbf{M}\dot{\boldsymbol{U}}_2 + \mathbf{B}_s\boldsymbol{U}_2 + \mathbf{K}\boldsymbol{U}_1 = \frac{4M_\infty^2\gamma}{\pi\mu}\left\{\mathbf{f}\left\{\mathbf{C}\boldsymbol{X} + \mathbf{D}\boldsymbol{U}\right\} + \begin{Bmatrix} -\overline{C_L} \\ 2\overline{C_{M_{ea}}} \\ 2\overline{C_H} \end{Bmatrix}\right\} \tag{2.96}$$

where $\mathbf{B_s}$ denotes the structural damping matrix and,

$$\mathbf{f} = \begin{bmatrix} -1 & 0 & 0 \\ 0 & 2 & 0 \\ 0 & 0 & 2 \end{bmatrix} \tag{2.97}$$

Using this formulation a set of ordinary differential equations that represent the structural motion can be generated as,

$$\begin{Bmatrix} \dot{U}_1 \\ \dot{U}_2 \end{Bmatrix} = \begin{bmatrix} 0 & \mathbf{J} \\ \mathbf{M^{-1}FC} & \mathbf{M^{-1}}\left[\mathbf{D} - \overline{\mathbf{K}}\right] \end{bmatrix} \begin{Bmatrix} X \\ U \end{Bmatrix} + \begin{Bmatrix} 0 \\ \overline{C} \end{Bmatrix} \tag{2.98}$$

where,

$$\mathbf{J} = \begin{bmatrix} 0 & 0 & 1 & 0 & 0 \\ 0 & 0 & 0 & 1 & 0 \\ 0 & 0 & 0 & 0 & 1 \end{bmatrix} \quad \overline{\mathbf{K}} = \begin{bmatrix} \mathbf{K} & \mathbf{B_s} \end{bmatrix} \quad \overline{C} = \mathbf{f} \begin{Bmatrix} \overline{C_L} \\ \overline{C_{M_{ea}}} \\ \overline{C_H} \end{Bmatrix} \tag{2.99}$$

Combining this representation of the structural motion equations with the aerodynamic state-space equation (2.64), the aeroelastic model of the system is obtained,

$$\begin{Bmatrix} \dot{X} \\ \dot{U}_1 \\ \dot{U}_2 \end{Bmatrix} = \begin{bmatrix} \mathbf{A} & \mathbf{B} \\ 0 & \mathbf{J} \\ \mathbf{M^{-1}FC} & \mathbf{M^{-1}}\left[\mathbf{D} - \overline{\mathbf{K}}\right] \end{bmatrix} \begin{Bmatrix} X \\ \begin{Bmatrix} U_1 \\ U_2 \end{Bmatrix} \end{Bmatrix} + \begin{Bmatrix} 0 \\ 0 \\ \overline{C} \end{Bmatrix} \tag{2.100}$$

With the state equations in this form it is possible to implement existing well developed aeroelastic analysis techniques that are usually used only for low speed analysis.

When non-linear stiffnesses are investigated, the additional non-linearities can easily be substituted with the relevant terms from the stiffness matrix removed if required. Therefore, the structural dynamics equation (2.98) becomes,

$$\begin{Bmatrix} \dot{U}_1 \\ \dot{U}_2 \end{Bmatrix} = \begin{bmatrix} 0 & \mathbf{J} \\ \mathbf{M^{-1}FC} & \mathbf{M^{-1}}[\mathbf{D} - \overline{\mathbf{K}}_s] \end{bmatrix} \begin{Bmatrix} X \\ \begin{Bmatrix} U_1 \\ U_2 \end{Bmatrix} \end{Bmatrix} + \begin{Bmatrix} 0 \\ \overline{C} \end{Bmatrix} + \begin{Bmatrix} 0 \\ \mathbf{M^{-1}} \begin{Bmatrix} M(h) \\ G(\alpha) \\ N(\beta) \end{Bmatrix} \end{Bmatrix} \tag{2.101}$$

where $\overline{\mathbf{K}}_s$ is now,

$$\overline{\mathbf{K}}_s = [0 \quad \mathbf{B_s}] \tag{2.102}$$

2.4 Ground Vibration Test Simulation

In industry Ground Vibration/Resonance Tests (GV(R)Ts) and shaker table tests are performed to validate finite element models of structures. These tests consist of suspending the aircraft or component from bungees or low frequency supports and applying vibrations through shakers. Accelerometers attached to the shakers and model then feed back information regarding the structural dynamics for a known applied load. After post-processing the signals from the accelerometers and the shakers, it is possible to generate Frequency Response Functions (FRFs) and to extract the mode shapes of the system, i.e. the deflected shapes that occur for a given input. This information is then analysed and information regarding damping and non-uniform stiffnesses is extracted which is then used to update the finite-element model of the structure. In linear system models the mode shapes and FRFs are easily extracted by knowing the mass, damping and stiffness matrices. When analysing the response of non-linear systems the linear amplitude relationship no longer holds. The amplitude relationship for linear system says that, if the force from the shakers is doubled then the amplitude also doubles. For non-linear systems this no longer holds true and, therefore, tests for different amplitude inputs must be performed.

Conventionally, GVTs and shaker tests take the form of sinusoidal oscillations at different frequencies with a fixed amplitude. The frequencies are usually swept through at a logarithmic rate as the width of any frequency peak also tends to vary logarithmically. Nowadays, random inputs are applied but with equal energy being applied at all the frequencies within the required frequency range. As equal energy is applied the dominant frequencies that are found are the same resonance peak that would have been found during frequency sweep type tests. However, it is shown that because, in non-linear systems, the amplitude of the oscillations seen does not vary linearly with the magnitude of the force applied, sinusoidal tests only can be used as a comparative method as both the frequencies and, more importantly, the magnitudes are known.

To allow better methods of model validation from GVTs it is desirable to analyse the system with any known or predicted non-linearities included. Therefore, to simulate ground vibration tests on non-linear structures, the standard equations of motion 2.75 and 2.78 have been analysed for the two and three degree-of-freedom cases respectively. The system has been analysed by recreating the test conditions with the aerodynamic functions being replaced by excitation forces simulating the excitation at different frequencies and magnitudes.

2.5 Concluding Remarks

The preceeding chapter Sdescribed the type of non-linearities that may exist in aircraft structures. The types of non-linearities described included both forms that could be described exactly by a single equation (continuous non-linearities) and systems that contained discrete discontinuities; the latter category included combinations of continuous and discrete non-linearities. A discussion of previous studies of the various aeroelastic structural non-linearities has also been made, highlighting the benefits and restrictions of the various methods adopted by the authors. Following this discussion, the basic system of aeroelastic equations was described in terms of two (heave and pitch) and three (heave, pitch and control rotation) degree-of-freedom systems including derivation from the basic Lagrange equations.

The aerodynamic models to be used in this work have also been discussed in this chapter, along with a description of how they are coupled together with the structural equations. The aerodynamic models were divided in to three basic forms low-speed models (less than approximately Mach 0.2), finite volume (Euler) models and Reduced Order Models (ROMs). The low-speed models are extensively used in the study of aeroelastic systems with non-linearities or when analysing control systems as they are simple to implement, well established and lend themselves to being expressed in the same form as the structural equations. The finite volume techniques are now also becoming well established and allow the simulation of transonic flows. The method suffers from long run times as the analysis usually takes the form of a time integration that requires many steps before a stable solution is reached. Recognising the problems of the finite volume technique, the Reduced Order Models (ROMs) express the aerodynamic forces in the same regimes as the Euler simulations in the same form as the structural equations and, as such, do not rely on time integration methods. The accuracy of the ROMs has as yet to be proven as it is a newly established technique but if it is successful, it should allow transonic aeroelastic problems to be solved more quickly than is currently possible.

In conclusion, this section has described the type of non-linearities that may be encountered in real aeroelastic structures, defined the aerodynamic models to be used in this work and shown how the various aerodynamic models can be coupled with both the linear and non-linear structural models. From this basic description of the coupled aeroelastic equations, this work goes on to describe the theory behind numerical continuation. This form of analysis is used extensively in this work to analyse both the discrete and continuous forms of non-linearities both with and without control laws.

Chapter 3

Continuation

This chapter introduces the theory and practice of numerical continuation. Firstly, the basic nature of dynamics is introduced with reference to form and stability of the possible solutions. The branch tracing theory of numerical continuation is then presented. This is followed by a brief overview of how this method can be implemented in practice, including a description of the progression of the solution branches along with the methods by which its stability may be assessed. Additionally, this chapter shows that numerical continuation allows the analysis of continuous sets of Ordinary Differential Equations (ODEs) or sets of algebraic equations.

3.1 Introduction

Throughout the fields of science and engineering there are many examples of dynamic systems, from simple systems such as the bending of a rod under an applied load through to the complexities of nerve impulses and climatic changes. Despite the range in complexity, all dynamic systems exhibit stationary, oscillatory or chaotic/quasi-periodic phenomena that can be either stable or unstable. Figures 3.1 to 3.3 show the basic forms that these systems can take by way of a time simulation. Figure 3.1 shows the stationary form of solution which is invariant with time. Figure 3.2 shows an oscillatory solution which, as the figure shows, does not have to be of a simple sinusoidal form. A chaotic or quasi periodic oscillation, as shown in figure 3.3, is characterised as being a non-repeating solution, i.e. the oscillatory pattern is never repeated. In these figures, it should be noted that transients in the motions would exist before the illustrated solution form is converged upon.

To analyse a system and its behaviour fully, it is not only necessary to characterise the form of

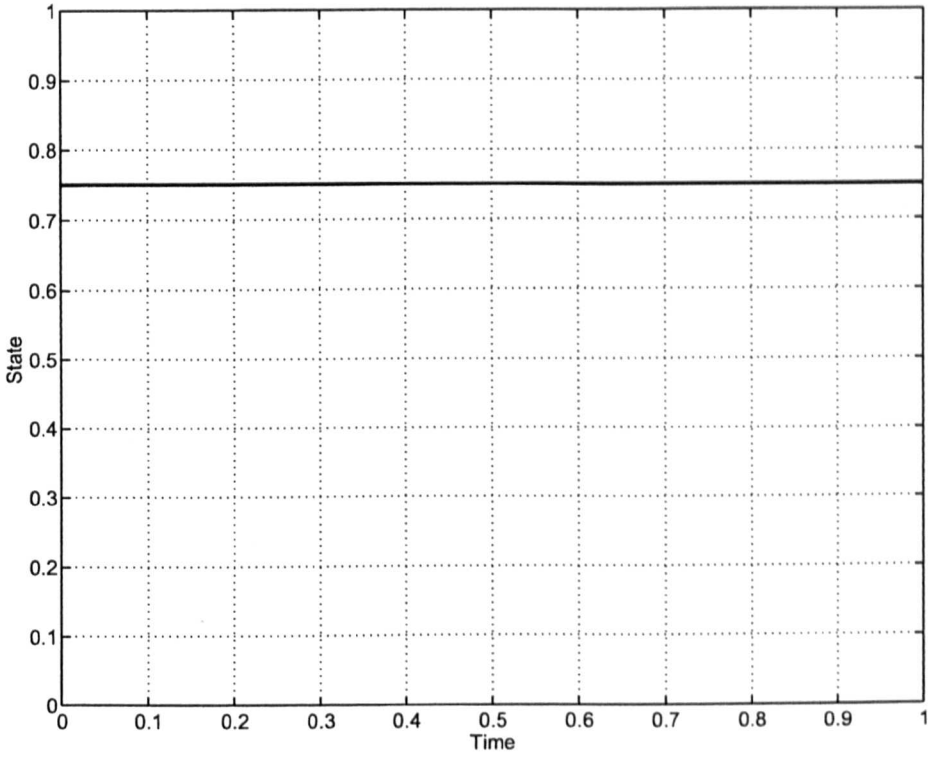

Fig 3.1: Example of Stationary Solution

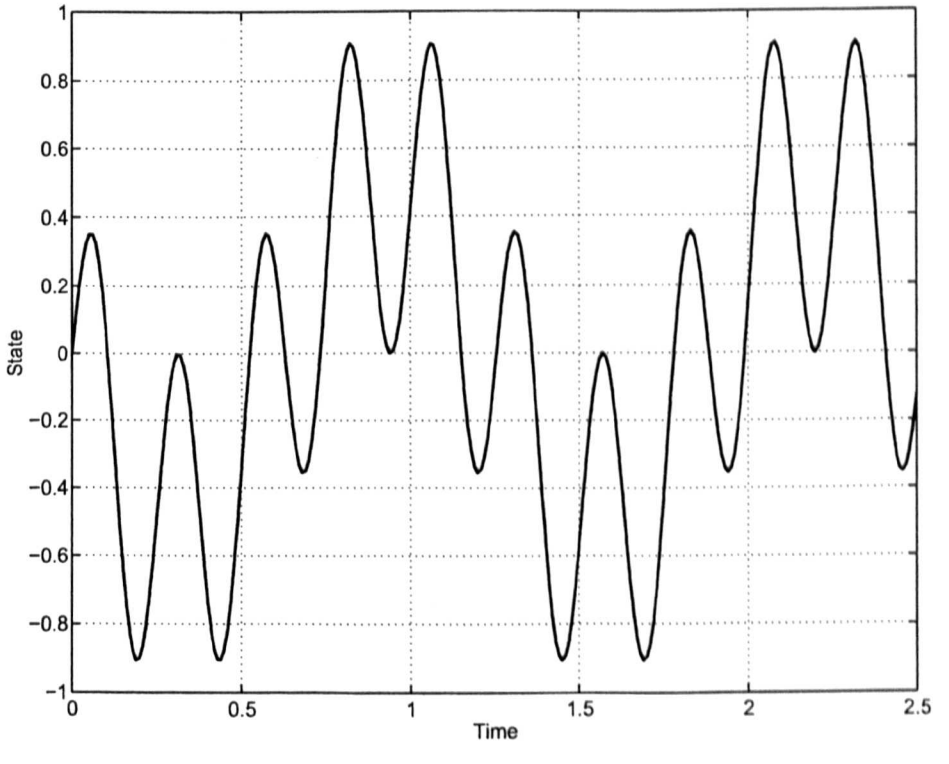

Fig 3.2: Example of Oscillatory Solution

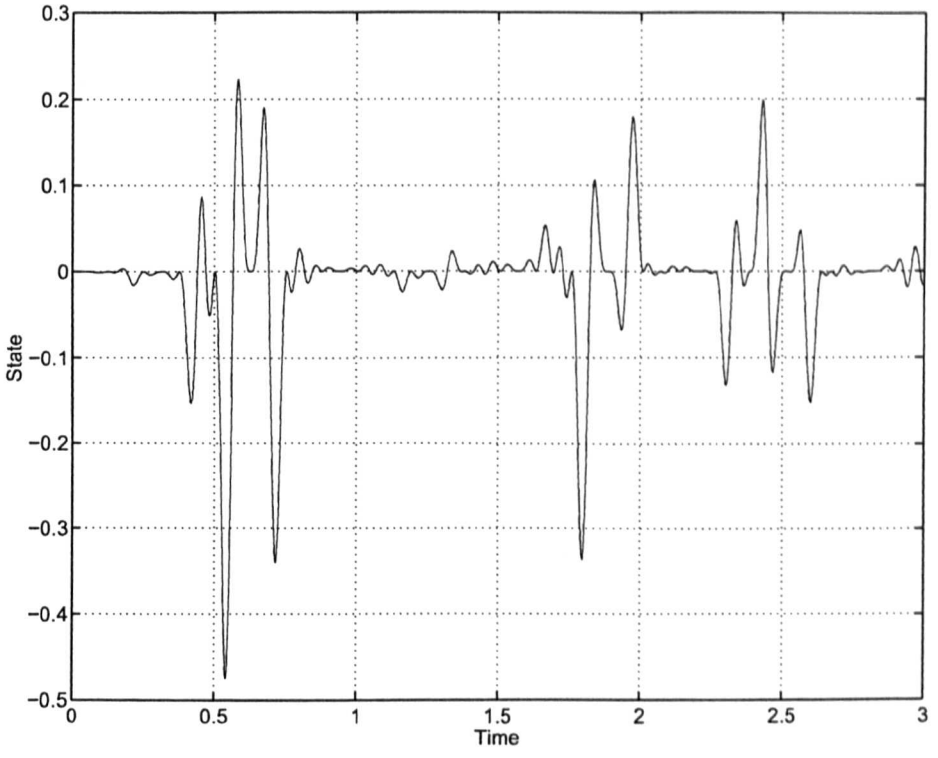

Fig 3.3: Example of Chaotic Solution

the solution, but it is also necessary to assess that system's stability. Consider, for example, a frictionless inverted pendulum is a valid stationary solution, but any deviation from the vertical would mean a loss in system stability with the system settling in the non-inverted position. Such stability classification is also possible for oscillatory systems where the system motions can either be attracted to a periodic orbit or repelled away from an orbit. Figures 3.4 and 3.5 show a source (stationary unstable solution) and a sink (stable stationary solution) respectively. The resultant motion shown in these figures are the responses of the system to a low amplitude sinusoidal forced displacement in to the system. Figure 3.4 shows that an unstable stationary solution departs from its solution when a small perturbation is applied whereas figure 3.5 shows that a stable solution returns to the stationary solution when subjected to a small perturbation. This behaviour is sometimes illustrated using a vector field which shows the direction of the motion of particles when released from within a system's phase space (see figure 3.8). Figures 3.6 and 3.7 show unstable and stable Limit-Cycle Oscillations (LCOs) solutions respectively. As with the stationary solutions these systems are subjected to a small perturbation from their initial LCO. When an unstable limit-cycle is subjected to a small perturbation its motion diverges from the limit-cycle on to a different solution or diverge to infinity (see figure 3.6. In comparison, a stable LCO returns on to the same solution when subjected to a small perturbation.

The following sections describes how dynamic systems are represented mathematically and

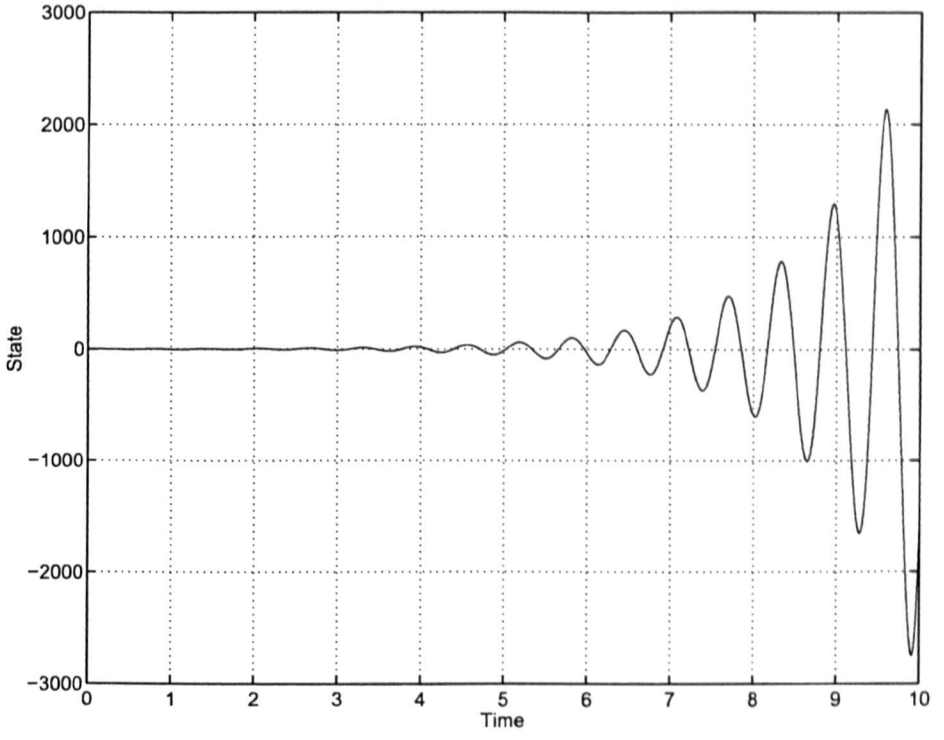

Fig 3.4: A Source or Unstable Stationary Solution

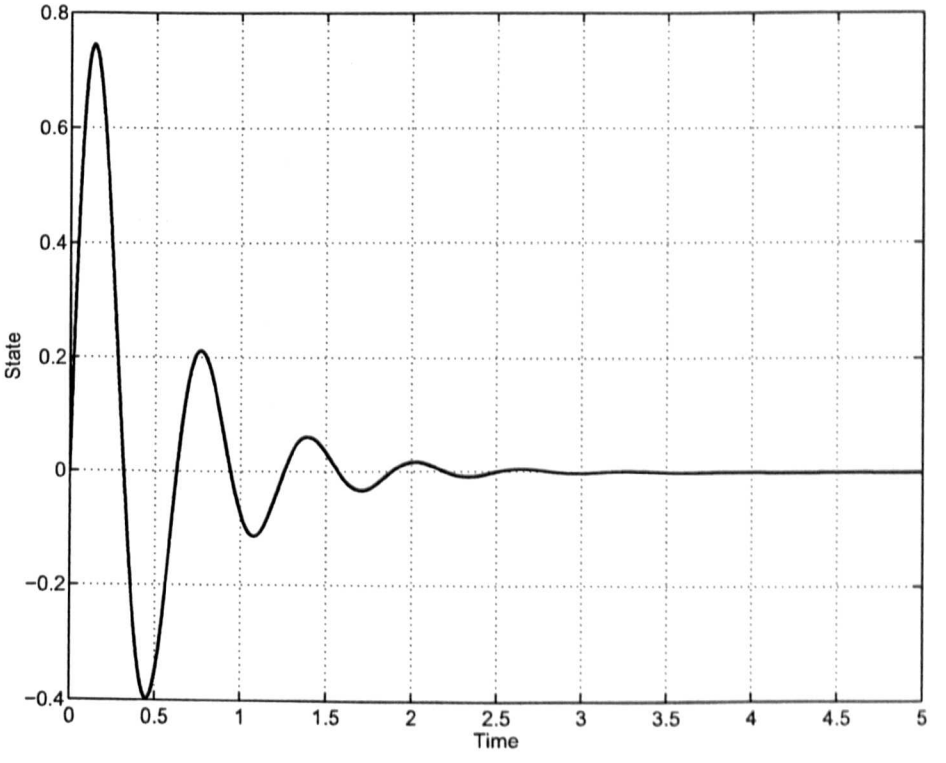

Fig 3.5: A Sink or Stable Stationary Solution

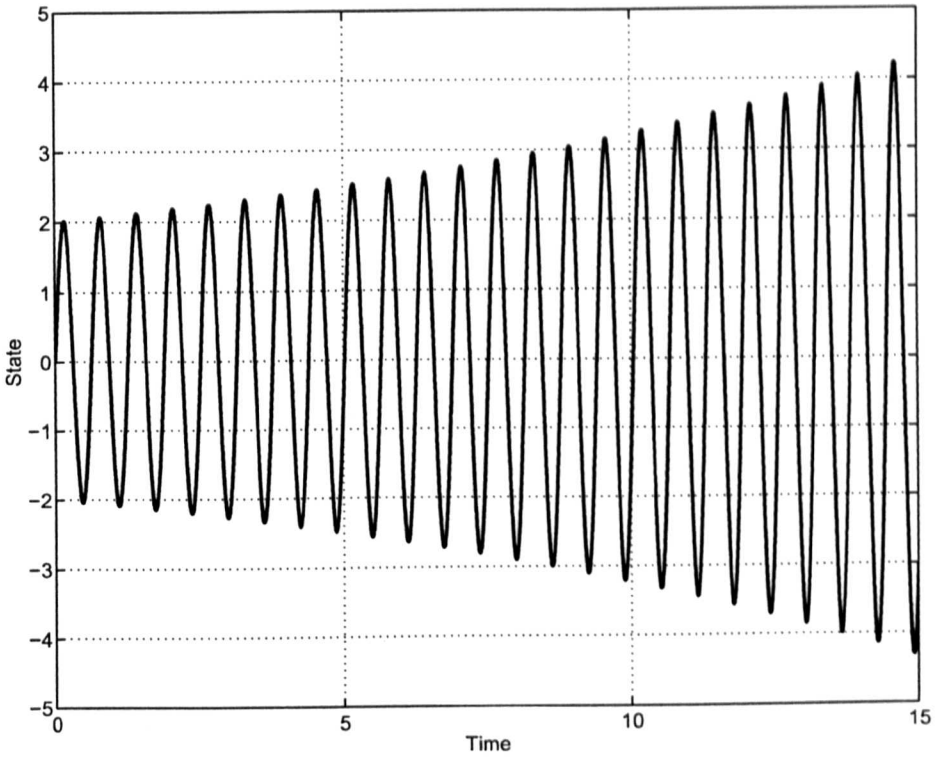

Fig 3.6: An Unstable Oscillatory Solution

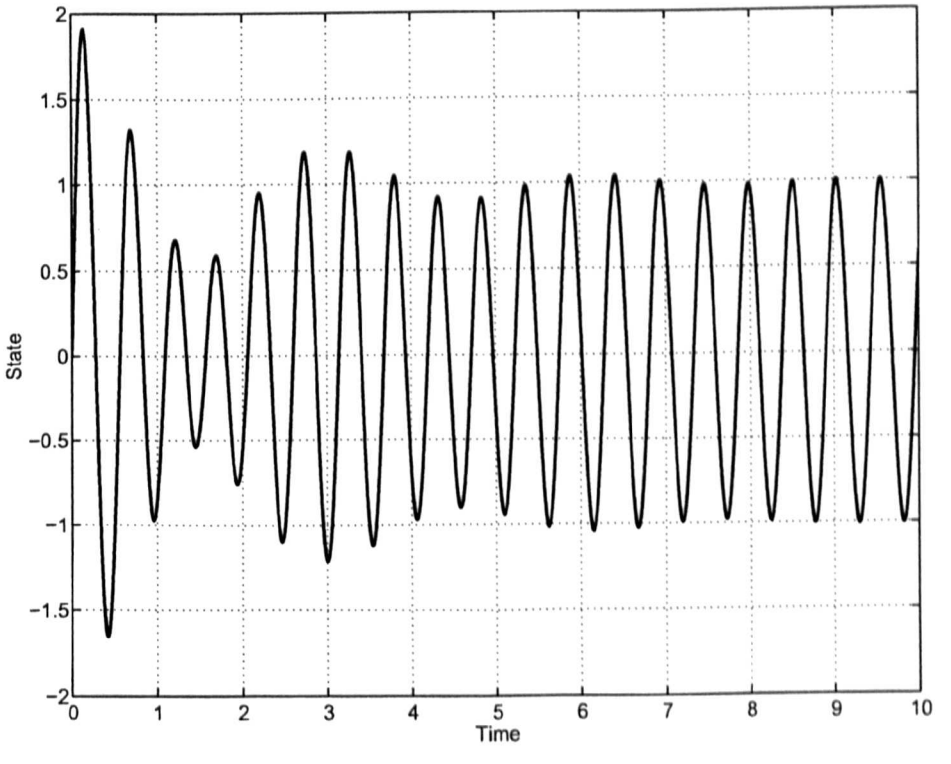

Fig 3.7: A Stable Osillatory Solution

analysed computationally along with an explanation of continuation techniques that can be used to rapidly predict the behaviour of these dynamic systems.

3.2 Solution Types

3.2.1 Stationary Points

Stationary points, as stated in the previous section, are locations at which a system is at a static equilibrium (this equilibrium maybe stable or unstable). For general dynamic systems it is possible to describe a system's motion in time by a set of Ordinary Differential Equations (ODEs). The n states of a system can be defined by functions $y_1(t), y_2(t), \ldots, y_n(t)$ where the state variables can, for example, represent system displacements, electrical potentials or magnetic flux. Commonly, the independent variable t represents time but could also represent other measures such as distance or velocity. If the system dynamics can be expressed by a set of ODEs, the system equations can be written such that the right hand side of the equations are not expressed as a function of t and are represented in vector form by,

$$\dot{\boldsymbol{y}} = \boldsymbol{f}(\boldsymbol{y}) \tag{3.1}$$

Given initial conditions of $\boldsymbol{y}(0)$, these systems can be integrated numerically using finite difference time integration techniques such as the Runge-Kutta method. Time integration allows the trajectory of a state to be plotted against the time variable (as was shown in figures 3.4 to 3.6). Following a series of such paths for different initial conditions, it is possible to generate a phase plane as shown in figure 3.8. A full phase plane representing the whole system would be n-dimensional and becomes somewhat more difficult to visualise.

With the ODEs defined in equation 3.1 the location of stationary (equilibrium) points can be found by setting,

$$\dot{\boldsymbol{y}} = \boldsymbol{0} \tag{3.2}$$

These equations define that all the derivative terms of the system are zero and therefore the system is at rest. This condition allows the system to be defined as,

$$\boldsymbol{f}(\boldsymbol{y}^s) = \boldsymbol{0} \tag{3.3}$$

Where $\boldsymbol{y}^s$ represents the state's stationary solution point as a vector of all of the states.

Techniques that are applied to the solution of ODEs are also equally applicable to the solution

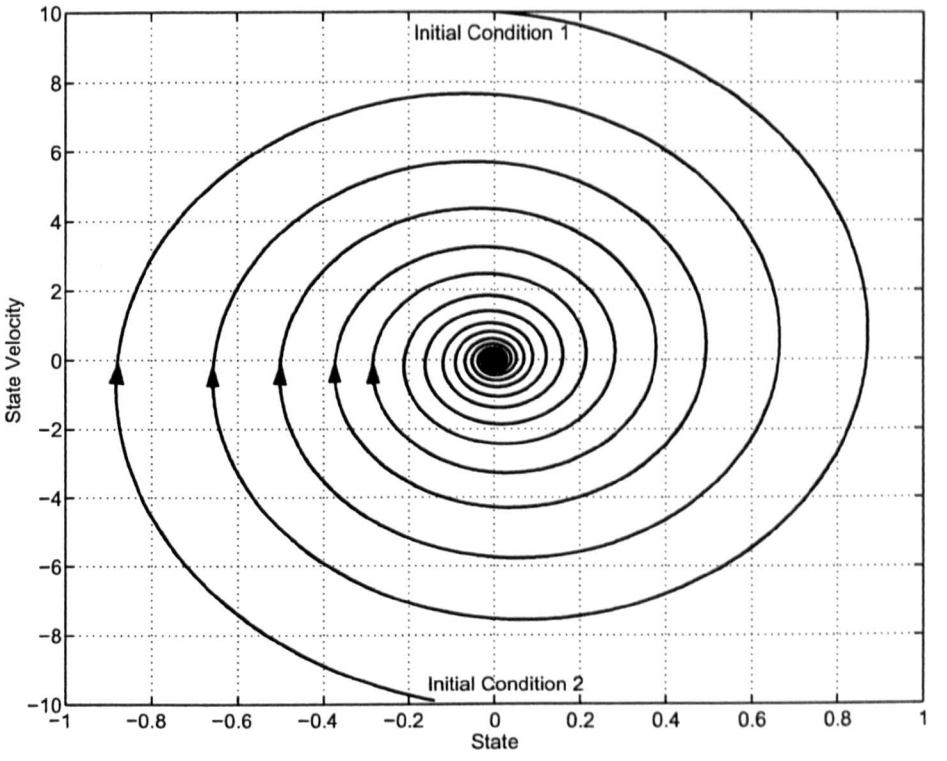

Fig 3.8: A Phase Plane Plot of a Stable Stationary Solution

of algebraic problems. Such problems can be defined as,

$$\boldsymbol{x} = \boldsymbol{f}(\boldsymbol{y}, \lambda) \tag{3.4}$$

where $\boldsymbol{x}$ are the desired system solutions and λ is an independent variable. This is simply rearranged to give an equation of the form.

$$\mathbf{0} = \boldsymbol{f}(\boldsymbol{y}, \lambda) - \boldsymbol{x} \tag{3.5}$$

It can be seen that, given the solution required, $\boldsymbol{x}$, λ can be varied and the states that satisfy the solutions calculated.

3.2.2 Limit-Cycle Solutions

With the dynamic system of ODEs represented by $\dot{\boldsymbol{y}} = \boldsymbol{f}(\boldsymbol{y})$, it is possible to define a cyclic oscillation as the solution of the equations. As with the stationary points, limit-cycle solutions may be attracting (stable) or repelling (unstable). Limit-cycles are distinguished from chaotic or quasi-periodic solutions in that they represent regular repeating motions. As the motion is repeatable, the solution states $\boldsymbol{y}$ must, after some time T, return to the same value.

$$\boldsymbol{y}(t + T) = \boldsymbol{y}(t) \tag{3.6}$$

This equation does not necessarily hold for all values of t, as most systems have some form of transients that damp out after a certain time, t_+, therefore the time t must be greater than this value. The time taken for one complete oscillation is the period of the system and is defined as the minimum value of T that satisfies the equation 3.6.

The way in which such limit-cycle solutions are calculated and their stability assessed as described later in this chapter.

3.2.3 Chaotic or Quasi-Periodic Solutions

Chaotic or quasi-periodic solutions are solutions where the state vector $\boldsymbol{y}$ that defines a system is never repeated at any time. An illustration of a chaotic system was shown in figure 3.3. The description of chaos is often misunderstood; it is a stable state with finite bounds on its amplitude, but an infinite period. As such, a chaotic motion cannot be unstable as every possible state combination within the vector $\boldsymbol{y}$ must be contained within the solution, given the bounds on the chaotic motion. However, this definition of chaos does not preclude the possibility of other stable or unstable solutions existing for state conditions outside of the range of the chaotic system.

3.3 Stability Assessment

3.3.1 Stationary Points

The stability of a given stationary point $\boldsymbol{y}^s$ is assessed by the response of a given system, $\dot{\boldsymbol{y}} = \boldsymbol{f}(\boldsymbol{y})$, to a small perturbation in one or more of the system states $\boldsymbol{y}$. An asymptotically stable solution, or sink, is defined as,

$$\boldsymbol{y}(t) \xrightarrow{t\to\infty} \boldsymbol{y}^s \tag{3.7}$$

This means that, after a perturbation, the system returns to its original state $\boldsymbol{y}^s$ as time approaches infinity.

Such systems do not always be globally attracting as, for some larger impulse, the system may tend to another stable solution. This is simply illustrated by assessing the stability of a ball on an undulating surface as shown in figure 3.9, where a small perturbation δ_1 results in the ball

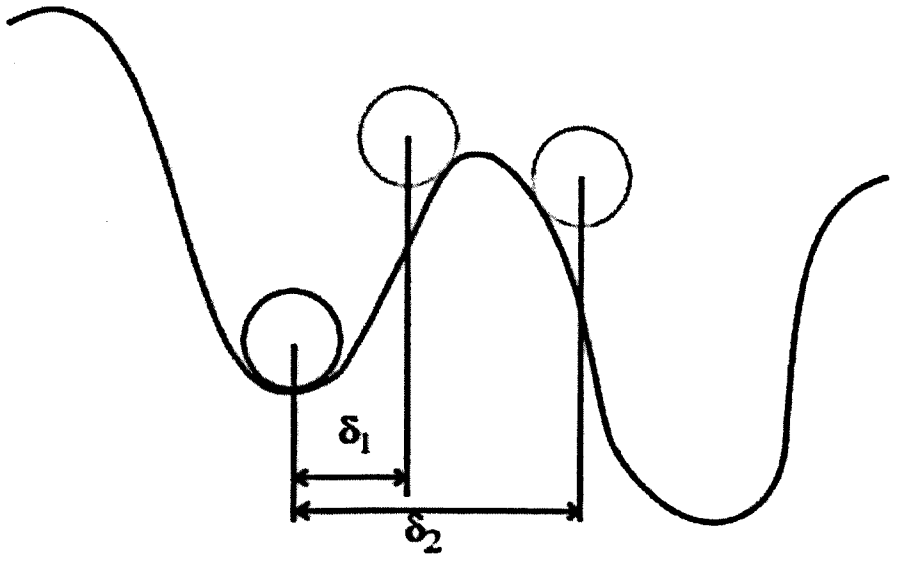

Fig 3.9: Stability Criteria

returning to its original position whereas some larger perturbation δ_2 results in the ball tending to another stable solution.

If a system response, defined by $\dot{y} = f(y)$, to a small impulse is to diverge from the solution, then the system is termed unstable. An unstable solution or source can be illustrated again with an undulating surface where the initial solution y_s is at the top of a peak and, therefore, any perturbation results in the system diverging on to another solution. Flutter is an example of such a phenomenon as for some wing setting there is no motion, but any small gust would cause flutter to occur. In many practical situations unstable solutions cannot be found as general noise and unsteadiness within the system precludes its detection.

3.3.2 Limit-Cycle Oscillations

The definition of stability for Limit-Cycle Oscillations (LCOs) follows from the definition of the previous section. A stable LCO is classified as when trajectories displaced from an LCO, either inside or outside, are attracted back on to the LCO. Similarly, orbits are classified as unstable when trajectories depart from the region of the LCO when displaced from it.

The stability of an LCO is not, just as with the stability of stationary points, global but within a certain domain of convergence. The detection of unstable LCOs is difficult as small perturbations can exist that tend to knock the system onto a stable point or oscillation. However, it is possible to detect solutions that are marginally unstable, as these are characterised by very

slow divergence from an unstable LCO onto an alternative solution.

3.4 Continuation Methods

3.4.1 Introduction

The principles of numerical continuation were developed in the 1960s but are, only now, seeing widespread application outside of the mathematics field. The continuation procedure uses a form of path following where, from an initial solution, the whole domain of solutions are traced out, including detection of stationary and limit-cycling solutions along with assessment of their stability.

The following sections describe the basic methods upon which numerical continuation is based along with the mathematical techniques that are implemented. The method that is discussed is the predictor-corrector technique, other forms of continuation are presently in development but are beyond the scope of this work.

3.4.2 The Predictor-Corrector Method

The predictor-corrector method is used to solve the basic set of equations that define solutions for ODEs (this can also be applied to PDEs),

$$0 = \boldsymbol{f}(\boldsymbol{y}, \lambda) \tag{3.8}$$

where λ is a variable defined as the continuation parameter which can be any non-state variable that is used within the system equations, e.g. for an aeroelastic system it may be velocity, air density or torsional stiffness.

This general description does not preclude the solution of LCOs as the vector $\boldsymbol{y}$ is not necessarily constructed of only the system states, but can include variables that can be used to identify a system as oscillatory and not just stationary. The procedure for the predictor-corrector is illustrated in figure 3.10 where, from an initial solution $(\boldsymbol{y}^j, \lambda^j)$, the next point is predicted as $(\tilde{\boldsymbol{y}}^{j+1}, \tilde{\lambda}^{j+1})$ and then corrected to give $(\boldsymbol{y}^{j+1}, \lambda^{j+1})$.

The method used in this work is not a simple two-step procedure as iterative techniques are usually required for the corrector step until the true solution is resolved. Further details of the method can be found in many good texts on the subject [86, 87]

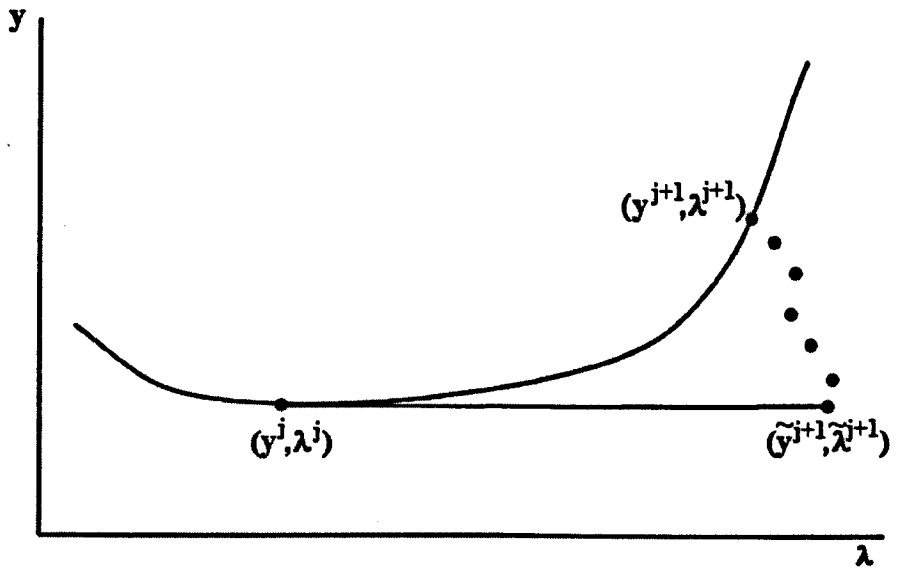

Fig 3.10: Predictor-Corrector Procedure

3.4.2.1 Parameterisation

Before the predictor-corrector method is presented it is necessary to introduce the concept of curve parameterisation. Parameterisation, instead of using the functions y_j and λ as a measure, uses a distance s along the solution curve, called the arclength. This concept is shown in figure 3.11. With this definition of curve parameterisation the system can be redefined as,

$$f(y_j(s), \lambda(s)) = 0 \tag{3.9}$$

and an additional scalar equation is added as,

$$p(y_j(s), \lambda(s), s) = 0 \tag{3.10}$$

Using the arclength parameter can be useful when gradients are such that the other systems have to resort to small stepping parameters. The form that equation 3.10 takes is described later within the context of its application to the problem.

3.4.2.2 The Predictor Step

The curve that uniquely defines the solutions to equation 3.8 is referred to as the manifold, M. In order to compute this curve, a start point near (or on) the curve is required $x^j = (y^j, \lambda^j)$.

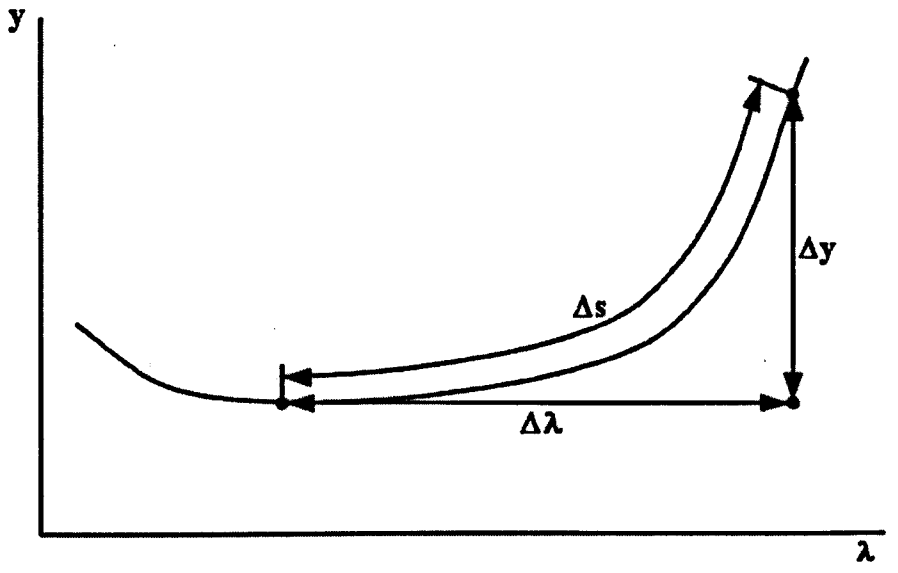

Fig 3.11: Arclength Parameterisation

Using the tangent method, the next point on the curve is estimated as,

$$\tilde{\boldsymbol{x}}^{j+1} = \boldsymbol{x}^j + h_j \boldsymbol{v}^j \tag{3.11}$$

where h_j is the step size and $\boldsymbol{v}^j$ is the normalised $(n+1)$-dimensional vector tangent to M at $\boldsymbol{x}^j$, i.e. $\|\boldsymbol{v}^j\| = 1$, or,

$$\left(\frac{dy_1}{ds}\right)^2 + \cdots + \left(\frac{dy_n}{ds}\right)^2 + \left(\frac{d\lambda}{ds}\right)^2 = 1 \tag{3.12}$$

If parameterisation is applied to the curve i.e. $\boldsymbol{x} = \boldsymbol{x}(s)$, where s is defined as an arclength (distance along the line) then the derivative of $\boldsymbol{f}(\boldsymbol{x}) = 0$ is calculated as,

$$J(\boldsymbol{x}^j)\boldsymbol{v}^j = 0 \tag{3.13}$$

where $J(\boldsymbol{y}^j)$ is the Jacobian of the state equations defined as,

$$J(\boldsymbol{x}^j) = \left.\frac{\partial \boldsymbol{f}}{\partial \boldsymbol{y}}\right|_{y=y^j} \tag{3.14}$$

In order to define a solution fully the scalar equation 3.12 must be solved (this was defined as scalar equation 3.10 in the previous section). Many numerical techniques are available for the solution, but one of the most efficient is the pseudo arclength method. This technique is a derivative of the arclength method which multiplies 3.12 by ds^2 to give,

$$0 = p(\boldsymbol{y}_j(s), \lambda(s), s) = \sum_{i=1}^{n} (y_i - y_i(s_j))^2 + (\lambda - \lambda(s_j))^2 - (s - s_j)^2 \tag{3.15}$$

This approach enables the solution of 3.8 to be uniquely fixed at an arclength distance Δs. The pseudo arclength employs an extra parameter, ς, which results in the equation,

$$0 = p(y_j(s), \lambda(s), s) = \varsigma \sum_{i=1}^{n} (y_i - y_i(s_j))^2 + (1-\varsigma)(\lambda - \lambda(s_j))^2 - (s - s_j)^2 \qquad (3.16)$$

where,

$$0 < \varsigma < 1 \qquad (3.17)$$

This formulation for the arclength is beneficial as it allows a weighting to be put on either the solution vector $\boldsymbol{y}$ or the continuation parameter λ.

By using this method the solution of equations 3.8 and 3.10 gives the tangent prediction for the solution at the next time-step, $\tilde{\boldsymbol{x}}^{j+1}$. Other techniques such as secant prediction are also possible and can be found in the books by Kuznetsov [87] and Seydel [86].

3.4.2.3 The Corrector Step

The corrector step of the process is iterative and usually relies on some form of Newton iteration type procedure. As the solution vector $\boldsymbol{f}(\boldsymbol{x})$ is only n-dimensional then an additional equation must be added to solve for the $n+1$ unknowns $(\boldsymbol{y}, \lambda)$. The Newton scheme is formulated such that the basic n equations are,

$$\boldsymbol{f}_y \Delta \boldsymbol{y} + \boldsymbol{f}_\lambda \Delta \boldsymbol{\lambda} = -\boldsymbol{f}(\boldsymbol{y}^j, \lambda^j), \quad \boldsymbol{y}^{j+1} = \boldsymbol{y}^j + \Delta \boldsymbol{y}, \quad \boldsymbol{\lambda}^{j+1} = \boldsymbol{\lambda}^j + \Delta \boldsymbol{\lambda} \qquad (3.18)$$

with the extra equation written as,

$$(\Delta \boldsymbol{y}^T, \Delta \lambda) \boldsymbol{v}^j = 0 \qquad (3.19)$$

This extra equation defines a corrector procedure that tracks along the hyperplane tangential to the vector $\boldsymbol{v}^j$. This means that the position of the solution is always a distance s (the pseudo arclength) along the curve, as opposed to systems which instead rely on a step length, defined by a constant distance λ or $\boldsymbol{y}_k$. These latter systems can become highly inefficient when gradients become large or small respectively.

The set of equations allow the Newton iteration procedure to be performed until the solution vector $(\boldsymbol{y}^{j+1}, \lambda^{j+1})$ is converged upon. The solution is the unique intersection of the hyperplane defined by 3.19, with the manifold defined by $\boldsymbol{f}(\boldsymbol{y}, \lambda)$.

3.4.2.4 Step-Size Control

In order to obtain solutions efficiently the arclength s must be modified. In areas that allow large variation in λ for small changes in $\boldsymbol{y}$, the predictor can be very close to the final solution and therefore larger steps can be taken. However, bounds do have to be enforced upon the system as if too large a time-step is taken, large regions may be skipped over. The number of iterations required for a solution within the corrector step is also a function of the accuracy of the solution required, as an example, for accuracy of the order of $\epsilon = 10^{-4}$, the optimal number of corrector steps is approximately 6 [86]. If the number of steps taken is actually N_j and the optimal number is N_{opt} optimal choice for $\tilde{\boldsymbol{x}}^{j+1}$ is given by,

$$\tilde{\boldsymbol{x}}^{j+1} = \boldsymbol{x}^j + \frac{N_{opt}}{N_j} h_j \boldsymbol{v}^j \tag{3.20}$$

This reformulation modifies the magnitude of the scalar factor h_j that determines how far the normal to the manifold is projected at each predictor step.

3.4.3 Problem Description for Limit-Cycle Oscillations

The solution for stationary points defined above is described in section 3.3, where a set of n-dimensional equations are solved for zero. The solution of the problem for limit-cycling systems is more complicated as $\dot{\boldsymbol{y}} = 0$ is not the solution. To solve the system for a periodic orbit a time must be fixed at t_0,

$$t_0 \geq t_+ \tag{3.21}$$

where t_+ is the time at which the transients have damped out and the solution lies on a periodic orbit. A limit-cycle is therefore defined by (see also equation 3.6),

$$\boldsymbol{y}(t_0) = \boldsymbol{y}(t_0 + T) \tag{3.22}$$

If a scalar equation is then defined such that it satisfies a phase relationship,

$$r(\boldsymbol{y}(t_0, \lambda)) = \dot{y}_j(t_0) = f_j(\boldsymbol{y}(t_0, \lambda)) = 0 \tag{3.23}$$

where y_j corresponds to one of the system states. This is just one of the possible phase conditions that could be applied but is convenient as, in bifurcation diagrams, the ordinate is usually plotted that satisfies this condition. If the system equations are then expanded to include T as an extra state such that,

$$\begin{Bmatrix} \dot{\boldsymbol{y}} \\ \dot{T} \end{Bmatrix} = \begin{Bmatrix} \boldsymbol{f}(\boldsymbol{y}, \lambda) \\ 0 \end{Bmatrix} \tag{3.24}$$

and an augmented boundary problem [86] is implemented as,

$$\begin{Bmatrix} \boldsymbol{y}(t_0) - \boldsymbol{y}(T) \\ r(\boldsymbol{y}(t_0, \lambda)) \end{Bmatrix} = 0 \tag{3.25}$$

the periodic solutions of $\boldsymbol{y}$ with minimum periods T can be found. If the time is normalised such that $0 \leq t \leq 1$ replaces $t_0 \leq t \leq t_0 + T$ the equations can be redefined as,

$$\begin{Bmatrix} \boldsymbol{y} \\ T \end{Bmatrix}' = \begin{Bmatrix} T\boldsymbol{f}(\boldsymbol{y}, \lambda) \\ 0 \end{Bmatrix}, \quad \begin{Bmatrix} \boldsymbol{y}(0) - \boldsymbol{y}(1) \\ r(\boldsymbol{y}(t_0, \lambda)) \end{Bmatrix} = 0 \tag{3.26}$$

where a prime represents differentiation with respect to the non-dimensional time. With the equations in the form described in equation 3.8, the predictor-corrector technique can be applied to the problem in the same way in which it is applied to the analysis of stationary solutions.

3.4.4 Stability Analysis

3.4.4.1 Stationary Solution Stability

In order to assess the stability of a system, the response to a small impulse in the states of $\boldsymbol{y}$ must be found. This stability of a stationary solution can be assessed directly by calculating the eigenvalues of the Jacobian matrix defined in equation 3.14. The n eigenvalues are complex and defined as,

$$\mu_j(\lambda) = \alpha_j(\lambda) + i\beta_j(\lambda), \quad j = 1, \ldots, n \tag{3.27}$$

The system's stability is defined by the real component $\alpha_j(\lambda)$ of the eigenvalues. A system is stable if all the values of α_j are negative. The system in unstable if any of the real components of the eigenvalues are positive. As the eigenvalues vary with changes in the continuation parameter λ a system bifurcation is defined as,

$$\alpha_j(\lambda) = 0 \tag{3.28}$$

It must be noted that this change in stability only applies to the specific branch but does not preclude other branches existing that are stable. This follows from the description in section 3.3 that the stability assessment is only localised and therefore no overall assessment of system stability can be made.

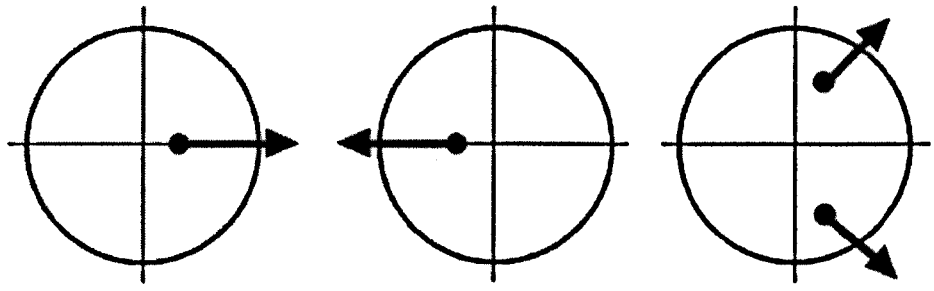

Fig 3.12: Limit-Cycle Stability Loss

3.4.4.2 Limit-Cycle Oscillation Stability

Due to the different method of construction of the system equations, the eigenvalues of the monodromy matrix are used to assess system stability as opposed to the eigenvalues of the Jacobian matrix. The monodromy matrix M is defined by,

$$\mathrm{M} = \frac{\partial \varphi(\mathrm{T}; \boldsymbol{z}^*)}{\partial \boldsymbol{z}} \tag{3.29}$$

where $\boldsymbol{z}^*$ is the initial condition of the vector $\boldsymbol{f}(\boldsymbol{y}(0), \lambda)$ on an LCO and T is the period of one oscillation. This matrix therefore describes if trajectories near to an LCO are closer to the LCO after one period (stable) or if they are further away (unstable).

The eigenvalues of the monodromy, known as the Floquet multipliers, give stability definitions as,

$$\begin{aligned} &\text{stable solutions are assured if } |\mu_j| < 1 \text{ for all } j = 1, \ldots, n; \\ &\text{unstable solutions are assured if } |\mu_j| > 1 \text{ where } j \neq n+1 \end{aligned} \tag{3.30}$$

where α_j is the real component of the multiplier. This therefore defines stability if the Floquet multipliers lie within a unit circle with the exception of $|\mu_{n+1}|$ as M always has an eigenvalue at $\alpha_{n+1} = 1$ [86]. This term exists as the length of a period is always uniquely defined for a given solution and therefore no perturbation in period can occur without a loss in stability occurring.

The ways in which a system loses stability is by one or more of the (Floquet) multipliers leaving the unit circle. The system looses stability in three basic ways as shown in figure 3.12. These are defined as,

$$\begin{aligned} &\mu(\lambda_0) = 1, \\ &\mu(\lambda_0) = -1, \\ &Im(\mu(\lambda_0)) \neq 0. \end{aligned} \tag{3.31}$$

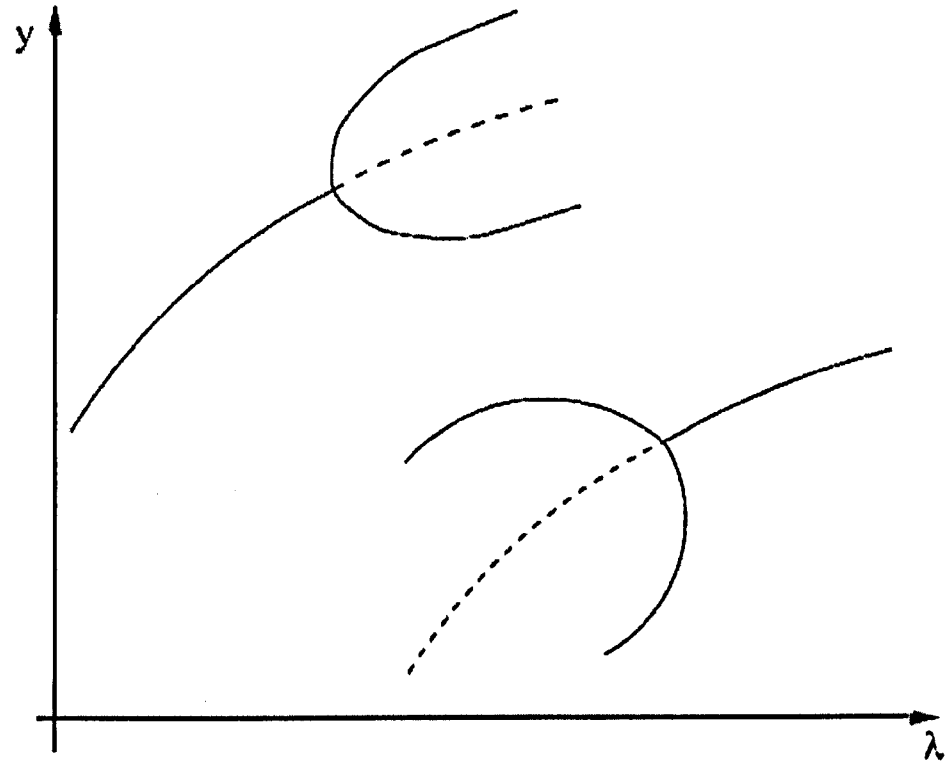

Fig 3.13: Example of Pitchfork Bifurcations

respectively from figure 3.12 with the respective methods of stability loss being branching, period doubling and toroidal bifurcations.

3.4.4.3 Types of Bifurcation

The pitchfork bifurcation is a form of branch point analogous to a simple loss in stability of the branch that is being followed. At the bifurcation two branches split off that define other stable branches. This is shown in figure 3.13 where the dotted lines represent unstable branches and the solid lines represent unstable branches. Another form of branching bifurcation is the turning point, where the stable orbits of an LCO are created or destroyed. This form of bifurcation occurs when two stable orbits collapse onto one orbit that is unstable. This is shown in figure 3.14 where the empty circles represent unstable LCOs and the filled circles represent stable LCOs.

A period doubling bifurcation, as its name suggests, is when a period T solution loses stability and becomes a period $2T$ oscillation. Figure 3.15 shows the way in which a period two oscillation can be transformed in to a period one oscillation by altering the continuation parameter. When such a bifurcation occurs there is a chance that another bifurcation shall occur, creating a bifurcation diagram of the form shown in figure 3.16. Period doubling can be a route by

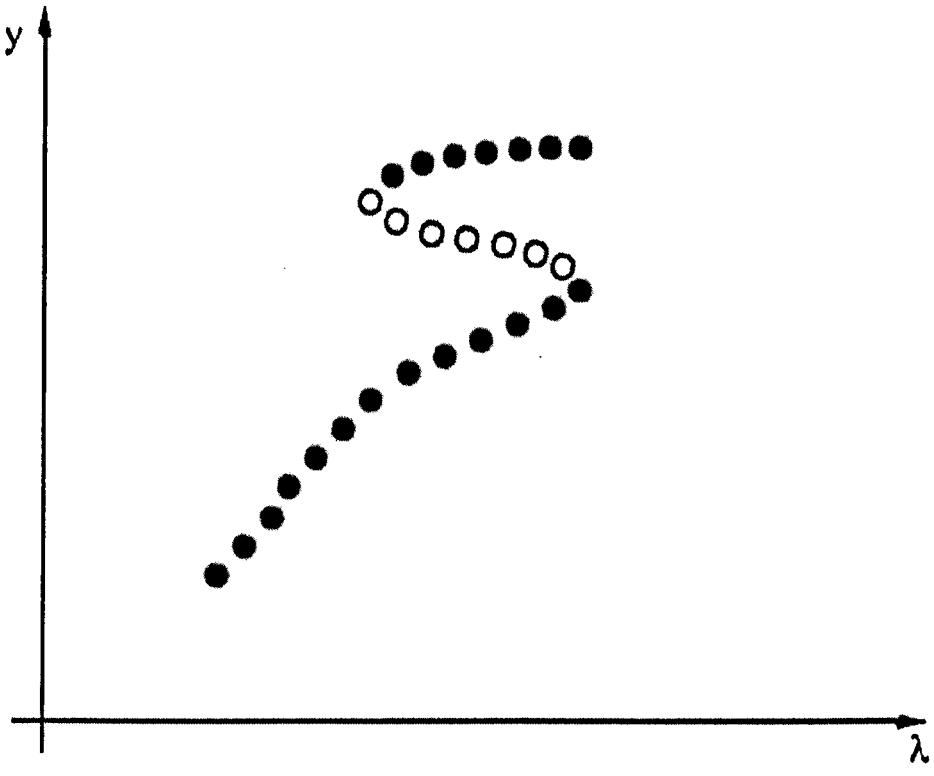

Fig 3.14: Example of a Turning Point Bifurcation

which chaos occurs as, if the period doubling as illustrated in figure 3.16 occurs, and the distance between doubling bifurcations decreases by a factor of 0.214169... there exists a finite limit at which chaos occurs [86].

The third form of bifurcation is the toroid bifurcation which requires a system with of order, $n > 3$. This form of bifurcation can be thought of as being the phase plane diagram rotating around at the same time as the oscillations so, as a result, an often simple periodic orbit can abruptly change into a period T orbit depending on the frequency of the phase plane rotation. This type of motion is not observed in this work so is not discussed further.

The mathematics behind these bifurcations and further descriptions may be found in the books by Seydel [86] and Kuznetsov [87].

3.5 Concluding Remarks

This section of the thesis has described the basic types of motions dynamic systems can undergo. The fundamental solution types are found to be, stationary, where the states are invariant with time, limit-cycling, where the system undergoes a repeating motion, and chaotic, where

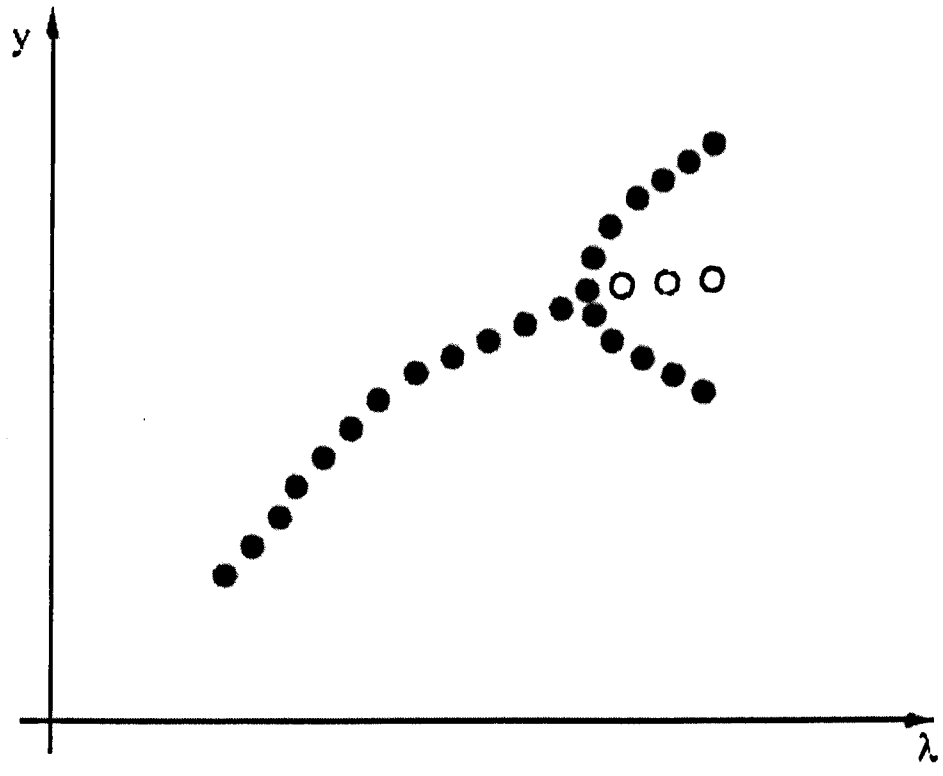

Fig 3.15: Example of a Period Doubling Bifurcation

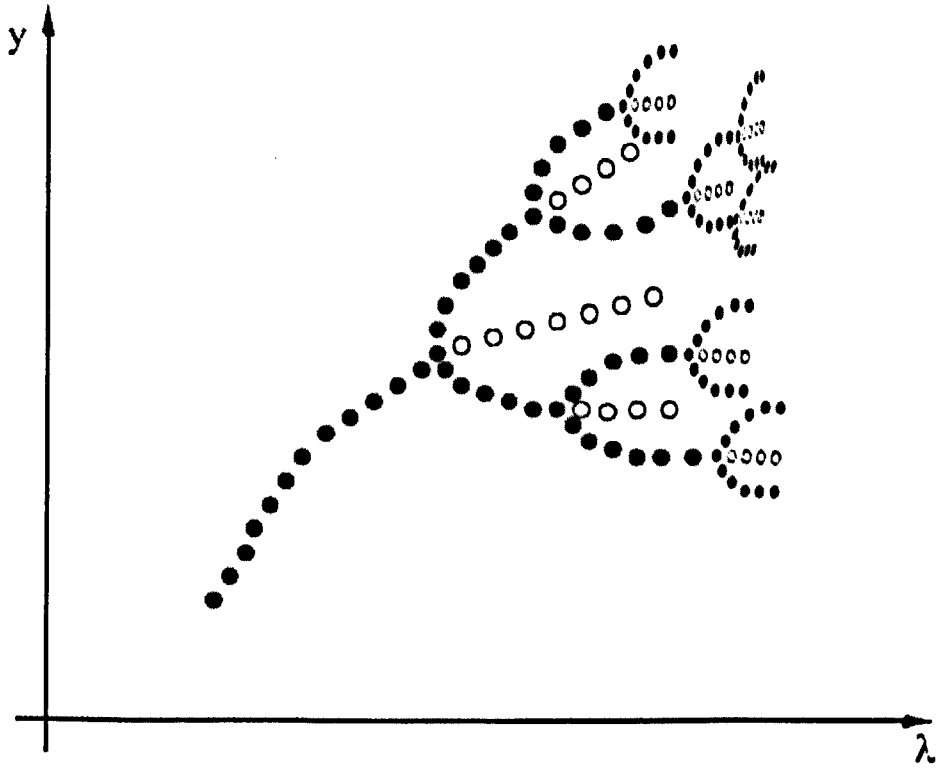

Fig 3.16: Example of Period Doubling Bifurcations to Chaos

the motion of the system is dynamic and non-repeating. All these forms of solution are seen within real dynamic systems and can either be stable or unstable. In its description, the preceding section has shown these various forms of solutions and how they can be represented mathematically. The theory behind numerical continuation has also been described including how the method is implemented computationally. The basis of numerical continuation theory is that unique solutions exist on a unique branch that can be tracked using a predictor-corrector technique. The chapter also described how the eigenvalues or floquet multipliers of the system define the stability of a type of motion. It was shown that when the eigenvalues or floquet multipliers cross specific boundaries stability is altered and the form that limit-cycle oscillations take is changed.

In conclusion, this chapter has described the theory behind continuation that can be used to analyse many forms of general dynamic problems. The following chapter describes the way in which the non-linearities present in aeroelastic systems (as described in Chapter 2) can be described mathematically. This description is then combined with the mathematical aeroelastic models of Chapter 2 in a way that allows the continuation method to be applied to the problem.

Chapter 4

Solution Techniques

In this section two new techniques not previously used in the aeroelastics field is described. The techniques allow the solution of generic non-linear aeroelastic problems identifying the frequency, stability and nature of any resultant non-linear motion. The first method, boundary identification, is applied to piecewise linear problems such as backlash and certain forms of hysteresis. The second method, using continuous representations of discrete functions, allows the rapid identification of aeroelastic behaviour for systems with non-linear, piecewise linear and piecewise non-linear properties. The means by which the systems can be applied within numerical continuation analysis is also described in the relevant sections. Finally, the benefits of the various techniques are highlighted along with the way in which they can be applied to the particular non-linear phenomenon of interest in the aeroelastic community.

4.1 Boundary Identification

In analysing piecewise linear systems such as freeplay, bilinear and certain forms of hysteresis non-linearities it is observable that, away from the switching points, the structural equations of motion are linear. Therefore, if the aerodynamics can also be described linearly it becomes possible to solve the equations of motion exactly with accurate switching point capturing. The following section describes a method by which these linear properties can be exploited to identify limit-cycle solutions rapidly.

4.1.1 Linear Equation Solution

Before considering piecewise linear solutions, lets consider the general solution for a linear system. If, for the purpose of illustrating this methodology the aerodynamic equations are represented by a vector $\boldsymbol{f}$ that represents both forces and moments, the equations of motion, in generalised linear form, are represented by,

$$\ddot{\boldsymbol{u}} = -\mathrm{M}^{-1}\mathrm{B}\dot{\boldsymbol{u}} - \mathrm{M}^{-1}\mathrm{K}\boldsymbol{u} + \mathrm{M}^{-1}\boldsymbol{f} \tag{4.1}$$

where M, B and K are the structural mass, damping and stiffness matrices and $\boldsymbol{u}$ is the vector of structural displacements. If $\boldsymbol{z} = \dot{\boldsymbol{u}}$ the equation of motion can be represented in state space form by,

$$\begin{Bmatrix} \dot{\boldsymbol{z}} \\ \dot{\boldsymbol{u}} \end{Bmatrix} = \begin{bmatrix} -\mathrm{M}^{-1}\mathrm{B} & -\mathrm{M}^{-1}\mathrm{K} \\ \mathrm{I} & 0 \end{bmatrix} \begin{Bmatrix} \boldsymbol{z} \\ \boldsymbol{u} \end{Bmatrix} + \begin{Bmatrix} \mathrm{M}^{-1}\boldsymbol{f} \\ 0 \end{Bmatrix} \tag{4.2}$$

This is of the general form,

$$\dot{\boldsymbol{x}} = \mathrm{A}\boldsymbol{x} + \boldsymbol{b} \tag{4.3}$$

If there are offsets in the system due to preloads , represented by $\boldsymbol{G}(\boldsymbol{u})$, the equation becomes

$$\dot{\boldsymbol{x}} = \mathrm{A}\boldsymbol{x} + \boldsymbol{h} \tag{4.4}$$

where

$$\boldsymbol{h} = -\left\{\mathrm{M}^{-1}\boldsymbol{G}\mathrm{u} + \mathrm{M}^{-1}\boldsymbol{f}\right\} \tag{4.5}$$

As the above equations are entirely linear the general form of the solution can be constructed as [88]

$$\boldsymbol{x}(t) = e^{\mathrm{A}t}\left\{\boldsymbol{x}_0 + \mathrm{A}^{-1}\boldsymbol{h}\right\} - \mathrm{A}^{-1}\boldsymbol{h} \tag{4.6}$$

where $\boldsymbol{x}_0$ are the initial states of the system at time $t = 0$.

4.1.2 Piecewise Linear Systems

When studying piecewise linear systems it can be seen that individual zones are linear with discrete switching points between the zones. The previous equation of motion is therefore valid in any given zone of the piecewise linear system. To simulate the motions of piecewise linear systems the switching point must be captured. If the ith component of the vector $\boldsymbol{u}$ is the non-linear state, it is possible to isolate this degree-of-freedom by multiplying by a vector transpose $\boldsymbol{c}^T$ which is a null vector, except for the ith component which is unity. Equation 4.6 therefore becomes,

$$x_i(t) = \delta = \boldsymbol{c}^T e^{\mathrm{A}t}\left\{\boldsymbol{x}_0 + \mathrm{A}^{-1}\boldsymbol{h}\right\} - \boldsymbol{c}^T\mathrm{A}^{-1}\boldsymbol{h} \tag{4.7}$$

In this form, the only unknown is the time ($t = t_s$) at which the system reaches the switching point $x_i(t) = \delta$.

To solve the equation note that the exponential of a matrix can be found as [89],

$$e^{\mathbf{A}} = \mathbf{V}\mathbf{e}^{\boldsymbol{R}}\mathbf{V}^{-1} \tag{4.8}$$

where $\mathbf{V}$, $\boldsymbol{R}$ and $\mathbf{e}^{\boldsymbol{R}}$ respectively represent the eigenvectors of $\mathbf{A}$, the vector of the eigenvalues of $\mathbf{A}$ and a diagonal matrix where the diagonal terms are the exponentials of the eigenvalues.

$$\boldsymbol{R} = \begin{Bmatrix} \lambda_1 \\ \lambda_2 \\ \vdots \\ \lambda_n \end{Bmatrix} \tag{4.9}$$

$$\mathbf{e}^{\boldsymbol{R}} = \begin{bmatrix} e^{\lambda_1} & 0 & \cdots & 0 \\ 0 & e^{\lambda_1} & \cdots & 0 \\ \vdots & \vdots & \ddots & \vdots \\ 0 & 0 & \cdots & e^{\lambda_n} \end{bmatrix} \tag{4.10}$$

Equation 4.7 has more than one root as, for any linear system, decaying oscillations exist and therefore the value of $x_i = \delta$ may be crossed several times. For the purpose of simulating the piecewise linear system, the required solution $x_i(t) = \delta$, is taken at the lowest positive value of $t = t_1 = t_s$. To solve this equation a numerical iterative technique must be used such as the bisection method or forms of Newton iterations [88].

The correct solution t_1 can then be substituted in to equation 4.6 and all the states found. These states then provide the initial condition vector x_0 for the following zone, which can contain a different offset vector $G(u)$ and/or stiffness matrix $\mathbf{K}$, or, more generally, any other new matrix.

Repeating the solution procedure as above and changing the matrices as appropriate to each zone, it is possible to perform the equivalent of a time simulation where, instead of iterating through a general time step, iterations are performed from one boundary to the next. In this way the problem of switching point identification is solved.

4.1.3 Application of Continuation to Boundary Identification

The method, as outlined in the previous section, serves to generate an accurate solution but can be as slow as time-integration techniques because the iterative procedure used to identify the

boundary can be slow. Additionally, this procedure does not overcome the difficulty of initial condition dependency. To overcome the difficulty of the slow solution time and much of the initial condition dependency problem, numerical continuation is applied to the set of boundary identification equations.

Let us consider a piecewise linear system where the order of the entry and exit to and from each zone is all ready known, i.e. the type of periodicity is already known. Equation 4.7, that isolates the ith degree-of-freedom, can be rewritten, generally as,

$$0 = \boldsymbol{c}^T e^{\mathbf{A}_1 t_1} \left\{ \boldsymbol{x}_0 + \mathbf{A}_1^{-1} \boldsymbol{h}_1 \right\} - \boldsymbol{c}^T \mathbf{A}_1^{-1} \boldsymbol{h}_1 - \delta_1 \tag{4.11}$$

where t_1 is the time at which $x_i(t_1) = \delta_1$ and δ_1 is now the boundary of the linear zone. The solution for the zone that follows t_1 is written as,

$$0 = \boldsymbol{c}^T e^{\mathbf{A}_2 t_2} \left\{ \boldsymbol{x}_1 + \mathbf{A}_2^{-1} \boldsymbol{h}_2 \right\} - \boldsymbol{c}^T \mathbf{A}_2^{-1} \boldsymbol{h}_2 - \delta_2 \tag{4.12}$$

where t_2 is the time at which x_i reaches the next boundary, δ_2, $\mathbf{A}_2$, $\boldsymbol{h}_2$ account for different stiffnesses and offsets and $\boldsymbol{x}_1$ is the solution of.

$$\boldsymbol{x}(t_1) = e^{\mathbf{A}_1 t_1} \left\{ \boldsymbol{x}_0 + \mathbf{A}_1^{-1} \boldsymbol{h}_1 \right\} - \mathbf{A}_1^{-1} \boldsymbol{h}_1 \tag{4.13}$$

If this boundary stepping routine is repeated until,

$$\boldsymbol{x}(t_i) - \boldsymbol{x}(t_i + T) = \mathbf{0} \tag{4.14}$$

where the period T is given by

$$T = \sum_{j=i+1}^{n} t_j \tag{4.15}$$

a limit-cycle has been found that can be defined as,

$$\mathbf{0} = \boldsymbol{f}(\boldsymbol{y}, \lambda) \tag{4.16}$$

In equation 4.16, $\boldsymbol{y}$ contains all the states and the times t_j. This is shown graphically for a flap freeplay of $\pm 2.5^0$, in figure 4.1, where the stars represent points at which the boundary identified and the line represents the equivalent time integration solution. This type of freeplay is described in section 2.1.4 and shown in figure 2.5.

With an initial set of solutions that solves this problem, it is possible to apply a numerical continuation strategy for algebraic equations. The continuation method, described in Chapter 3, traces out all possible solutions to the specified problem by using a predictor-corrector technique to alter the times and states. In this way all the solutions, for a specified periodicity, e.g. period one with a harmonic, can be found for the range of the continuation parameter, λ, required.

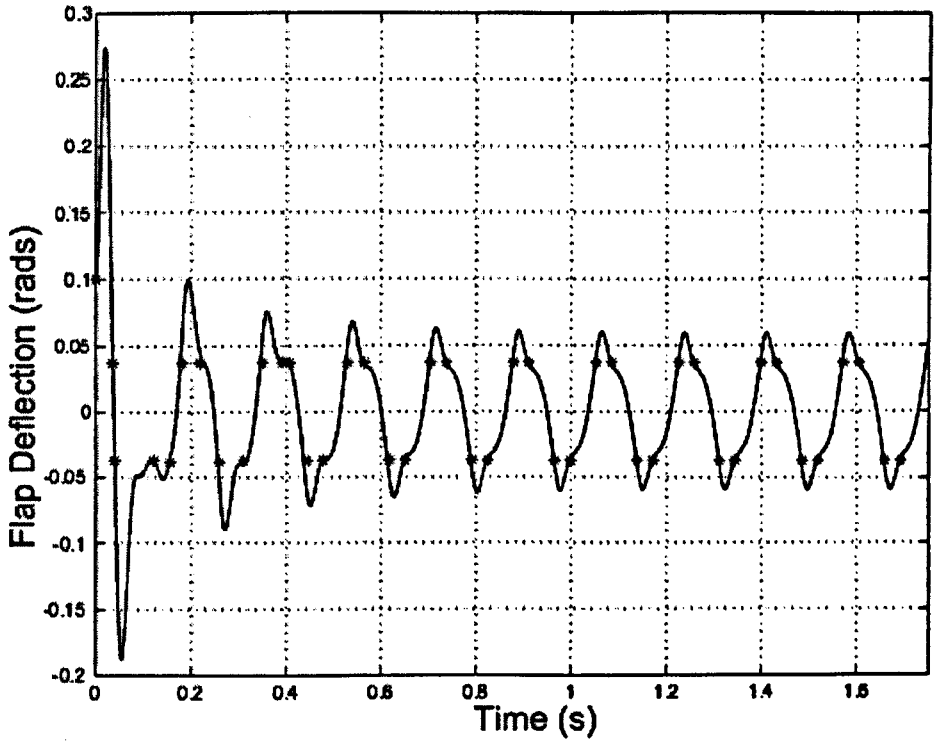

Fig 4.1: Boundary Identification Solution Method

Using this technique the stability cannot be directly assessed but can be inferred as the way in which the algebraic system bifurcates is found to be similar to the way in which a set of ODEs bifurcates. This process means that, from the inferred stability, when areas are found that are unstable the procedure from equations 4.11 to 4.16 can be repeated and the solution for a different periodicity, e.g. period two harmonic, found and the continuation method repeated. In this way, the domain is built up with layers of periodicity which give an overall picture of system stability. Where chaotic solutions occur due to period doubling, the solutions can be inferred by noting the ratio of lengths between bifurcations and comparing it to the value of 0.214169... [86] which is the ratio described in section 3.4.4.2 as the route to chaos.

4.2 Continuous Representation of Discrete Functions

The techniques outlined in the previous section are restricted in their applicability to piecewise linear systems. A method by which continuous functions can be used to approximate both piecewise linear and non-linear systems is described in this section. The approximations take the form of tanh and logarithmic functions which are to be shown to have benefits over polynomial functions when applied within numerical continuation techniques.

4.2.1 tanh functions

The use of combinations of tanh functions in representing piecewise non-linear functions is explained in this section. Numerical continuation software requires that the set of ordinary differential equations is continuously differentiable in the range studied. As systems with discrete non-linearities are not continuously differentiable at the switching points, some smooth function must be employed which can approximate the discrete function to very high levels of accuracy. The benefit of the tanh and, later described, logarithmic approximations to the discrete non-linearities is that the quality of the fit can be simply varied. As shown later, this greatly assists when implementing continuation. In the following sections it is shown that for tanh and log approximations varying a single parameter changes the quality of the fit, unlike polynomial approximations which require an increase in the order of the equation for increased accuracy. In the sections below it is shown that tanh functions can describe common non-linearities effectively.

4.2.1.1 Modeling Freeplay using tanh Functions

Figure 4.2 shows a typical restoring moment/control surface angle graph for a freeplay non-linearity. The representation of a freeplay with a single function has been performed previously by Alighanbari and Price [49]. In their studies a rational function approximation to the freeplay was used which proved to be lacking in some areas. In their results, Alighanbari and Price [49] showed limit-cycle oscillation occurring solely within the central freeplay region which, is not physical because the system of equations for this region is completely linear. A better approximation of freeplay, which is valid over a wider range and is less prone to spurious LCOs, is constructed as the sum of two tanh functions,

$$G(\alpha) = \frac{1}{2}[1 - \tanh(\epsilon(\alpha - \alpha_l))](\alpha - \alpha_l) + \frac{1}{2}[1 + \tanh(\epsilon(\alpha - \alpha_u))](\alpha - \alpha_u) + G_0 \quad (4.17)$$

where α_l and α_u are the lower and upper boundaries of the freeplay region respectively (-0.2 and -0.025 in figure 4.2), G_0 is a vertical offset of the freeplay (0.5 in figure 4.2) and represents preload upon the system and ϵ is a scaling factor which determines the accuracy of the approximation. As ϵ tends to infinity the approximation approaches the actual freeplay.

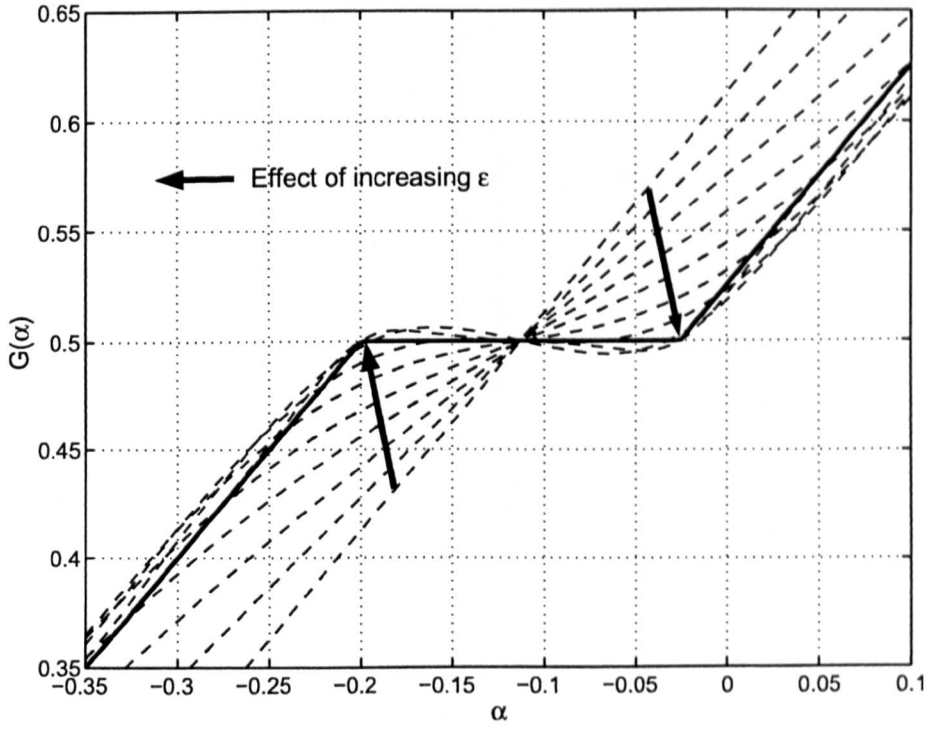

Fig 4.2: tanh *Representation of a Generic Freeplay Non-Linearity including Offset*

4.2.1.2 Heaviside

A heaviside function is a useful tool in many areas of engineering as it can be used as a switch so that a function is either present or not. Also physically it can be used to represent a system containing stiction. A typical heaviside function is shown in figure 4.3 with its tanh approximations represented by,

$$G(\alpha) = \frac{1}{2}[1 - \tanh(\epsilon(\alpha - \alpha_s))]f(\alpha_1) + \frac{1}{2}[1 + \tanh(\epsilon(\alpha - \alpha_s))]f(\alpha_2) \tag{4.18}$$

In this equation the $f(\alpha_1)$ and $f(\alpha_2)$ terms represent the magnitudes of the heaviside function to the left and right of the step respectively ($f(\alpha_1) = 1$ and $f(\alpha_2) = 0$ in figure 4.3). α_s is the position at which the step occurs ($\alpha_s = 0.$ in figure 4.3) and ϵ is again a scaling factor which determines how close the approximation is to the actual heaviside.

4.2.1.3 Hysteresis

Hysteresis non-linearities are observed in most dynamic systems and arise when friction couples with other non-linearities such as freeplay. Representing a hysteresis curve by tanh func-

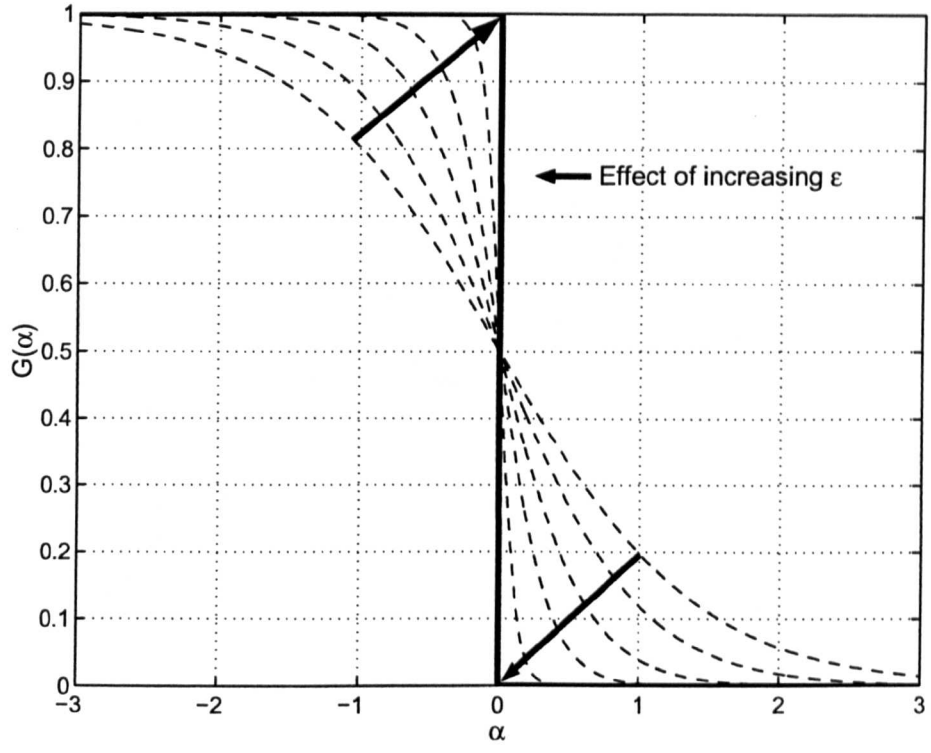

Fig 4.3: tanh *Representation of a Heaviside Non-Linearity*

tions, as shown in figure 4.4, is an important application as it allows a system that is inherently non-linear to be smoothly represented. When hysteresis is present within a system, two different paths are followed depending on whether the velocity of the particular degree-of-freedom is positive or negative. In figure 4.4 the direction of velocity is represented by the arrows on the curves. In approximating an hysteresis non-linearity note that, in this form of hysteresis, the non-linearity is essentially two offset freeplays. Therefore, using heaviside functions, it becomes possible to switch between the two freeplays using the boundary between positive and negative pitch rate, $\dot{\alpha}$, as the heaviside boundary. This implementation allows a hysteresis to be approximated by,

$$\begin{aligned} G(\alpha) = & \frac{1}{4}(1-\tanh(\epsilon\dot{\alpha}))[[1-\tanh(\epsilon(\alpha-\alpha_{l+}))](\alpha-\alpha_{l+}) \\ & +[1+\tanh(\epsilon(\alpha-\alpha_{u+}))](\alpha-\alpha_{u+})+G_{01}] \\ & +\frac{1}{4}(1+\tanh(\epsilon\dot{\alpha}))[[1-\tanh(\epsilon(\alpha-\alpha_{l-}))](\alpha-\alpha_{l-}) \\ & +[1+\tanh(\epsilon(\alpha-\alpha_{u-}))](\alpha-\alpha_{u-})+G_{02}] \end{aligned} \tag{4.19}$$

α_l and α_u represent the upper and lower boundaries of the freeplay and the subscripts $+$ and $-$ are the curves for $\dot{\alpha}$ positive or negative respectively. G_{01} and G_{02} are the magnitudes of the system preloads that offset the curves from the $G(\alpha) = 0$ axis. For this particular case it is noted that the representations of oscillations that occur solely within the loop of the hysteresis

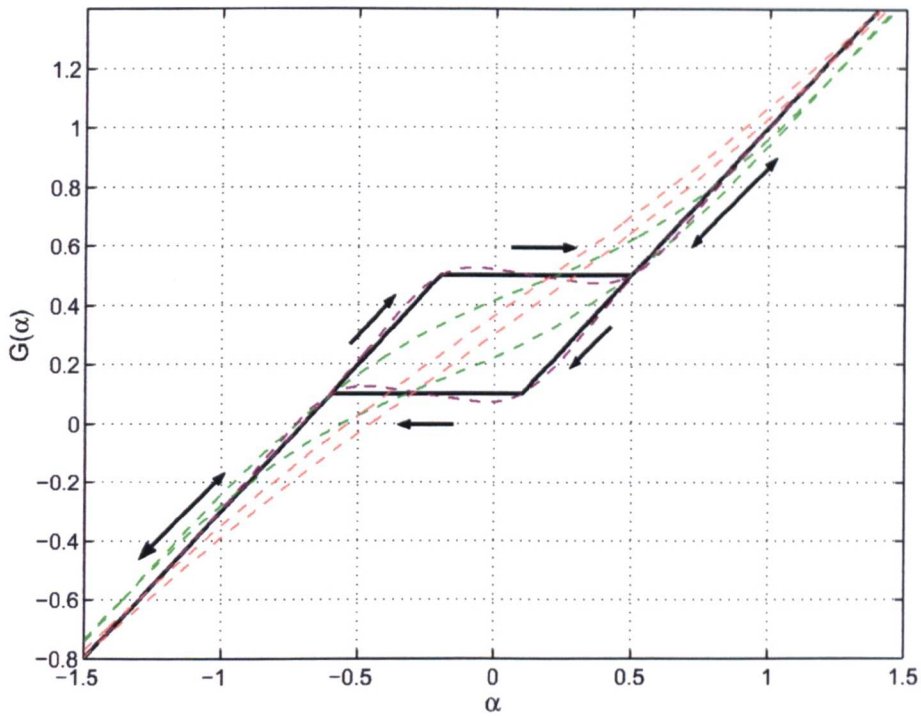

Fig 4.4: Hysteresis Loop and tanh *Approximations with Different* ϵ

curve, is not be accurately represented. This limitation occurs because it is widely assumed that the behaviour of the system within this low amplitude range is usually defined by a simple linear slope bisecting the hysteresis box.

4.2.1.4 Piecewise Non-Linear Systems

Using the tanh functions described previously it can be seen that it is possible to represent a large range of basic non-linearities. Additionally, more realistic combinations of non-linearities can be represented. Common types of non-linearity observed within actual aircraft are combined cubic and freeplaying non-linearities [26, 27, 32, 43]. Using the tanh functions it becomes possible to simulate such systems as shown in figure 4.5.

This form of non-linearity is simply written as a cubic non-linearity as represented by,

$$G(\alpha) = P(\alpha)(1 + \psi_3 P(\alpha)^2) + G_0 \tag{4.20}$$

except that $P(\alpha)$ is the freeplay equation ($G(\alpha)$ in equation 4.17 without preload),

$$P(\alpha) = \frac{1}{2}[1 - \tanh(\epsilon(\alpha - \alpha_l))](\alpha - \alpha_l) + \frac{1}{2}[1 + \tanh(\epsilon(\alpha - \alpha_u))](\alpha - \alpha_u) \tag{4.21}$$

Another widely reported phenomenon that occurs in aircraft control systems is a combined hysteresis and cubic non-linearity [26, 27, 32, 63, 43]. This form of non-linearity can be

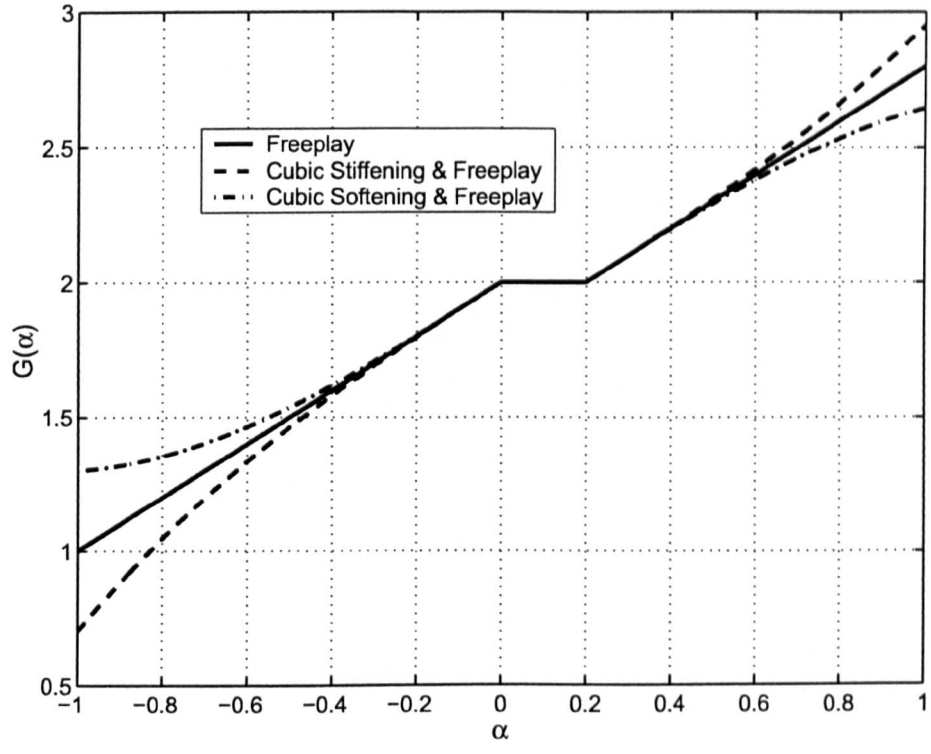

Fig 4.5: tanh *Representation of a Combined Freeplay and Cubic Non-Linearity*

represented by

$$G(\alpha) = P(\alpha)(1 + \psi_3 P(\alpha)^2) \tag{4.22}$$

where here $P(\alpha)$ is of the same form as $G(\alpha)$ in equation 4.19. However, G_{01} and G_{02} are not the constant offsets but Tataglia's solution of a cubic equation ($x^3 + ax + b = 0$) [90]. The solution is,

$$x = \left\{ -\frac{b}{2} + \sqrt{\frac{a^3}{27} + \frac{b^2}{4}} \right\}^{1/3} + \left\{ -\frac{b}{2} - \sqrt{\frac{a^3}{27} + \frac{b^2}{4}} \right\}^{1/2} \tag{4.23}$$

where x is the values of G_α to give the offset G_{0i} (where $i = 1$ for the upper part of the hysteresis loop and $i = 2$ for the lower part of the hysteresis loop) and,

$$a = \frac{1}{\psi_3}, \quad b = -\frac{f_0}{\psi_3} \tag{4.24}$$

This method is only applicable to cubic stiffening systems as Tataglia's method requires that ψ_3^{-1} must be positive definite. Using this method the combined hysteresis/cubic non-linearity are generated as shown in figure 4.6.

4.2.2 Logarithmic and Exponential Functions

The application of logarithmic functions to the piecewise linear/non-linear phenomenon is described as a continuation from the previous section. It has been demonstrated that the appli-

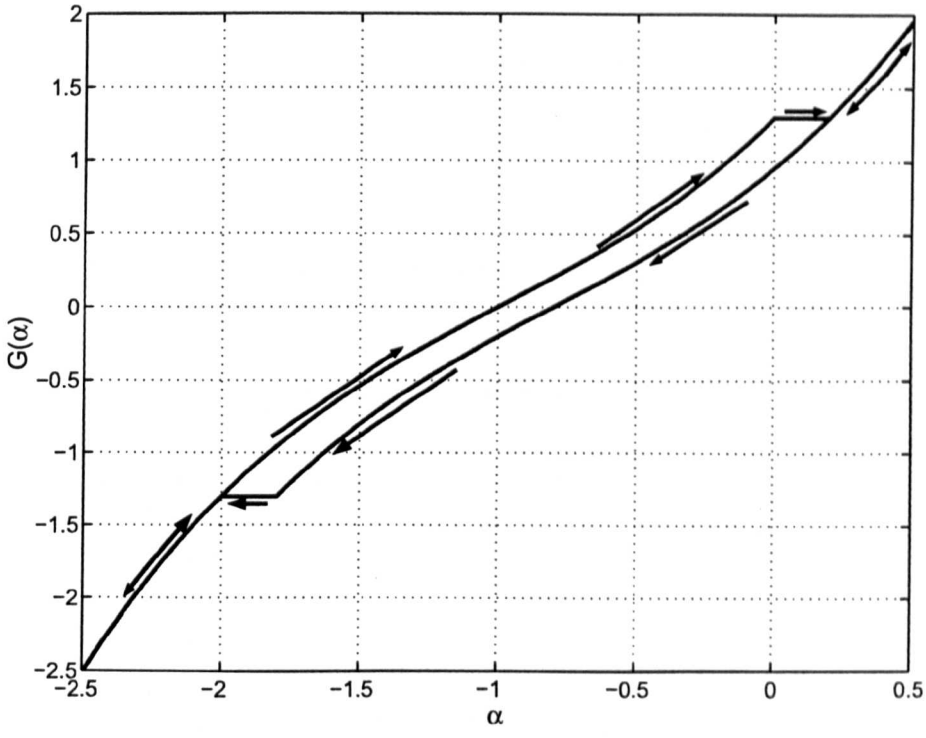

Fig 4.6: tanh *Representation of a Combined Hysteresis Cubic and Non-Linearity*

cation of continuous representations to non-linearities relies on the chosen function's ability to generate freeplay non-linearities and/or heaviside functions. From these basic functions it becomes possible to build up the non-linearities outlined in the previous section. The work described herein, draws from the original work of Kollár et al. [91] who applied the method to a symmetrical system without preload.

The basic equation for a logarithmic approximation to a freeplay non-linearity as given by Kollár et al. [91] is,

$$G(\alpha) = \frac{1}{\epsilon} \ln \frac{1 + e^{\epsilon(\alpha - a_0)}}{1 + e^{-\epsilon(\alpha + a_0)}} \tag{4.25}$$

where increasing the value of ϵ increases the accuracy of the function's approximation to the freeplay and the freeplay limit is set at $\pm a_0$. Figure 4.7 shows a more general freeplay case represented by the equation,

$$G(\alpha) = \frac{1}{\epsilon} \ln \frac{1 + e^{\epsilon(\alpha - \alpha_u)}}{1 + e^{-\epsilon(\alpha - \alpha_l)}} + G_0 \tag{4.26}$$

where G_0 is a vertical offset and α_l and α_u are the lower and upper boundaries of the freeplay region respectively. Representing a freeplay non-linearity with logarithmic functions is preferable as the function never overshoots the true freeplay curve unlike the tanh as shown in figure 4.8.

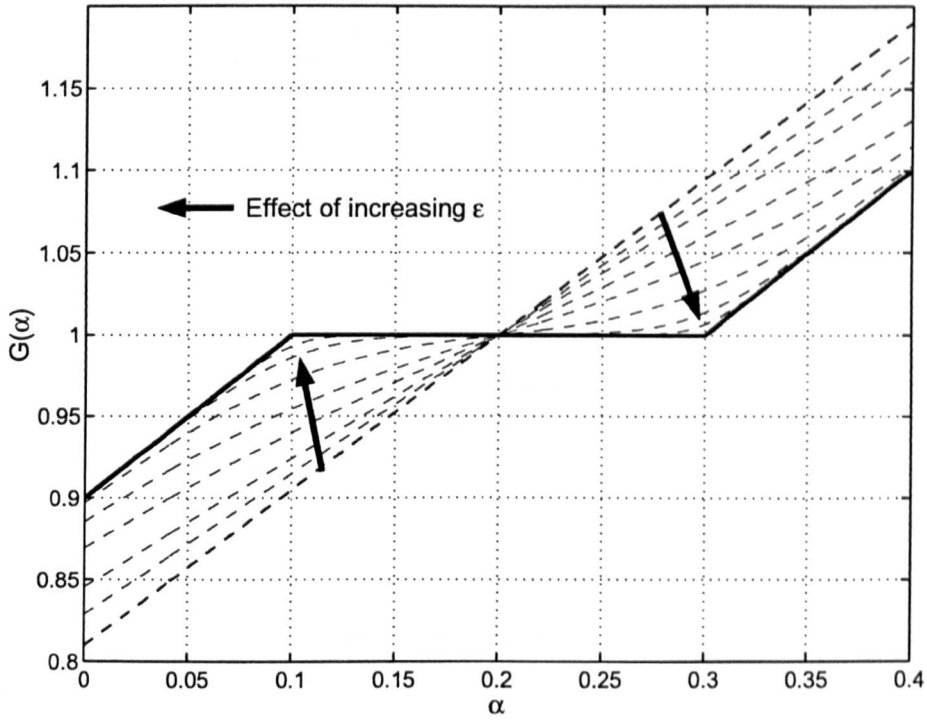

Fig 4.7: Logarithmic Representation of a Freeplay Non-Linearity

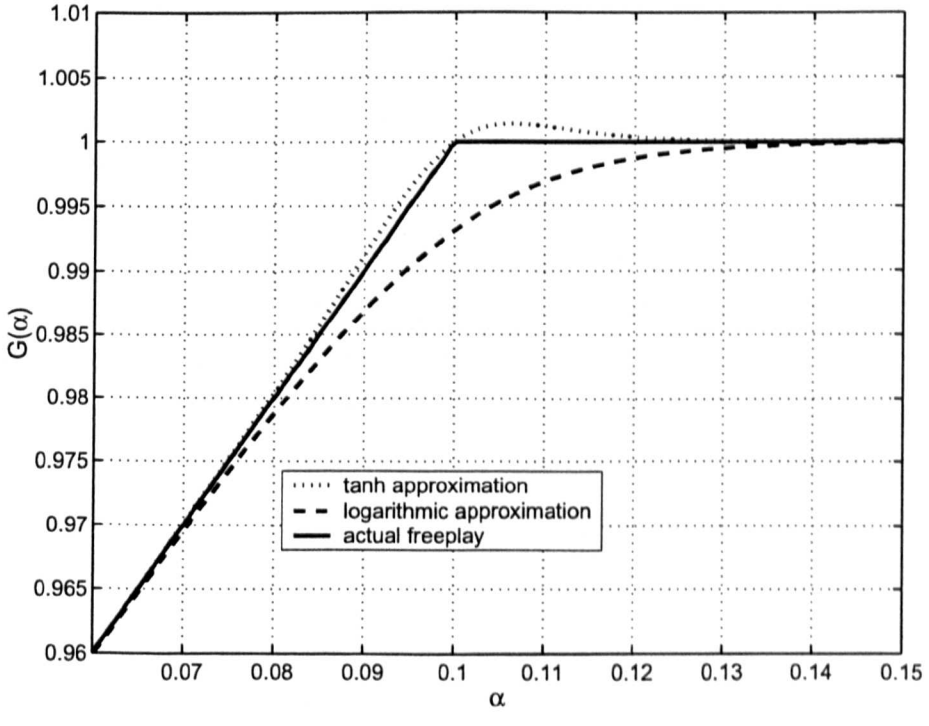

Fig 4.8: Comparison of Approximations to a Freeplay Non-Linearity

This asymptotic behaviour tends to give the logarithmic system better behaviour as negative gradients never occur. With the tanh representation the overshoot can lead to non-physical stiffening, extra turning points and reduced robustness as the continuation method to identifies non-physical LCOs around the turning points. However, the representation of the heaviside function with the tanh function is still adopted as it is based on the basic function $y = \tanh(x)$ which tends to its limits asymptotically without overshoot and the associated problems occurring.

4.2.3 Applications within Aeroelastics

Representing discrete non-linearities with continuous functions has major advantages when analysing aeroelastic systems. The major restrictions on the identification of LCOs resulting from piecewise linear or non-linear systems are, initial condition dependency, switching point capture and non-smooth changes in LCO amplitude.

As has been identified by many authors, piecewise linear - and also piecewise non-linear - systems have dependency upon their initial conditions. As a result, at a given value of a parameter e.g. velocity, there are multiple stable solutions depending on the initial conditions from which the system is released or perturbed. Furthermore, it is possible for systems to switch to other stable LCOs under the influence of effects such as random noise on the input. For aerospace applications noise would include random turbulence and gusts. This was previously illustrated in section 3.3 where a ball on an uneven surface would settle into one of the troughs depending on where the ball was released.

The problem of switching point identification was highlighted by Conner et al. [44] who found that, if the switching point was not captured accurately, some of the oscillations were missed. This phenomenon was mainly found around the edge of stable regions - before instability onset - as the incorrect identification can cause the harmonics to be effectively "damped out". As the sub-harmonics tend to be of small amplitude they spend much time around the switching point, if the resolution of the time-step is not sufficient to capture the point at which the stiffness switches, then the oscillation sees a moveable switching point which can result in the artificial damping of the motions.

The problem of non-smooth changes in LCO amplitude has not been addressed, as far as the author is aware, by any authors in the aerospace field. However, the phenomenon has been shown to occur in real systems in many papers [30, 7] as the system often jumps from a stable solution to a finite LCO amplitude equal to the size of the freeplay region. Many established

techniques, such as continuation and centre manifold theory, have previously failed when applied to this real phenomenon. As a result, authors have resorted to applying polynomial fits [49] that are of only limited accuracy at low-orders and, as such, encounter the switching point problem. Additionally, it has been found that high-order polynomial functions and highly accurate ($\epsilon \rightarrow \infty$) tanh/logarithmic functions suffer problems when there are rapid changes in solution gradient, resulting in longer computational times.

In an attempt to overcome all three of the problems highlighted above, the continuation method, as defined in section 3.4, was applied in conjunction with the continuous functions defined in the preceding chapters. The initial condition problem is automatically overcome by the continuation software as it traces all possible solutions both stable and unstable, therefore allowing the whole range to be mapped for the parameter of interest. The second problem of switching point identification is overcome by the application of the tanh/logarithmic functions with high values for ϵ which result in low errors between the actual stiffness curve and the approximated stiffness curve. The final restriction on analysis are the jumps in LCO amplitude that occur. This is overcome by being able to change the fit parameter ϵ within the continuation algorithm. Initially, a low value of ϵ is used for the tanh/logarithmic functions and the basic results found. As there is a low value of ϵ the system is smooth and, as such, the Hopf bifurcation to the LCO solutions is smooth. If points are then taken from these curves and ϵ is set as the continuation parameter, the approximation to the non-linearity is gradually improved until it is within the desired tolerance. The continuation parameter can then be changed back to the originally chosen parameter (e.g. velocity) and the domain fully mapped for the full piecewise non-linear system. Applying the technique in this way the problem of jumps in the bifurcation diagram is circumvented as gradients are always maintained at finite values.

With the above solution to the piecewise linear/non-linear problem it becomes possible to analyse all the non-linear problems that have been described previously by authors. Nevertheless, hysteresis non-linearities must be thought of as a separate issue as the behaviour if the oscillations are contained completely within the hysteresis loop are much different to the systems behaviour outside of the hysteresis loop. When oscillations occur purely within the hysteresis loop the motion is assumed linear whereas outside of these values the motion is assumed to follow the non-linear phenomenon described by the hysteresis loop. As a result of this phenomenon the analyses showing oscillations entirely within the hysteresis loop must be ignored and a linear analyses performed separately. It should be noted that it is perfectly feasible to construct a system with linear behaviour within the hysteresis loop but this has not been tackled here due to time constraints.

4.2.4 Application to Ground Vibration Test Simulation

Using the methodology above it is possible to simulate ground vibration tests by replacing the aerodynamic loads with equivalent sinusoidal forcing loads at specific points. This results in an equation of the form,

$$M\ddot{z} + B\dot{z} + Gz = F\sin(\omega t) \tag{4.27}$$

In this system there is still the time dependent term in the forcing function which must be decoupled before analysis using the continuous functions, as described previously, can take place. The time dependence can be eliminated by the addition of two extra ordinary differential equations [50].

$$\dot{x} = x + \omega y - x(x^2 + y^2) \tag{4.28}$$

$$\dot{y} = -\omega x + y - y(x^2 + y^2) \tag{4.29}$$

This pair of ODEs have solutions

$$x = sin(\omega t), \quad y = cos(\omega t) \tag{4.30}$$

It is therefore possible to replace the sinusoidal term in the equations of motion with x. F must initially be used as a continuation parameter, before continuation can be performed, as the motion cannot simply start from a finite sinusoidal oscillation. From the form of the equation it can be seen how this method can be extended to multi degree-of-freedom systems with the sinusoidal inputs being applied to one or more degrees-of-freedom. With this representation it becomes possible to predict results of ground resonance tests where known non-linearities are present.

4.3 Concluding Remarks

This chapter has defined two new ways in which non-linear aeroelastic problems can be analysed.

The first technique described - boundary identification - is only applicable to the solution of the piecewise linear forms of non-linearity. These types of non-linearity are characterised by having linear regions separated by discrete discontinuities. The technique itself showed relatively few benefits over time-integration methods as it relies on iterative methods to calculate a solution. With the equations in this new formulation, however, the problem can be analysed us-

ing numerical continuation of a set of algebraic equations that uniquely describe a limit-cycle oscillation.

The second method of analysis was to use the continuation method directly to analyse a set of continuous ordinary differential equations. Normally this application would not be possible when analysing systems with discrete non-linearities but it was shown that the discrete non-linearities could be described to high accuracy using tanh and logarithmic functions. These functions contain a single parameter that can be varied to increase the accuracy of the continuous representation of the discrete function. The fact that these types of discontinuity can be described with such functions lends itself to analysis using continuation methods, unlike polynomial representations.

This section has described how non-linear aeroelastic equations can be cast in a way that allows the application of continuation methods to obtain solutions more rapidly. The benefits of the continuation method are described in the Results chapter with assessment of both the accuracy and speed of solution. The following chapter describes basic control systems and how they can be added in to the aeroelastic equations to give sets of aeroservoelastic equations. The way in which various controllers work and their possible benefits to non-linear systems is also discussed.

Chapter 5

Control

In this chapter the development of various forms of controllers is described. The way in which controllers are integrated into the aeroelastic systems is then defined along with descriptions of the control systems to be applied within the aeroelastic systems. The subsequent section demonstrates how controllers are implemented within the analysis.

5.1 Introduction

Aircraft control systems have traditionally been designed to stabilise unstable rigid body modes, allowing control of marginally unstable aircraft. Additionally, the use of control systems as motion dampers has been implemented to allow stable motions to converge more rapidly, an example being yaw dampers and gust alleviators for rigid body lateral and longitudinal instabilities respectively. Control dampers have been implemented in both the military and civil field to improve crew and passenger comfort. Military aircraft are often designed to have unstable rigid body modes as this characteristic allows better manoeuvring performance therefore requiring sophisticated control systems. Both these control systems are designed to modify the open loop rigid body response of the aircraft.

The implementation of control systems to attenuate flexible body modes was often ignored as both military and civil requirements mandate that open loop unstable oscillations must not exist up to 1.15 times the velocity on the design envelope. However, since the 1970s the military field has looked at implementing flutter suppression systems (FSS) which would allow aircraft to fly up to and through the flutter boundary. In much of this work [20, 92] a clear distinction is made between hard and soft flutter. Hard flutter is defined as a high frequency instability

with rapid oscillatory divergence until failure. Soft flutter is a low frequency instability with a relatively long time until failure. Due to the relatively rigid nature of fighter aircraft structures the aeroelastic instabilities that are commonly observed are of the hard type (crudely frequency being proportional to the square root of stiffness [1]).

The analysis of soft flutter was commonly made whilst ignoring the aerodynamic terms related to control surface rates (quasi-static) and, as the control surface motion was relatively slow, the control surface power unit dynamics could be ignored. For the hard flutter, both velocity and acceleration terms, related to control surface movement, were retained as well as the inclusion of power control unit transfer functions. For hard flutter, Turner [20] proposed the implementation of pole placement control systems, which, as the name suggests, positions the system eigenvalues such that stability is maintained throughout the range of interest. The importance of designing optimal flutter suppression systems, i.e. systems that kept control surface motion to a minimum, was shown in this work. Turner [20] showed that optimal control existed when the poles from the open loop (uncontrolled) system where used but with any positive real components mirrored in the imaginary axis. This system provided minimal control movement whilst maintaining the required gain and phase margins of $6dB$ and $\pm 60^o$.

When studying any form of dynamic system the role of observers and observability is important. In the classic state-space formulation,

$$\begin{aligned} \dot{\boldsymbol{X}}(t) &= \mathbf{A}\boldsymbol{X}(\mathrm{t}) + \mathbf{B}\boldsymbol{U}(\mathrm{t}) \\ \boldsymbol{Y}(t) &= \mathbf{C}\boldsymbol{X}(\mathrm{t}) + \mathbf{D}\boldsymbol{U}(\mathrm{t}) \end{aligned} \tag{5.1}$$

the observable states are $\boldsymbol{Y}$. These may contain system states $\boldsymbol{X}$ or any other measure of system state e.g. lift coefficient. As all the states cannot be measured directly different observers where introduced to allow the states to be read indirectly. Work performed at BAC (now BAE SYSTEMS) [20, 92] was the first to highlight the importance of system observers. Two observer methods were proposed. Firstly the Dressler observer, which used the relationship between state and observer, $\boldsymbol{x} = \mathrm{C}^{-1}\boldsymbol{y}$, coupled with the state-space equation for the system. These equations were simultaneously integrated until the state vector could be reconstructed. The second method proposed was the Kalman observer which is optimised to minimise error in the reconstructed states in the presence of random vibration. This system results in extra poles being introduced that can be positioned so as to stabilise the aeroelastic system by appropriate gain scheduling. The effect of control rate limiting was also observed but the limit of $160^o/sec$ was found to enable control up to 20% above the flutter speed (theoretical) with this rate varying almost linearly e.g. $80^o/sec$ gives a 10% margin.

In the 1980s American research, lead by NASA, made great advances in the suppression of

flutter within aeroelastic systems including full scale in flight testing. Adaptive flutter suppression was the subject of a paper published by Abel and Noll [21]. Adaptive control systems continually monitored the state of a system and used the information to update the flight control laws. The research performed showed that the wing flutter boundary for an F-16 aircraft model could be increased by 30% for soft flutter and 18.5% for hard flutter whilst maintaining the required phase and gain margins. Tests were also performed during simulated wing tip missile release, where system dynamics change rapidly but the system's integrity remained, although the impact of store release in hard flutter cases is not made clear. For such hard flutter cases it is supposed that some form of a priori information is known, so that the system could adapt quickly enough.

The use of Kalman filters was applied to eigensystem/eigenstructure assignment [93] and modified optimal control [94, 22] configurations. Eigenstructure assignment is an extension to the optimal controller, discussed above, that allows the same number of poles to be assigned as measurements (observers plus directly measured states) as well as the fixing of a number of the eigenvector elements (equal to the number of inputs). The modified optimal control methodology uses the Kalman filters as a first stage estimator for the generation of low-order state space controllers. This methodology then goes on to use non-linear optimisation on a cost function with robustness maximised by loop transfer recovery techniques [94].

Chan-Gi Pak [24] and Guillot & Friedmann [95] used an Auto-Regressive Moving Average (ARMA) controller in order to suppress subsonic/transonic flutter and LCO behaviour. The model used a strong coupled finite volume formulation of the aeroelastic problem in order to generate a high fidelity transonic aeroelastic response on to which the control system was applied. The results showed much promise in the subsonic regime, and highlighted the requirement for aerodynamic load based control law design for the transonic cases to give improved system response. The technique implemented by the authors used on-line control law design and moving average terms to minimise a quadratic performance index that was then used to generate the appropriate control gains.

Djayapertapa and Allen [96] examined the transonic control problem on a two dimensional, three degree-of-freedom aerofoil section. In their paper they implemented an active control algorithm based on the states, their velocities and accelerations. The system implemented by the authors looked at varying the gains (weighting factors) on the different parameters. Their studies concluded that rate feed back gave the best LCO suppression, allowing the flutter boundary to be increased by up to 19%. However, the problems of having a design point was shown in that the suppression effects were localised around the design point Mach number and

therefore not generally attenuating the whole envelope. These factors highlight an inherent problem with active control systems in that their gains have to be scheduled against factors such as Mach number in order to obtain high fidelity control.

The work classified above is concerned with the suppression of flutter, with the aim of extending an aircraft's flight envelope. The focus of such work is, for reasons of certification, restricted to military applications, but such schemes are also being considered for commercial aircraft with the aim of flying aircraft closer to the flutter boundary, as at present flutter clearance schemes are conservative. Another focus of the above work is on the transonic flutter problem where non-linearities in the aerodynamics complicate the control algorithms required. In extreme circumstances the transonic aerodynamics can cause control surface buzz, where small control surface motions cause an attached shock to move from the main surface onto the control surface. The resulting step change in hinge moment causes an elastic deformation of the control surface so the shock moves back on to the main surface. This shock motion then results in the moment decreasing and the surface deflecting in the opposite direction. This repetitive process causes high frequency oscillation of the control surface and, in extreme circumstances can result in structural failure.

The buzz problem, described above, is a case when non-linearities cause oscillations in the structure that, in turn, results in fatigue that causes failure. Structural non-linearities, as outlined in 2.1.2, can also cause oscillations within the aeroelastic system at levels far below the flutter boundary. Using an analogy with flutter, the effects of structural non-linearities tend to be of a soft type of LCO whereas aerodynamic non-linearities can be of soft or hard LCO type. Soft LCOs are classified as being of relatively low amplitude and frequency, thus the fatigue is slow to build up until failure occurs. Hard LCOs such as buzz, which cause almost immediate failure, are still of low amplitude but of high frequency. The control of all forms of LCOs, especially soft LCOs, has been the focus of relatively little research with only a limited number of papers published as discussed below.

Dimitriadis and Cooper [57] looked at the control of LCOs in a quasi-steady simulation of a freeplaying system. After performing energy analysis they proposed a simple feedback system as,

$$F(t) = -F_A\dot{\beta} \tag{5.2}$$

where,

$$F_A = \frac{\dot{\beta}_{amp}}{\beta_{amp}} \tag{5.3}$$

β is the freeplaying degree-of-freedom and $F(t)$ is a force added to the control surface. This system showed rapid attenuation of the LCOs. Unfortunately such a system underestimates

the complexity of the physical system. The authors interpreted the freeplay region as fixed, and it was assumed that the control surface was under constant control. However, freeplay is a function of the control system demand as it emanates from the control system linkages. So if the control system is at a demanded angle the freeplay acts around that deflected position. Similarly, the frequent application of preload to systems is often interpreted differently from the physically reported system [85, 45], as the freeplay is around the control system demand, but loads on the surface cause deflection into the stiffer regions. It must also be understood that the control surface is not under constant control as, if the control surface is in one of the stiff regions and the control position deflects in the opposite direction, control is not achieved until the system has moved into the stiff region at the opposite side of the freeplay. This is when it is energetically advantageous to deflect the control surface as opposed to causing elastic deformations.

Djayapertapa, in his thesis [85], implemented control of a freeplaying system both with and without preload. His work examined a three degree-of-freedom aerofoil section in transonic flow. It was shown that the amplitude of the LCOs present could be greatly attenuated with the implementation of active control. The control was implemented in this work with no force being applied to the system in the freeplay region. The system, as with the paper of Djayapertapa and Allen [96], used the heave and pitch states, their velocities and accelerations as observers to control the motion. The observability in this case is assumed to be possible through a pair of transducers that, when coupled, give both a heave and pitch approximation.

Clark et al. [23] implemented a novel control system based on the analysis of the linear system. The authors used a H_2-synthesis method in this scheme, to obtain optimal control that varied with the flow velocity. As with the work of Chan-Gi Pak [24] a cost function was used to optimise the control gains. The work used the low-speed aerodynamics model of Edwards et al. [2] (as presented in section 2.2.2.2), for their three degree-of-freedom model. The author's addition of actuator dynamics enhanced the applicability of the work to realistic situations. The linearly scheduled gains were shown to give good attenuation of the heave and pitch amplitudes, but suffered from an increase in flap LCO frequency. This was due to the cost function giving a greater weighting to the pitch mode.

5.2 Aeroservoelastic Equations of Motion

The basic equations of motion for a three degree-of-freedom system from section 2.1.8.1 are given as,

$$\begin{aligned} m\ddot{h}(t) + mx_\alpha b\ddot{\alpha}(t) + mx_\beta b\ddot{\beta}(t) + c_h\dot{h}(t) + k_h h(t) &= P(t) \\ mx_\alpha b\ddot{h}(t) + mr_\alpha^2 b^2\ddot{\alpha}(t) + [(C_\beta - a_h)mx_\beta b^2 + mr_\beta^2 b^2]\ddot{\beta}(t) + c_\alpha\dot{\alpha}(t) + k_\alpha\alpha(t) &= R(t) \\ mx_\beta b\ddot{h}(t) + [(C_\beta - a_h)mx_\beta b^2 + mr_\beta^2 b^2]\ddot{\alpha}(t) + mr_\beta^2 b^2\ddot{\beta}(t) + c_\beta\dot{\beta}(t) + k_\beta\beta(t) &= Q(t) \end{aligned} \tag{5.4}$$

The addition of a control system in the flap degree-of-freedom results in the last of these equations becoming,

$$mx_\beta b\ddot{h}(t) + [(C_\beta - a_h)mx_\beta b^2 + mr_\beta^2 b^2]\ddot{\alpha}(t) + mr_\beta^2 b^2\ddot{\beta}(t) + c_\beta\dot{\beta}(t) + k_\beta(\beta(t) - \beta_c(t)) = Q(t) \tag{5.5}$$

where β_c is the control surface deflection. If a general non-linearity $N(\beta)$ is included within the system the equation of motion becomes.

$$mx_\beta b\ddot{h}(t) + [(C_\beta - a_h)mx_\beta b^2 + mr_\beta^2 b^2]\ddot{\alpha}(t) + mr_\beta^2 b^2\ddot{\beta}(t) + c_\beta\dot{\beta}(t) + k_\beta(N(\beta(t)) - \beta_c(t)) = Q(t) \tag{5.6}$$

As an example, this non-linearity would result in equation 2.12, for a bilinear spring, becoming,

$$N(\beta) = \begin{cases} N_0 + \beta - (\beta_c - 1/2\delta) & \text{for } \beta < \beta_c - 1/2\delta \\ N_0 + N_f(\beta - (\beta_c - 1/2\delta)) & \text{for } \beta_c - 1/2\delta \le \beta \le \beta_c + 1/2\delta \\ N_0 + \beta - (\beta_c + 1/2\delta) + \delta(N_f - 1) & \text{for } \beta > \beta_c + 1/2\delta \end{cases} \tag{5.7}$$

With this formulation the bilinear stiffness is correctly defined about β_c. This form is equally applicable to all systems where the non-linearity is present between the actuator and control surface. Some systems, such as some forms of cubic stiffening, have non-linearities that are unrelated to the controller position. In these systems the controller acts on top of, as opposed to part of, the non-linearity. Such a formulation would result in the equation of motion becoming,

$$mx_\beta b\ddot{h}(t) + [(C_\beta - a_h)mx_\beta b^2 + mr_\beta^2 b^2]\ddot{\alpha}(t) + mr_\beta^2 b^2\ddot{\beta}(t) + c_\beta\dot{\beta}(t) + k_\beta(N(\beta) - \beta_c) = Q(t) \tag{5.8}$$

The implementation of control on the equations is, therefore, a simple modification to the equations of motion. Also this is simply implemented within the continuous representation of discrete functions, as described in section 4.2.

5.3 Control Systems

5.3.1 Basic Feedback Control

Basic feedback control systems use the difference between an observer and its desired value to vary the control surface position. In order to achieve better controllers a number of these states may be combined to allow a control law to be designed. These terms are usually multiplied by further constants, known as gains. Increasing gains gives the difference between required and actual position more weighting meaning that the system reacts more quickly to the system involved.

The initial control system to be studied, is a simple feedback controller of the form,

$$\beta_c(t+1) = K(\xi_R - \xi(t)) \tag{5.9}$$

where ξ_R is the required heave displacement and K is a scalar gain that can be modified to give an improved flap response. ξ can be replaced with any other terms such as pitch or flap controller position.

In order to increase effectiveness of the controller further, velocity and acceleration terms are also added.

$$\beta_c(t+1) = K_1(\xi_R - \xi(t)) + K_2\dot{\xi}(t) + K_3\ddot{\xi}(t) \tag{5.10}$$

This formulation allows a more tailored response to the systems requirements. The velocity and acceleration terms, in general for aeroelastic systems, have no ξ_R type terms as it is generally required that the systems are simply stationary. With a further expansion made by adding terms related to pitch, an active control system similar to that of Djayapertapa [85, 96], can be created.

Varying the values of the gains allows the system stability to be altered to give improved system response over the open loop system.

5.3.2 Linear Quadratic Regulator (LQR)

The Linear Quadratic Regulator (LQR) is a form of controller that is designed to minimise controller deviation displacement for its various states. When implementing most State Variable Feedback (SVF) control systems to models, no optimal analytical control law exists. However, if the system is assumed linear and the controller is restricted to a quadratic Performance Index (PI) form, an approximate solution can be calculated.

To describe the LQR system it is first necessary to introduce the Performance Index (PI). This metric is illustrated in the following paragraphs.

Assume the aeroelastic system is of state-space form.

$$\dot{X} = \mathbf{A}X + \mathbf{B}U$$
$$Y = \mathbf{C}X + \mathbf{D}U \tag{5.11}$$

A cost function or penalty is then applied to certain states or controller degrees-of-freedom e.g. more emphasis on pitch than on heave. A PI is then established by firstly minimising the squares of these functions or, in other words, minimising the energy expenditure. If this cost function is then integrated over time the steady-state error can be minimised. This is usually represented in the form,

$$J = \int_{t_0}^{t_f} \left[\boldsymbol{x}^T \mathbf{Q} \boldsymbol{x} + \boldsymbol{u}^{\mathrm{T}} \mathbf{R} \boldsymbol{u}\right] dt \tag{5.12}$$

where $\mathbf{Q}$ and $\mathbf{R}$ are matrices containing the penalty functions. This summation also allows differences and sums of states or controllers to be minimised. The bracketed terms in equation 5.12 are of the quadratic form as the states and controller terms are squared. At this point it is worth noting that the cost function J is a scalar and therefore can be directly used to ascertain the cost or effectiveness of the control system.

The LQR controller is usually implemented by means of an algorithm that uses a search function to minimise the cost function by producing and varying gains as appropriate. The particulars of the algorithm used to minimise the cost function can be found in [47]. For this work the LQR controller system as contained in MATLAB is used.

It may be noted that the above method is only applicable to linear systems. For the purpose of this work the controller is implemented for a linear aeroelastic system and the same linear designed system is applied to the non-linear problem to assess its validity.

The specific regulators are only applicable to specific parameters, e.g. Mach number and altitude, but if the LQR problem is solved at various different conditions it is possible to have a number of optimal control systems. Using this method is termed scheduling where the gains become functions of the condition of the system. As the dominant variables in an aeroelastic system are Mach number and altitude it is possible to implement both Mach number and altitude scheduling. In addition, between the individual optimised points linear or higher order splines can be used to calculate the gains used for control creating what should be a reasonably optimised controller throughout the operational envelope.

Using an *optimal* control system of this form does not necessarily guarantee the optimal de-

sired response. To obtain optimal system response the cost function variables must be altered such that the optimal response can be found. However, with such systems, appropriate system gains can be quickly established, for quick analyses.

5.3.3 Minimal Control Synthesis (MCS) Algorithm

There are, at present, a vast number of papers published on adaptive control systems. Adaptive control systems, as their names suggest, automatically vary their gains to obtain improved system response. Such adaptive system have great potential in areas such as reconfigurable flight vehicles which vary gains when systems or control surfaces are lost in flight. A problem for many such controllers is termed gain wind-up where the gains continually increase (or decrease if negative), this is usually due to noise or transients causing the gains to constantly increase to obtain improved performance.

The scheme in the work described in this thesis is the Minimal Control Synthesis (MCS) algorithm as described by Stoten and Hodgson [97]. The MCS system was chosen as it requires no a priori model identification and can quickly adapt its gains from arbitrary initial conditions. The following section describes the MCS algorithm in brief, more detail can be found in work by Stoten and Benchoubane [98, 99]. This particular form of problem simplifies the control law somewhat as the system is trying to set any motions to zero and, as such, has no complex set of reference parameters to follow.

If a general aeroelastic system is described by a state equation,

$$\dot{\boldsymbol{x}}(t) = \mathbf{A}\boldsymbol{x}(t) + \mathbf{B}\boldsymbol{u}(t) + \boldsymbol{d}(t) \tag{5.13}$$

and the control parameter is expressed as,

$$\boldsymbol{u}(t) = \mathbf{K}(t)\boldsymbol{x}(t) + \mathbf{K}_r(t)\boldsymbol{r}(t) \tag{5.14}$$

where,

$$\begin{aligned}
\mathbf{K(t)} &= \int_0^t \alpha_{MCS}\boldsymbol{y}_e^T(\tau)\boldsymbol{x}(\tau)d\tau + \beta_{MCS}\boldsymbol{y}_e^T(t)\boldsymbol{x}(t) \\
\mathbf{K}_r\mathbf{(t)} &= \int_0^t \alpha_{MCS}\boldsymbol{y}_e^T(\tau)\boldsymbol{r}(\tau)d\tau + \beta_{MCS}\boldsymbol{y}_e^T(t)\boldsymbol{r}(t) \\
\boldsymbol{y}_e(t) &= \boldsymbol{r}(t) - \boldsymbol{x}(t)
\end{aligned} \tag{5.15}$$

and $\boldsymbol{r}(t)$ is the reference signal to be followed e.g. ξ_R. To apply this technique within the aeroelastic system, the discrete-time version of the equations must be created. This objective

can be accomplished by using zero-order hold equivalence, giving,

$$\begin{aligned}
\boldsymbol{u}(k) &= \mathbf{K}(\mathbf{k})\boldsymbol{x}(\mathbf{k}) + \mathbf{K_r}(\mathbf{k})\boldsymbol{r}(\mathbf{k}) \\
\mathbf{K}(\mathbf{k}) &= \mathbf{K}(\mathbf{k-1}) + \beta_{\mathbf{MCS}}\boldsymbol{y}_{\mathbf{e}}^{\mathbf{T}}(\mathbf{k})\boldsymbol{x}^{\mathbf{T}}(\mathbf{k}) - \sigma_{\mathbf{MCS}}\boldsymbol{y}_{\mathbf{e}}^{\mathbf{T}}(\mathbf{k-1})\boldsymbol{x}(\mathbf{k-1}) \\
\mathbf{K_r}(\mathbf{k}) &= \mathbf{K_r}(\mathbf{k-1}) + \beta_{\mathbf{MCS}}\boldsymbol{y}_{\mathbf{e}}^{\mathbf{T}}(\mathbf{k})\boldsymbol{r}^{\mathbf{T}}(\mathbf{k}) - \sigma_{\mathbf{MCS}}\boldsymbol{y}_{\mathbf{e}}^{\mathbf{T}}(\mathbf{k-1})\boldsymbol{r}(\mathbf{k-1}) \\
\boldsymbol{y}_e(k) &= \boldsymbol{r}(k) - \boldsymbol{y}(k)
\end{aligned} \tag{5.16}$$

where

$$\sigma_{MCS} = \beta_{MCS} - \alpha_{MCS}\Delta t \tag{5.17}$$

In these equations α_{MCS} and β_{MCS} are constants that are arbitrarily set by the user. Stoten [100] suggested that the best results are achieved if the ratio between α_{MCS} and β_{MCS} is 10:1. The author suggested that the values be set at 1 and 0.1 initially, and, if the system is too sluggish, it should be increased by a factor of 10 or, if the performance is above the system bandwidth, decrease the values by a factor of 10. Further tuning of these values is not required after this stage [100].

The system, as described above shows good response and adaptivity for various signal forms in practical mechanical engineering situations although authors [97, 98, 99, 100] have noted the problem of gain wind-up. This is expected, as the higher the gain the faster the system can react to the adapting situation. Several methods for overcoming gain wind-up have been proposed, including: a "forgetting" factor that tends to diminish the gains from their high levels [100], gain bounding of the MCS system and implementing MCS for only short periods at a time so the gains are updated then maintain fixed values [101]. This latter system could be particularly useful for aerospace application such as store or missile release where the gains could be altered and then the fixed gain system used later.

5.4 Concluding Remarks

This section has described basic forms of control systems and how they can be applied to rigid body or elastic dynamic systems. The demand from the aerospace industry for "smarter" controllers has been driven by the desire to expand the envelope of aircraft whilst maintaining low risk. In the military field the advent of Unmanned Air Vehicles (UAVs) has reduced the risk of loss of life considerably facilitating flight beyond the flutter boundary.

The different types of control laws can be split into three types fixed gain, active and adaptive, which have been discussed in the preceding chapter. Fixed gain, as the name suggests, fixes

the proportion of a system state, e.g. pitch, that is fed back to a controller. Active systems use optimisation procedures to generate optimal gains prior to implementation. Adaptive control systems cover a large range of controllers that allow the gains to vary during operation to maintain optimal performance. The specific types of controller implemented in this work are summarised below.

Fixed gain controllers vary the demand on a control surface such as an aileron by weighting measurable states of the system, e.g. pitch rate, and feeding back the information.

The Linear Quadratic Regulator (LQR) is a more advanced form of controller that determines the gains of the controller through an optimisation routine. Firstly, the user selects which of the system parameters are most important and weights them appropriately, e.g. if pitch rate is more important than heave rate the weightings could be set as 5 and 1 respectively. The matrices containing these weightings are then past through the LQR algorithm that minimises the functions generating appropriate system gains.

The final controller considered was the Minimal Control Synthesis (MCS) algorithm. This is an adaptive control system that varies gains depending on selected variables. This system is usually used for quite complex position tracking, e.g. robot arms, but for the cases in this work it simply requires parameters such as pitch and heave to be zero. As the system is adaptive, the gains of the system vary constantly such that there is reaction to any perturbation. As the system is always varying, a truly steady state would never be reached which precludes analysis using continuation method as it can only track solutions with static or repeating motions. A major drawback to adaptive systems is certification as, without certain limits being applied, the system gains could reach levels where the physical system cannot react quickly enough (saturation).

The three basic controllers described above cover the main areas of control systems that exist. These control laws are combined with both linear and non-linear aeroelastic systems to ascertain the possibility of delaying flutter onset or suppressing the amplitude of limit-cycle oscillations. The fixed gain and LQR regulators are studied through the use of continuation and time integration techniques. The MCS adaptive system is analysed through time integration only due to the restrictions highlighted in this section.

Chapter 6

Results

The results presented in this chapter are intended, firstly, to validate the techniques described in this work and, secondly, demonstrate the wider applicability of the methods to a variety of problems. The first part of the results demonstrate the application of the methods described to general non-linear aeroelastic problems, this includes the study of new forms of non-linearities that have not been previously analysed in the related literature. The second part of the results concentrates on the study of aeroservoelastic control, including both linear and non-linear structural models as testcases. Applications of the techniques used to other related areas of analysis are then discussed, with simplified examples given to demonstrate the basic methodologies.

6.1 Introduction

6.1.1 Testcase Summary

This section briefly describes the testcases to be examined in this chapter and summarises the results that these cases should highlight.

Testcase 1 - Low-Speed Two Degree-of-Freedom Case

a) Cubic non-linearities are examined to assess the accuracy of the continuation method and software as a means of analysing non-linear systems.

b) The accuracy and benefits of using the boundary identification and tanh/logaritmic approximation methods are established by analysing an aeroelastic model containing non-linearities

in the pitch degree-of-freedom.

Testcase 2 - Ground Vibration Test Cases

a) ODEs that represent sinusoidal forcing functions are used to demonstrate how continuation methods can be used to simulate vibration testing.

b) The effects of non-linearities on resonant peaks in response curves is demonstrated.

Testcase 3 - Low Speed Three Degree-of-Freedom Case

a) This is an extension of Testcase 1 to establish the accuracy of the boundary identification and tanh/logarithmic approximation methods for a three degree-of-freedom model.

Testcase 4 - Transonic Analysis

a) Euler and ROM methods are coupled with two and three degree-of-freedom linear structural models to establish the accuracy with which they can capture flutter boundaries.

b) The ROMs accuracy is ascertained by comparison with a full Euler simulation (weak and strong coupled) and a linearised Euler simulation.

Testcase 5 - Transonic Analysis with Structural Non-Linearities

a) Two and three degree-of-freedom structural models with free play non-linearities are combined with the ROM to ascertain the accuracy with which the ROM can capture LCOs when compared to the full Euler simulation.

b) The efficiency with which the boundary identification and the tanh/logarithmic approximation methods can be used to analyse a type hystersis non-linearity is demonstrated.

c) A combined freeplay and cubic non-linearity is examined to show the pre- and post-flutter (as predicted by the equivalent linear structural model) LCO effects.

Control

a) Linear Structural Models

i) The effectiveness of various control methodologies on suppressing flutter is established.

ii) The detrimental effects of Flutter Suprression Systems (FSSs) away from the flutter boundary are demonstrated.

b) Structural Models Containing Backlash

i) The correct method of incorporating backlash in to control systems is demonstrated.

ii) It is established if control systems designed to supress flutter also attenuate Limit-Cycle Oscillations.

Fatigue

a) A demonstration of how damage due to non-linear oscillations can be calculated by combining continuation methods and simple fatigue methods.

6.1.2 Results Presentation

Phase-plane plots are presented throughout the results as a method of visualising the periodic oscillations of limit-cycling systems. A periodic orbit exists in the phase-plane when the plot traces a closed path, and the number of loops required before the cycle becomes closed demonstrates periodicity. Sub-harmonics within oscillations can be seen as small loops within a major larger loop. Super-harmonics appear as oscillation loops of a similar size to the fundamental harmonic from which they occur. Example of different forms of phase plane are shown in figures 6.1 to 6.5 which show a period one (p1), period one with a sub-harmonic (p1h), period two (p2), a period two motion with sub-harmonics (p2h) and chaotic oscillations respectively.

The bifurcation diagram is a second method of presenting the results and is used in this work, it plots the maximum value that a state takes during an oscillation, e.g. the maximum amplitude of the pitch, against a continuation parameter e.g. speed. It therefore allows the user an overview of the scale and magnitude of the oscillations that are likely to be encountered.

6.2 Testcase 1 - Low Speed Two Degree-of-Freedom Case

6.2.1 Description

The first testcase is taken from the paper of Wong et al. [7]. The aeroelastic system analysed is a two degree-of-freedom model (free to pitch and plunge). The aerodynamic model is as described in section 2.2.2.1, as derived by Fung [1] and extended by adopting the coupling of

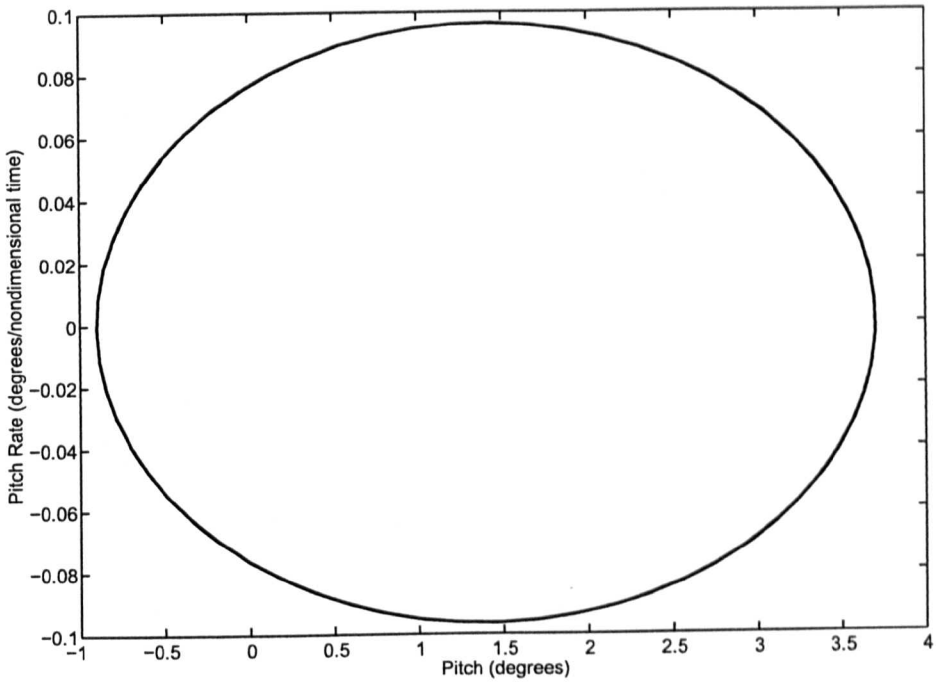

Fig 6.1: Phase Plane of a Period 1 Oscillation

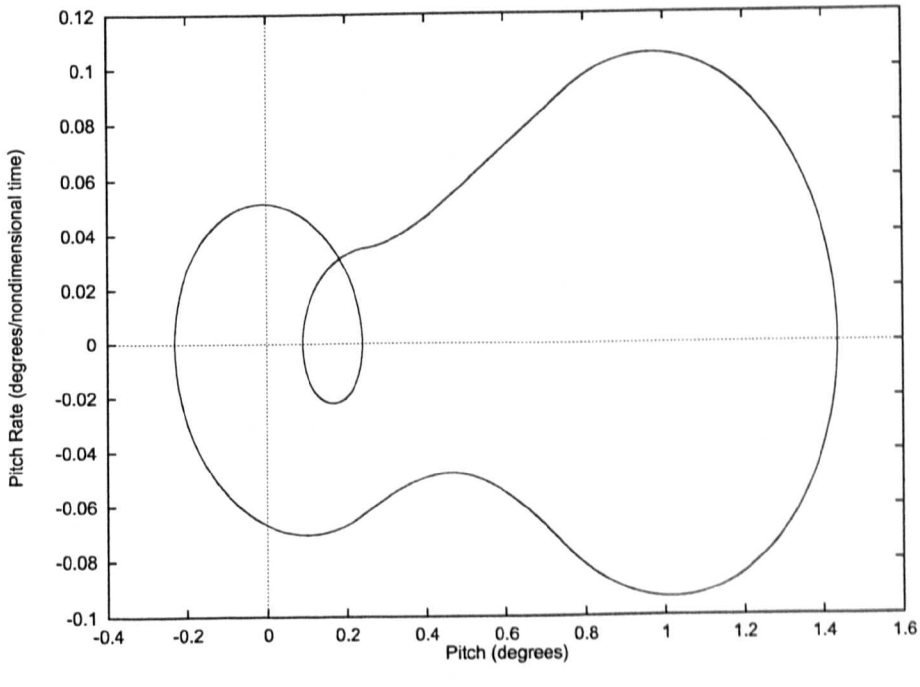

Fig 6.2: Phase Plane of a Period 1 Oscillation with a Harmonic

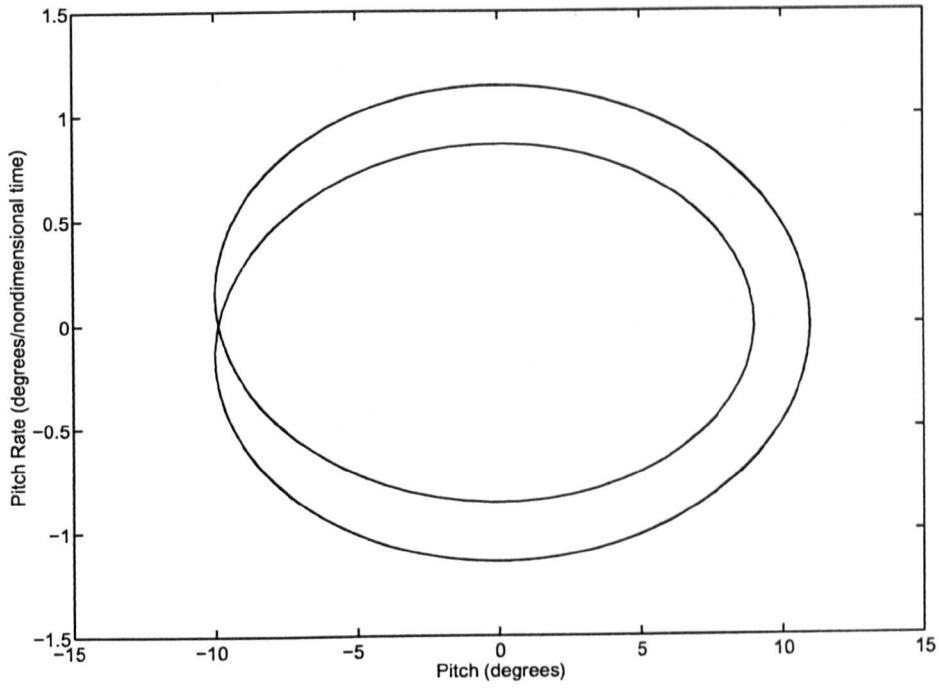

Fig 6.3: Phase Plane of a Period 2 Oscillation

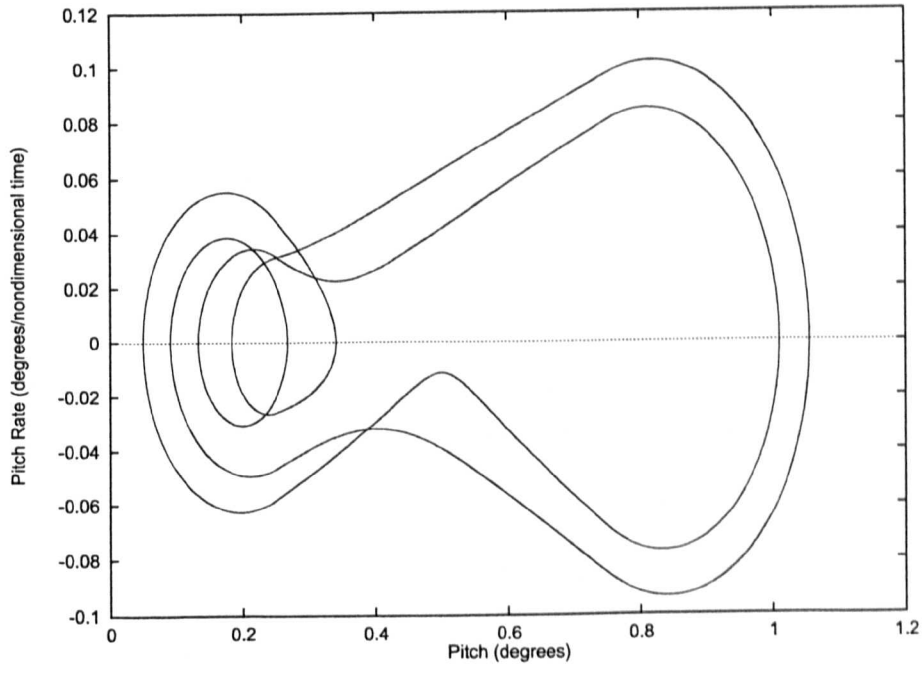

Fig 6.4: Phase Plane of a Period 2 Oscillation with a Harmonic

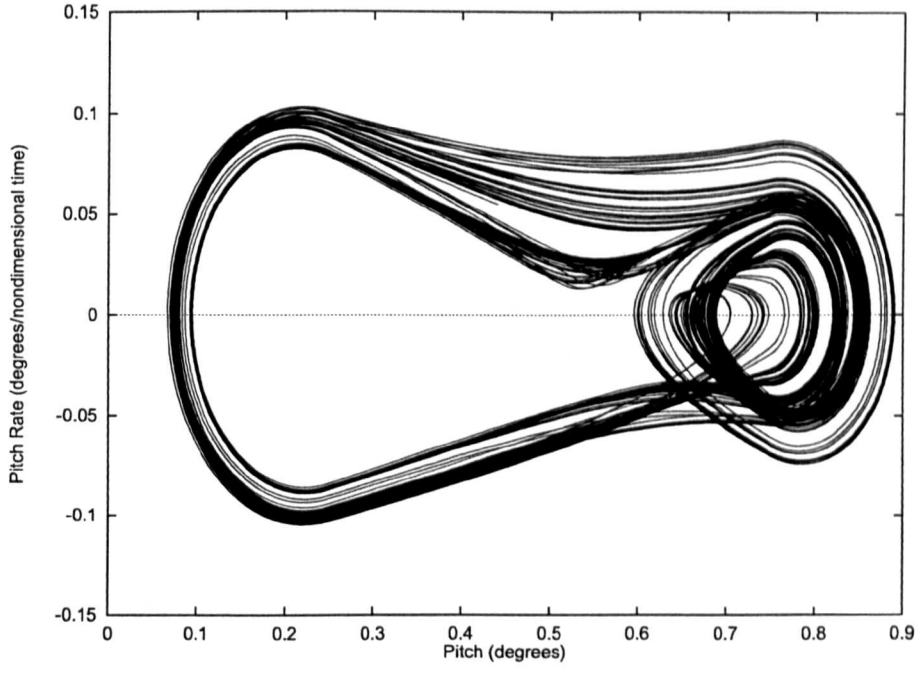

Fig 6.5: Phase Plane of a Chaotic Oscillation

Lee et al. [35] (section 2.3.1). The parameters, as defined in equation 2.25 and figure 2.11 are,

$$\mu = 100, \quad a_h = -0.5, \quad x_\alpha = 0.25, \quad \zeta_\xi = \zeta_\alpha = 0, \quad r_\alpha = 0.5, \quad \varpi = 0.2 \tag{6.1}$$

With this basic system adopted, Wong [7] calculated a non-dimensional flutter velocity of $U_L = 6.2851$ when a linear structural model is used.

Non-linearity is introduced in to the system firstly, via a cubic non-linearity and secondly, a freeplay non-linearity. The cubic non-linearities to be studied are,

- $G(\alpha) = \alpha + 3\alpha^3, \quad M(\xi) = \xi$
- $G(\alpha) = \alpha + 40\alpha^3, \quad M(\xi) = \xi + 0.1\xi^3$

where $G(\alpha)$ and $M(\xi)$ are the pitch and heave elastic stiffnesses respectively. For the first case, the cubic non-linearity acts only in the pitch degree-of-freedom whereas the second case has non-linearities in both degrees-of-freedom, although the non-linearity in the pitch degree-of-freedom is much stronger.

The freeplay non-linearity is shown in figure 6.6 and is only applied in the pitch degree-of-freedom. This non-linearity is defined by,

$$G(\alpha) = \begin{cases} \alpha - 0.25^o & \text{for} \quad \alpha < 0.25^o \\ 0 & \text{for} \quad 0.25^o \leq \alpha \leq 0.75^o \\ \alpha - 0.75^o & \text{for} \quad \alpha > 0.75^o \end{cases}$$

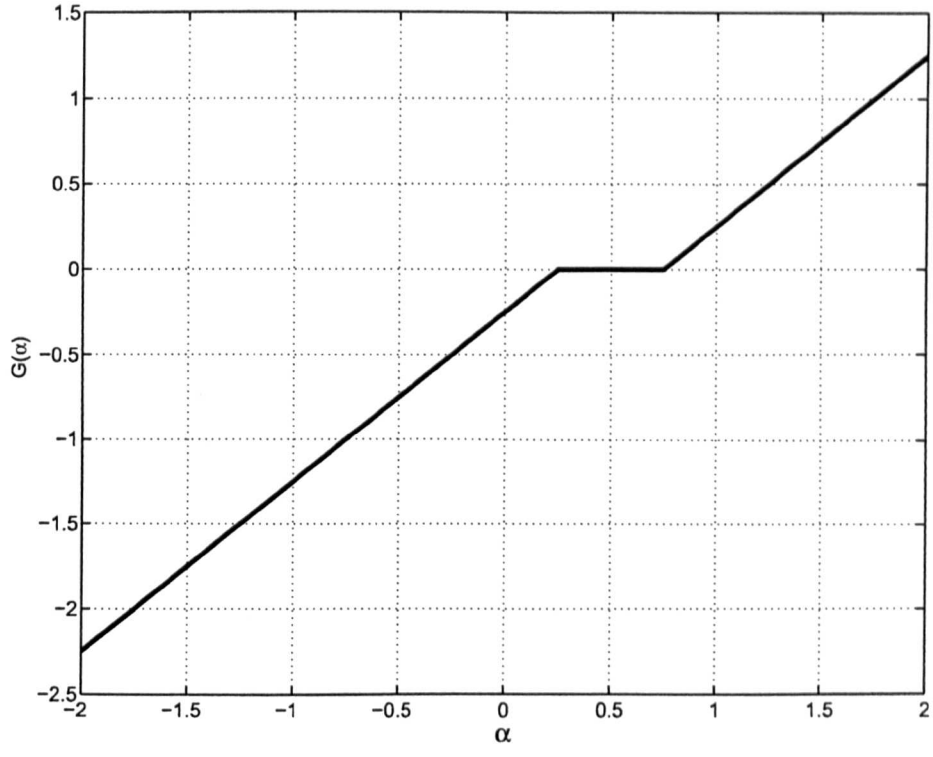

Fig 6.6: Low Speed, Two Degree-of-Freedom Testcase Freeplay

6.2.2 Results

Describing the cubic non-linearities by a set of continuous Ordinary Differential Equations (ODEs) the amplitude of the pitch Limit-Cycle Oscillations (LCOs) are shown in figure 6.7 and 6.8 for the first and second cubic non-linearity testcases respectively. In these figures the amplitudes of the oscillations are shown for various velocities, where U/U_L is the fraction of the linear systems flutter velocity. The results of Wong et al. [7] are presented alongside the results generated using the continuation method and the results generated using a fourth-order Runge-Kutta time simulation. Excellent agreement between all three techniques can be seen in the figures. As the boundary identification technique is only applicable for piecewise linear systems it cannot be applied to these cubic testcases.

From the results it is seen that the oscillations are entirely dominated by a single frequency as shown in the pitch versus pitch rate phase-plane plot, figure 6.9.

The freeplay non-linearity was next analysed using both boundary identification and continuous approximation techniques. Figure 6.10 shows a bifurcation diagram for the pitch degree-of-freedom at various velocities up to the flutter velocity. The plot is adapted from the results of Wong et al. [7], with only a subset of points shown for clarity. The figure also shows

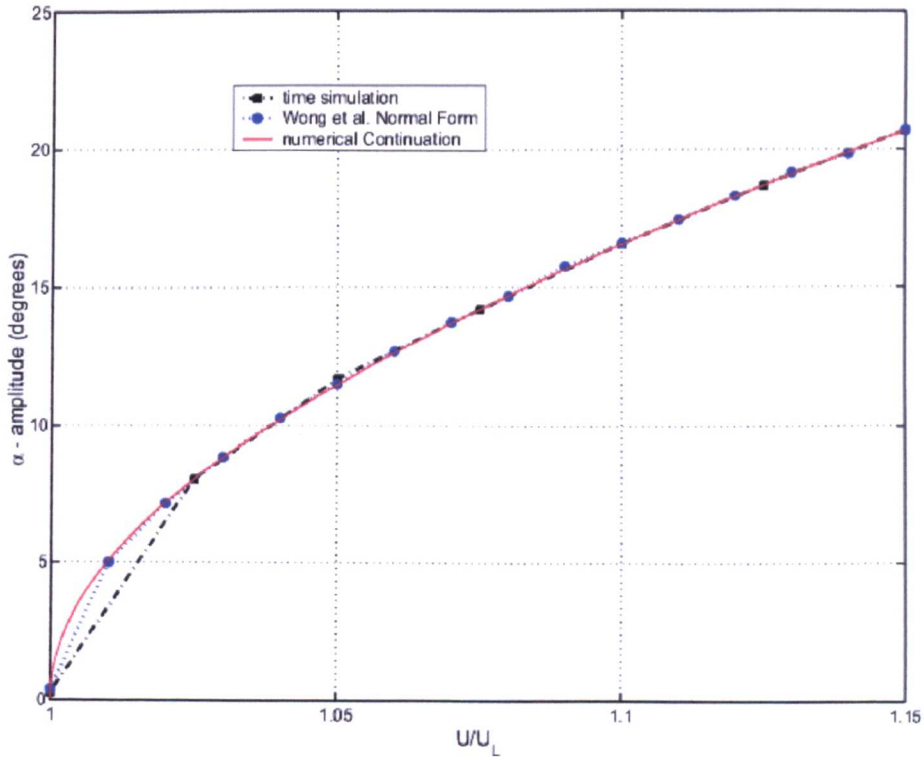

Fig 6.7: Pitch Amplitude versus Freestream Velocity for a Cubic Non-Linearity in Pitch described by $G(\alpha) = \alpha + 3\alpha^3$

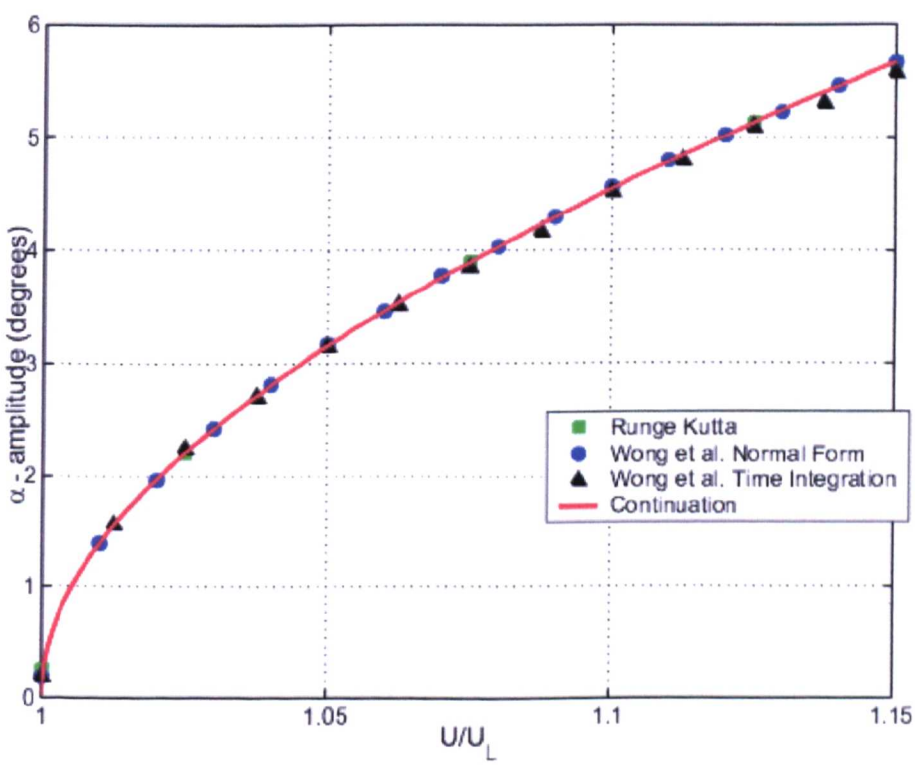

Fig 6.8: Pitch Amplitude versus Freestream Velocity for a Cubic Non-Linearity in Pitch and Plunge described by $G(\alpha) = \alpha + 40\alpha^3, \quad M(\xi) = \xi + 0.1\xi^3$

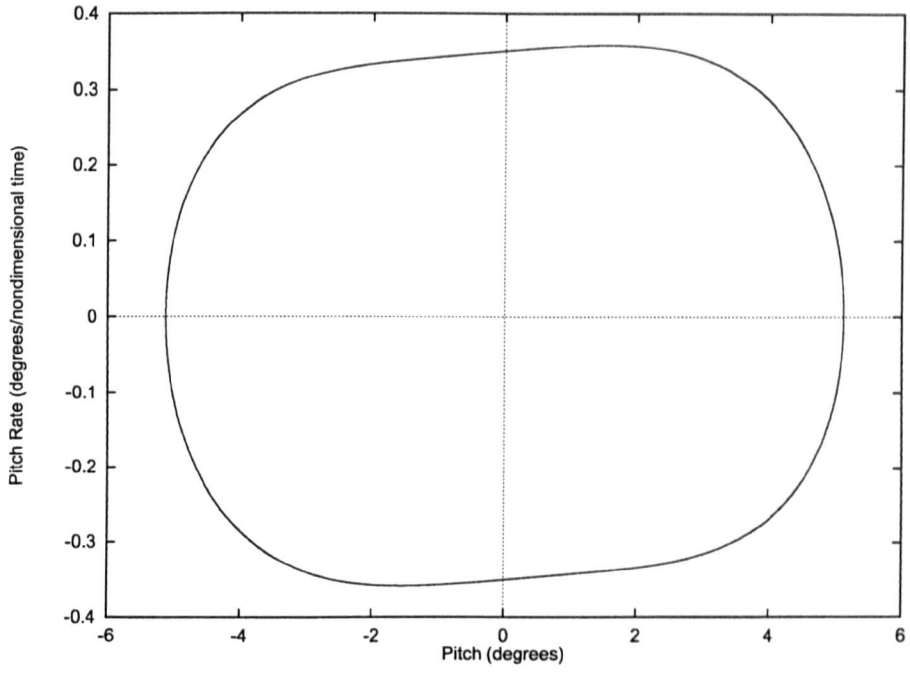

Fig 6.9: Phase Plane of a Period 1 Oscillation from Cubic Non-Linearity in Pitch Only, from Wong et al [7]

that, for freeplay non-linearities, the amplitude of the oscillations increases rapidly close to the flutter velocity with, in theory, infinite amplitude at the boundary itself.

A bifurcation diagram for period is shown in figure 6.11. In this figure, again taken from Wong et al. [7], the periodicity of the oscillations can be clearly seen. If a system evolves from a period 1 oscillation with harmonic (p-1-h) in to a period 2 oscillation with harmonic (p-2-h) the period approximately doubles, and the evolution is, therefore, a period doubling bifurcation and can be seen in the figure. In the figure chaotic regions are labelled but cannot be plotted on the figure as the period is infinite because chaos is a non-repeating orbit. Also labelled in the figure are the period 1 harmonic (p-1-h) and period 2 harmonic (p-2-h) oscillations.

Comparison between the bifurcation diagrams of Wong et al. [7] and the boundary identification technique are shown in figure 6.12 and 6.13 for pitch and period respectively. The figures show that good correlation exists between both techniques, which is expected as the techniques are based around a similar method. However, the technique adopted in this work requires far fewer analysis stages to be performed and allows identification of both unstable and stable branches. Figure 6.14 is the period 1 branch from figure 6.13 and illustrates how stability can be inferred from the nature of the solutions as branching from the main solution branch infers a change in stability of the given solutions (as described in Chapter 3). This is illustrated in the figure by the stable solutions appearing as solid lines and the unstable solutions being represented by dotted lines.

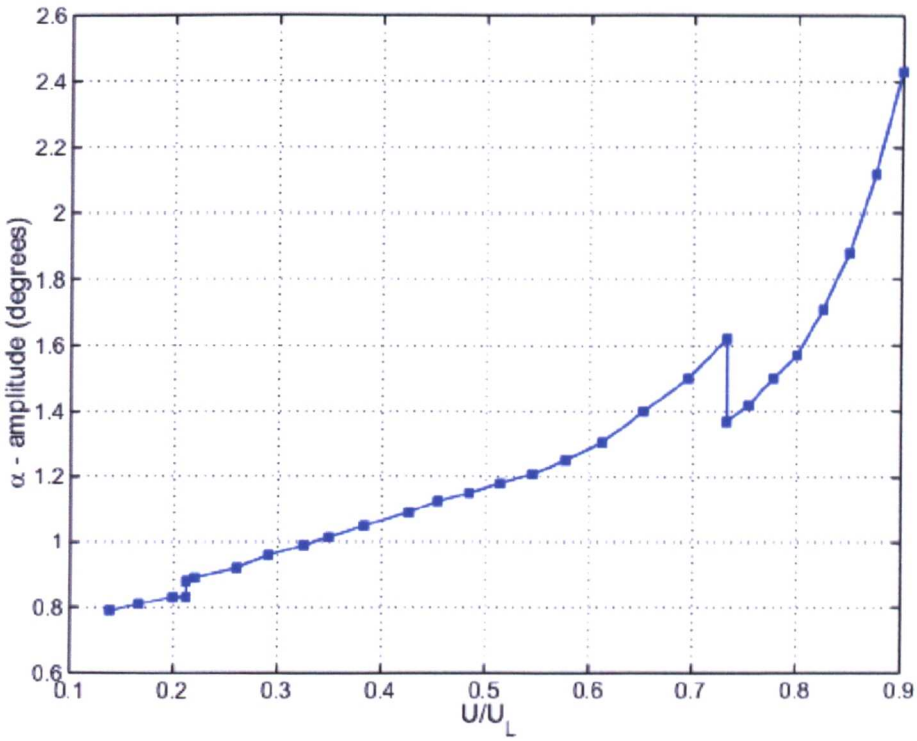

Fig 6.10: Pitch Bifurcation Diagram for a Freeplay Non-linearity

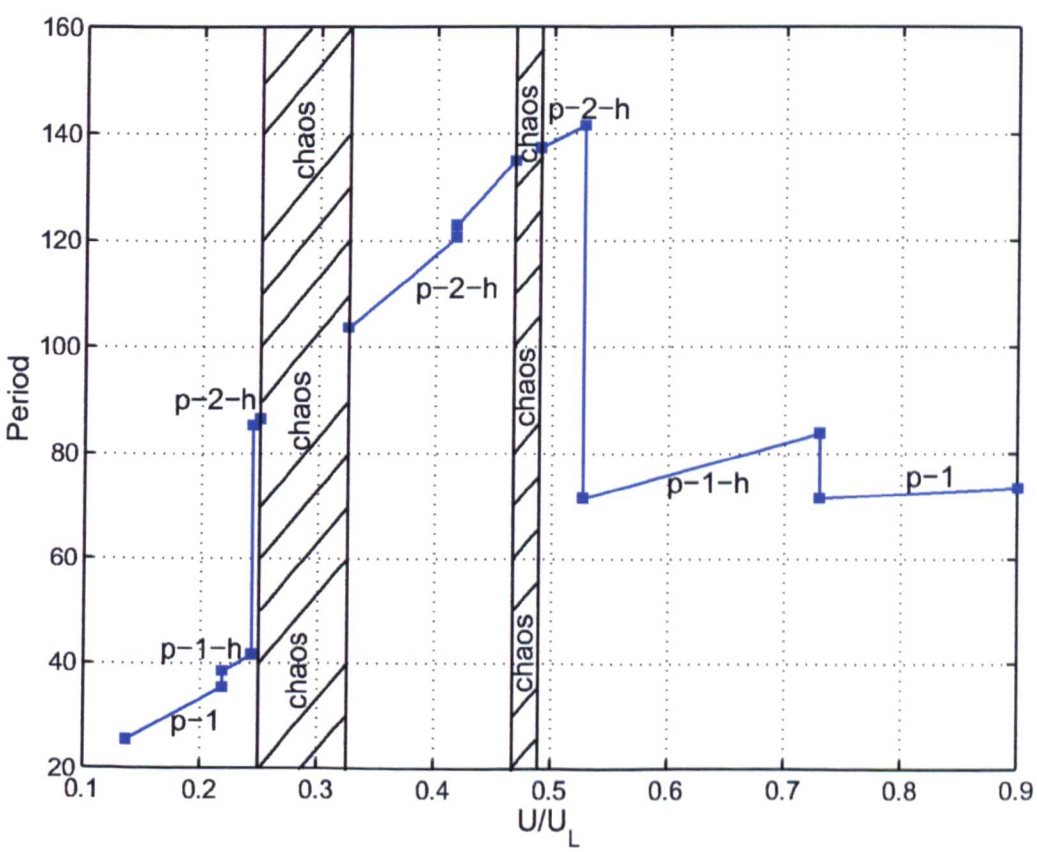

Fig 6.11: Period of LCOs for a Freeplay Non-linearity

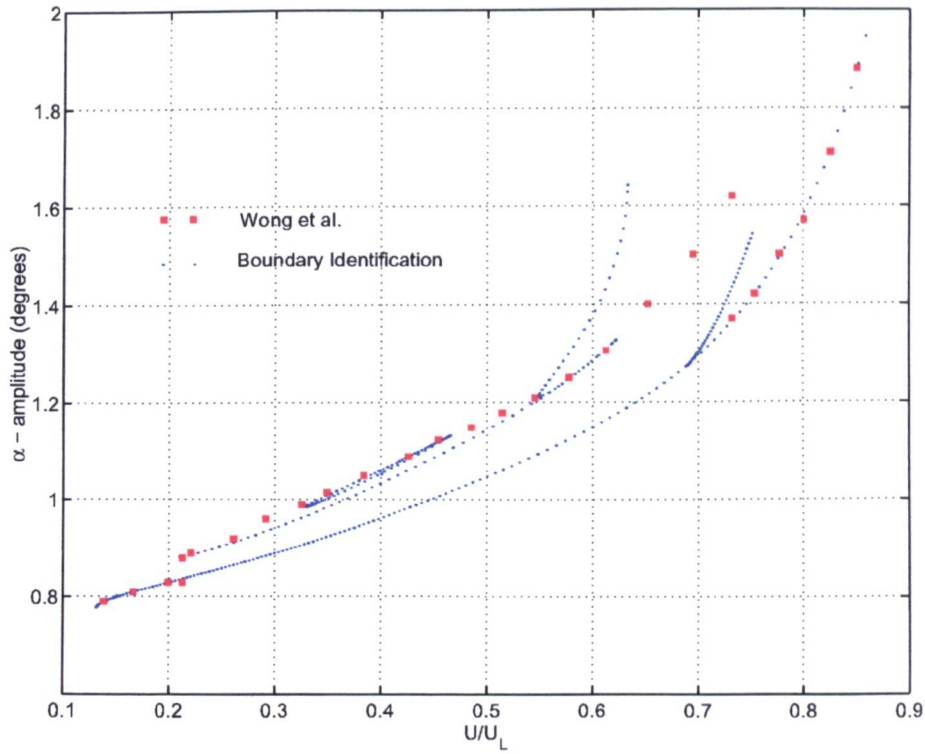

Fig 6.12: Maximum Pitch LCO Amplitude using Boundary Identification Compared with Results of Wong et al. [7]

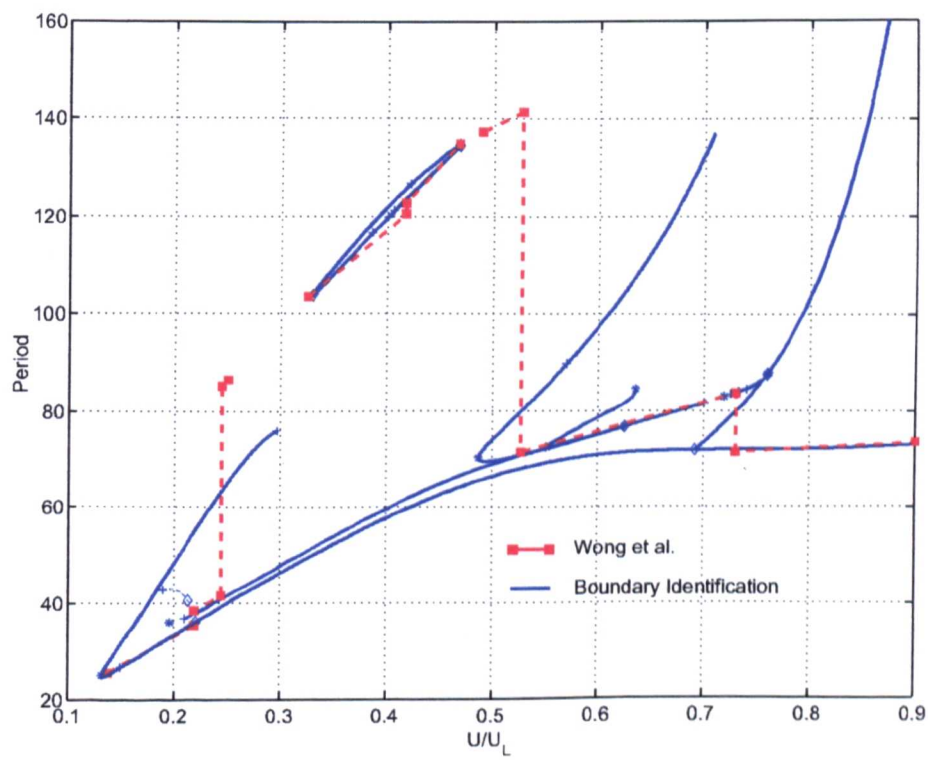

Fig 6.13: Period of LCOs for a Freeplay Non-Linearity as Generated by the Boundary Identification Technique

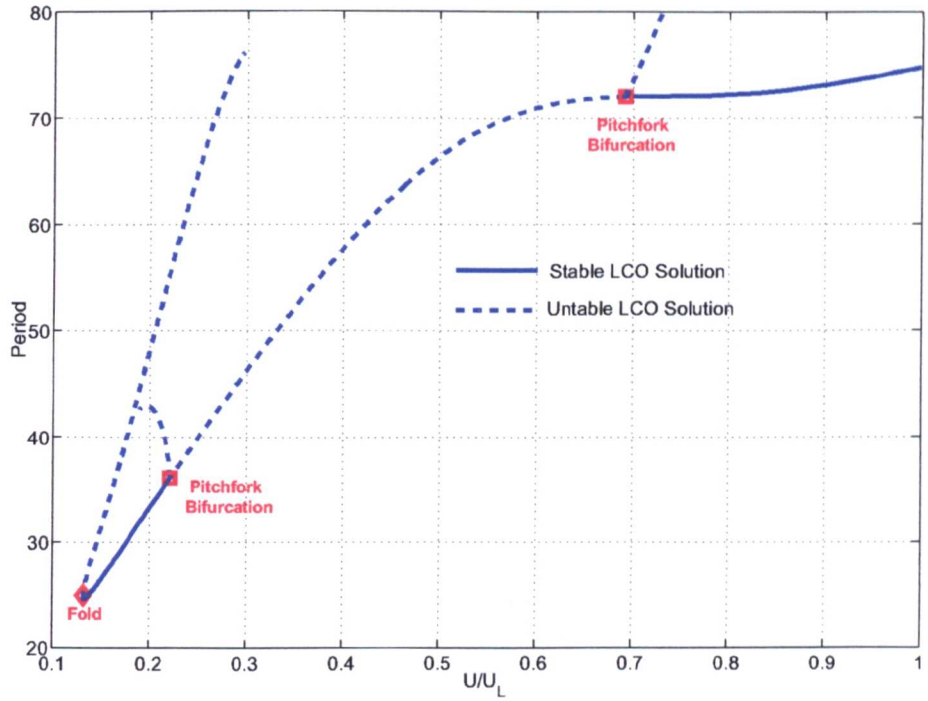

Fig 6.14: Inferred Stability for Boundary Identification Technique for a Period 1 Oscillation

Applying a tanh approximation to the freeplay non-linearity resulted in a good correlation between bifurcation diagrams as shown in figures 6.15 and 6.16. Using the continuation software to solve the state-space representation also allowed the stability of the solutions to be directly determined with solid and hollow circles representing stable and unstable solutions respectively. Additional benefits of using the solutions of the ODEs is that any parameter can be selected for the bifurcation diagram without requiring additional equations, as is required in the boundary identification technique. It should also be noted that identical results were generated using a logarithmic approximation to the freeplay. As the software used [50] allows the user to select specific points along the bifurcation diagram and plot the result against time or against any other system state. This allows phase-plane diagrams to be rapidly generated and therefore allows more direct access to solutions by the user. Figure 6.17 shows a phase-plane plot for a period 1 motion with a harmonic solution (p1h). This figure shows results taken from a logarithmic representation alongside results generated from boundary capturing time simulations. These figures are shown to match exactly therefore validating the continuation technique used. In generating the results it was found that using the tanh functions it was very difficult to capture the period 2 harmonic (p-2-h) branch between the two chaotic areas. This is due to the tanh function having positive gradients around the discontinuities which numerically effects the solutions. Overall, fewer problems were found using the logarithmic function because of its tangential tendancy toward the accurate solution.

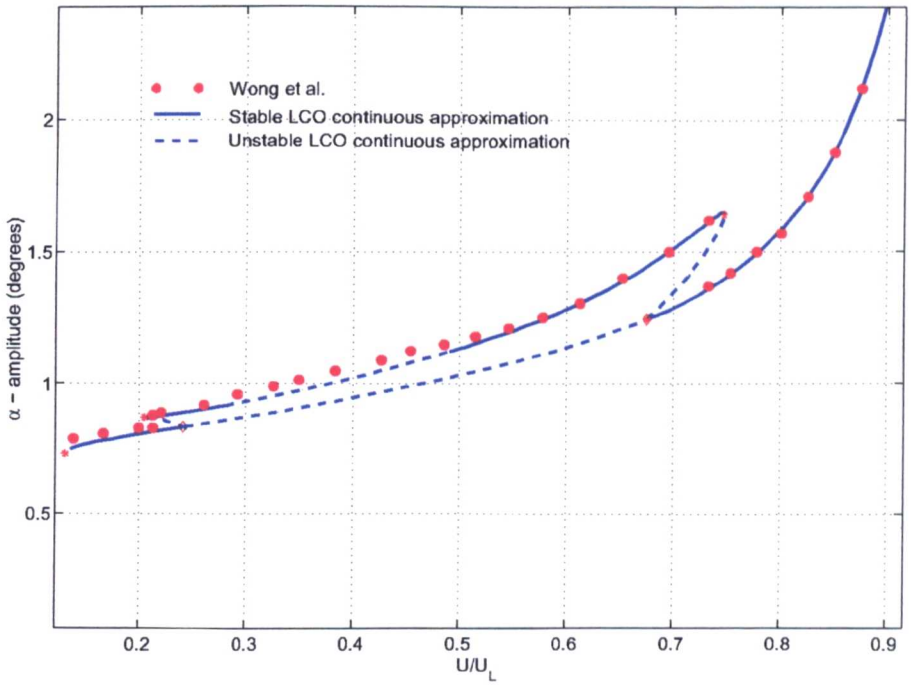

Fig 6.15: Maximum Amplitude of Pitch LCO Amplitude

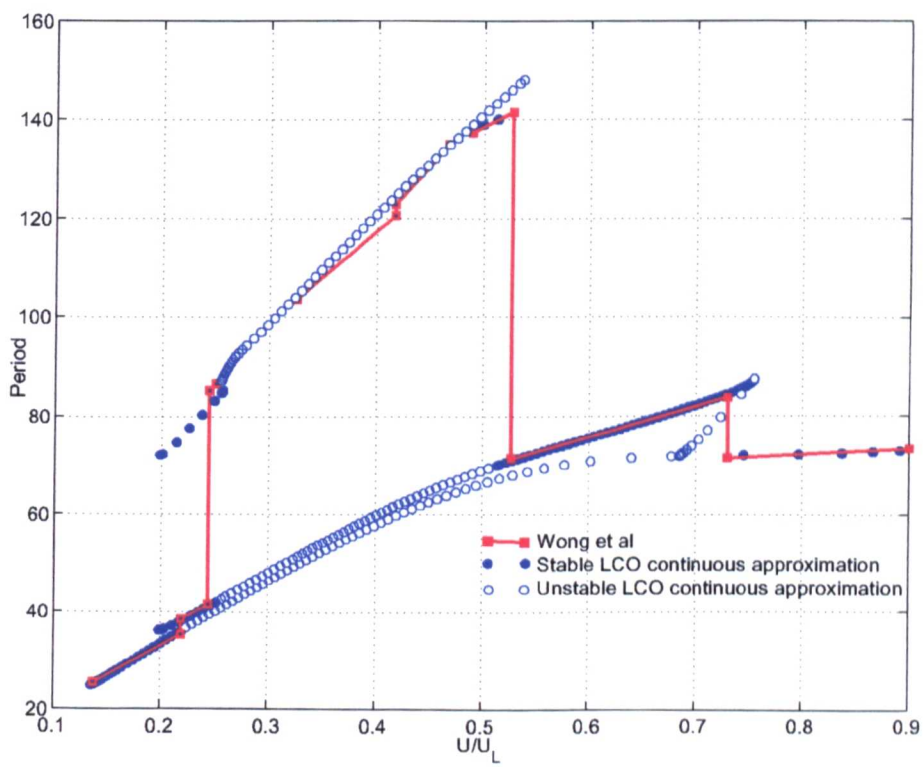

Fig 6.16: LCO Period Bifurcation Diagram Generated using Continuous Approximation to a Freeplay Non-Linearity

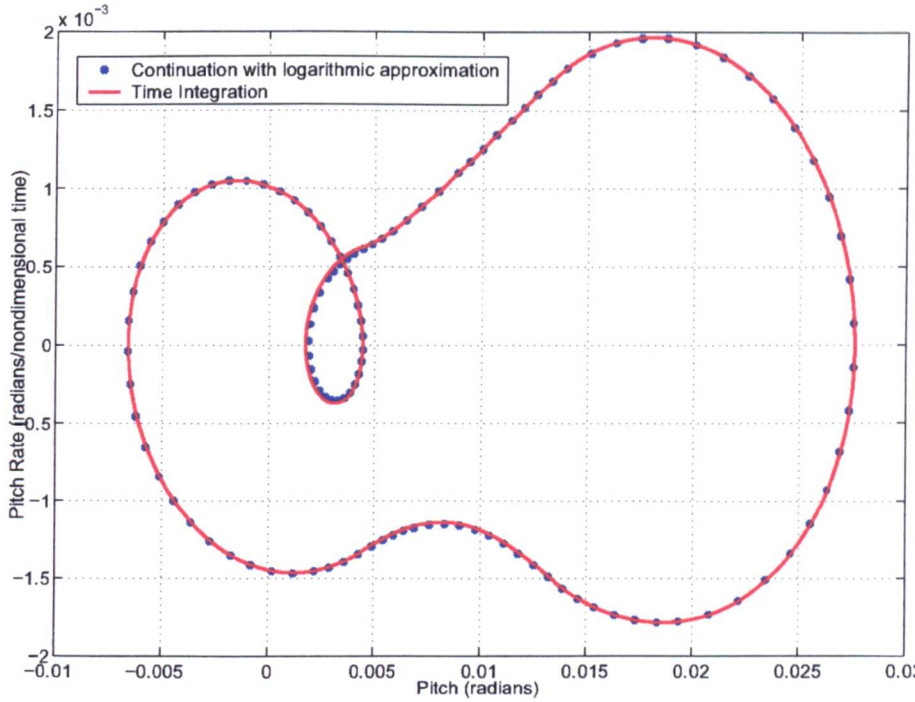

Fig 6.17: A Phase Plane of a Period 1 with Harmonic at $0.72U_L$

In figure 6.16, the period 2 harmonic branch between the chaotic regions is assessed to be unstable by both the tanh and logarithmic representation of the freeplay when in actual fact, if time simulations are performed, the solutions are stable. The reason for this erroneous solution is that all the states are symmetrical, with the pitch being symmetrical about 0.5 degrees. This symmetry leads to the co-existence of equal but symmetrical solutions for all solutions as shown in figure 6.18. The symmetry of such solutions is determined, in the continuation software, by the eigenvalues of the Jacobian matrix. Figure 6.19 shows which of the symmetrical solutions the system remains on depending on initial conditions for a period 1 when a small change in the continuation parameter, velocity, is made. Figure 6.20 shows a similar plot to Figure 6.19 for the period 2 harmonic solution that cannot be captured. Comparing the figures shows a much more patchy region of attraction for this case. As the Jacobian matrix is constructed from the solutions with small perturbations in initial conditions it seems likely that the unstable branch is detected because the regions of attraction are too small within the calculations. This was validated when using a more dense analysis where small areas of stable solutions are observed.

The analysis of the non-linear aeroelastic problem as defined by Wong et al. [7] has shown that the continuation techniques both accurately and rapidly identify the correct solutions (see figure 6.21). Discrepancies in the magnitudes within the figures are credited to the data from the paper by Wong et al. [7] having to be read off by hand. Additionally the results of Wong

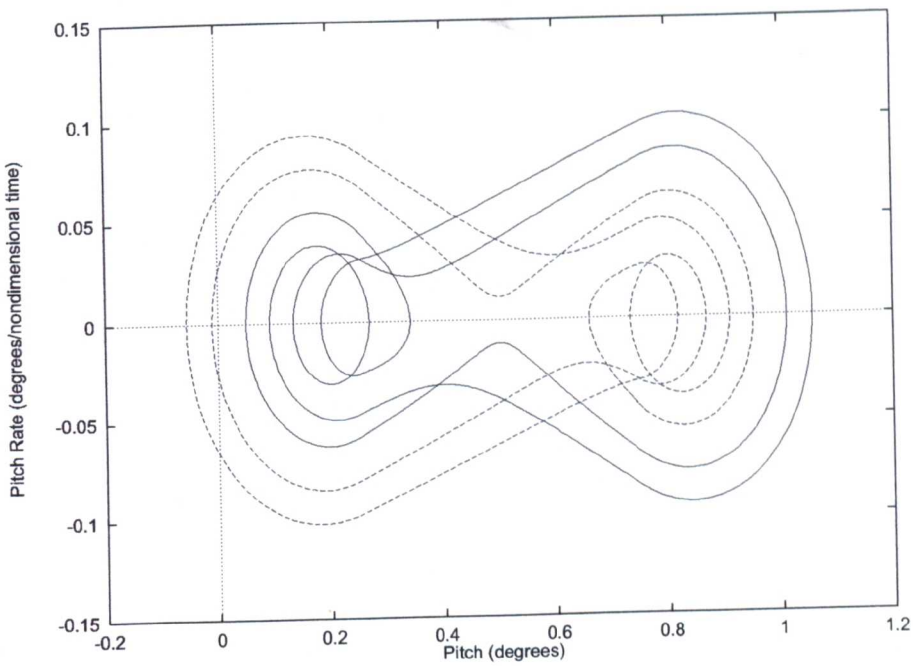

Fig 6.18: Symmetrical Period 2 Harmonic Oscillations

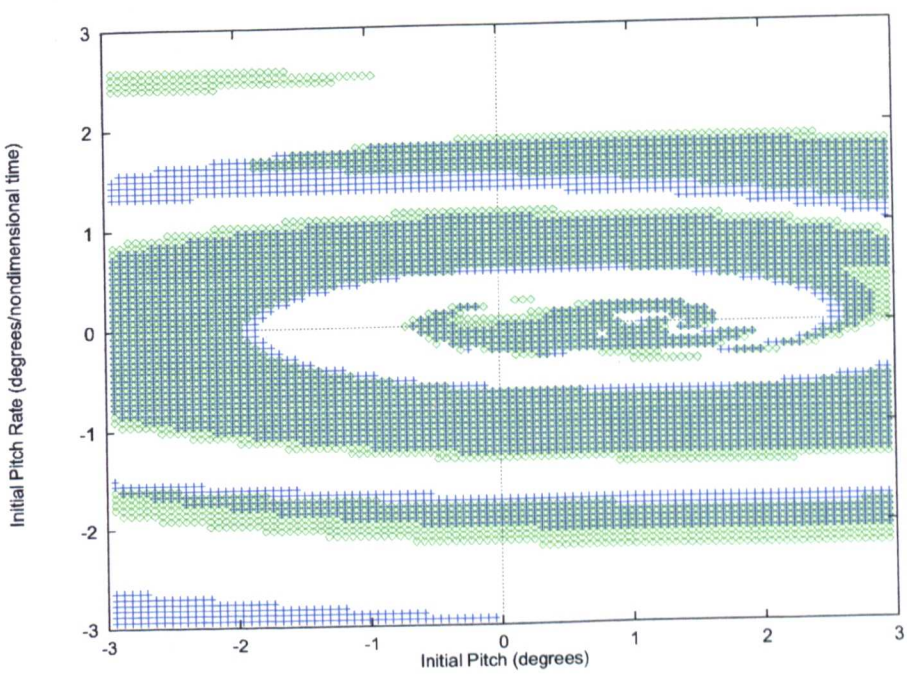

Fig 6.19: Basin of Attractions at Close Velocities for Stable Calculated Solutions, Blue - Stable LCOs at $0.6U_L$ *and Green - Stable LCOs at* $0.61U_L$

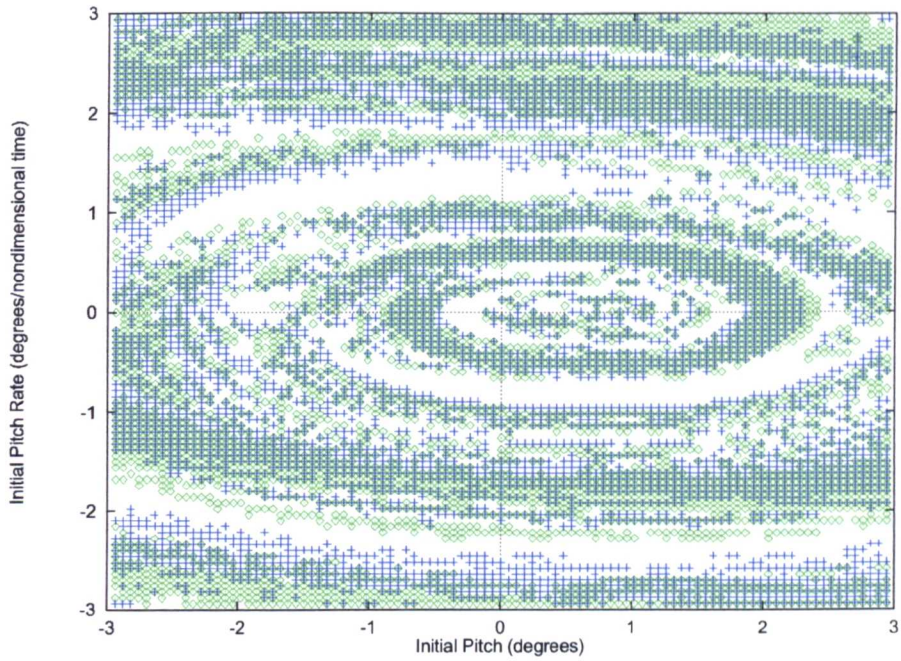

Fig 6.20: Basin of Attractions at Close Velocities for Unstable Calculated Solutions, Blue - Stable LCOs at $0.4U_L$ *and Green - Stable LCOs at* $0.41U_L$

et al. [7] are presented for one set of initial conditions only and therefore the existence of two stable solutions for a given velocity is not presented in their work.

The boundary identification technique was found to be an extremely accurate and rapid method of identifying all the various forms of oscillations with only a limited number of time integration runs being required to generate the initial conditions for the continuation. However, the requirement for the addition of extra equations to generate bifurcation diagrams is a disadvantage in that for every degree-of-freedom two extra equations are required, one to identify the maxima and another to identify the time at which the maxima occurs. For the cases studied in this thesis with only two or three structural degrees-of-freedom this poses only a minor problem, in higher order systems this could pose a significant computational penalty. Additionally, if higher harmonics are required, the number of equations to be solved is doubled every time a period doubling is encountered. This second point is only fairly minor for mechanical systems in that damping tends to eliminate most higher order oscillations.

The continuous representation of a freeplay non-linearity is seen to allow rapid generation of bifurcation diagrams with a level of accuracy that depends on the ϵ parameter in the approximation. The solution for coarser approximations was seen to generate results in a much shorter time than was found using a more accurate representation. The benefits of using continuous functions over a boundary identification technique are clear in that the software already exists to perform the calculations, analyse stability and generate any figures that may be appropriate.

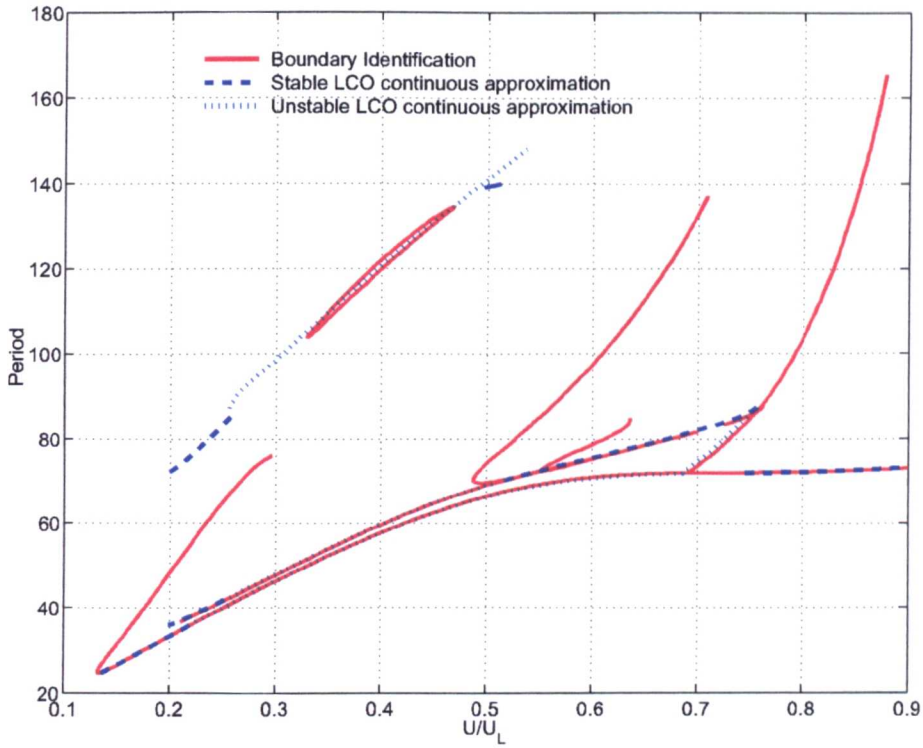

Fig 6.21: A Comparison of Boundary Identification and Continuous Approximation LCO Periods for a Low-Speed 2-DOF Aeroelastic System

The results presented in this section have validated the boundary identification and ODE continuation as a way of analysing continuous non-linear and piecewise non-linear aeroelastic systems. The applicability of the results is not certain, however, as the aerodynamic theory mandates a small angle approximation which is not applicable for all cases as the oscillations captured have amplitudes up to 20^0.

6.3 Testcase 2 - Ground Vibration Test Cases

6.3.1 Description

The simulations of Ground Vibration Tests (GVTs) is demonstrated with the following testcases. This work demonstrates a more rigorous mathematical analysis of a general dynamics problem and uses testcases from the paper by Lee et al. [35]. The first equation studied is the single degree-of-freedom Duffing equation that contains a cubic non-linearity,

$$\alpha'' + c\alpha' + k\alpha + \beta\alpha^3 = F\sin(\omega t) \tag{6.3}$$

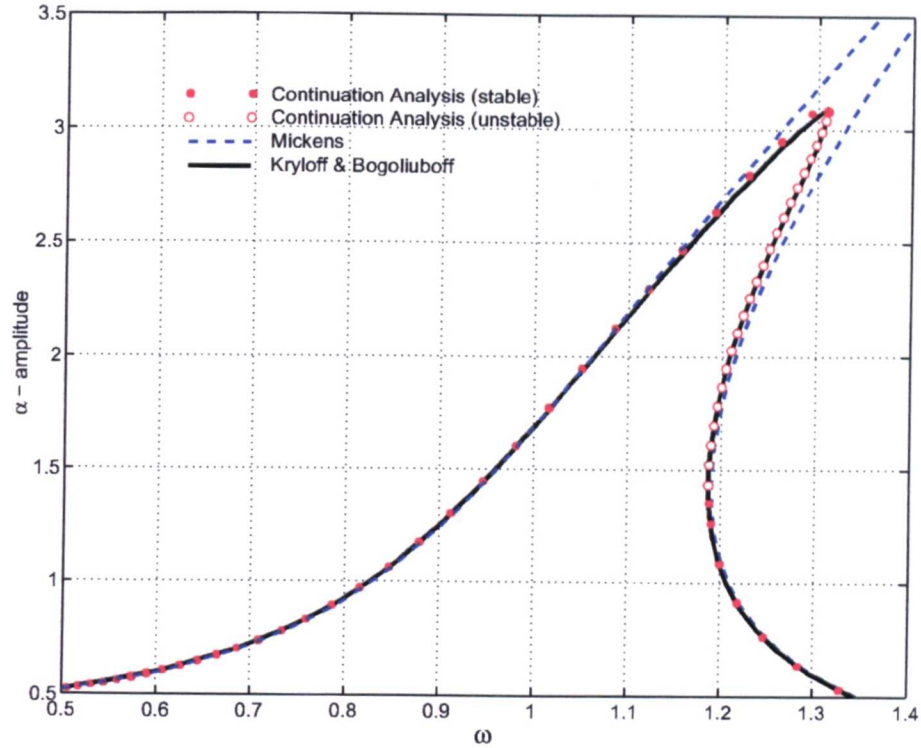

Fig 6.22: Response Curves for Duffing Equation described by Equation 6.3

where the parameters are set to $c = 0.1$, $k = 1$, $\beta = 0.1$ and $F = 0.4$. The second testcase is analogous to the two degree-of-freedom aerofoil system with cubic non-linearities in both heave and pitch. Using an excitation force in the pitch degree-of-freedom gives the equations,

$$\begin{aligned} 0.25\alpha'' + \xi'' + 0.25\xi' + \xi + 0.25\xi^3 &= 0 \\ \alpha'' + 0.25\xi'' + 0.25\alpha' + \alpha + 0.25\alpha^3 &= F\sin(\omega t) \end{aligned} \tag{6.4}$$

These results are also compared with the uncoupled system,

$$\alpha'' + 0.25\alpha' + \alpha + 0.25\alpha^3 = F\sin(\omega t) \tag{6.5}$$

by setting the ξ dependant terms to zero.

In all the cases outlined above the response of the system is to be studied for its dependency on excitation frequency and amplitude.

6.3.2 Results

Using continuation methods to analyse the basic Duffing equation as defined by equation 6.3 results in a response as shown in figure 6.22.

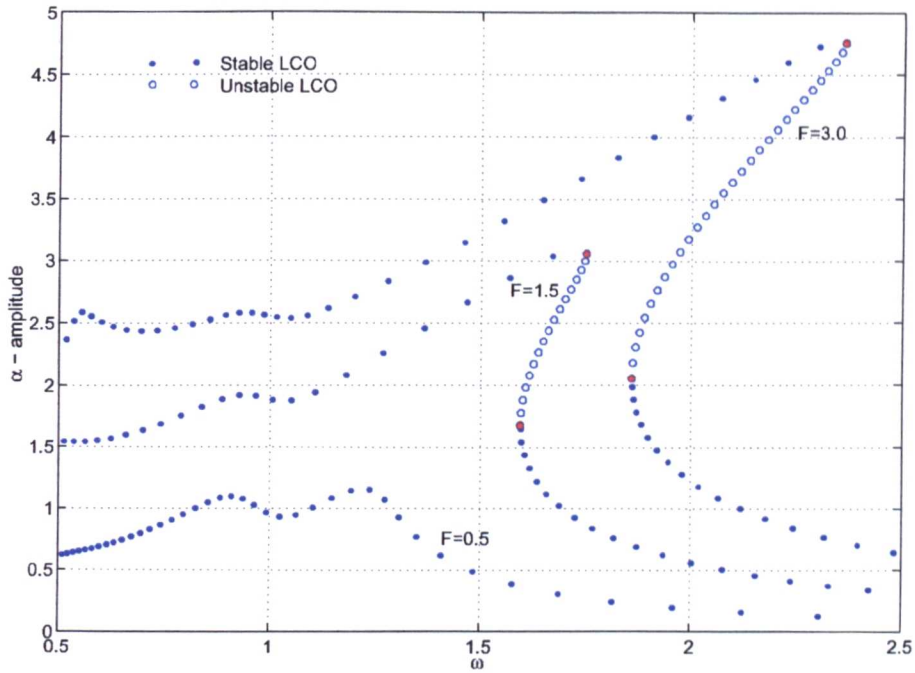

Fig 6.23: Response of Decoupled Dynamic System described by Equation 6.5

This figure shows the response to a sinusoidal forcing with an amplitude of 0.4, results are also presented from analyses performed by Mickens [102], who performed early work of the non-linear problem, and Kryloff and Bogoliuboff [103] who derived equations that give an accurate representation for the relationship between response and input, and the exact solution of the Duffing equation. The continuation technique is shown to give an excellent correlation with the exact solution, with the added benefit that the solution stability is indicated directly. For this particular case the stability could be directly derived as the loss of stability is due to turning points in the curve.

The response of the decoupled dynamic model represented by equation 6.5 is shown in figure 6.23 for excitations of 0.5, 1.5 and 3.0 in magnitude.

This figure illustrates the non-linear behaviour of the system response in that, for a given frequency of excitation ω, a doubling in the excitation amplitude does not lead to a doubling in the systems response. The regions of instability are also seen not to vary linearly thus requiring such complicated analysis. This decoupled system is similar in form to that of figure 6.22 as the system is another form of Duffing equation.

The responses of the dynamic system represented by equation 6.4 to sinusoidal forcing in the pitch degree-of-freedom are seen in figures 6.24 and 6.25 for the heave and pitch degrees-of-freedom respectively.

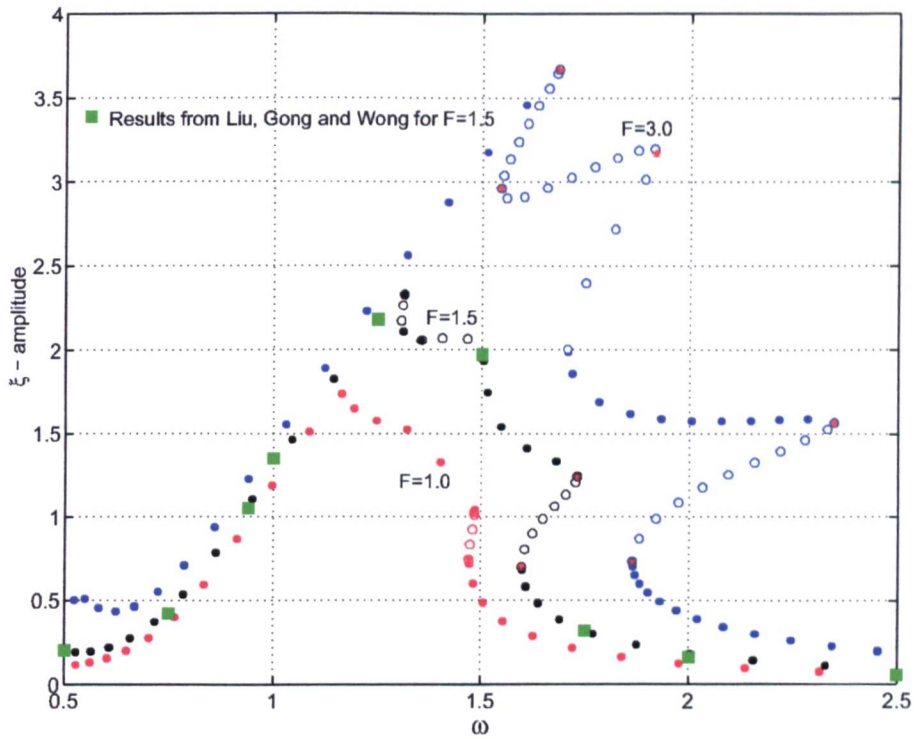

Fig 6.24: ξ Response of a Two Degree-of-Freedom System to Various Excitations (Equation 6.4)

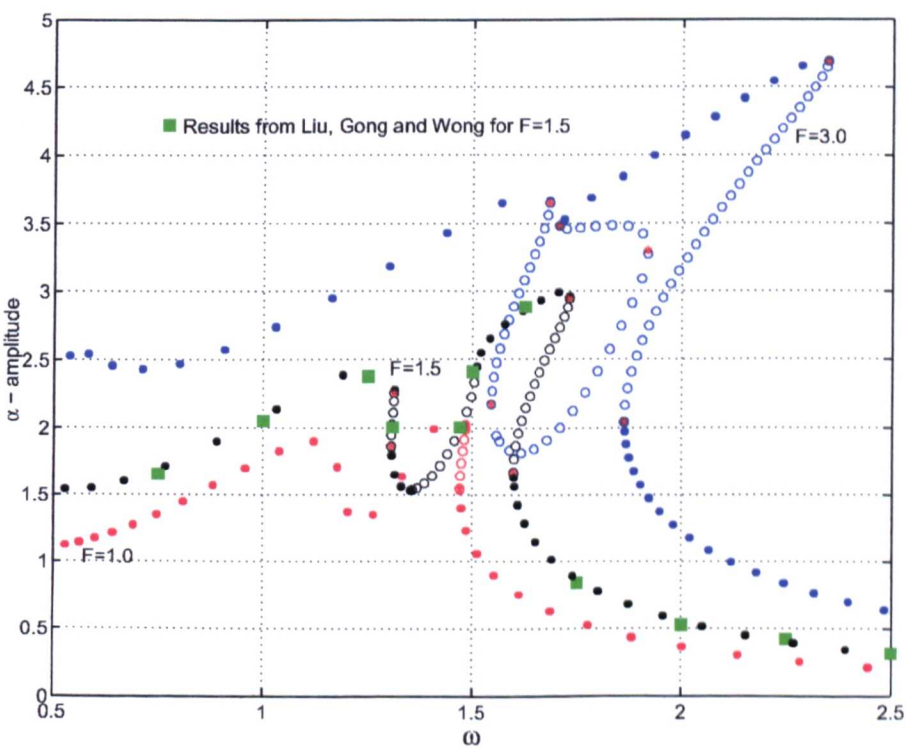

Fig 6.25: α Response of a Two Degree-of-Freedom System to Various Excitations (Equation 6.4)

The non-linear nature of the response introduced into the system through the inclusion of cubic stiffening in both degrees-of-freedom is clear from the figures. In the figures the results of Lee et al. [35] are also shown for a forcing amplitude of 1.5. The close correlation between both solution methods is shown in these figures. The ability of the continuation technique to identify the stable solutions directly is clearly shown. For these complicated motions, the technique adopted by Lee et al. [35] is unable to determine the stability directly without further analyses being performed.

From the analysis of coupled and uncoupled dynamic equations it is clear that the ability to identify oscillations rapidly in high order systems requires more sophisticated analyses than the simple relationships derived by Lee et al. [35]. The method of Lee et al. [35] reduces the equations to a simple relationship between the pitch and plunge for a given value of ω. In their analysis it is assumed that the response of higher order harmonics is negligible in systems containing low-order polynomial stiffening. However, it was found that their method, being based on basic algebraic manipulation, become complicated for higher order systems and not possible for discrete non-linearities.

These results show that the use of continuation for the analysis of forced dynamic problems is a relatively simple task and enables results to be generated accurately and rapidly. The extension to higher order systems is possible by the addition of extra equations of motion but can create computational penalties due to the size of Jacobian required to be generated.

The system responses in figures 6.24 and 6.25 are seen to be highly non-linear but also seem to show some form of relationship with the results of the uncoupled response shown in 6.23. However, after exhaustive analysis simple relationships between the response curves could not be ascertained.

6.4 Testcase 3 - Low Speed Three Degree-of-Freedom Case

6.4.1 Description - Low-Speed Three degree-of-freedom Aeroelastic Analysis with a freeplay Non-linearity

Conner et al. [44] analysed a three degree-of-freedom aeroelastic system using the aerodynamic model of Edwards et al. [2]. The parameters used were generated from an experimental set-up with the damping model extracted from a wind-off linear model vibration analysis. The

parameters used in the analysis were,

$$b = 0.127m, \quad a_h = -0.5, \quad C_\beta = 0.5, \quad m = 0.62868kg, \quad m_a = 0.18597kg,$$
$$S_\alpha = 0.08587kgm, \quad S_\beta = 0.00395kgm, \quad x_\alpha = 0.434, \quad x_\beta = 0.01996,$$
$$I_\alpha = 0.01347kgm^2, \quad I_\beta = 0.0003264kgm^2, \quad r_\alpha = 0.7321, \quad r_\beta = 0.11397,$$
$$\kappa = 0.03984, \quad K_\alpha = 1486s^{-2}, \quad K_\beta = 155s^{-2}, \quad K_h = 1809s^{-2},$$
$$\zeta_\alpha = 0.01626, \quad \zeta_\beta = 0.0115, \quad \zeta_h = 0.0113$$

From their tests, Conner et al. [44] calculated the flutter velocity at $23.9ms^{-1}$ whereas the experimental model had a flutter velocity of $20.6ms^{-1}$. These values correspond to a non-dimensional velocity of 3.249 and 2.825 respectively. Three freeplay gaps are used, and correspond to those of the authors, they are $\pm 1.15^o$, $\pm 1.83^o$ and $\pm 2.12^o$. The freeplay gaps occur in the flap degree-of-freedom only and have no preload applied.

6.4.2 Results - Low-Speed Three degree-of-freedom Aeroelastic Analysis with a freeplay Non-linearity

Unfortunately, comparative results for the technique described by Conner et al. [44] could not be generated. The parameters given were used within the calculations but did not seem to duplicate Connor's results. The author was contacted with regard to the discrepancies but no adequate explanation was reached.

In order to isolate the problem an analysis was firstly performed using a linear aeroelastic model described by Edwards et al. [2]. This model was chosen as it was the aerodynamics as derived by Edwards that were used by Conner et al. [44]. Varying the velocity the systems eigenvalues were plotted, these results compared exactly with the values generated by Edwards et al. [2]. From this basis it was therefore surmised that both the aerodynamic and structural models were correct, the only model that is not validated is the structural damping matrix as this was not used by Edwards et al. [2]. Replacing the parameters within the structural matrices with those used by Conner et al. [44] and including the damping matrices the above process was repeated over the velocity range applicable. The eigenvalues traces generated showed the same tendencies as those of Conner et al. [44] but the velocities observed differed with flutter occurring at $18.1ms^{-1}$ compared to $23.4ms^{-1}$. A better comparison was achieved by using the uncoupled resonant frequencies within the modal damping matrix but this was still sufficiently far away to be of any utility.

After varying several parameters it was seen that it was not possible to recreate the results as

generated by Conner et al. [44]. By demonstrating the analysis techniques on the two degree-of-freedom low-speed and the two and three degree-of-freedom transonic model it is thought that sufficient evidence can be presented in this work for validation to be achieved. The major drawback to the inability to perform such analyses is that the case presented by Conner et al. [44] is one of the only cases to present both experimental and theoretical results.

6.5 Testcase 4 - Transonic Analysis

The results in this section provide validation of the Reduced Order aerodynamic Model (ROM) of Gaitonde and Jones [6]. The ROM has previously been validated for prescribed motions by Gaitonde and Jones but requires validation when applied to fully coupled aeroelastic systems. Two testcases are considered with comparisons being made between the ROM, the full Euler simulation and the work of other authors in the field. The non-linear testcases of Djayapertapa [85] where not adopted in order to verify the continuation method as the testcases failed to demonstrate the LCO and chaos phenomena of interest.

In the previous results the computational inefficiency of the boundary identification continuation technique has been highlighted. The remaining results are therefore calculated using the numerical continuation of continuous ODEs only using approximations to discrete non-linearities where appropriate.

6.5.1 Description - Two Degree-of-Freedom

The first testcase, taken from the thesis of Djaypertapa [85], is a two degree-of-freedom transonic aeroelastic testcase as shown structurally by figure 2.11. The model has been previously studied by many authors, [104, 105, 106] and is based on a NACA64A010 aerofoil section. The aerodynamic mesh uses 121 points around the aerofoil (191 including the wake) and 36 points normal to the aerofoil which go from the aerofoil surface to the far field boundary approximately 20 chords away. The whole grid is shown in figure 6.26 with detail around the surface shown in figure 6.27. The structural model parameters are,

$$a_h = -0.2, \quad x_\alpha = 0.2, \quad r_\alpha = 0.5, \quad \omega_h/\omega_\alpha = 0.3, \quad \mu = 23.48 \tag{6.6}$$

In this testcase the flutter boundary in the transonic regime is studied and found to vary with the Mach number selected. Only the finite volume coupled method from section 2.3.3 and the

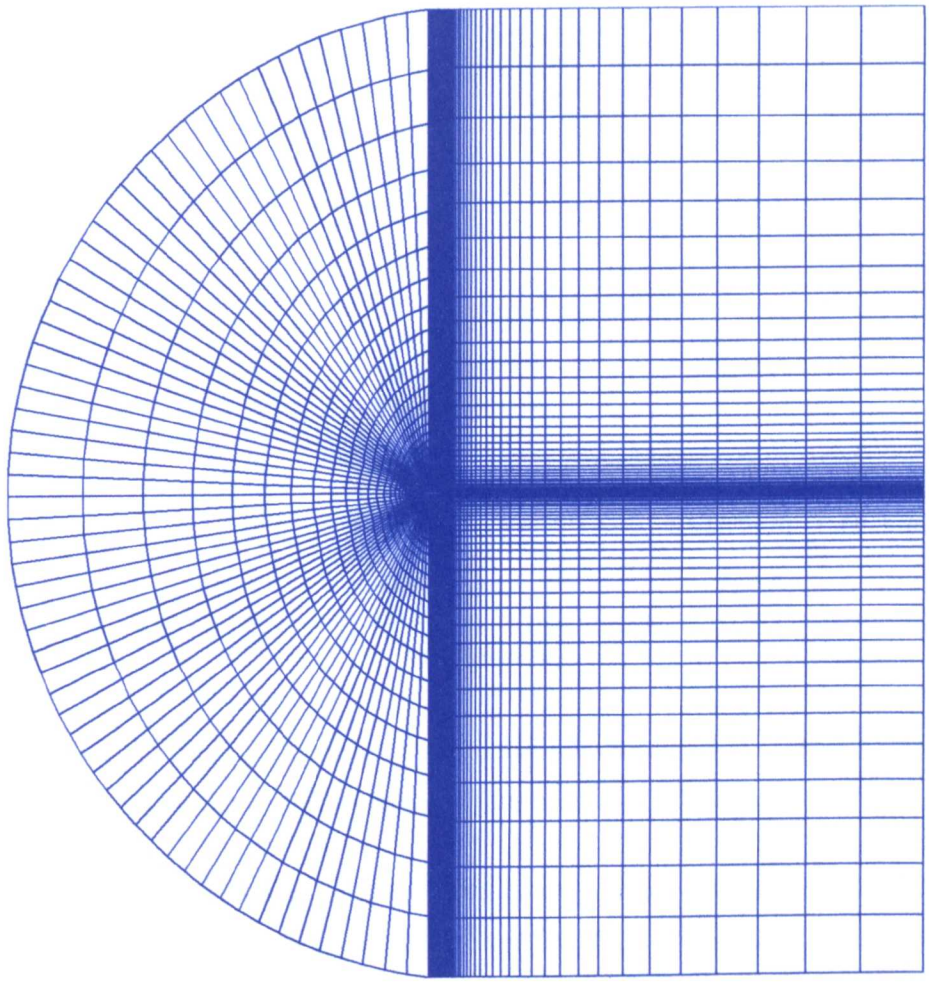

Fig 6.26: Farfield View of the Finite Volume Grid used for the CFD Solution Procedure

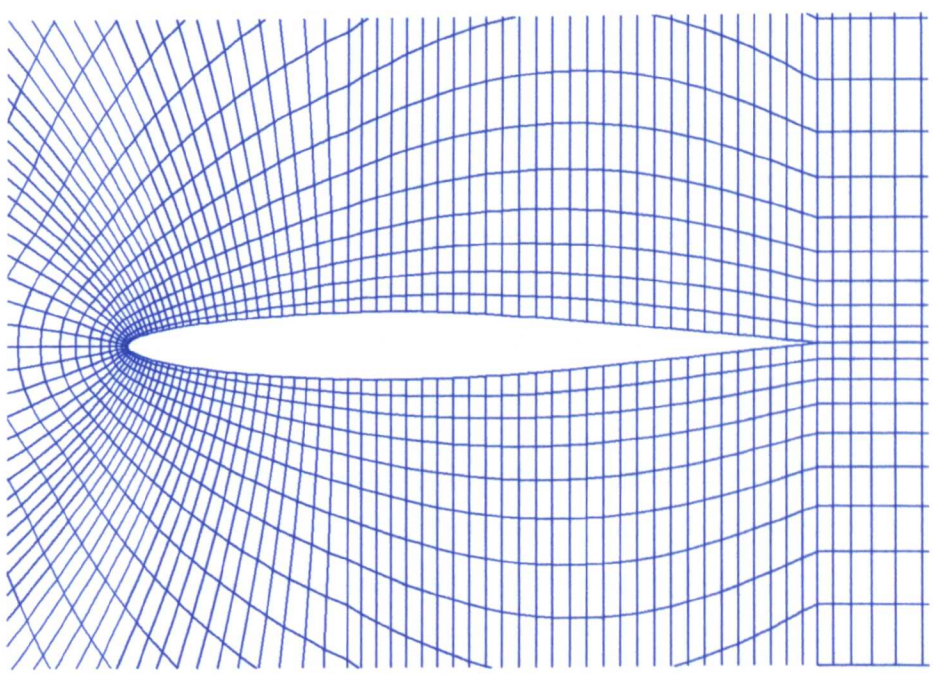

Fig 6.27: Nearfield View of the Finite Volume Grid used for the CFD Solution Procedure

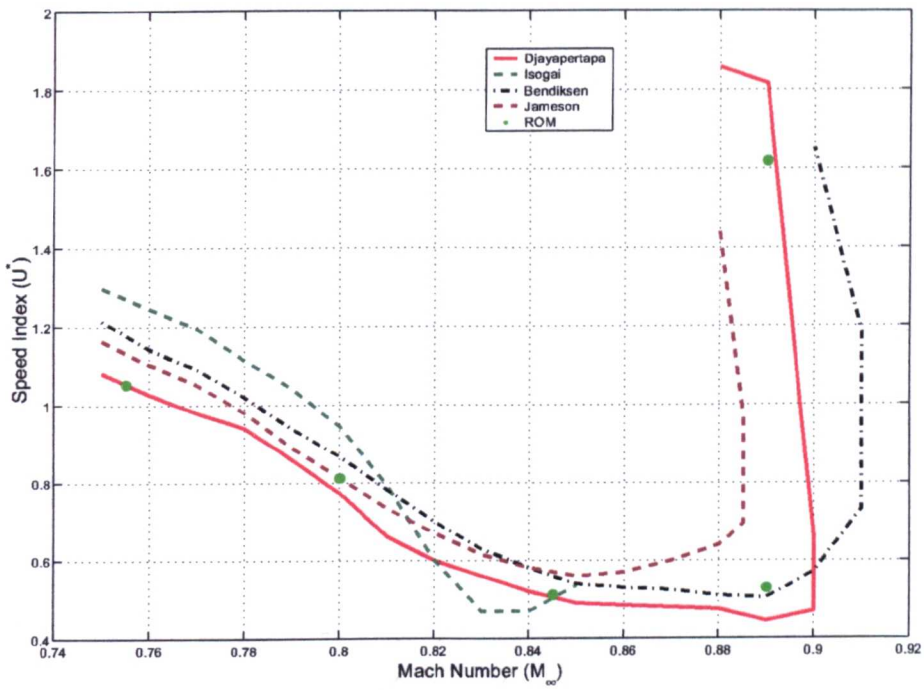

Fig 6.28: Comparison of Flutter Boundaries for a Transonic Two Degree-of-Freedom Aeroelastic System using Different Analysis Techniques

Reduced Order Model (ROM) of 2.3.4 are used to analyse the testcase as the other methodologies described in this work, sections 2.2.2.1 and 2.2.2.2, are limited in applicability to the analysis of low-speed aerodynamic flows and are thus not valid in this case.

6.5.2 Results - Two Degree-of-Freedom

The main criterion for validating the ROM is the correct identification of the flutter boundary. The flutter boundary is defined on a graph of Mach number (M_∞) versus speed index ($U^\star$). The Mach number gives a relationship to the velocity whereas the speed index is related to the magnitude of the wing loading as it is a function of the air density. The flutter boundary for this testcase is presented in figure 6.28 alongside other results generated by Djayapertapa [85], Isogai [104], Alonso and Jameson [105] and Kousen and Bendiksen [106].

The flutter boundary itself denotes a change in system stability from stable, below the boundary, to unstable above the boundary. Such figures are used in industry to calculate the flight envelope of an aircraft with appropriate safety factors being applied.

From figure 6.28 it can be seen that the results from the ROM are within the tolerances of the other codes. In general, all the models show the same trends with the transonic dip before

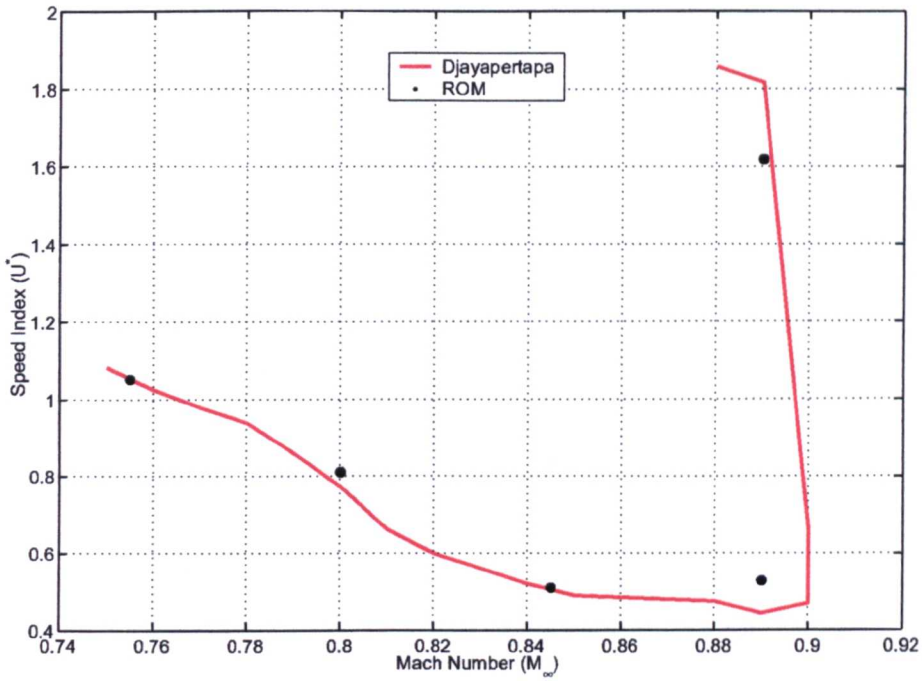

Fig 6.29: Flutter boundary for a Transonic Two Degree-of-Freedom Aeroelastic System

a rapid increase in the speed index on the flutter boundary. For further clarity figure 6.29 shows the results from the ROM and those generated using the full Euler code which are identical to those of Djayapertapa [85]. In this figure it can be seen that the method also predicts the upper limit of the flutter boundary as captured by Djayapertapa. The accuracy to which the ROM correlates to the full Euler code is seen to reduce at higher Mach numbers when compared to the lower Mach numbers. The loss of fidelity is attributed, mainly, to the non-linear aerodynamic characteristics not being captured within the ROM. To overcome the oscillatory problems artificial dissipation was increased to damp out the oscillations but this resulted in a smoothing of pressures throughout the mesh and therefore the shock phenomenon becomes more distributed. However, in general a good correlation is seen and if any errors of concern are observed then a full Euler simulations can be performed.

Figure 6.30 and 6.31 show sample time simulations for $U^\star = 0.86$ and $U^\star = 0.50$ respectively at a Mach number of $M_\infty = 0.8$. Figure 6.30 shows results of a strong and weak coupled simulation (see chapter 2.3.3), a strong coupled linearised simulation (see chapter 2.2.4.2) and the ROM all calculated on the same computational mesh. The strongly coupled full Euler solution is the most accurate simulation and is taken as the baseline solution. The ROM is shown to predict the damping of the system more accurately than the weak coupled simulation but suffers from a difference in the frequency of the solution. During the Eigenvalue Realisation Algorithm (ERA) the eigenvalues of the system are estimated and any errors in the magnitude of these values would result in such a phase shift. This possibility is further supported by

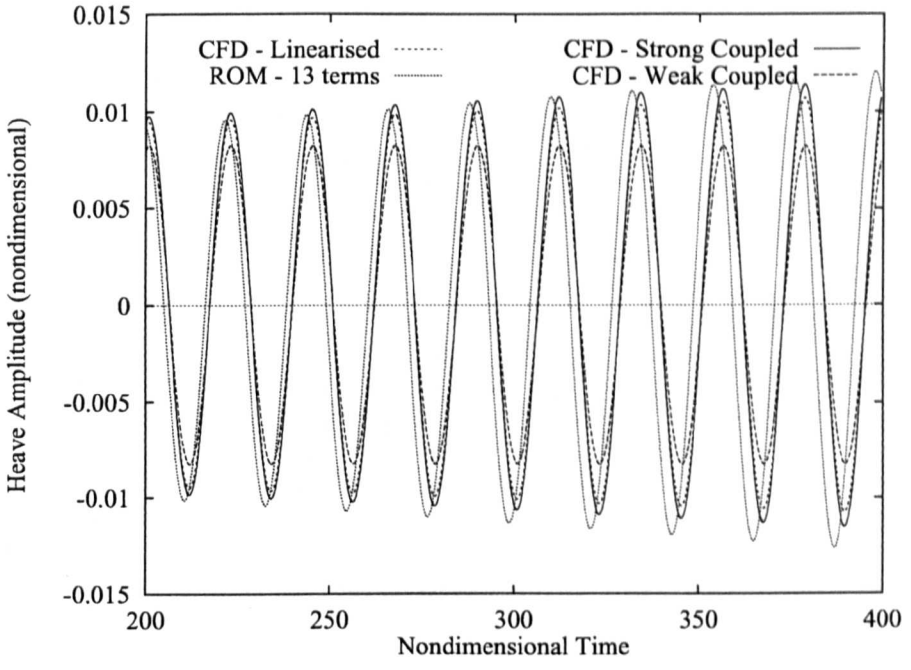

Fig 6.30: Time Simulation Results Comparison at $M_\infty = 0.8$ and $U^\star = 0.86$

the fact the ROM solution is slightly more divergent than the linearised solution which is also symptomatic of discrepancies in the eigenvalues. Additionally, in reducing the model certain modes are not captured therefore some differences in time simulation would be expected. As the eigenvalues are defined by a limited number of points from the impulse responses, they may be identified with an error. Comparative results between the strong coupled and ROM only are shown in figure 6.31, this figure also shows discrepancies in both amplitude and frequency, however these are much smaller. In this case the oscillation is decaying and omitted modes are damped out whereas in the first case they could either be very slowly decaying or even growing so the error is larger.

The chosen model provides useful information due to the elastic centre of the section being located ahead of the leading edge. Such a testcase enables the simulation of highly swept all moving tailplanes where, at a given section, it is possible that the structure could twist about a position ahead of the leading edge. The positioning of the elastic axis means that any small variation in lift on the main surface results in relatively large changes in pitching moment due to the length of the moment arm. As a result any discrepancies in the Euler model or the ROM are accentuated.

The order of the aerodynamic model used for these analyses is small, with the state space matrix (A) being between 10x10 and 13x13 in size depending on the Mach Number. As the structural equations add 2N equations, where N is the number of degrees-of-freedom, the resultant aeroelastic systems are of the order of a 14x14 to 17x17 matrix for the two degree-of-

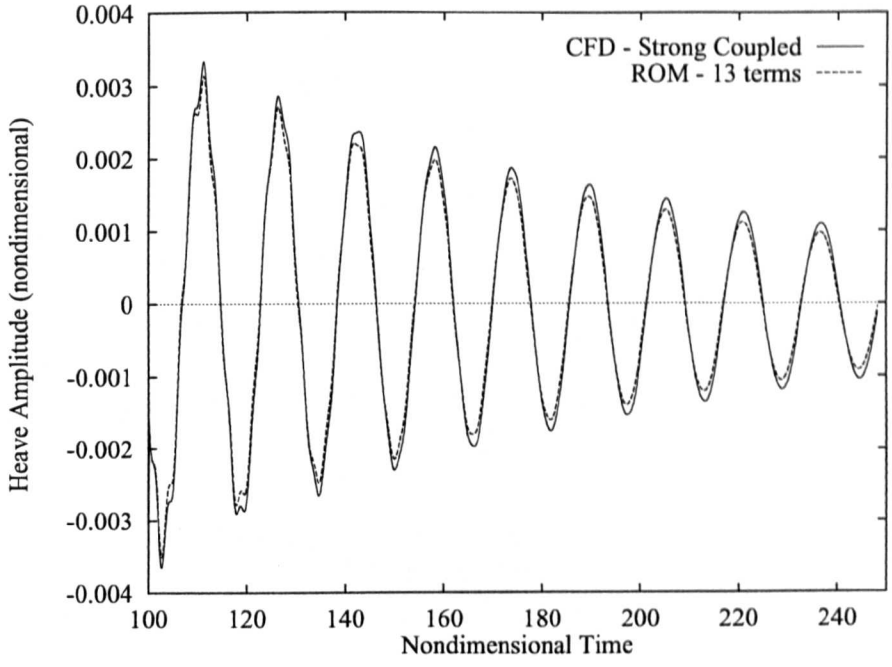

Fig 6.31: Time Simulation Results Comparison at $M_\infty = 0.8$ *and* $U^\star = 0.50$

freedom system. This represents a major reduction in calculation time compared to full Euler solutions and gives the engineer a more useful predictive tool. Additionally, the format of the system allows structural modifications to be made freely as the ROM requires no *a priori* knowledge of the structural model.

6.5.3 Description - Three Degree-of-Freedom

The second testcase taken from Djayapertapa's thesis [85] is a three degree-of-freedom model with the same NACA64A010 aerofoil section as for testcase 3a. The three degree-of-freedom parameters are,

$$\begin{aligned} a_h &= -0.2, \quad x_\alpha = 0.2, \quad r_\alpha = 0.5, \quad \omega_h/\omega_\alpha = 0.3, \quad \mu = 23.48 \\ x_\beta &= 0.008, \quad r_\beta = 0.06, \quad \omega_\beta/\omega_\alpha = 1.5, \quad C_\beta = 0.5 \end{aligned} \tag{6.7}$$

where the flutter velocity is dependent on the Mach Number. The finite volume methods described in section 2.3.3 and the ROM of 2.3.4, are the techniques used to analyse this test case.

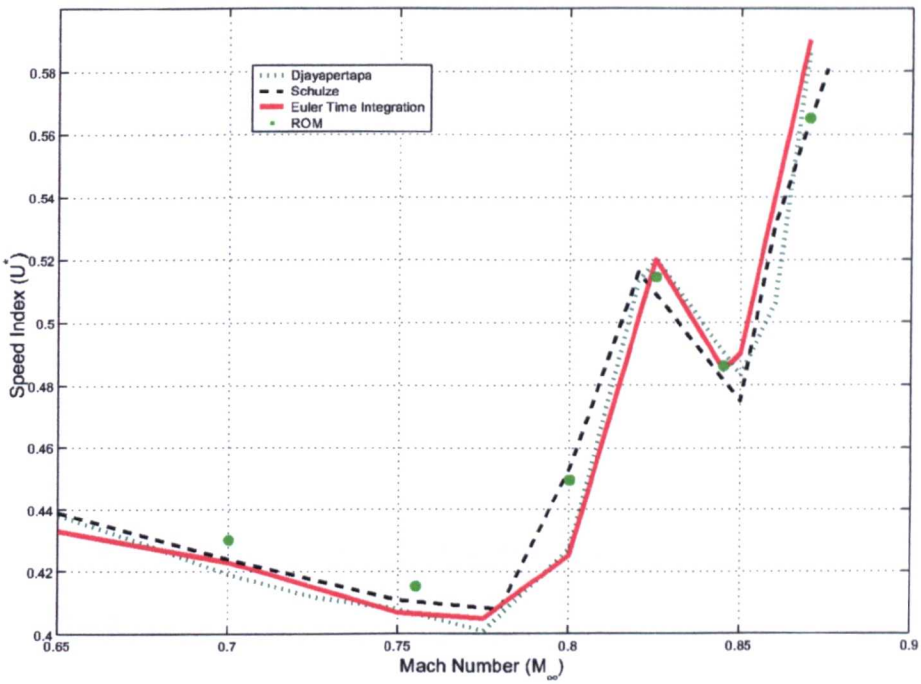

Fig 6.32: Flutter Boundary for a Transonic Three Degree-of-Freedom Aeroelastic System

6.5.4 Results - Three Degree-of-Freedom

The flutter boundary for the three degree-of-freedom aeroelastic model described in the section above is shown in figure 6.32. In the figure results of Schulze [107] and Djayapertapa [85] are presented alongside the results from the ROM and the strong coupled Euler analysis. Similar to the two degree-of-freedom testcase, the results show a good correlation between all four models. The largest differences between models occurs between $M_\infty = 0.8$ and $M_\infty = 0.86$ where the curve gradients are relatively large. The differences are attributed to the shock location being on the flap to main aerofoil interface. The shock moves on and off the flap surface and the prediction of the loads is dependent on the method and grid used. Finer grids and solution adaptive meshes would yield a better resolution of this phenomenon. Although a grid refinement study was outside the scope of this work, the results available demonstrate adequate agreement with other published data. The discrepancy between the ROM and Euler simulations, from which the ROM is derived, suggests that the ROM did not capture all the important system properties. It can be noted that discrepancies in the boundary position of the Euler simulation may be attributed to the time integration runs not being allowed to run for sufficient time to ascertain whether the system is in fact neutrally stable, divergent or convergent. This second effect is thought to be only very minor component of any inaccuracy.

6.6 Testcase 5 - Transonic Analysis with Structural Non-Linearities

In the following sections various forms of non-linearities are analysed and presented for two and three degree-of-freedom transonic aeroelastic models. The parameters for the models are those as presented in sections 6.5.1 and 6.5.3 for the two and three degree-of-freedom sections respectively.

6.6.1 Description - Two degree-of-freedom Aeroelastic Analysis with Non-linearities

The two degree-of-freedom models studied contain non-linearities in the pitch degree-of-freedom. This is equivalent to the actuated freedom within an all-moving tailplane or canard. Only brief results are presented as the more general three degree-of-freedom case to be presented later has been the primary focus of this study.

The non-linearities to be applied to the system are freeplay and hysteresis non-linearities within the pitch degree-of-freedom. The freeplay is defined by the non-linear stiffness $G(\alpha)$

$$G(\alpha) = \begin{cases} \alpha + 0.25^o & \text{for} \quad \alpha < -0.25^o \\ 0 & \text{for} \quad -0.25^o \leq \alpha \leq 0.25^o \\ \alpha - 0.25^o & \text{for} \quad \alpha > 0.25^o \end{cases}$$

and as such is a symmetrical freeplay about the zero pitch position as shown in figure 6.33.

The hysteresis non-linearity is shown in figure 6.34 and is symmetrical about the neutral position. The non-linearity is defined by,

$$G(\alpha) = \begin{cases} \alpha + 0.25 & \text{for } \alpha < -0.125 \text{ and } \dot{\alpha} > 0 \\ \alpha - 0.25 & \text{for } \alpha > 0.125 \text{ and } \dot{\alpha} < 0 \\ 0.125 & \text{for } -0.125 \leq \alpha \leq 0.375 \text{ and } \dot{\alpha} > 0 \\ -0.125 & \text{for } -0.375 \leq \alpha \leq 0.125 \text{ and } \dot{\alpha} < 0 \\ \alpha - 0.25 & \text{for } \alpha > 0.375 \text{ and } \dot{\alpha} > 0 \\ \alpha + 0.25 & \text{for } \alpha < -0.375 \text{ and } \dot{\alpha} < 0 \end{cases} \tag{6.9}$$

Analyses of these testcases are to be performed at $M_\infty = 0.845$ and at a variety of speed indexes.

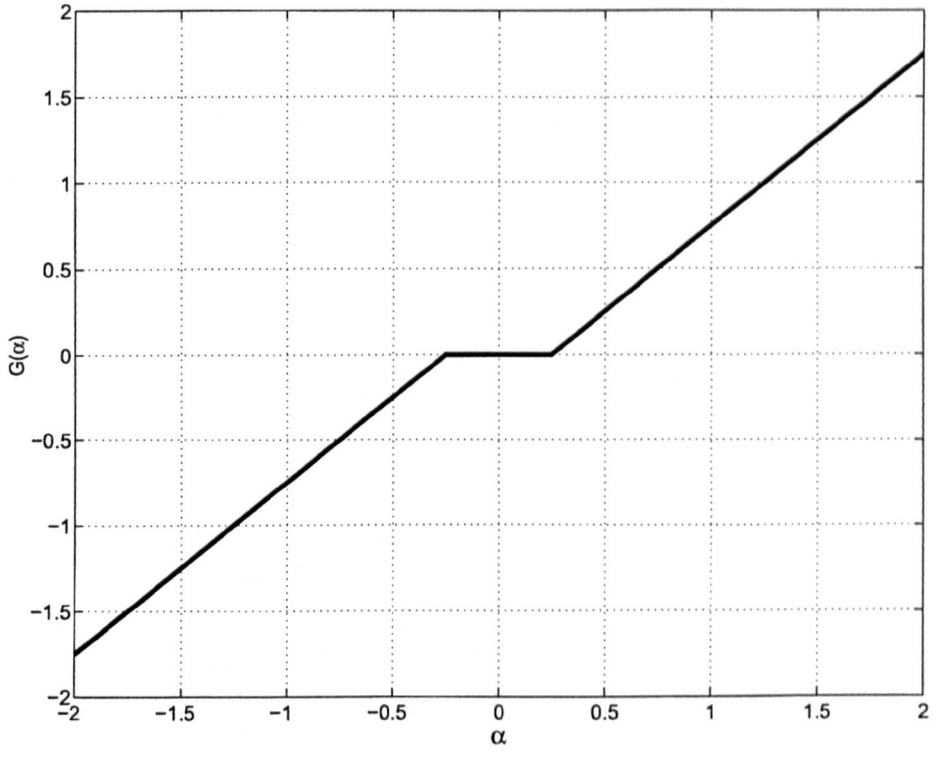

Fig 6.33: Transonic, Two Degree-of-Freedom Testcase Freeplay

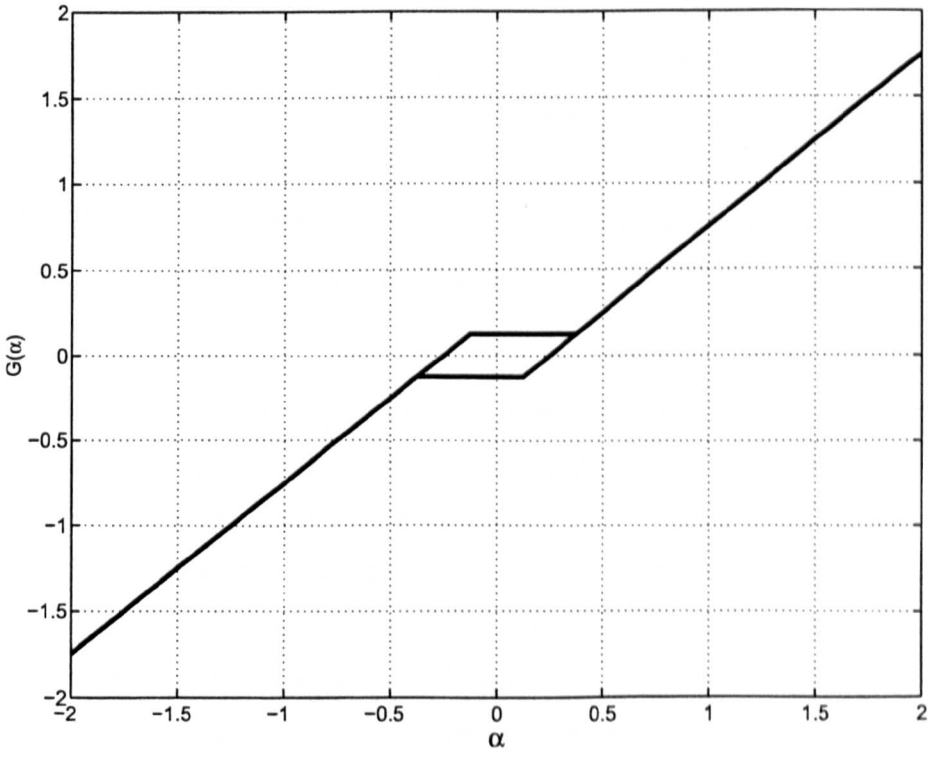

Fig 6.34: Transonic, Two Degree-of-Freedom Testcase Hysteresis

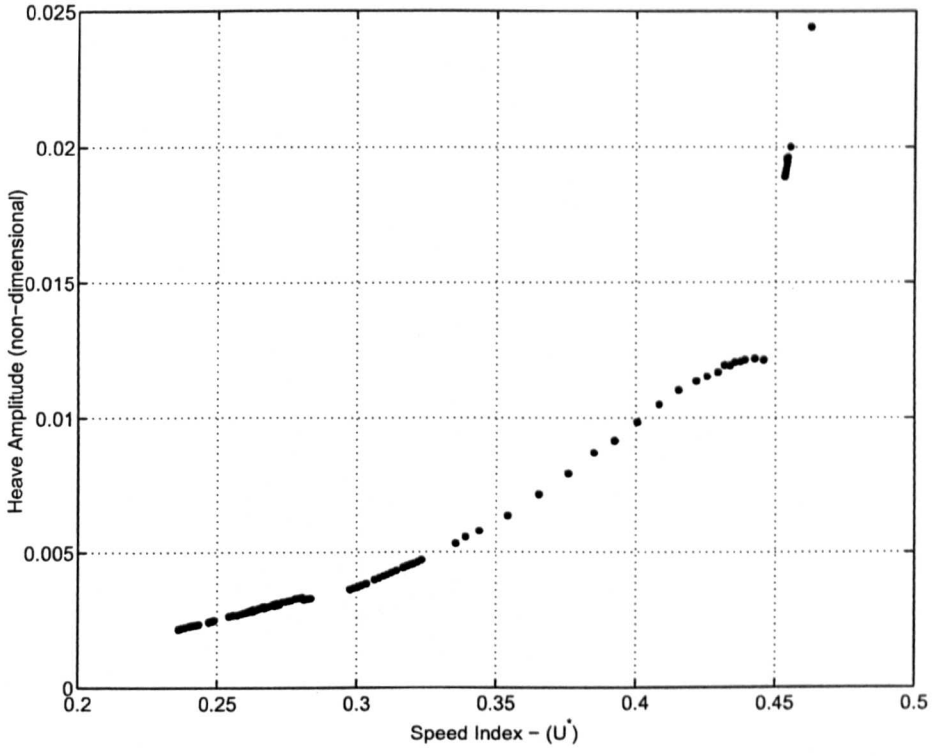

Fig 6.35: Pitch and Plunge Aerofoil Section with a Freeplay Non-linearity, Heave Bifurcation Diagram at $M_\infty = 0.845$

6.6.2 Results - Two degree-of-freedom Aeroelastic Analysis

Figures 6.35 and 6.36 show bifurcation diagrams for the heave and pitch degrees-of-freedom with a freeplay non-linearity at $M_\infty = 0.845$. Some areas show no solutions, at these point the bifurcation solution program, AUTO, could not find solutions for the standard solution sequence. However, it was found to be possible to identify most solutions if small arclength steps were taken. However, using such small steps led to excessive computational times.

From the bifurcation diagram a sample point of $U^\star = 0.236$ is taken and a comparison of the time integration analyses made, this is shown in figure 6.37 for the pitch freedom. The figure shows that the same basic trends as exhibited by the linear system can be observed with slight differences in amplitude and frequency being present. However, the ROM is seen to generate good results with the oscillations being within acceptable tolerances. For the hysteresis non-linearities a sample phase plane diagram was generated at $U^\star = 0.504$ and is shown in figure 6.38. The figure shows the almost exact matching of the continuous approximation to the hysteresis non-linearity when compared to the time simulation. This shows that the continuation technique is generating accurate results for the ROM when compared to time simulations using the ROM. The errors that are shown in the figure are believed to be due to differences between the ROM and the full Euler code. The errors are both in amplitude and frequency difference

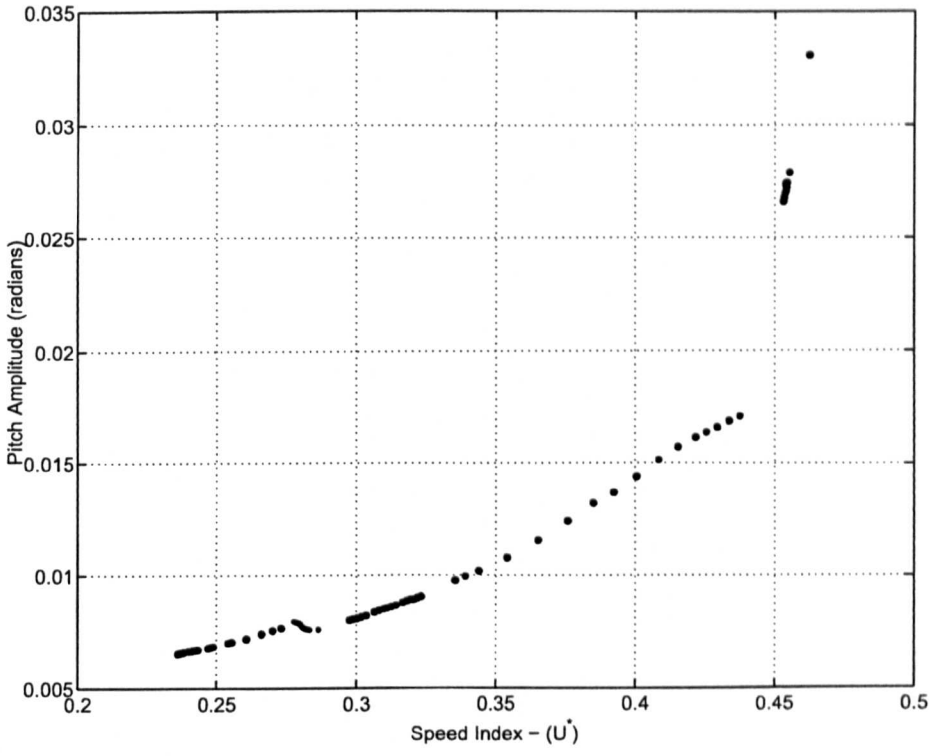

Fig 6.36: Pitch and Plunge Aerofoil Section with a Freeplay Non-linearity, Pitch Bifurcation Diagram at $M_\infty = 0.845$

and are thought to be due to some of the full Euler model modes not being included in the ROM representation.

The bifurcation diagrams for the hysteresis non-linearity are shown in figures 6.39 and 6.40 for the heave and pitch degrees-of-freedoms. As any oscillations that exist must pass entirely around the hysteresis loop the existence of sub-harmonics is not observed. Additionally, the speed index values at which oscillations occur are close to the flutter boundary as it is only at these levels of wing loading that it is energetically possible for the oscillations to be maintained.

From both the freeplay and hysteresis non-linearities it is seen that the ROM and Euler method agree closely with only small differences existing. It is expected that, for the results presented, the discrepancies could be further attributed to the large oscillations that are observed. The oscillations seen were in the region of 6 degrees and, at such levels, the linearisation required to generate the ROM is not applicable as small motion assumptions have been made.

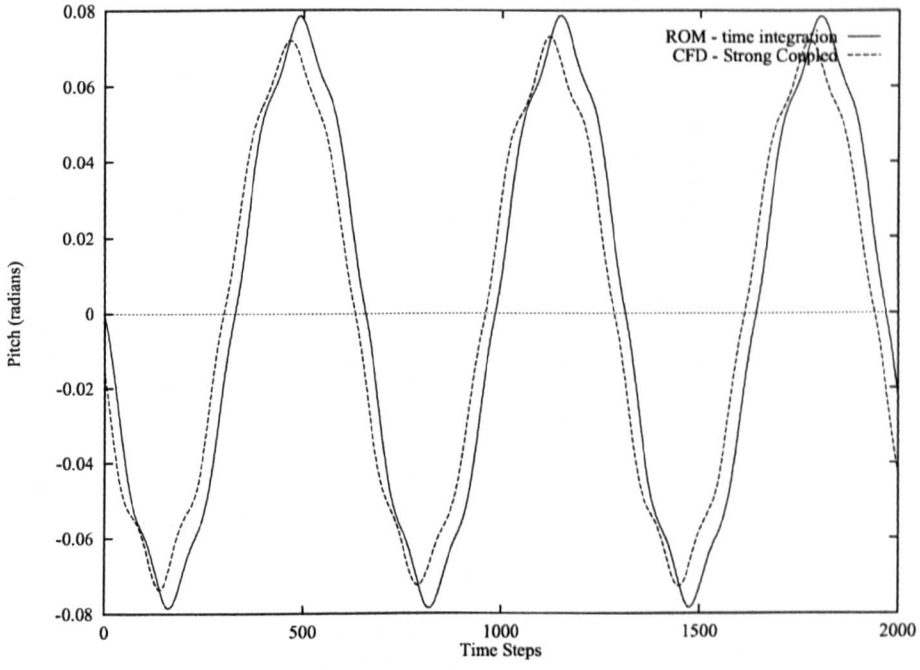

Fig 6.37: Time Evolution of Pitch LCO with a Freeplay Non-Linearity at $M_\infty = 0.845$ *and* $U^\star = 0.236$

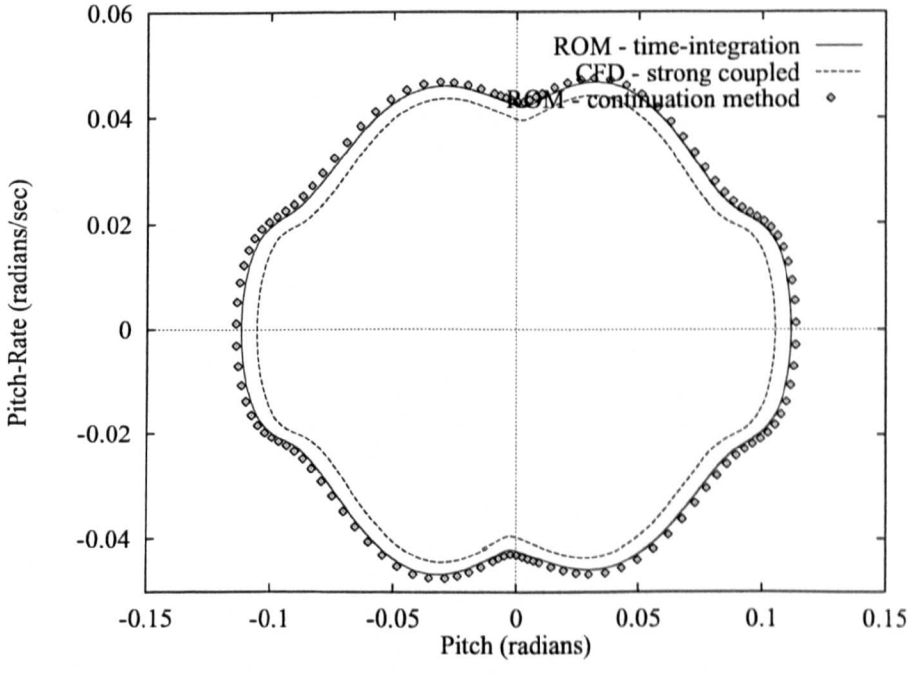

Fig 6.38: Phase Plane of Pitch LCO with Hysteresis Non-Linearity at $M_\infty = 0.845$ *and* $U^\star = 0.504$

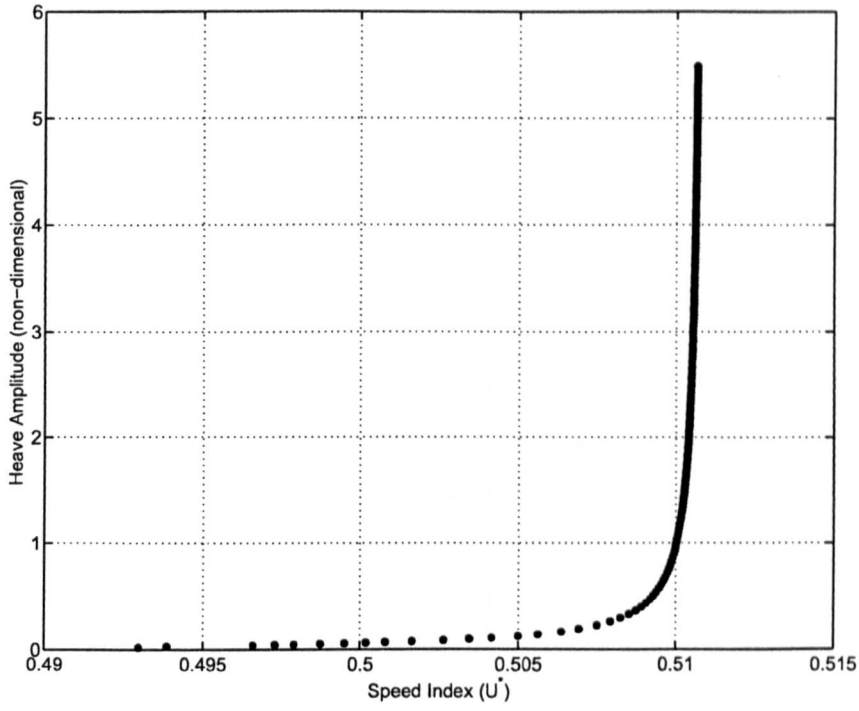

Fig 6.39: Pitch and Plunge Aerofoil Section with Hysteresis Non-linearity, Heave Bifurcation Diagram at $M_\infty = 0.845$

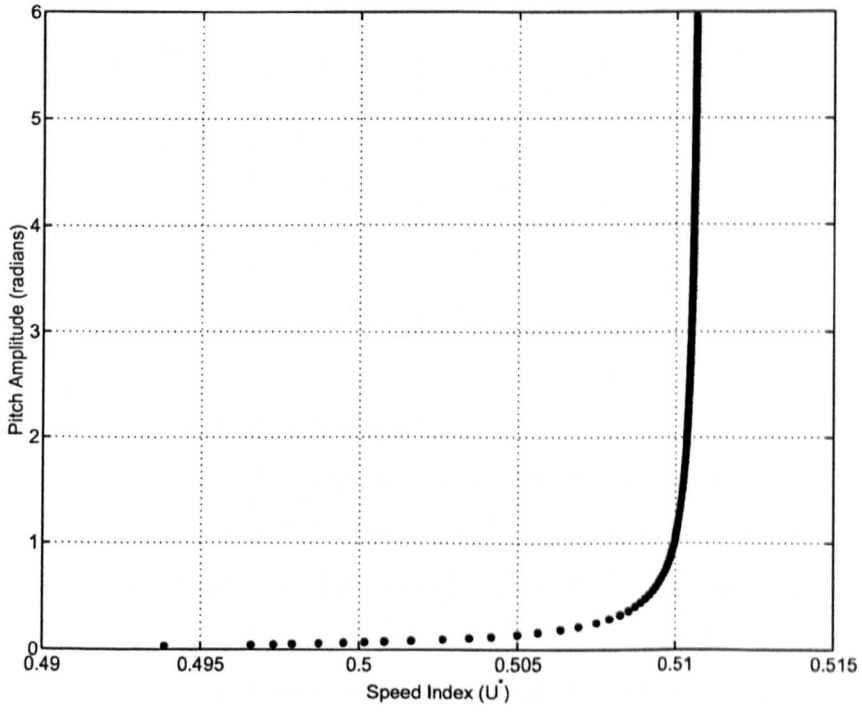

Fig 6.40: Pitch and Plunge Aerofoil Section with Hysteresis Non-Linearity, Pitch Bifurcation Diagram at $M_\infty = 0.845$

6.6.3 Description - Three degree-of-freedom Transonic Aeroelastic Analysis with Non-linearities

Using the three degree-of-freedom aeroelastic model as outlined in section 6.5.3, various forms of structural non-linearities were studied to determine the effects of non-linearities on transonic dynamics. The testcase is primarily performed at $M_\infty = 0.845$ with more general results reported as appropriate.

The first case studied was a freeplay of ± 0.1 degrees in the flap degree-of-freedom. Djayapertapa [85] selected a testcase with a larger non-linearity, ± 1.0 degrees. This testcase was not adopted as it showed few LCOs as the freeplay was too large and therefore the combined aerodynamic and inertial forces where insufficient to maintain oscillations such that the system tended to rest at one of the extremities of the freeplay. A second freeplay testcase of ± 0.25 degrees is also tested in this section for a range of Mach numbers such that an overall LCO map can be generated.

A hysteresis non-linearity is also considered for the three degree-of-freedom testcase with the non-linearity again applied in the flap degree-of-freedom. The non-linearity is shown in figure 6.41 and is described by,

$$N(\beta) = \begin{cases} \beta + 0.5 & \text{for } \beta < -0.25 \text{ and } \dot{\beta} > 0 \\ \beta - 0.5 & \text{for } \beta > 0.25 \text{ and } \dot{\beta} < 0 \\ 0.25 & \text{for } -0.25 \leq \beta \leq 0.75 \text{ and } \dot{\beta} > 0 \\ -0.25 & \text{for } -0.75 \leq \beta \leq 0.25 \text{ and } \dot{\beta} < 0 \\ \beta - 0.5 & \text{for } \beta > 0.75 \text{ and } \dot{\beta} > 0 \\ \beta + 0.5 & \text{for } \beta < -0.75 \text{ and } \dot{\beta} < 0 \end{cases} \tag{6.10}$$

If any oscillations exist wholly within the hysteresis loop it is assumed that the stiffness is the equivalent linear oscillation that intersects the corners of the hysteresis box. Such restrictions also effect the sub-harmonics such that they also cannot exist solely within the hysteresis loop. The method as discussed by Breitbach [31] where the hysteresis loop scales down if the oscillations act completely within the loop is not widely adopted for analyses and, as such, is not considered here. Additionally, these scaling effect would complicate the way in which the non-linearities are represented and requires further in-depth study.

A combined cubic and freeplay non-linearity is also to be studied without preload applied. As no testcases of such a non-linearity have been found in the literature a combination consisting

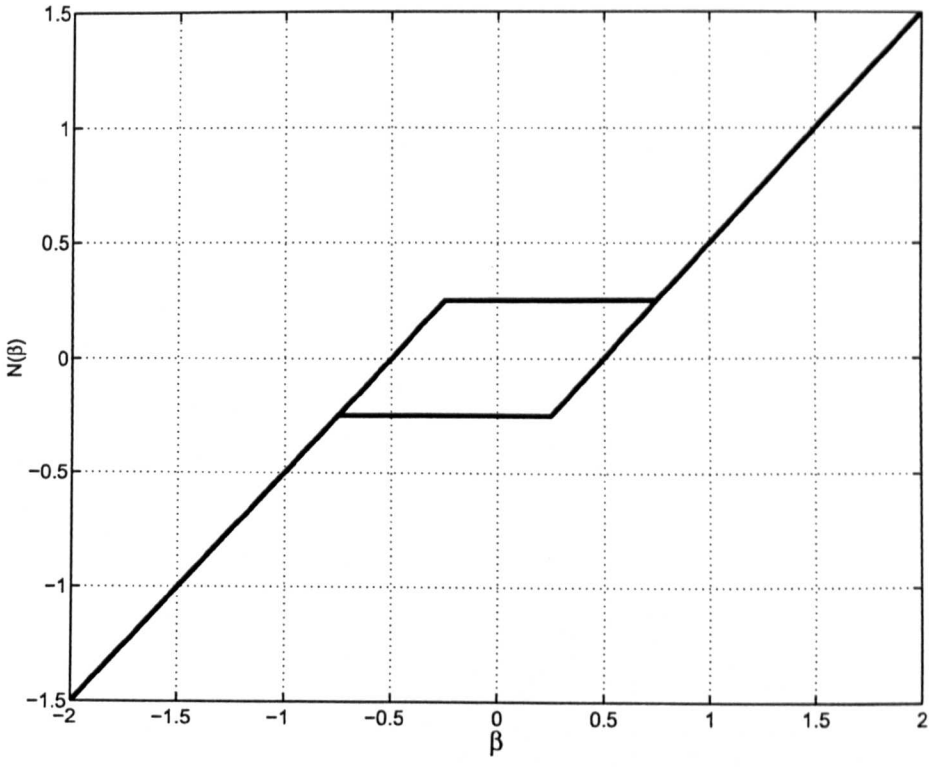

Fig 6.41: Transonic, Three Degree-of-Freedom Testcase Hysteresis

of a freeplay of ± 0.1 degrees is studied with various weightings applied to the cubic term. The cubic non-linearities to be studied are restricted to stiffening types as these are the most common forms found within aircraft structures. It is expected that, due to the incorporation of such non-linearities, both pre- and post-flutter oscillations occur.

An extensive study has been made using the ROM continuation technique to allow rapid generation of bifurcation diagrams. Full Euler studies have been used at various points so as to enable assessment of the validity of the coupled ROM system.

6.6.4 Results - Three degree-of-freedom Aeroelastic Analysis with Non-linearities

6.6.4.1 Results - Three degree-of-freedom Aeroelastic Analysis with a Freeplay Non-linearity

The first non-linear testcase to be studied for the three degree-of-freedom, transonic aeroelastic system is that of a symmetrical freeplay. Figures 6.42 to 6.44 show bifurcation diagrams for heave, pitch and flap rotation for a freeplay of amplitude 0.1 degrees in the flap hinge and at a

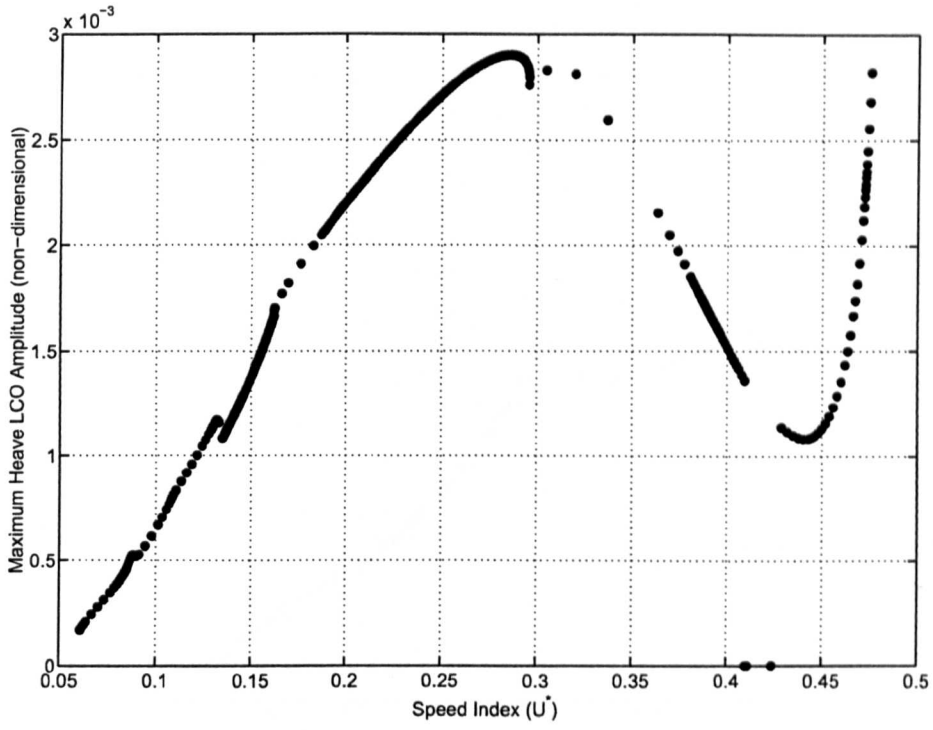

Fig 6.42: Maximum Heave LCO Amplitude for a Three Degree-of-Freedom Aerofoil with a Freeplay Non-Linearity at $M_\infty = 0.845$

freestream Mach number of $M_\infty = 0.845$. The figures were generated using a continuous approximation to the freeplay non-linearity. This approximation shows a much simpler response than observed with the low-speed aerodynamic models and is due to the strong aerodynamic damping effects. The discontinuities observed within the solutions occur due to transition between various periodic forms e.g. p-1 to p-1-h. Figure 6.44 shows, unlike for the low speed testcases, a region near the flutter speed index ($U^\star = 0.485$) where the LCOs disappear before reappearing as the flutter speed is approached. The oscillations disappear when the amplitude of the LCO is equal to or less than the amplitude of the freeplay i.e. 0.1 degrees or 0.001745 radians. As the aerodynamics are linearised, the motions with an amplitude less than the freeplay are within an entirely linear regime and therefore oscillations cannot exist.

Using the boundary identification technique similar, although more complex, results were generated as shown in figure 6.45. As can be seen in the figure, the problems were encountered as the identification of change of stability points did not work causing many spurious branches to be generated. Additionally, generating the bifurcation diagram was found to be computationally expensive with 32 simultaneous equations being solved. As the code utilised - AUTO [50] - is a general bifurcation analysis system it is believed that a specifically optimised code would generate solutions much more quickly, likewise for the continuation of the continuous approximation solutions. Due to the computational penalty imposed by the use of boundary

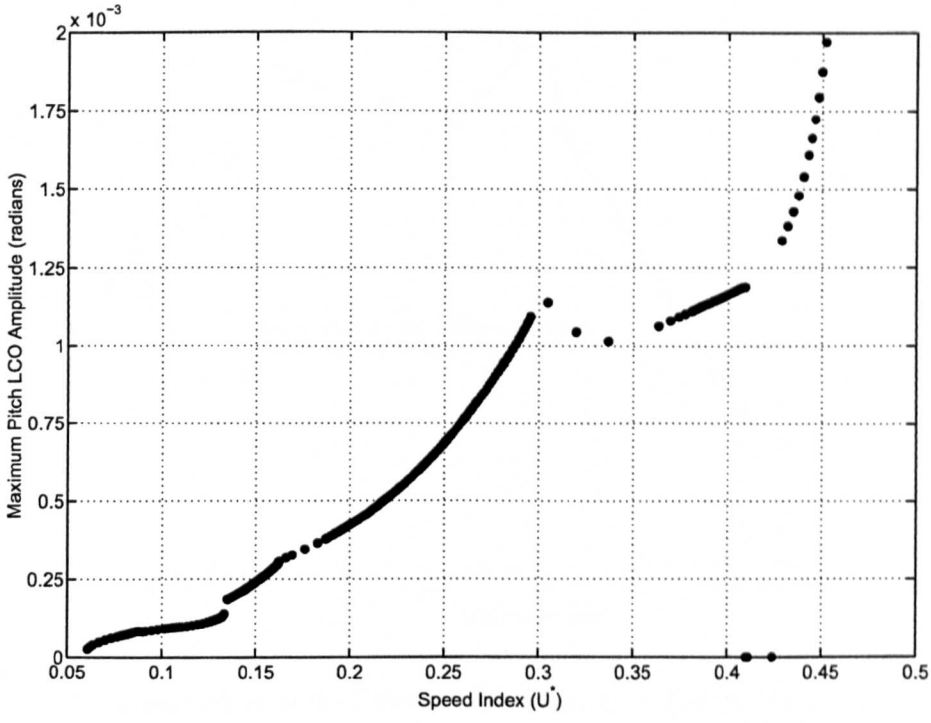

Fig 6.43: Maximum Pitch LCO Amplitude for a Three Degree-of-Freedom Aerofoil with a Freeplay Non-Linearity at $M_\infty = 0.845$

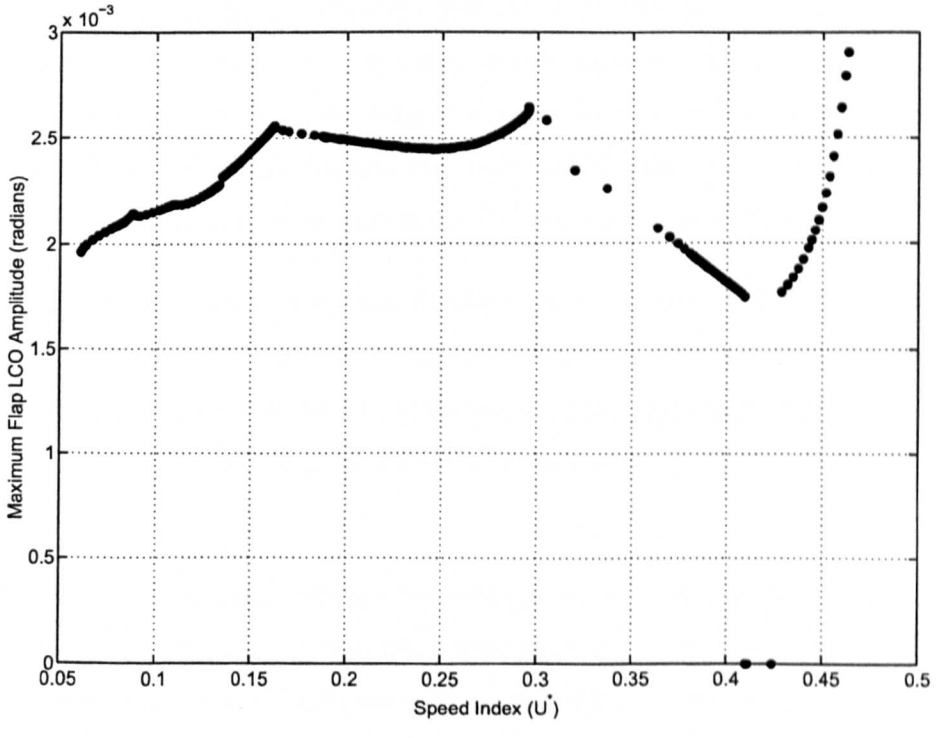

Fig 6.44: Maximum Flap LCO Amplitude for a Three Degree-of-Freedom Aerofoil with a Freeplay Non-Linearity at $M_\infty = 0.845$

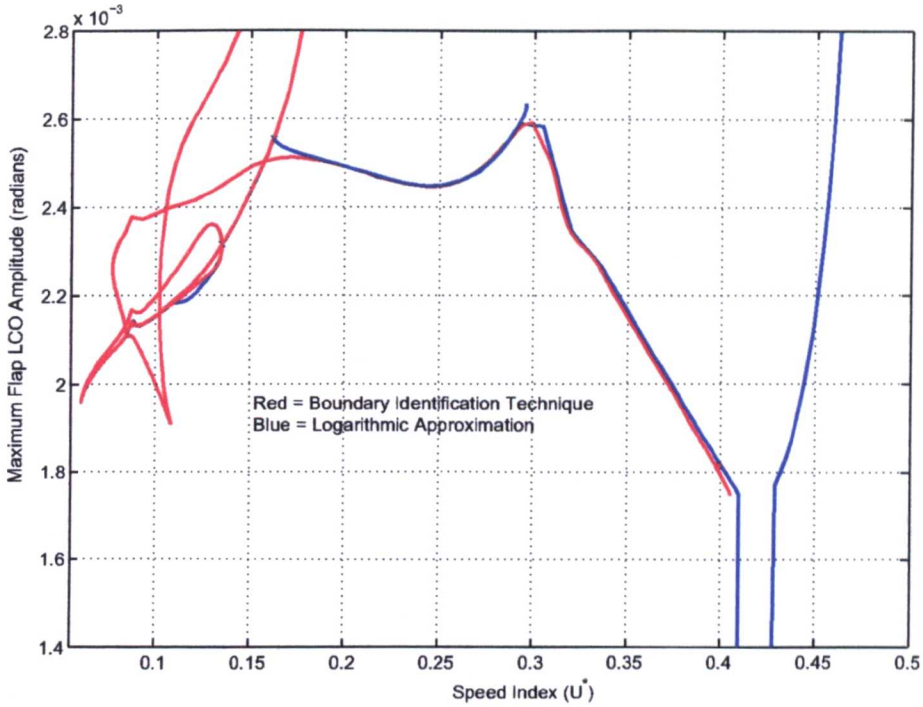

Fig 6.45: A Comparison of the Bifurcation Diagrams Generated by the Boundary Identification Method and the Continuous Approximation, for a Freeplaying System at $M_\infty = 0.845$

identification the remaining results are presented for the continuous approximations only.

As was mentioned earlier, the main freeplay testcase of Djayapertapa [85] used a larger freeplay gap (± 1.0 degrees). With this level of freeplay, oscillations were only observed near the flutter speed index where the combined inertial and aerodynamic forces were sufficient to maintain the motions. This is explained by the gap that is observed for the small freeplay testcase shown in figure 6.44 which would become very large for large amplitude oscillations.

From the bifurcation diagram generated by the continuous approximation technique (figure 6.44) phase plane plots for the flap at various values of speed index were selected. This approached enabled an assessment of the accuracy of the continuation method to be made. Figures 6.46 to 6.50 show phase plane plots for speed indexes 0.176, 0.295, 0.320, 0.396 and 0.450 respectively.

The figures show comparisons between time-integration and continuation solution using the ROM and full Euler solutions. The continuation method is validated as the plots show that for the ROM continuation and ROM time-integration solutions, close correlation is achieved. Differences between ROM and full Euler simulations are observed at high values of speed index. This characteristic seems to be consistent with the errors observed in the two degree-

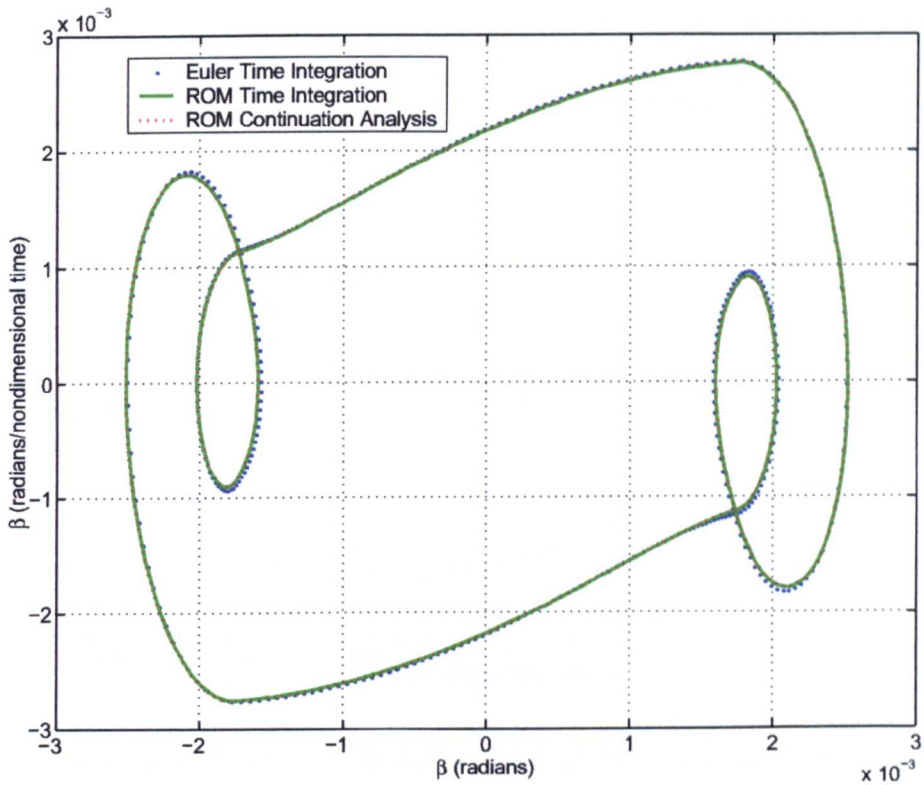

Fig 6.46: Phase Plane Plot for a Flap with a Freeplay Non-linearity at $M_\infty = 0.845$ *and* $U_\star = 0.176$

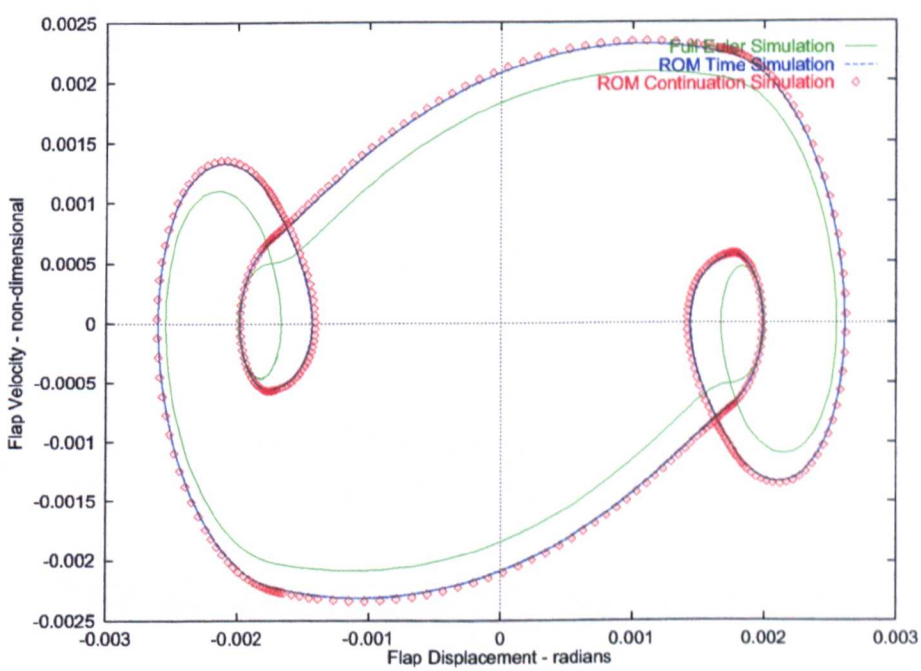

Fig 6.47: Phase Plane Plot for a Flap with a Freeplay Non-linearity at $M_\infty = 0.845$ *and* $U_\star = 0.295$

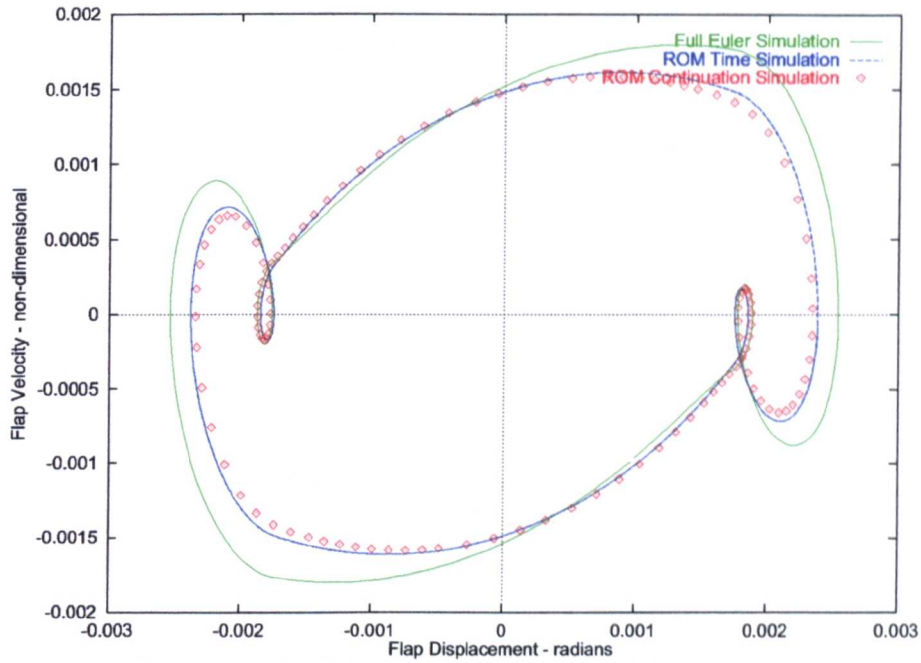

Fig 6.48: Phase Plane Plot for a Flap with a Freeplay Non-linearity at $M_\infty = 0.845$ *and* $U_\star = 0.320$

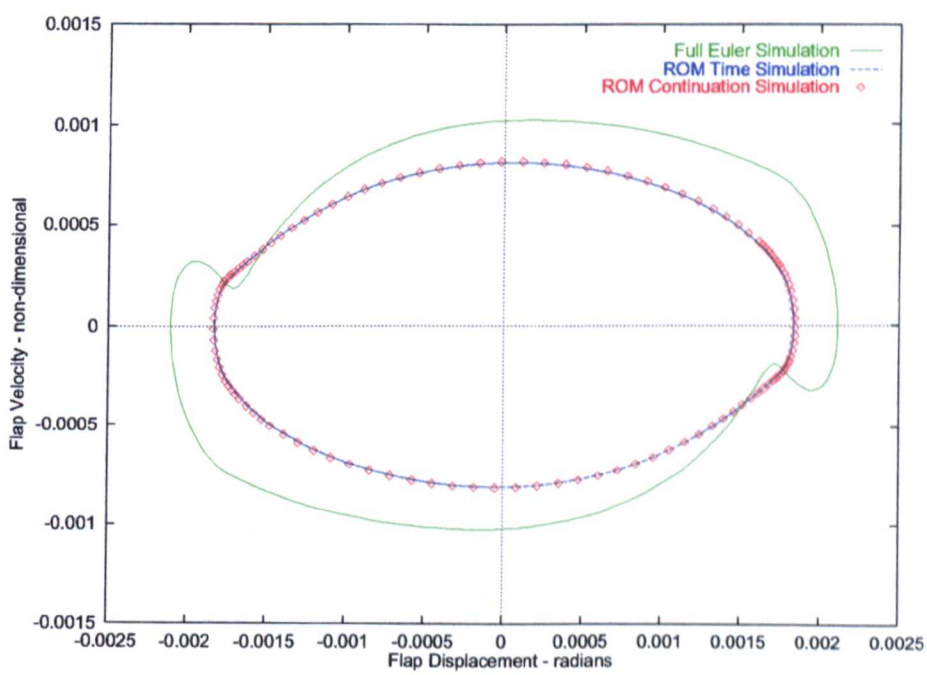

Fig 6.49: Phase Plane Plot for a Flap with a Freeplay Non-linearity at $M_\infty = 0.845$ *and* $U_\star = 0.396$

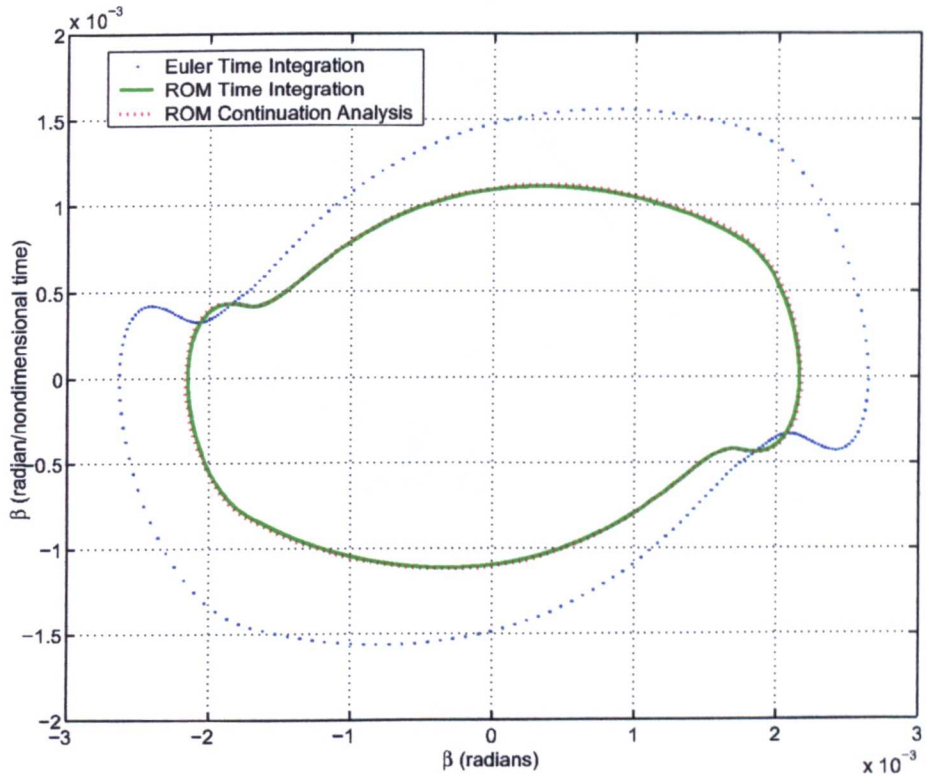

Fig 6.50: Phase Plane Plot for a Flap with a Freeplay Non-linearity at $M_\infty = 0.845$ *and* $U_\star = 0.450$

of-freedom linear and non-linear testcases. The deficiency is attributed to the eigenvalue realisation algorithm that uses a least squares difference method for eigenvalue assessment. Using ERA with an output optimisation algorithm, an improvement in the accuracy with which the eigenvalues can be isolated could be made. This would increase the accuracy of the solutions but the fact that some modes are not included would mean that some differences would always be observed.

From the analyses performed in these studies a better understanding of the boundary identification problem has been found. Conner et al. [44] cited that incorrect identification of switching points resulted in incorrect solutions being achieved. The nature of this inaccuracy is in that the rigid speeds over which LCOs are found become smoothed such that solutions away from the LCO onset have negligible error when comparing coarse approximations to the boundary identification techniques whereas near the boundaries errors occur. Accordingly, the logarithmic approximation to the non-linear problem is seen to be sufficient to generate oscillatory boundaries without the necessity of resorting to the more computationally expensive boundary identification methods.

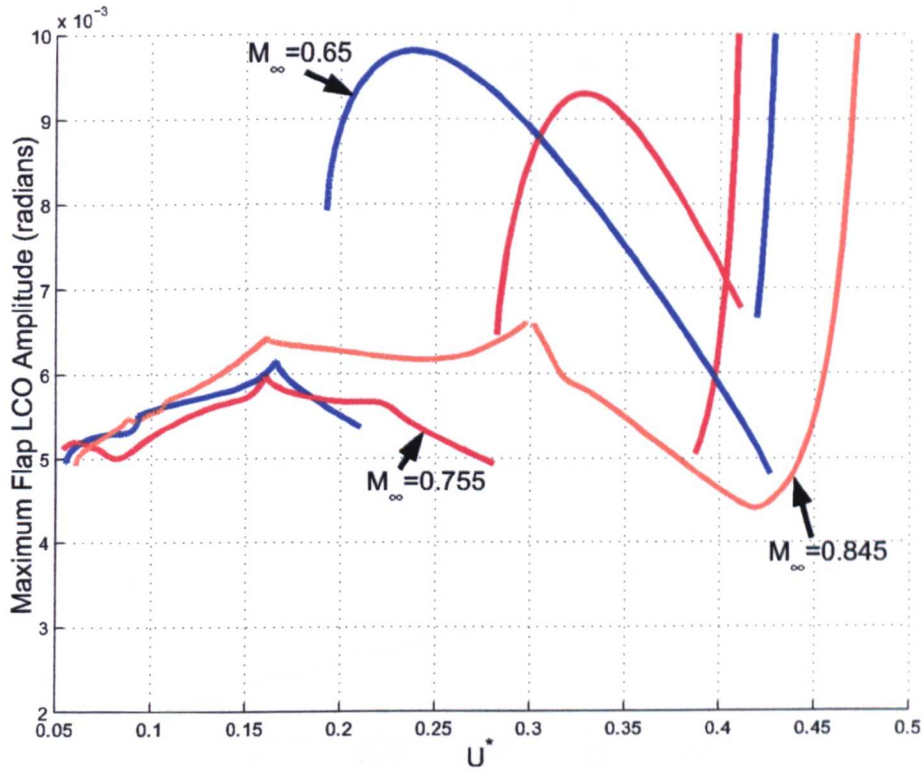

Fig 6.51: Maximum Flap LCO Amplitude for Various Mach Numbers

6.6.4.2 Results - Three degree-of-freedom Aeroelastic Analysis with a Hysteresis Non-linearity

The hysteresis non-linearity in the flap degree-of-freedom defined by equation 6.10 was applied to the transonic testcase. The initial study was performed at $M_\infty = 0.845$. The bifurcation diagram created by such a non-linearity is extremely simple as shown in figure 6.52 for the flap degree-of-freedom. The oscillations observed were simple period one LCOs. The oscillations took this form as sub-harmonics are prevented, since the hysteresis does not take into account the motion if it occurs within the hysteresis loop alone. This factor is explained in the phase plane of figure 6.53, which demarks the boundaries of the freeplay regions for positive and negative velocities. The definition of the hysteresis mandates that, for LCOs to exist, each of the boundaries must be crossed in the correct order shown in the figure, i.e. boundary 1 to 4 consecutively. As sub-harmonic oscillations usually occur over switching point boundaries, it would be impossible to cross the boundaries sequentially i.e. boundary i cannot be crossed twice in a row during an oscillation. As the period amplitude of the oscillation is of the magnitude of the hysteresis it means only super-harmonics could exist.

The situation is further exacerbated by the particular testcase chosen, as the linearly stiff re-

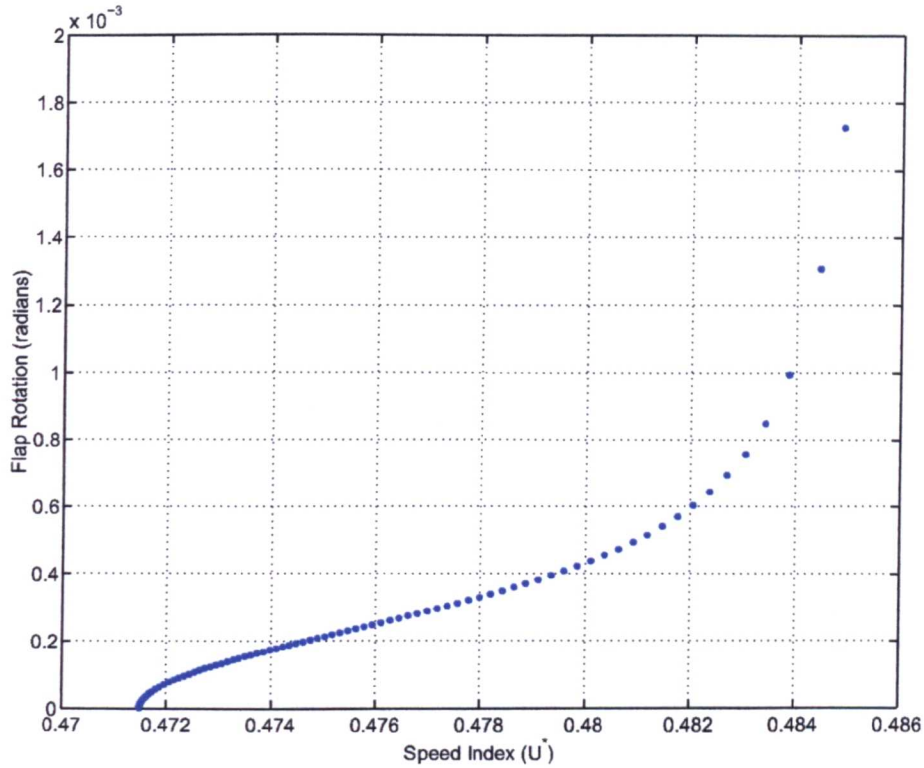

Fig 6.52: Flap Bifurcation Diagram for a Three Degree-of-Freedom Aeroelastic Model with a Hystersis Non-Linearity at $M_\infty = 0.845$

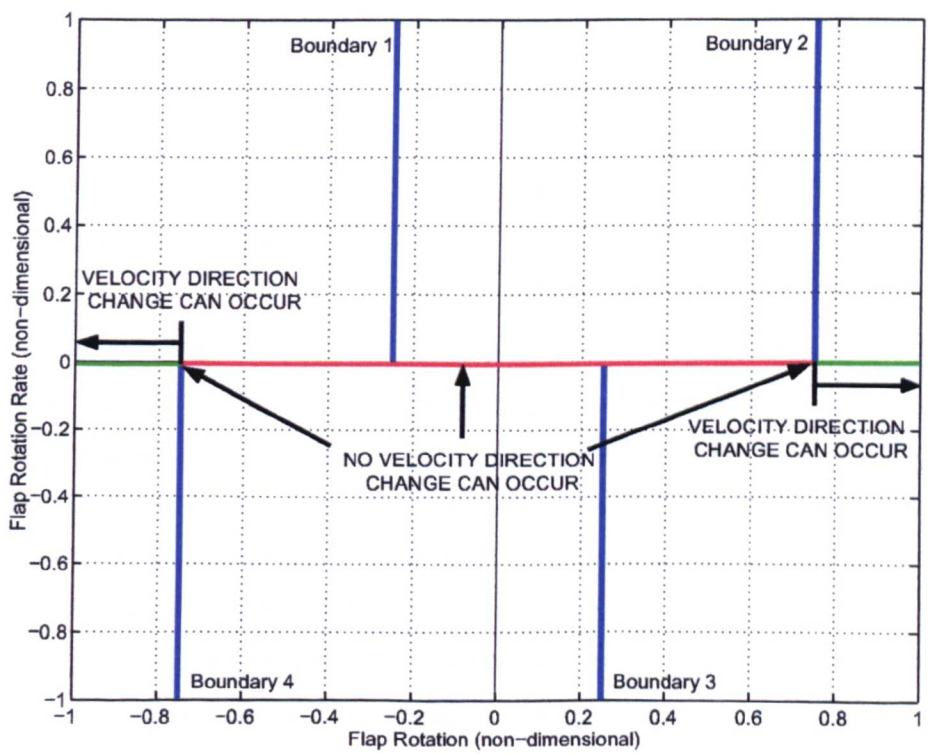

Fig 6.53: Hystersis Boundaries that must be Crossed Sequentially

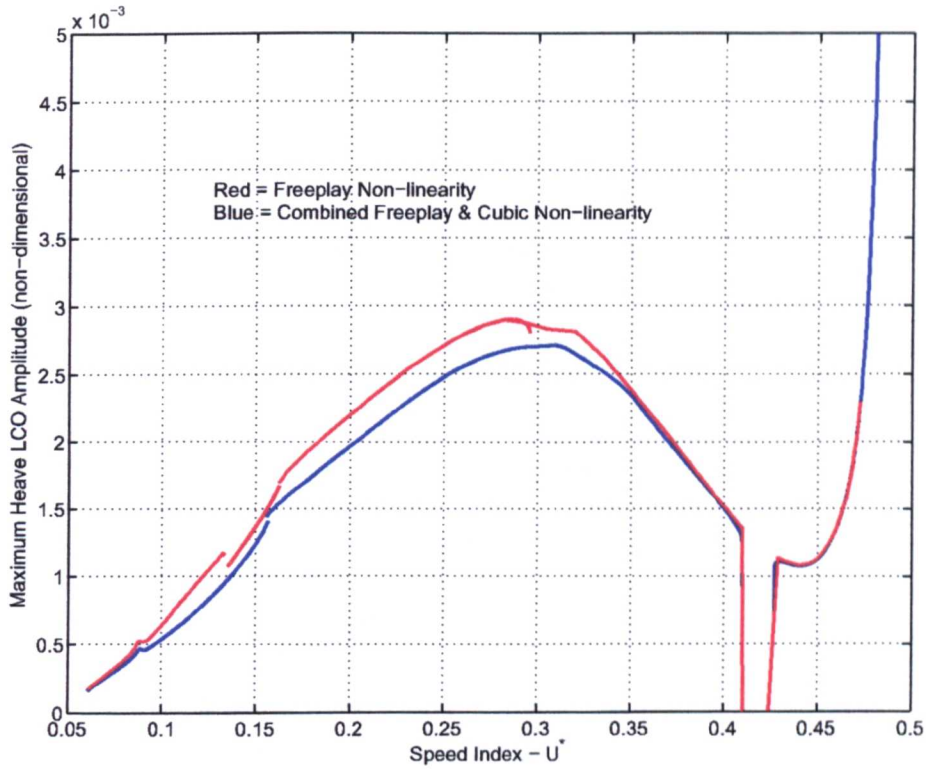

Fig 6.54: Heave LCO Amplitude for a Freeplay and a Combined Freeplay/Cubic Non-Linearity

gions are much stiffer than the freeplay areas. This particular feature was highlighted in figure 6.44 where the penetration of oscillations in to relatively stiffer regions is negligible except close to the flutter boundary.

6.6.4.3 Results - Three degree-of-freedom Aeroelastic Analysis with a Combined Freeplay and Cubic Non-linearity

The combination of a freeplay and cubic non-linearity is thought to demonstrate a more physically realistic implementation of the analytical technique. Figures 6.54 to 6.56 show bifurcation diagrams in heave, pitch and flap rotation for the combined non-linearity at $M_\infty = 0.845$, where the freeplay is ± 0.1 degrees and $\psi_3 = 10^7$. For comparative purposes the basic freeplay bifurcation diagram is also shown in these figures. As can be seen the addition of the cubic stiffening reduces the amplitude of the LCO motion compared to the basic freeplay motion. Additionally, figure 6.57 shows an extension to the flutter velocity when the cubic non-linearity is included. This system therefore shows both pre- and post-linear flutter velocity phenomena.

As with the hysteresis non-linearity the relatively stiff linear stiffness region means that any

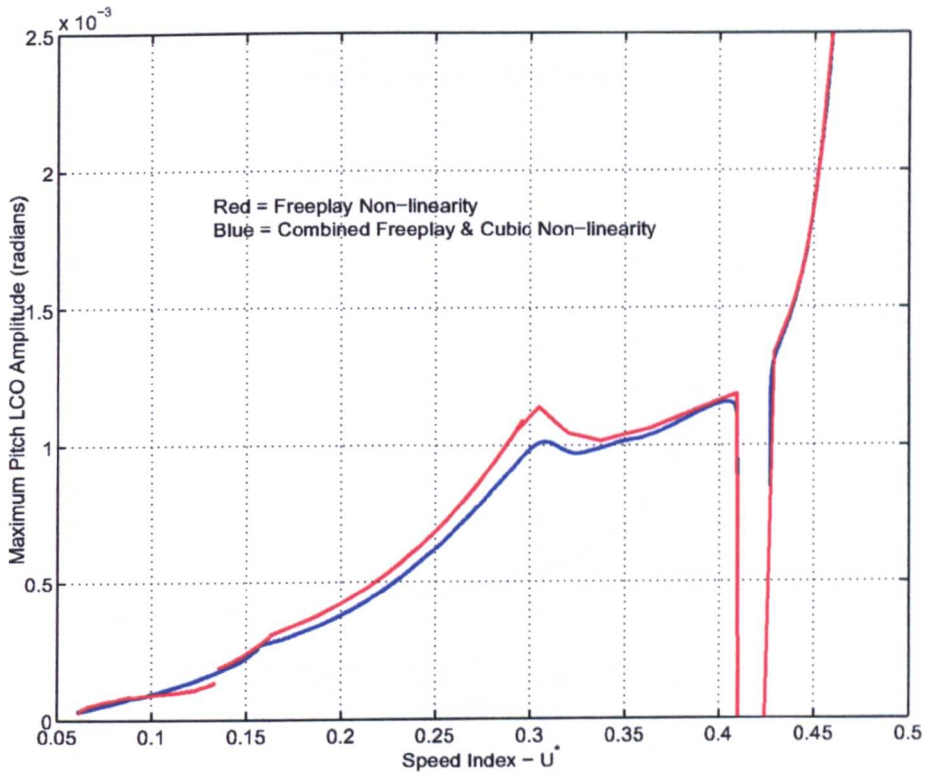

Fig 6.55: Pitch LCO Amplitude for a Freeplay and a Combined Freeplay/Cubic Non-Linearity

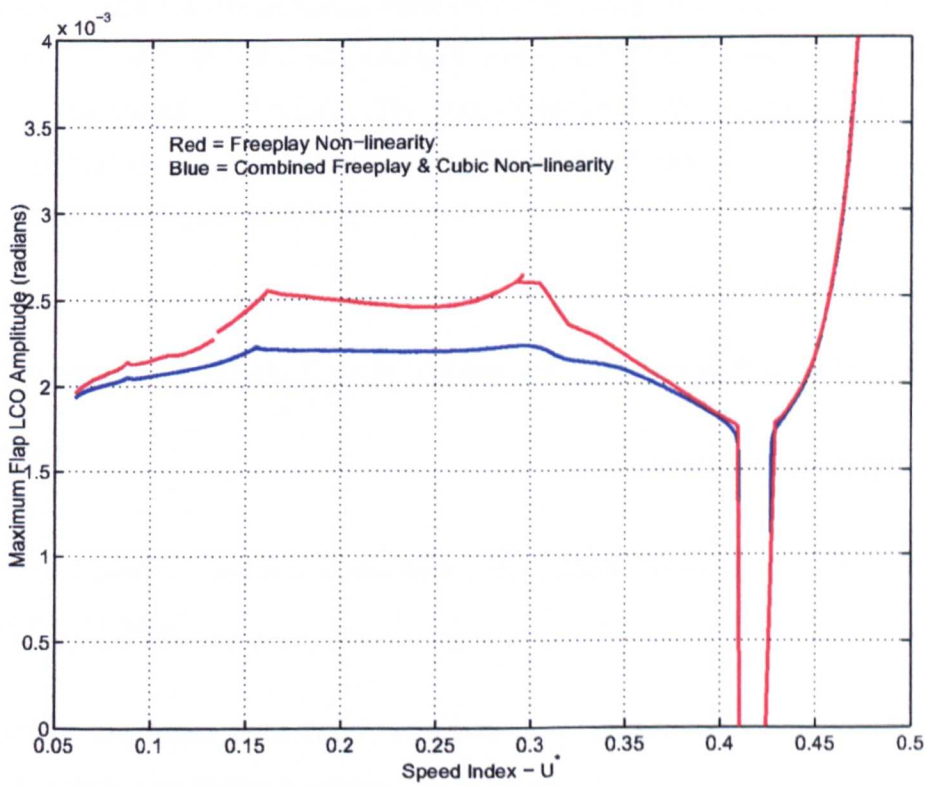

Fig 6.56: Flap LCO Amplitude for a Freeplay and a Combined Freeplay/Cubic Non-Linearity

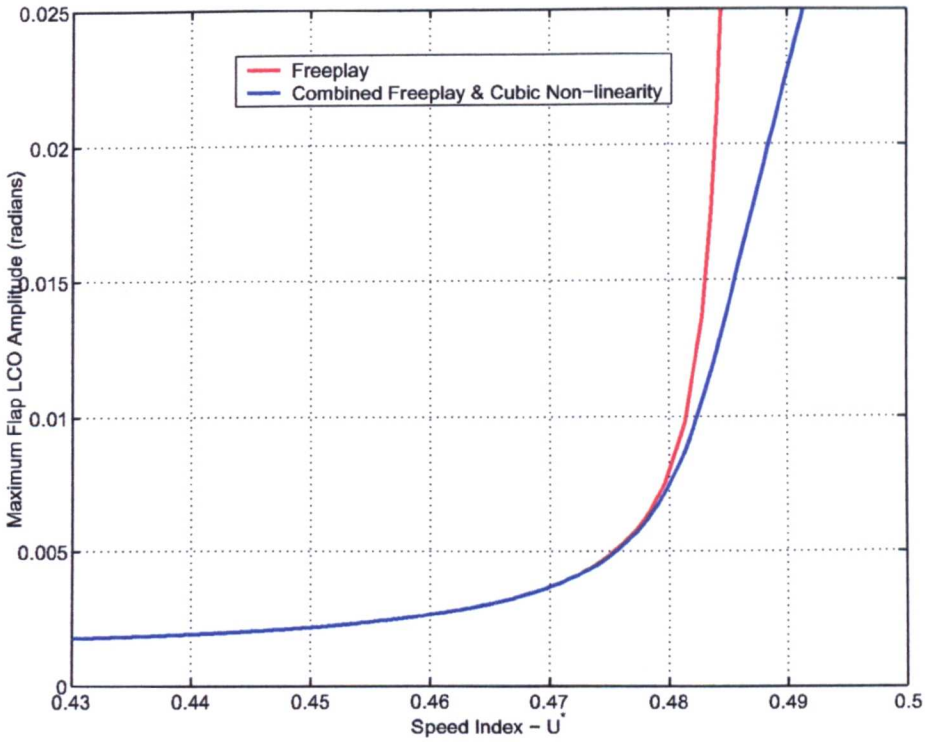

Fig 6.57: Flap LCO Amplitudes Near the Linear Flutter Speed Index for a Freeplay and a Combined Freeplay/Cubic Non-Linearity

major differences are not highlighted until ψ_3 is taken to relatively high values. If ψ_3 is increased the pre- and post-linear flutter phenomena are clearly observable, as shown in figure 6.58 where $\psi_3 = 10^{10}$. With this non-linearity implemented the flap oscillations extend, only slightly, into the linearly stiff region. The flutter boundary extension shown in the figure is much clearer than the previous examples. With such a large stiffness parameter used the stiff region becomes more like a rigid stop.

6.7 Control - Limit-Cycle Attenuation and Flutter Suppression

The implementation of control systems within the context of an aeroelastic system is performed for two reasons:

- control of the linear three degree-of-freedom aeroelastic system as defined in section 6.5.3 such that the flutter boundary can be extended; and
- the control of the same three degree-of-freedom aeroelastic system both below the flut-

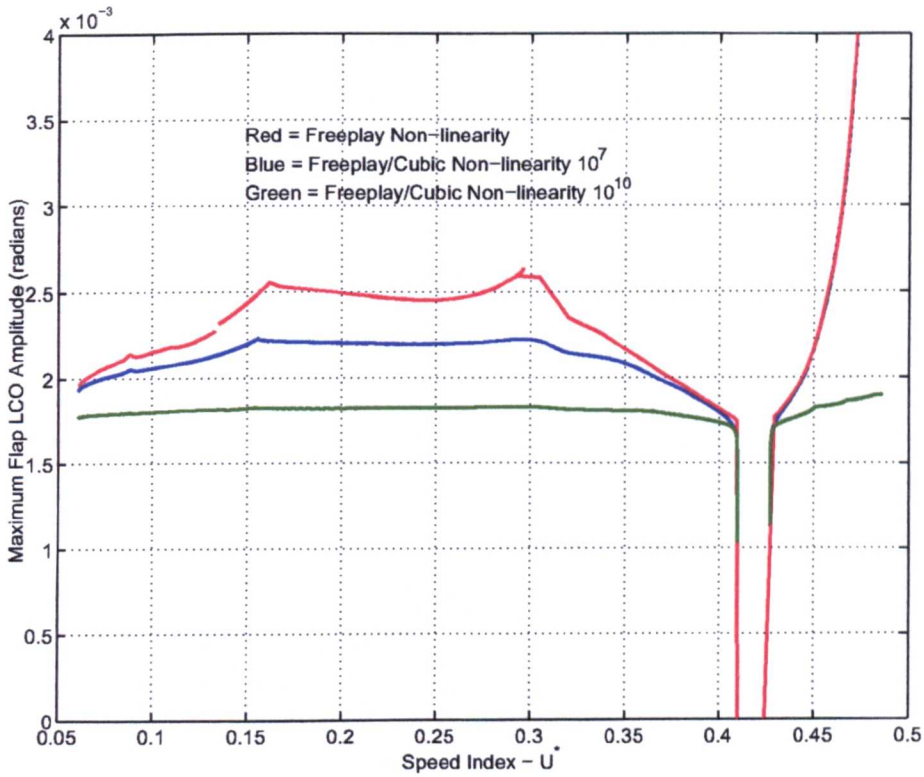

Fig 6.58: Comparison of Combined Freeplay/Cubic Non-Linearities with Various Strengths

ter boundary, where LCOs are encountered, and above the boundary where unsteady oscillations occur.

The aerodynamic model used within the context of this work is the ROM.

As the systems oscillatory frequencies were found to be relatively low in the area of concern the inclusion of full actuator dynamics is not made as its effects would be negligible and would be beyond the central scope of this work.

6.7.1 Fixed Gain Control - Linear Aeroelastics

Fixed gain control was applied to the three degree-of freedom transonic aeroelastic system in order to assess its influence on the linear flutter boundary. The fed back terms were the heave and pitch degrees-of-freedoms and their associated rates. The first control systems implemented are single term feedback control, i.e. pitch or pitch rate etc. Positional feedback i.e. heave or pitch, provided little attenuation to post flutter boundary motion but was seen to provide damping to the divergent motion. Pitch rate feedback, however, successfully attenuated post flutter oscillations and with a gain set to -8.0 the flutter boundary could be successfully extended by up to 1.32 times the linear flutter speed index.

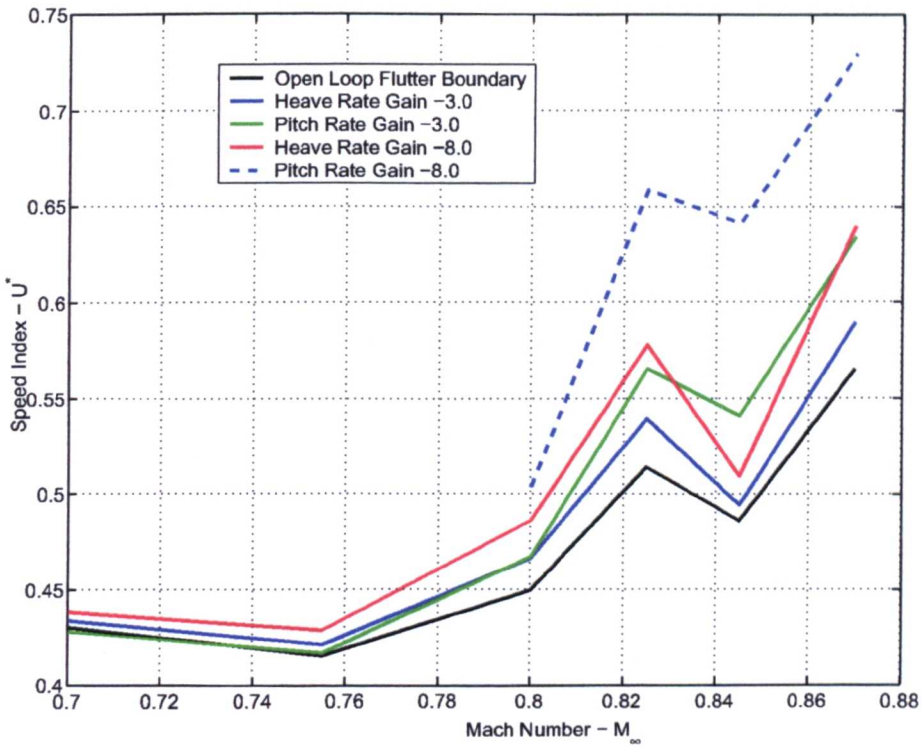

Fig 6.59: Effect of Single Fixed Gain Feedback on the Flutter Boundary

Control systems conventionally rely on the feedback of rates to provide the major damping with positional feedback added if required. Applying heave and pitch rate feedback independently with gains of +3.0 and -8.0 was shown to provide good extension to the flutter boundary particularly above $M_\infty = 0.8$. The results of the implementation are shown in figure 6.59 along with the open loop flutter boundary. In the figure pitch rate feed back of -8.0 is only shown down to $M_\infty = 0.8$ because below this level the feedback causes self induced oscillations far below the flutter boundary. Additionally, many of the systems exhibited unstable zones at very low values of speed index. This is due to the density at low speed indexes not allowing the generation of sufficient forces to counter displacement.

The use of multiple feedback systems were then analysed with the aim of extending the flutter boundary even further beyond its current limits. As rate feedback was seen to be the most effective form of suppression, combined pitch rate and heave rate control was then implemented. Such a system was chosen by Djayapertapa [85] as it successfully extended the flutter boundary by up to 20% over a large range of Mach numbers. The system implemented by Djayapertapa set both of the rate gains to -3.0. The flutter boundary provided by such a system is shown in figure 6.60. The feedback of combined heave and pitch proved to be less effective than the combined rate feedback with motions taking much longer to decay. Various combinations of gains were also applied with good extension of the flutter boundary being possible

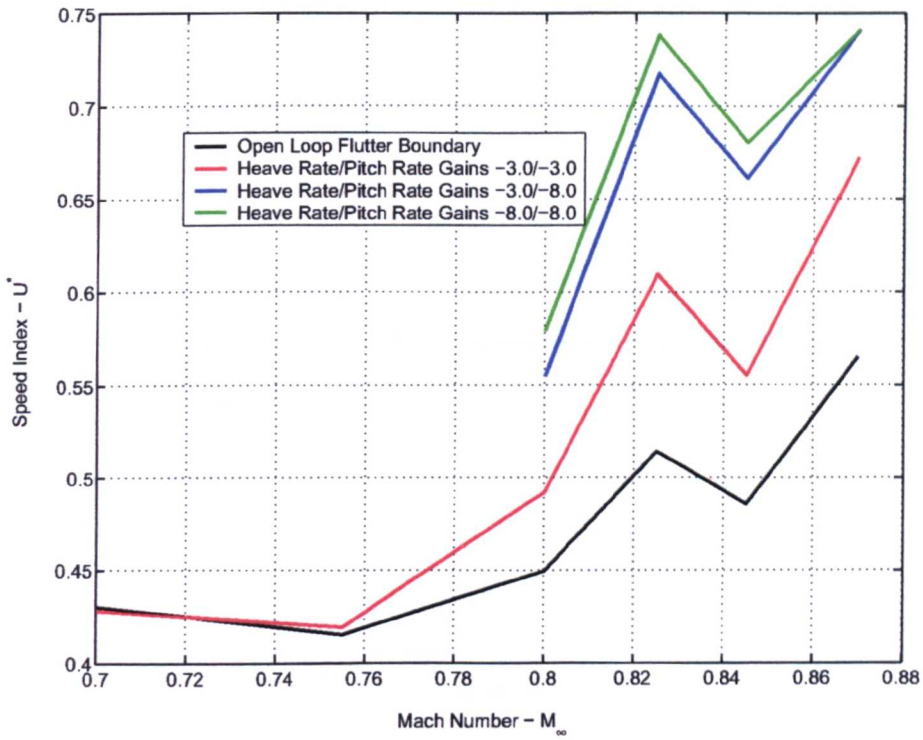

Fig 6.60: Effect of Combined Fixed Gain Feedback on the Flutter Boundary

of up to 44%.

As with single rate feed back, the inclusion of a pitch rate feedback of -8.0 caused instabilities far below the linear flutter speed index. The system described by Djayapertapa [85] was found to be one of the best, providing some extension to the flutter boundary at high Mach numbers without pre flutter instabilities being excessive. However, the system did show instabilities at very low speed indexes for the reasons described previously. The results from both the single and multiple rate feedbacks both showed little extension to the flutter velocities below Mach 0.8 without excessive penalties at higher Mach numbers.

Further analysis showed that the inclusion of pitch and pitch-rate feedback at speeds below Mach 0.8 was the cause of many of the oscillations below the actual flutter boundary. Pitch-rate was seen to be the most susceptible with very large areas of instability being encountered. Figure 6.61 shows an example of the instabilities that exist prior to flutter with the pitch and pitch-rate terms fed back.

The analysis of such fixed gain control systems proved to be somewhat arbitrary as the large number of control gains that could be varied prohibited a thorough analysis and control system optimisation. However, single state feedback optimisation was possible by selecting a desired flight speed index level and using continuation to vary the gains until stability is found, a

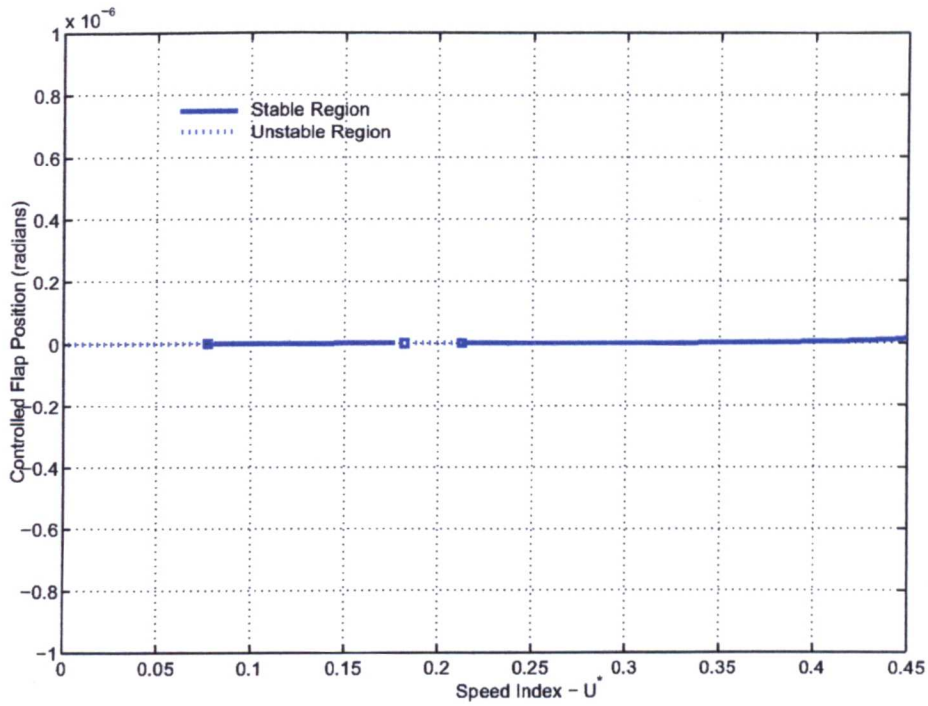

Fig 6.61: Regions of Stability for a Closed Loop Three Degree-of-Freedom System

similar technique was used to vary gains of multiple state feedback control systems. The variation of the gains required for different Mach numbers is also seen as a problem as set gains cannot be used, instead, some form of Mach number gain scheduling was seen to be required. To solve all these problems by simple selection of various gains is highly impractical and therefore alternative means of generating the gains were used, as described in the following sections.

6.7.2 MCS Adaptive Control - Linear Aeroelastics

The Minimal Control Synthesis (MCS) algorithm was applied to the flutter boundary extension problem. The technique automatically varies the gains in order to attain improved system performance. As the system is constantly changing the application within continuation software is not possible since the gain would never reach a steady state condition and, additionally, the system requires historical data which cannot be simply implemented under a state-space formulation. The analyses presented were performed at $M_\infty = 0.845$ only.

The MCS algorithm was first implemented at $U^\star = 0.54$ which corresponds to 1.1 times the linear flutter speed index. The algorithm was initially applied to the pitch rate and heave rate as, as mentioned in earlier sections, these factors usually provide the best attenuation. Figure 6.62 shows the adaptation of the gains for the system. As can be seen in the figure, the gains

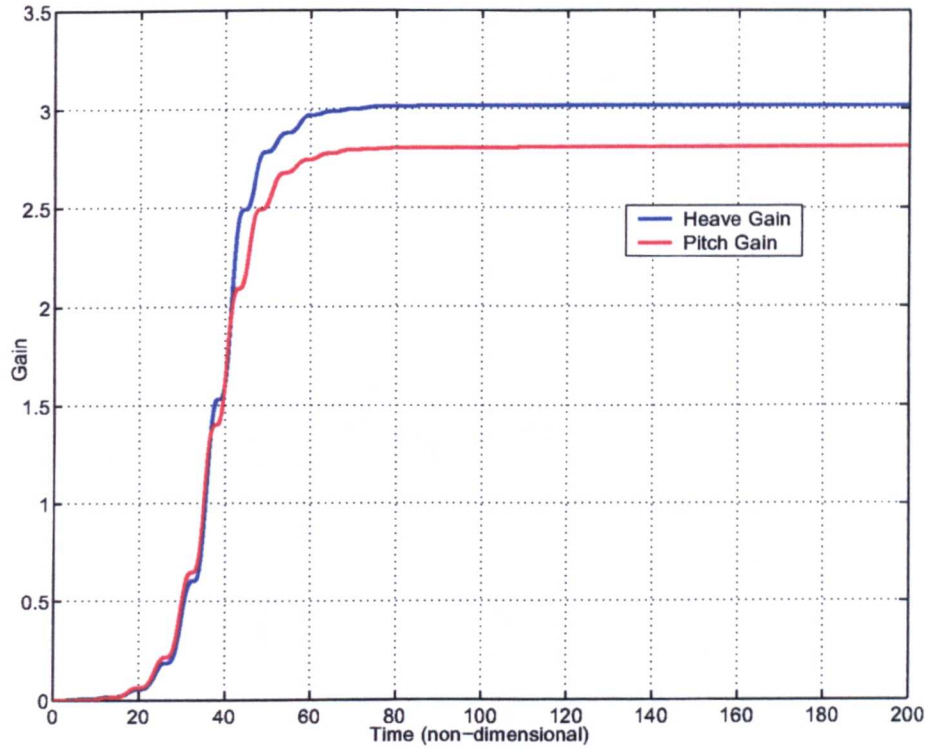

Fig 6.62: Gain Adaptation for a Three Degree-of-Freedom Aerofoil Control at 1.1 Times the Linear Flutter Speed Index at $M_\infty = 0.845$

quickly adapt and settle down at a steady state value.

The corresponding system response to the gain adaptation is shown in figure 6.63. In this figure the oscillations are seen to initially build up until the gains reach a value sufficient to damp out the motions.

The MCS algorithm was then applied to the system at 1.2 times the linear flutter speed index. For this case MCS was incapable of suppressing the oscillations as the speed of adaptation of the gains was very sensitive to the α_{MCS} parameter described in section 5.3.3. However, if an initial estimate of the gains is added at time zero, the system was capable of adapting and controlling the motions. The corresponding gains and structural motions are shown in figures 6.64 and 6.65 respectively.

For both the cases shown, the gains are seen to settle to a stable finite level. As the system is linear and contains no noise once the system has reached a steady state there is no requirement for the gains to increase. For realistic systems noise and turbulence would cause the system to keep adapting, increasing the gains constantly. This characteristic is unacceptable, as the control system would eventually saturate. Implementation would therefore require the gains being allowed to adapt and then, after a specified time, be fixed such that gain wind-up does

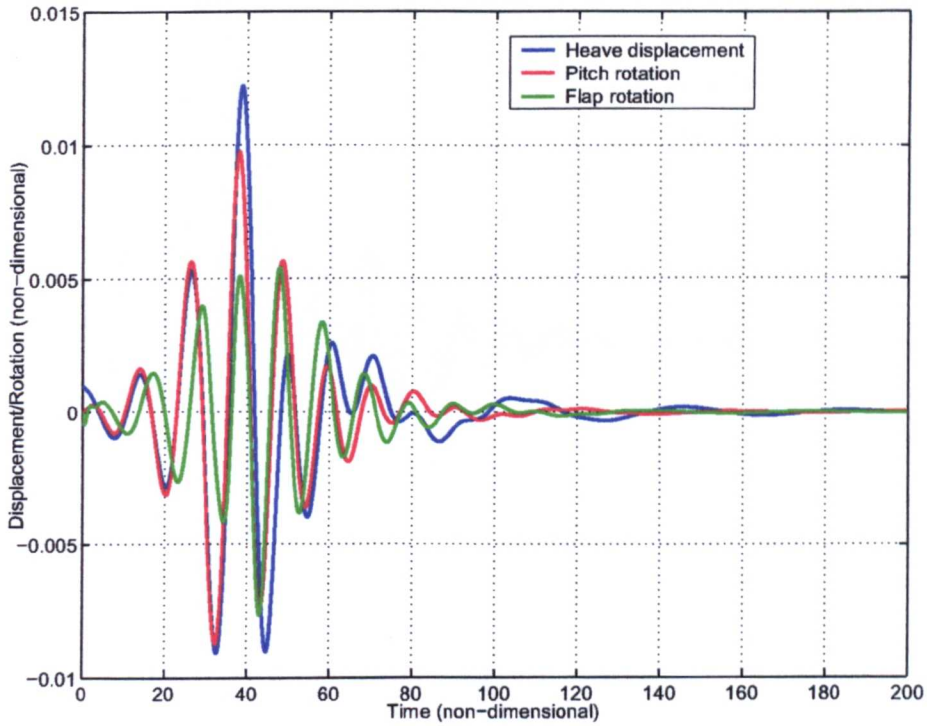

Fig 6.63: System Dynamics for a Three Degree-of-Freedom Aerofoil Control at 1.1 Times the Linear Flutter Speed Index at $M_\infty = 0.845$

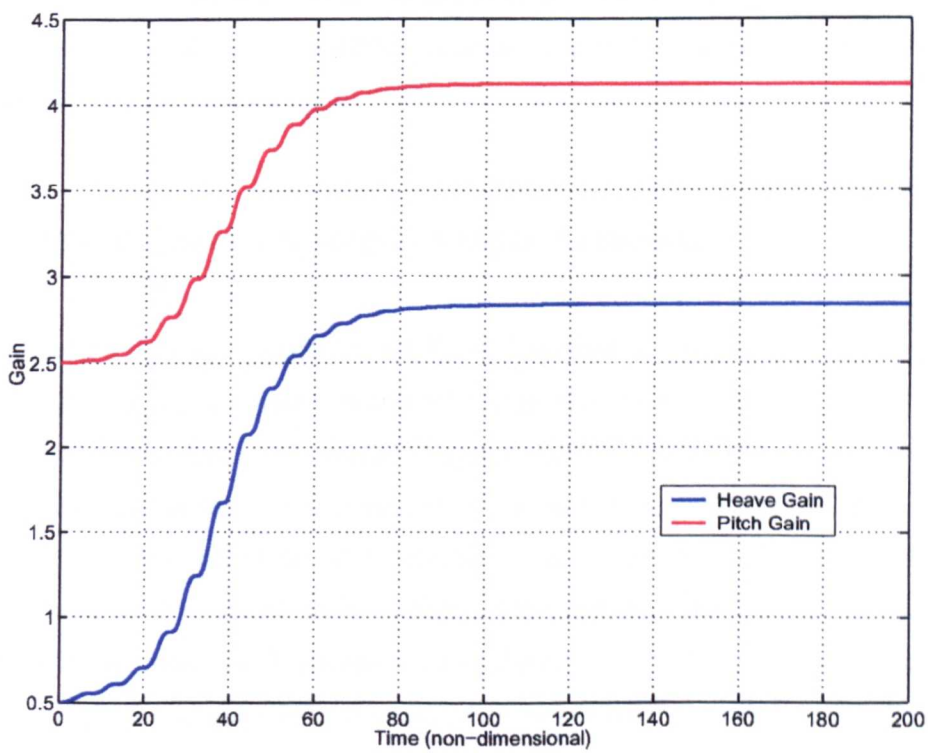

Fig 6.64: Gain Adaptation for a Three Degree-of-Freedom Aerofoil Control at 1.2 Times the Linear Flutter Speed Index at $M_\infty = 0.845$

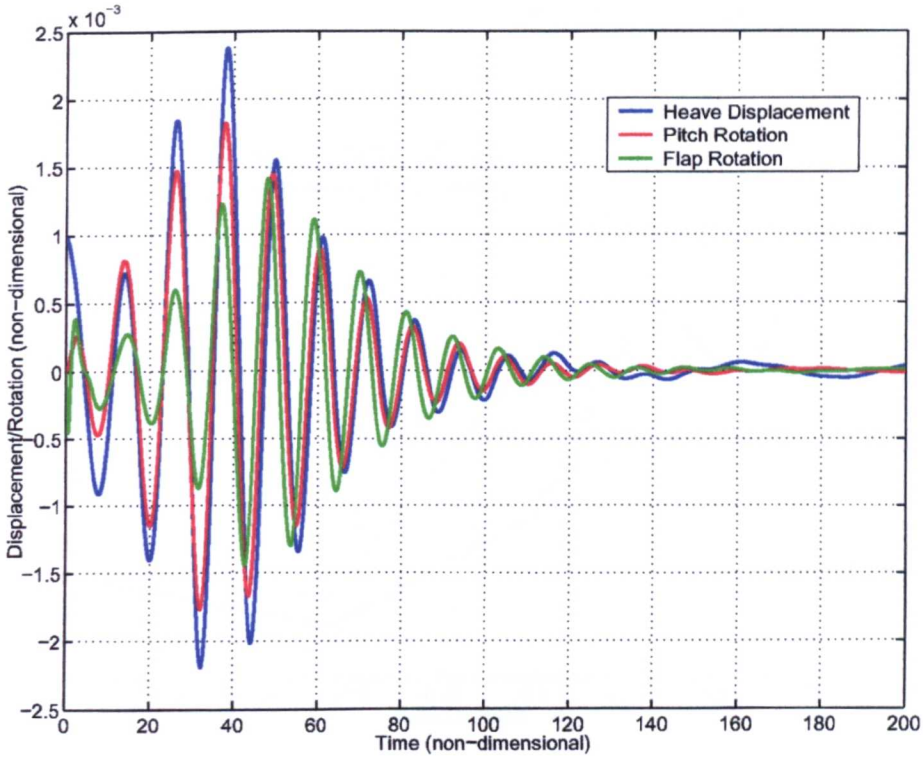

Fig 6.65: System Dynamics for a Three Degree-of-Freedom Aerofoil Control at 1.2 Times the Linear Flutter Speed Index at $M_\infty = 0.845$

not occur. If the gains are updated at regular intervals it would seem that the application of MCS would be practical. This would be particularly useful when system properties change, for example when stores are dropped.

6.7.3 Optimal Control Systems - Linear Aeroelastics

Using the Linear-Quadratic Regulator (LQR) as described in section 5.3.2 it was possible to design an optimised control system that would allow the linear aeroelastic system to operate beyond the flutter boundary. The optimised system firstly required that some combination of states and control inputs were used as minimisation parameters. As many of the states within the matrix are aerodynamic states, the weightings were restricted to the structural freedoms and rates as well as the control surfaces demanded position. The weightings were initially placed on the heave, pitch and flap rotations with the ratio of 1:1:1 respectively. A speed index then had to be chosen about which the system is optimised. The value was selected as the linear flutter speed index. Applying the system within MATLAB gave a set of gains that were applied to all the system states but allowed optimisation as prescribed. The gains that were applied to the aerodynamic states were rejected as they would not be measurable in the real

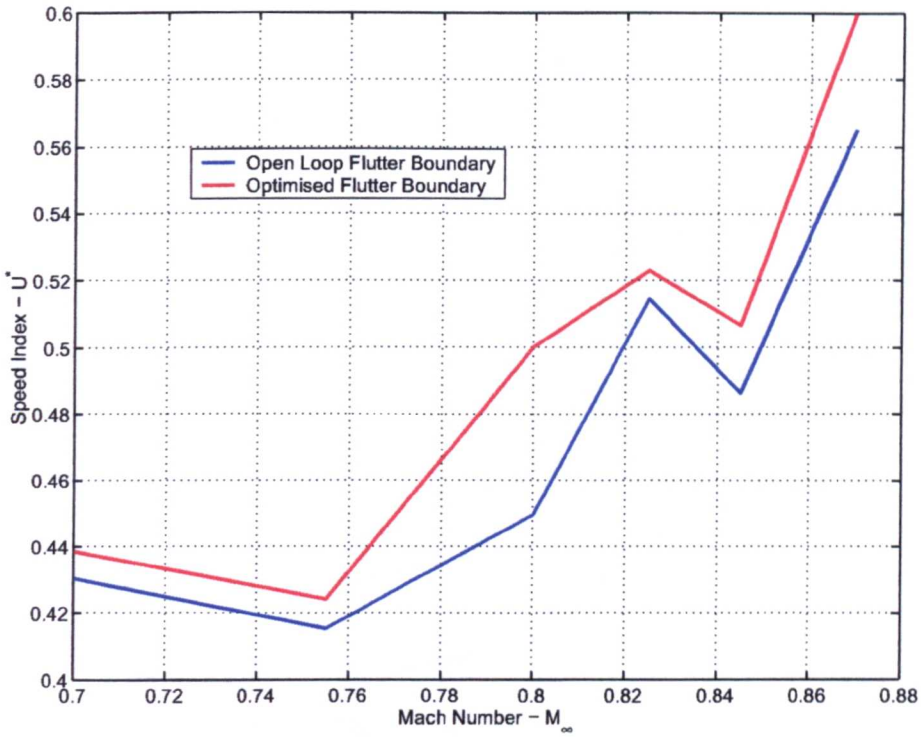

Fig 6.66: Closed Loop Flutter Boundary Optimised at the Flutter Speed Index

system. Figure 6.66 shows the flutter boundary for the linear aeroelastic system with the above criteria applied.

As can be seen an extension in speed index is achieved over that of the open loop case. Extending the system further such that the control system is optimised around 1.2 times the linear flutter speed index with the same weightings (1:1:1) is shown in figure 6.67

As with the fixed gain analysis, the susceptibility to pitch and pitch-rate feedback induced oscillations below the flutter boundary was also seen. For both the LQR optimised systems studied above pre-flutter oscillations were only seen at Mach numbers of $M_\infty = 0.8$ and below. Removing the pitch-rate feedback from these optimisation resulted in much reduced pre-flutter oscillation pockets but with detrimental effects upon the flutter boundary extension, as shown in figure 6.68.

In order to further study the effects of the control in the pre-flutter regime an optimisation was performed at 0.4 times the linear flutter speed index. The resultant change in the flutter boundary is shown in figure 6.69.

From this scheme the flutter boundary is extended negligibly or even reduced. However, it is observed that the large areas of pre-flutter instability no longer exist. For all these methods, a large increase of the peak at approximately Mach 0.825 is seen. This is believed to be due to

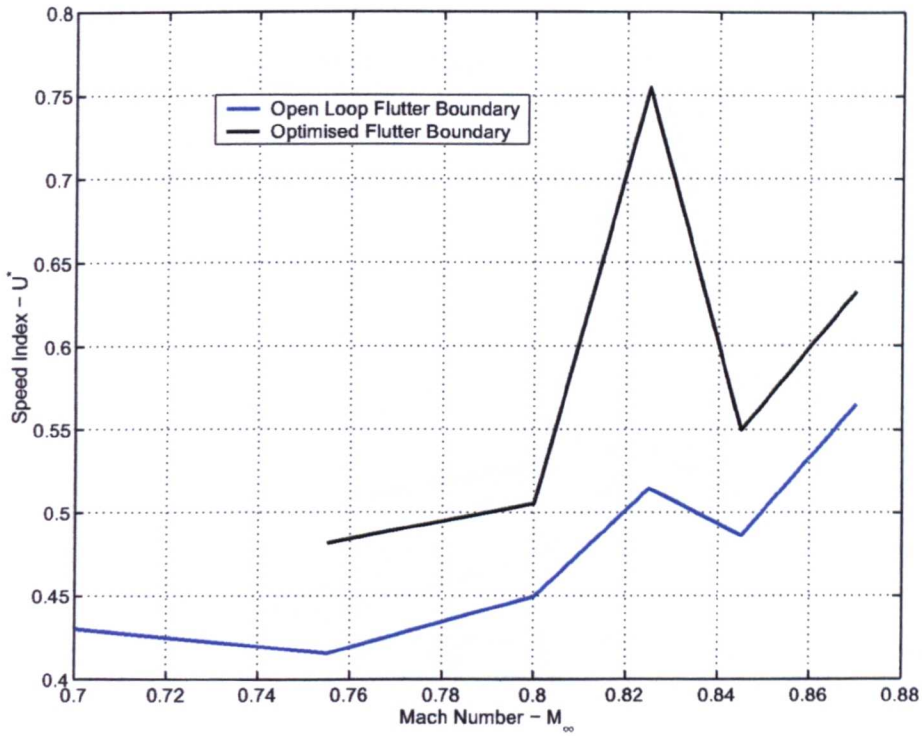

Fig 6.67: Closed Loop Flutter Boundary Optimised at 1.2 Times the Flutter Speed Index

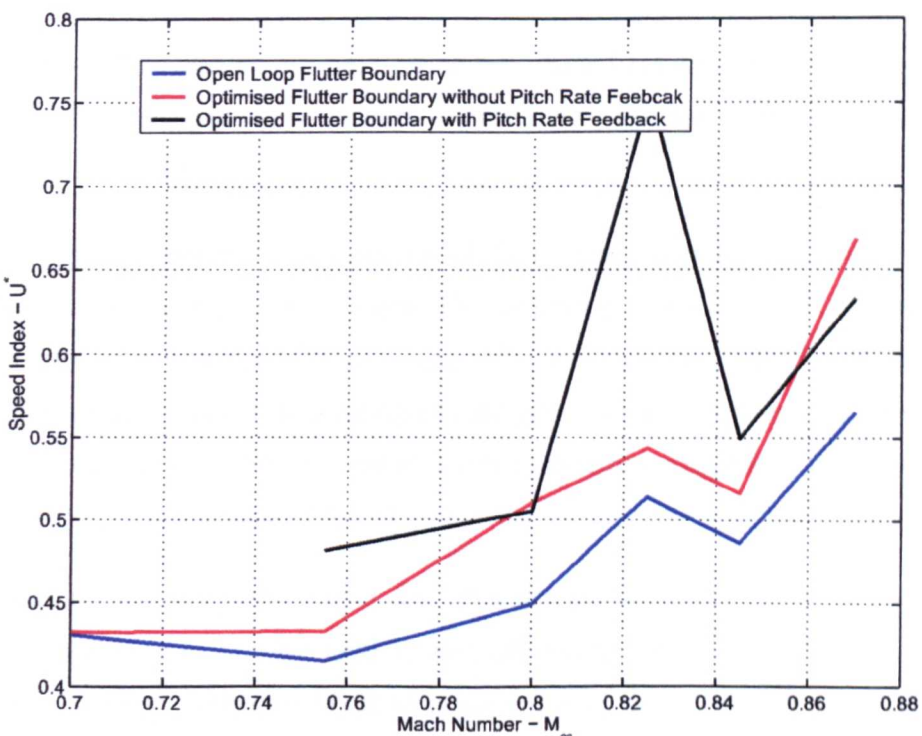

Fig 6.68: Closed Loop Flutter Boundary Optimised at 1.2 Times the Flutter Speed Index without Pitch Rate Feedback

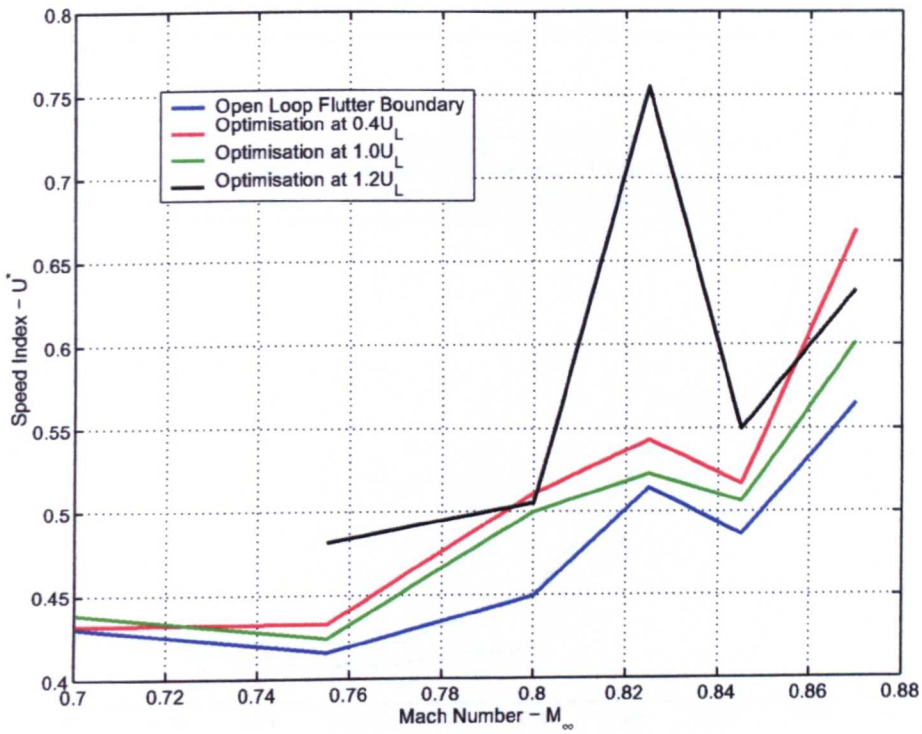

Fig 6.69: Closed Loop Flutter Boundaries Optimised at 0.4, 1.0 and 1.2 Times the Flutter Speed Index

the shock positioning giving the controller particular effectiveness.

Extending this system further, a linear spline was placed between the gains at 0.4 and 1.2 times the flutter speed index in an attempt to extend both the flutter boundary and eliminate the pre-flutter oscillations.

Using the weighting parameters of Vipperman [25], analyses were again performed at 0.4, 1.0 and 1.2 times the linear flutter speed index. The weightings were set to 1:5:1 for heave, pitch and flap respectively. Figures 6.70, 6.71 and 6.72 show the results for the respective speed indices with comparisons made to their equally weighted forms. The extra weighting on pitch is particularly relevant to aeroelastic systems as the important aerodynamic drag characteristics are more dependant on the twist of the wing than the vertical displacement.

The results from these comparisons tended to show that the best performing system is achieved when equal weightings (1:1:1) are used in the LQR routine with a lower boundary observed for the 1:5:1 weighting. At higher Mach Number, however, the 1:5:1 controller showed better performance than the equally weighted equivalent.

As the LQR algorithm used generated gains for aerodynamic derivatives that cannot be directly measured and are dismissed the control system is not strictly optimal.

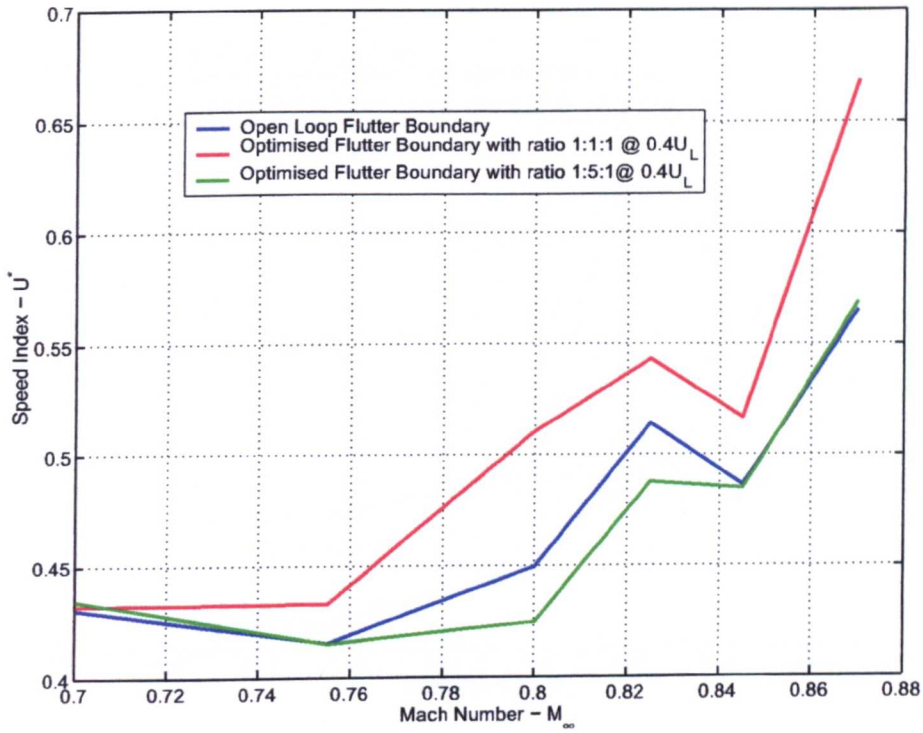

Fig 6.70: Closed Loop Flutter Boundaries Optimised at 0.4 Times the Flutter Speed Index with Different Parameter Weightings

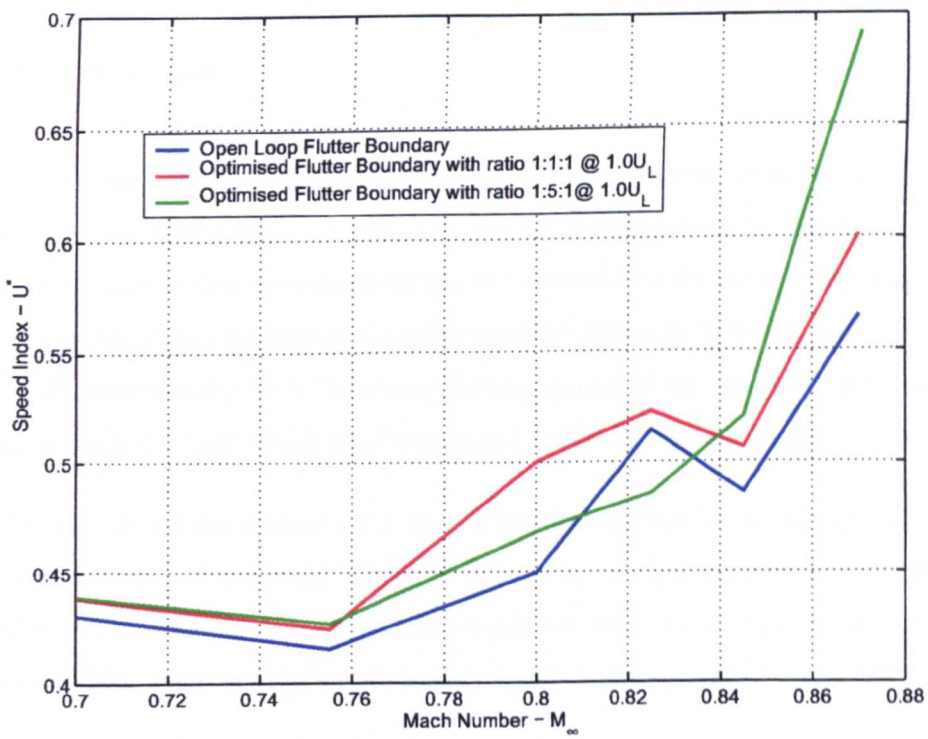

Fig 6.71: Closed Loop Flutter Boundaries Optimised at the Flutter Speed Index with Different Parameter Weightings

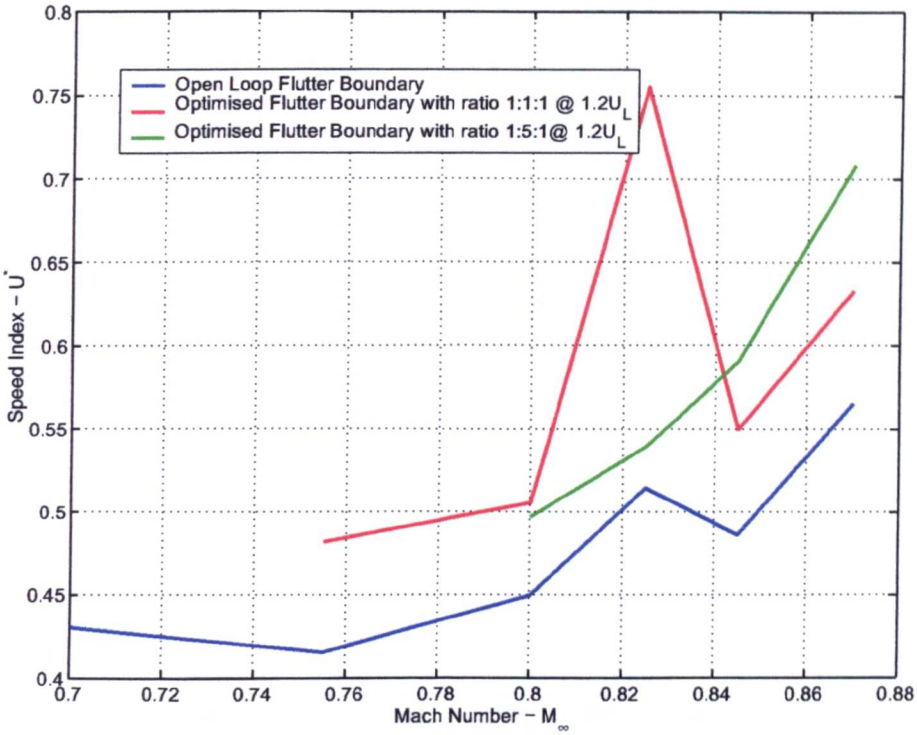

Fig 6.72: Closed Loop Flutter Boundaries Optimised at 1.2 Times the Flutter Speed Index with Different Parameter Weightings

6.7.4 Control of Freeplaying Aeroelastic Systems

6.7.4.1 Basic Dynamics

Application of control within freeplaying systems has often been misinterpreted when applied to modern aeroservoelastic analysis, [85, 57]. As the freeplay within an actuated degree-of-freedom is attributed to free movement within the control system the non-linearity is always about the actuators defined position and not the actuated degree-of-freedom position. This phenomenon is illustrated in figure 6.73, where the boundaries of the freeplay region are marked out by two sinusoidal waves which are δ above and below the sinusoidal actuator position.

Figure 6.73 also shows the motion of a flap within the system for a low speed index (and therefore low density and loading). The flap is seen to be stationary until it enters the stiff region and it is moved along with the freeplay boundary until the change in direction. Figure 6.74 shows the same systems response to a more rapid actuator motion.

The high frequency motion acts more like a impact, driving the system with large velocities between the different stiff zones. If the low frequency motion is repeated at a higher values of speed index, as shown in figure 6.75 it can be seen that the control surface deflects more into

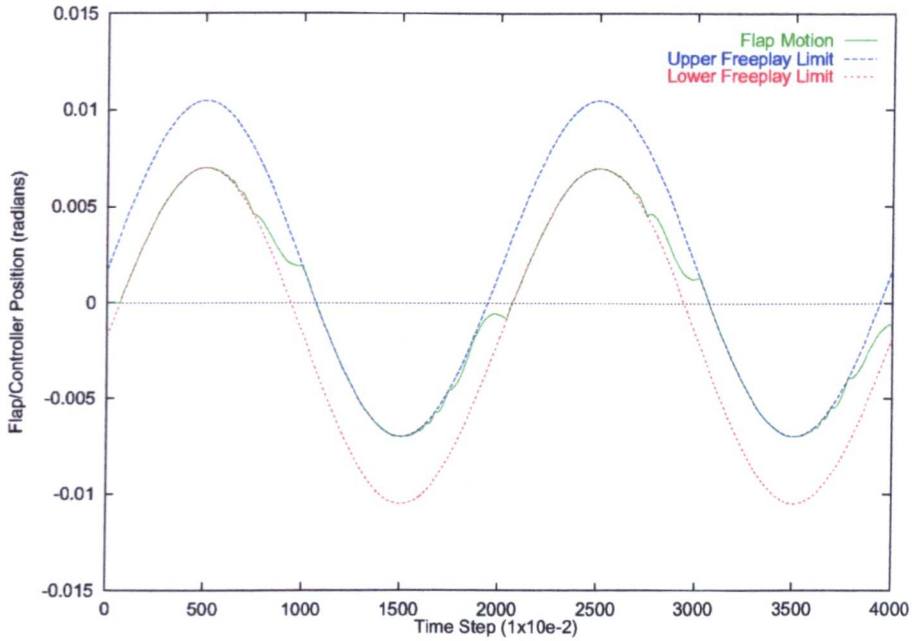

Fig 6.73: Low frequency Control Surface Excitation at Small Values of Speed Index

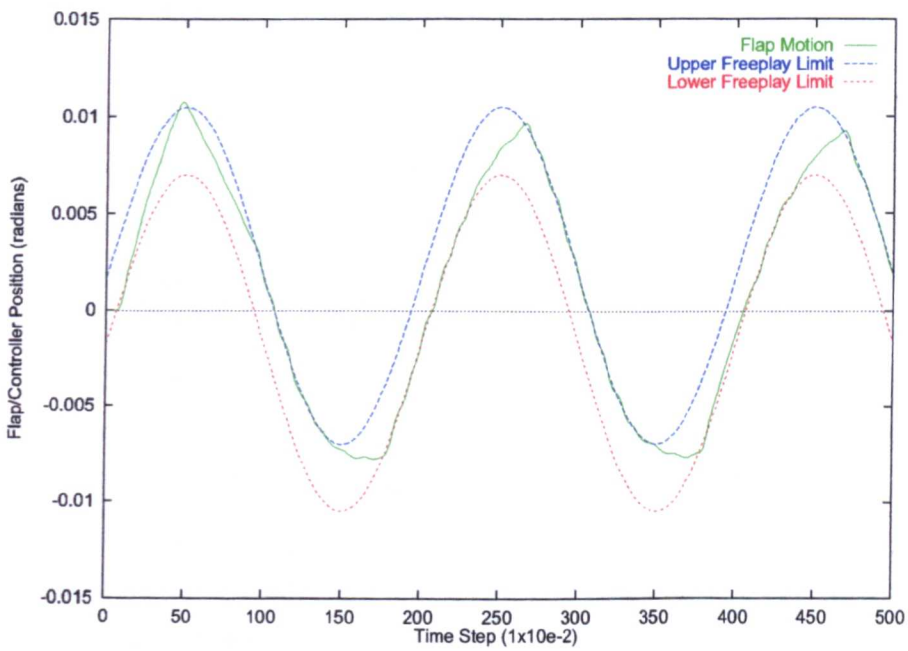

Fig 6.74: High Frequency Control Surface Excitation at Small Values of Speed Index

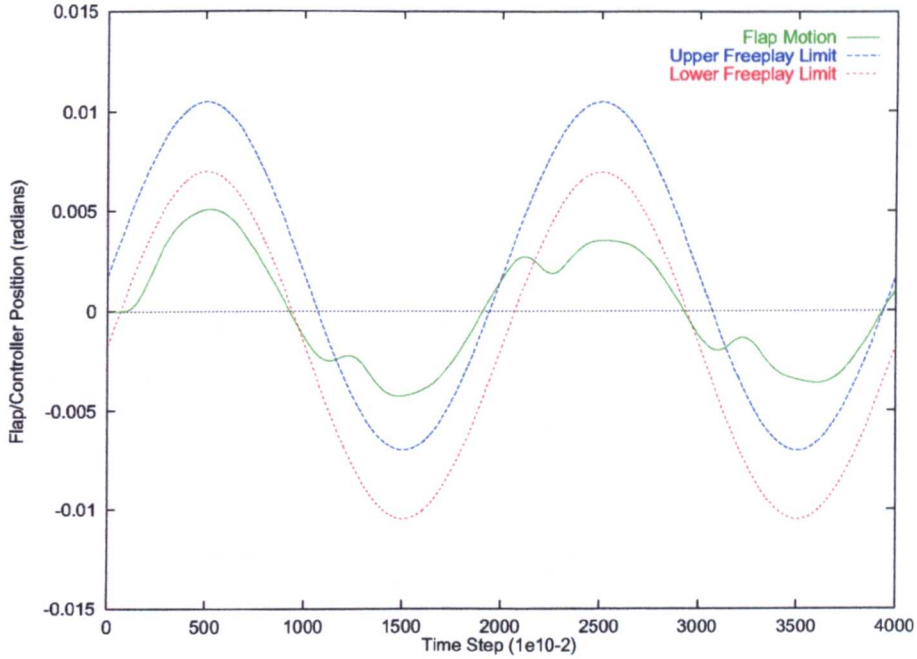

Fig 6.75: Low frequency Control Surface Excitation at Large Values of Speed Index

the stiff domain due to the aerodynamic forcing effects.

As the correct system dynamics are now understood it becomes possible to apply control systems to the non-linear aeroelastic problem to assess the possibility of LCO suppression.

6.7.4.2 Non-linear Aeroeservolastic Response

Fixed gain, adaptive and optimal control was applied to a freeplaying, transonic aeroelastic system. The aeroelastic model used for the problem is as defined in section 6.5.3, with the freeplay gap set to ± 0.1 degrees. The bulk of the analyses were performed at $M_\infty = 0.845$ so that detailed information on the system could be attained with broader analyses presented where required. Presently there are few control systems developed to optimise for non-linear aeroelastic phenomenon. Therefore, the control designed for the linear systems was applied to ascertain its applicability to more realistic systems than the linear aeroelastic model. The control analyses were performed using the continuation method with a logarithmic approximation to the freeplay non-linearity coupled with the ROM to model the aerodynamics. The exception is the adaptive control system where gain wind-up prevents stable-solution detection, such that continuation cannot be used. In these cases time-simulations have been performed as an alternative.

The application of fixed gain control to the aeroelastic problem is shown in figure 6.76, which

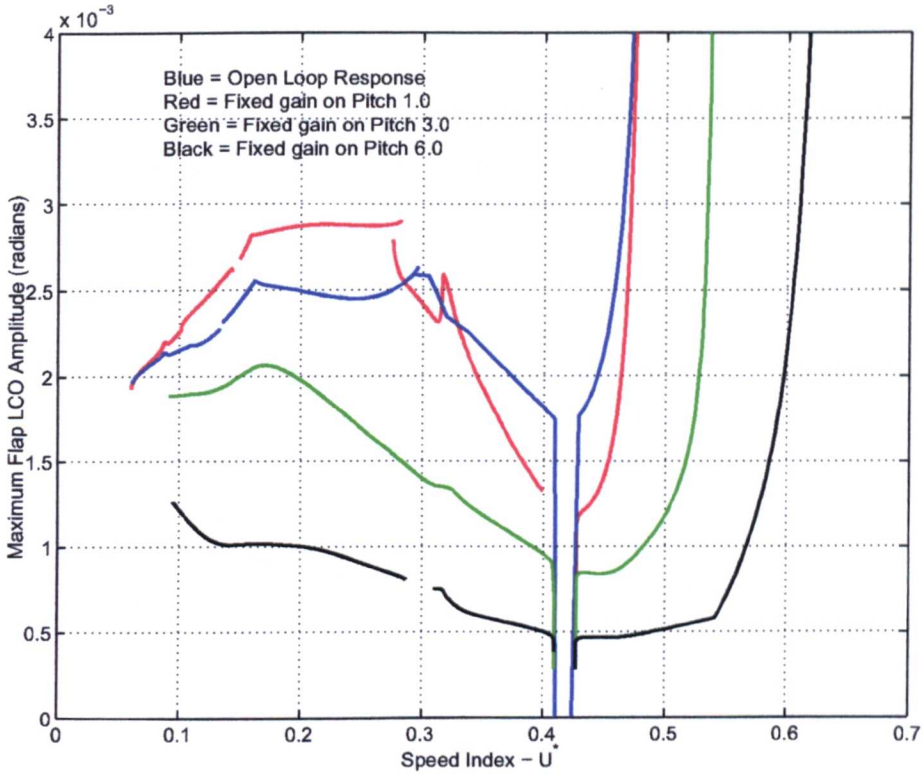

Fig 6.76: Application of Single Gain Feedback Control to Freeplaying Systems

shows the flap amplitude variation with speed index.

In the figure the basic bifurcation diagram can be seen, as well as the system with pitch feed back. The figure shows that suppression of the oscillations can be achieved with good effect when applying the linearised system's gains to the non-linear problem. The level of suppression is observed to reduce the oscillation and extend the flutter boundary by up to 25%.

Extending the fixed gain principal to combined gains, figure 6.77 shows the response of the same aeroelastic systems as discussed previously when using combined gains.

In the figure, various combinations of gains are applied to the systems heave rates and pitch rates in the ratios of, -3:-3 (as used by Djayapertapa [85]), and -6:-6. The systems exhibited similar suppression characteristics to those of the linear system with, in general, the best systems for the linear case exhibiting the best characteristics for the non-linear case. However, at speed index values far below the flutter value the systems performance altered with some of the optimal system showing large LCO responses. This is thought to be linked to the pre-flutter unstable areas observed within the linear systems. Unstable phenomenon and large LCOs seen at lower velocities within the freeplaying system suggests that control surface effectiveness at controlling motions at low speed is a significant factor in the problem.

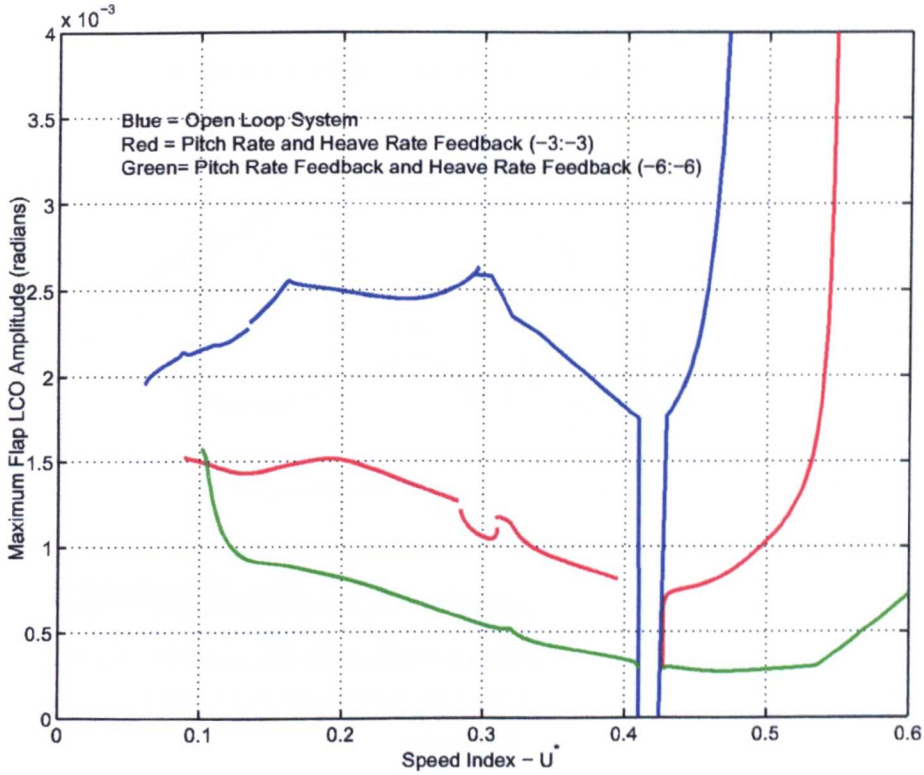

Fig 6.77: Application of multiple Gain Feedback Control to Freeplaying Systems

The optimal control systems designed in section 6.7.3 were applied to the freeplaying system. The freeplay was set to ± 0.1 degrees and tests were performed at $M_\infty = 0.845$. Figures 6.78 and 6.79 shows the response of the basic freeplaying system as well as the control systems optimised at 0.4, 1.0 and 1.2 times the linear flutter speed index, for weighting 1:1:1 and 1:5:1 (heave:pitch:control rotation) as described in section 6.7.3.

From both systems the optimisation at 1.2 times the linear flutter speed index gave the best suppression of oscillations. Studying the full effect on the plunge and pitch degrees-of-freedom demonstrated that the system with the 1:5:1 weightings gave the best overall response, indicating that pitch is the most important degree-of-freedom to control. However, it is noted that, as for the linear case, this ascertion may not be valid at lower Mach numbers.

Using the MCS adaptive control methodology time simulations were performed at 0.3, 0.6, 0.9 and 1.2 times the linear flutter speed index. The response of the system after initial transients and gain adaptation is shown in figures 6.82 to 6.84 for the three lower speeds. The response of the system at 1.2 times the linear flutter speed index is not shown as the control system was incapable of suitable control.

The system applied allowed adaptation in heave, pitch, heave-rate and pitch-rate. The gain adaptation for the different cases are shown in figures 6.85 to 6.87 from time integration anal-

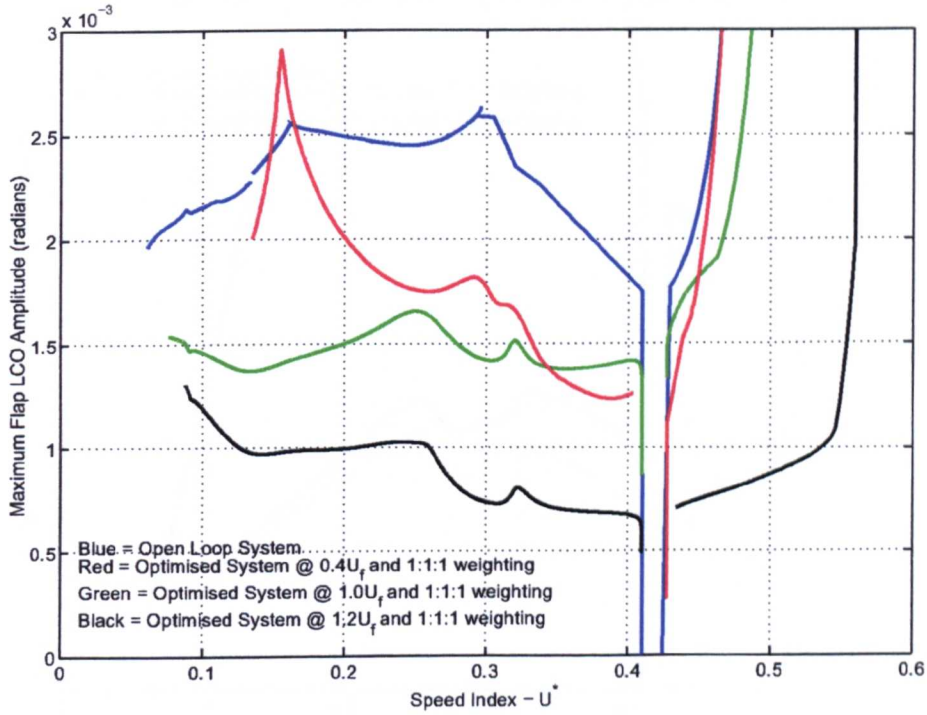

Fig 6.78: Comparison of Linear Optimised Systems Response to a Freeplaying Non-Linearity with Weightings of 1:1:1

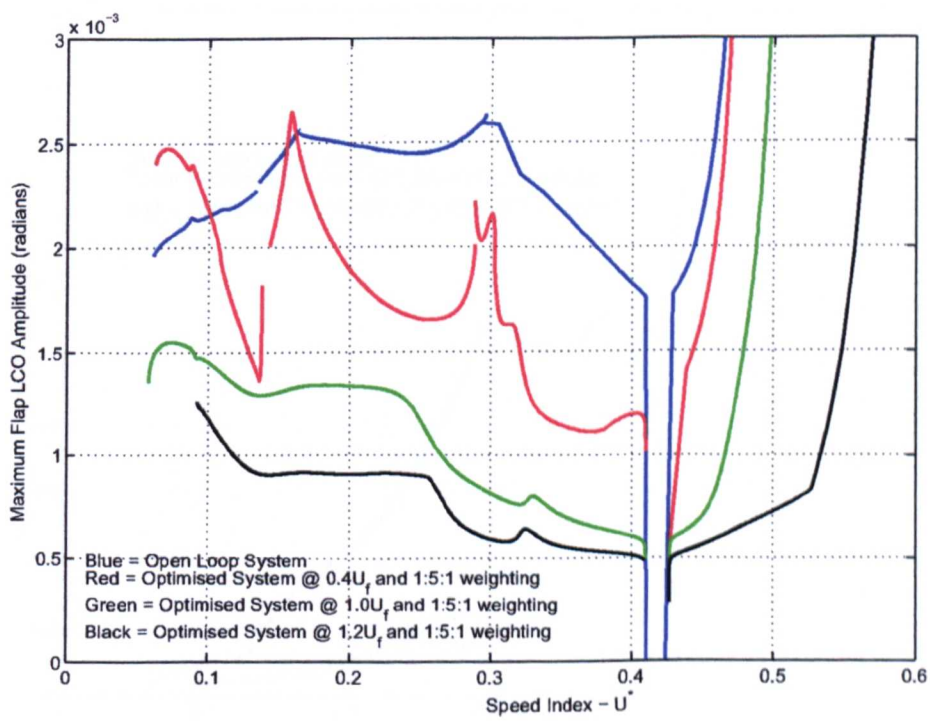

Fig 6.79: Comparison of Linear Optimised Systems Response to a Freeplaying Non-Linearity with Weightings of 1:5:1

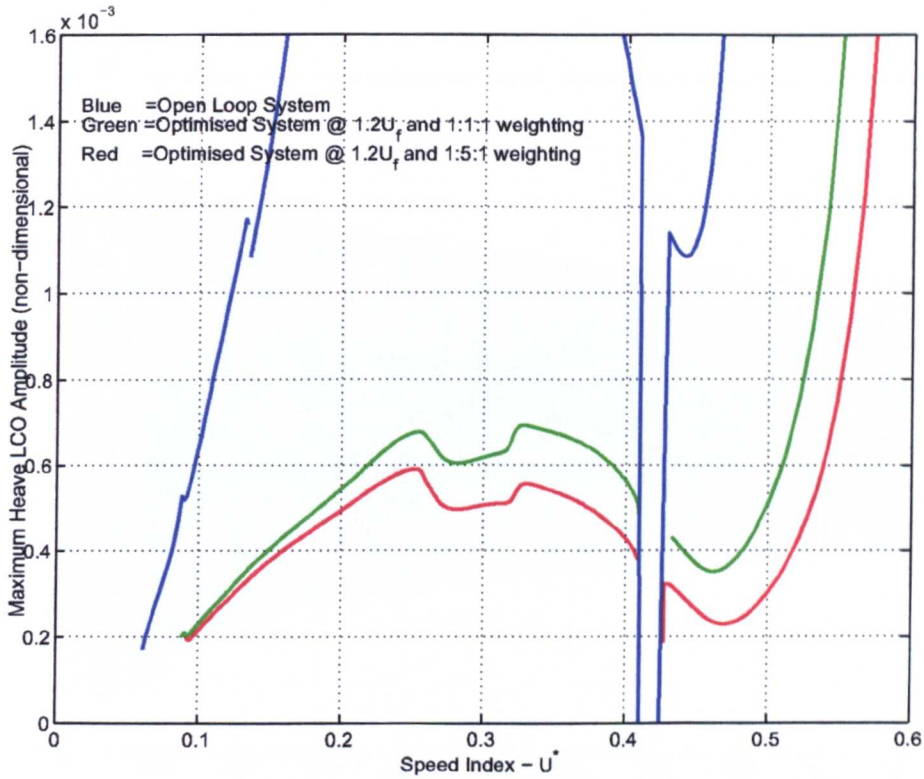

Fig 6.80: Heave Response for Control Systems Optimised at 1.2 Times the Linear Flutter Speed Index

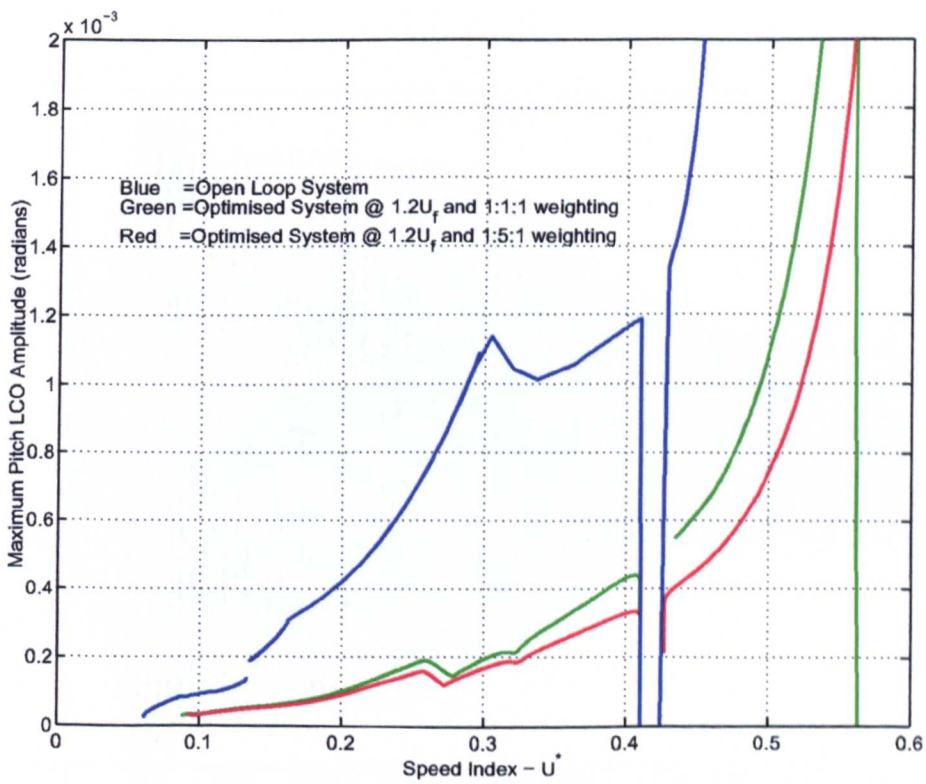

Fig 6.81: Pitch Response for Control Systems Optimised at 1.2 Times the Linear Flutter Speed Index

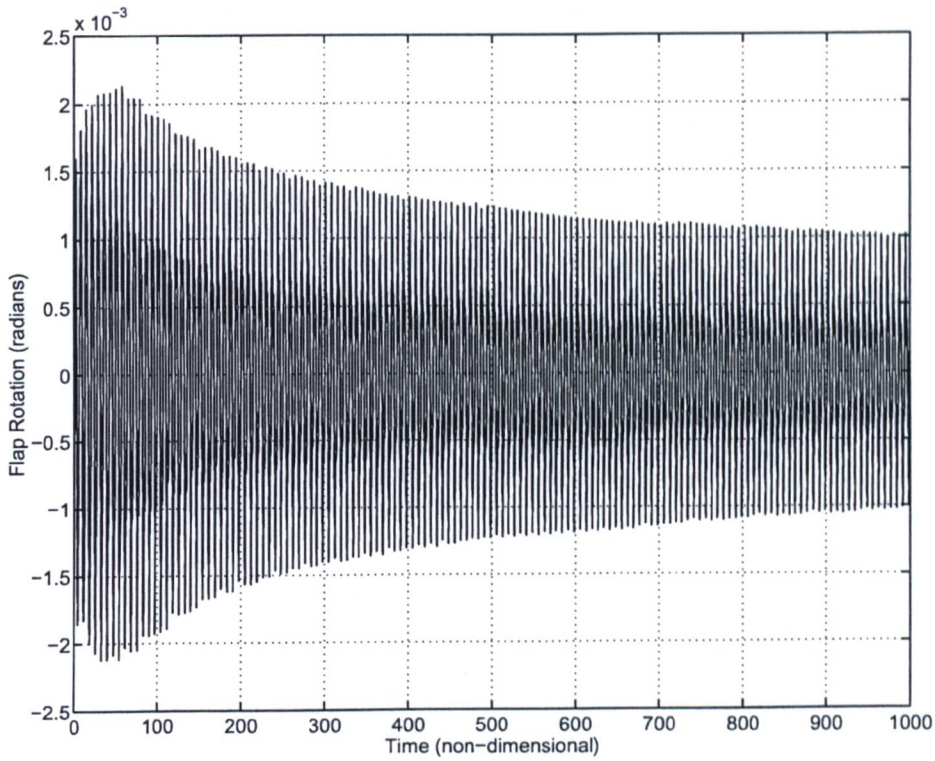

Fig 6.82: Flap Motion for Freeplaying System with Adaptive Control at $0.3U_l^\star$ *and* $M_\infty = 0.845$

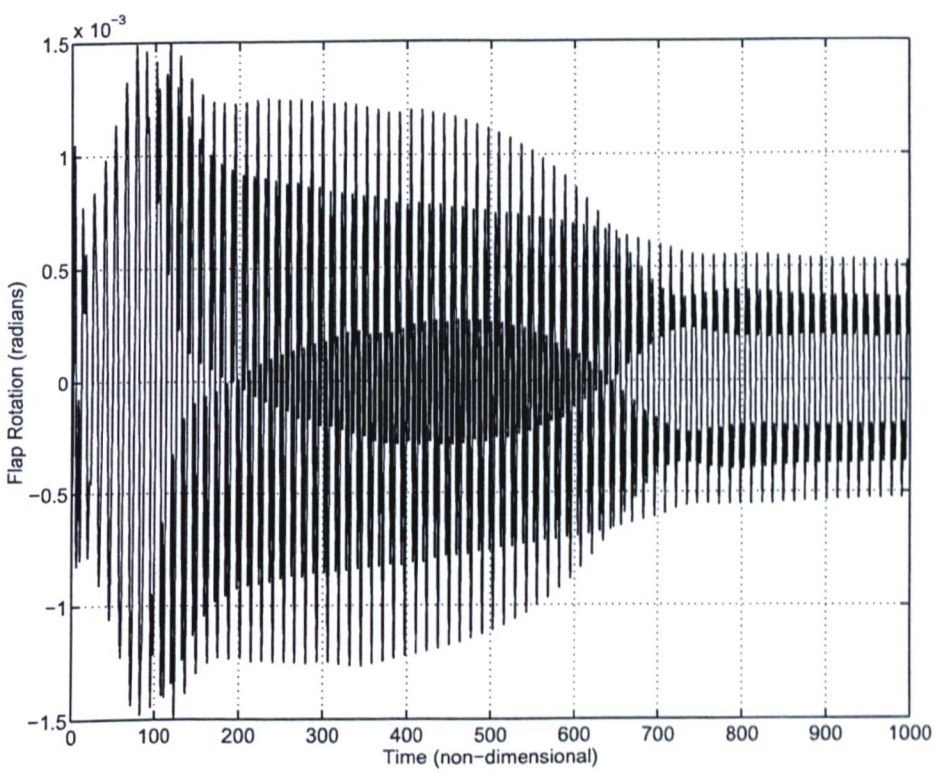

Fig 6.83: Flap Motion for Freeplaying system with Adaptive Control at $0.6U_l^\star$ *and* $M_\infty = 0.845$

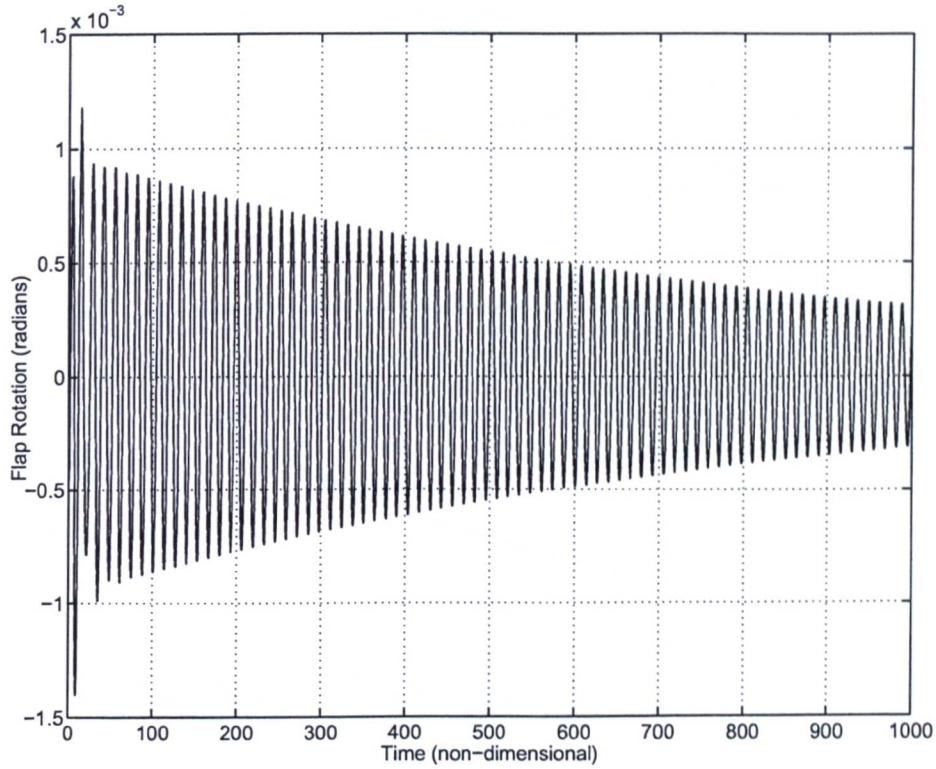

Fig 6.84: Flap Motion for Freeplaying System with Adaptive Control at $0.9U_l^\star$ *and* $M_\infty = 0.845$

yses.

The gains presented here for the heave and heave-rate are -2 times the actual values due to the non-dimensional form of the heave rate used in the analysis. As with the gains, the 1.2 times the linear flutter speed index results are not shown as they were found to diverge rapidly to infinity.

6.8 Further Applications - Fatigue

Pre-flutter LCOs due to structural non-linearities can have a major effect upon the fatigue life of aircraft structural components. Using the analysis outlined in the previous sections it is possible to determine the amplitude of any oscillations induced by non-linearities and therefore predict its fatigue properties. The following section describes a simplistic method by which simple fatigue analysis can be performed. However, implementation of the analysis within a structural Finite Element (FE) code would allow more complex structures to be analysed and various analyses to be performed using the prescribed motions from the continuation results.

The model studied in this section uses the aerodynamics of Wong et al. [7] and, as such, is

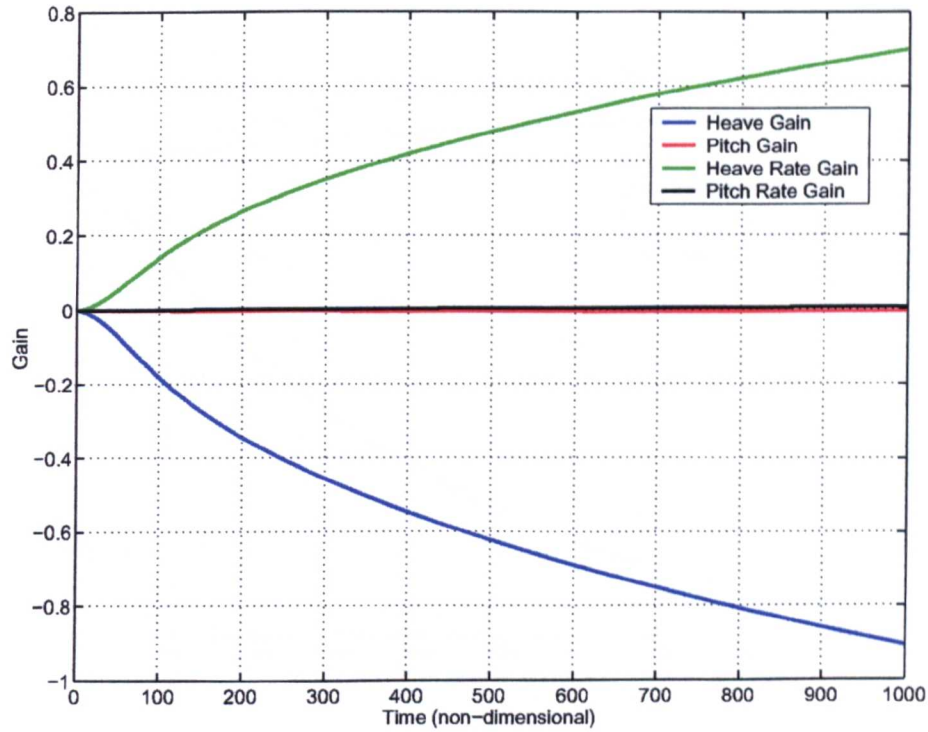

Fig 6.85: MCS Gain Adaptation at $0.3U_l^\star$ *and* $M_\infty = 0.845$ *for a Three Degree-of-Freedom Case*

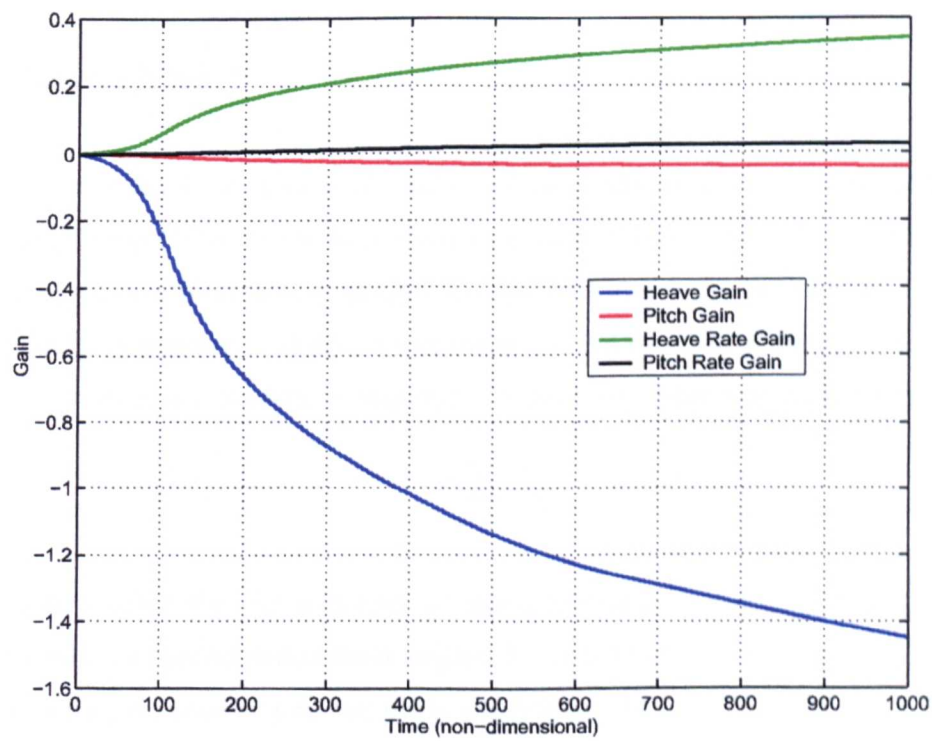

Fig 6.86: MCS Gain Adaptation at $0.6U_l^\star$ *and* $M_\infty = 0.845$ *for a Three Degree-of-Freedom Case*

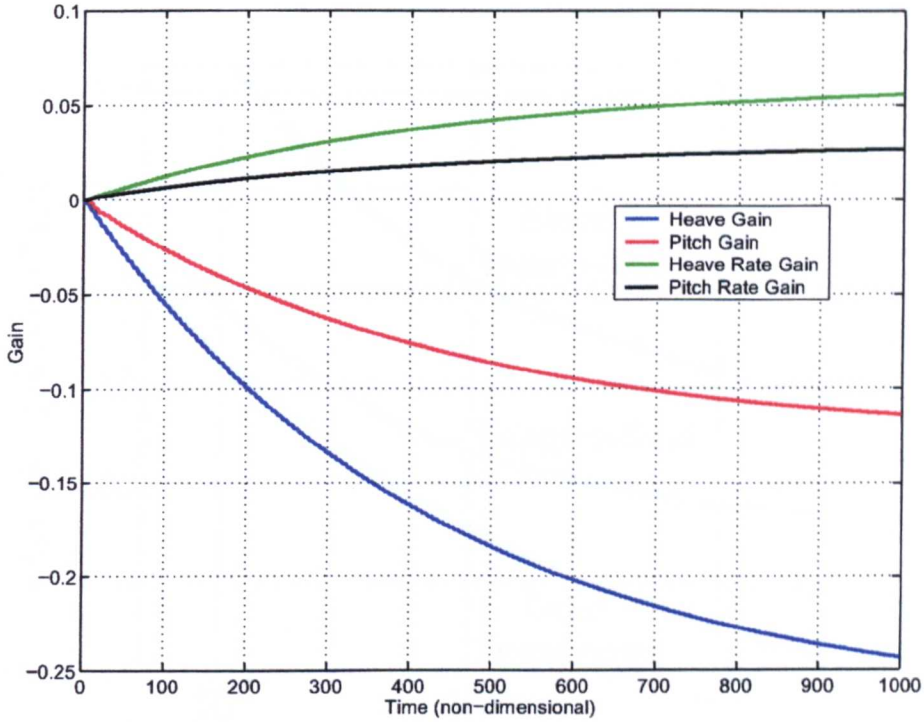

Fig 6.87: MCS Gain Adaptation at $0.9U_i^\star$ *and* $M_\infty = 0.845$ *for a Three Degree-of-Freedom Case*

applied to a two degree-of-freedom aerofoil with freedoms in pitch and plunge.

6.8.1 Fatigue Model

Fatigue for components of structures are calculated using fatigue curves as shown in figure 6.88 which is taken from [108]. From these curves the number of cycles that a specified material could endure when subjected to a sinusoidal oscillating stress can be calculated. However, systems undergo a number of different amplitude oscillations throughout their lifecycle and therefore the damage accumulated is required. The amount of damage sustained is defined as,

$$D = \sum_i \frac{n_i}{N_i} \tag{6.11}$$

where n_i is the number of cycles with a stress amplitude indexed by i and N_i is the endurance of the material when subjected to this stress amplitude i as defined in material fatigue curves. The summation is the total over all possible stress amplitudes taken. If this damage is accumulated over m operations of the system then the predicted life (P.L.) becomes,

$$P.L. = \frac{m}{D} \tag{6.12}$$

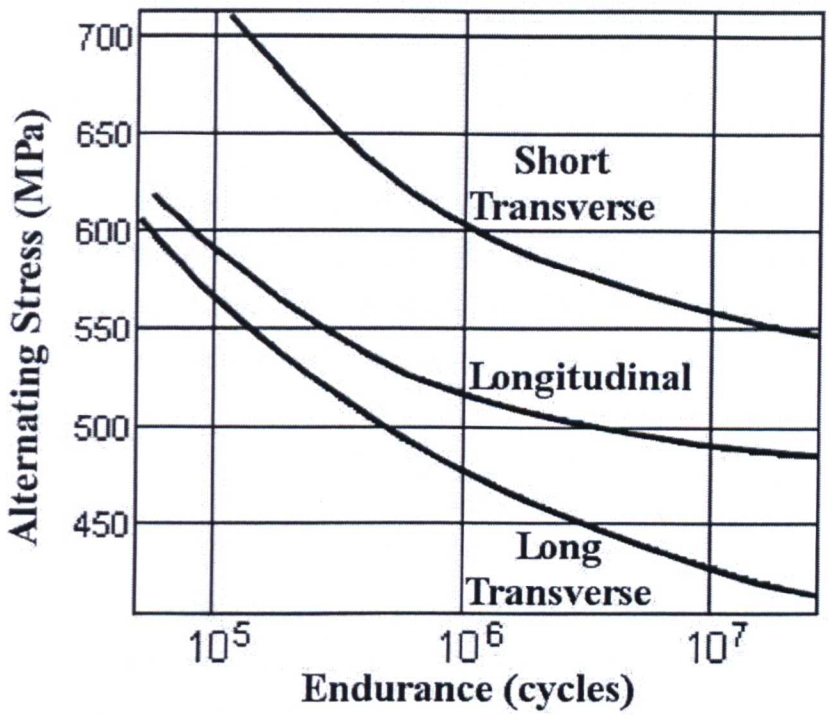

Fig 6.88: Fatigue Curves for Ti-6Al-4V when Stressed along Different Crystal Axes

Depending on variation in operational parameters and inclusion of safety factors this life may be modified according to best practice.

When the motion of a system is not sinusoidal these equations no longer hold and therefore equivalent sinusoidal motions are used. Many different methods for studying fatigue in non-sinusoidal oscillating systems have been developed [109]. The accuracy of these models is dependent on the particular method but for the purposes of this study the Rainflow technique is used as it is seen to be one of the most effective ways of accurately predicting fatigue life [109]. The method is described in detail by Dowling [109], and results in non-sinusoidal oscillations being converted into a set of equivalent sinusoids from which the method of predicting life in equation 6.11 and 6.12 can be used.

6.8.2 Aeroelastic Fatigue Model

As Wong's aeroelastic state space system is non-dimensional [7] the associated fatigue analysis is likewise non-dimensional. In equation 2.77 the terms before $G(\xi)$ and $M(\alpha)$ represent the stiffness of the system in heave and pitch which are EI and GJ in the dimensional system

respectively.

$$E = \frac{\overline{\omega}^2}{U^{*2} I} \tag{6.13}$$

$$G = \frac{1}{U^{*2} J} \tag{6.14}$$

The attachment from the surface to a rigid structure, e.g. the attachment between the aerofoil and the fuselage of the aircraft, considered in this study is a simple cylinder with internal and external radii given as r_{in} and r_{out} when non-dimensionalised with respect to the semi-chord. This representation allows the Cartesian and polar second moments of area, I and J to be calculated as,

$$I = \frac{\pi}{4}(r_{out}^4 - r_{in}^4) \tag{6.15}$$

$$J = \frac{\pi}{2}(r_{out}^4 - r_{in}^4) \tag{6.16}$$

These parameters allow the Youngs' and Torsional Modula (E and G) can be calculated. Comparing the non-dimensionalised Youngs' Modulus with the actual modulus a scaling factor is obtained for the analysis. For the testcase studied here a forged and annealed titanium alloy (Ti-6Al-4V) is used with a Youngs' Modulus of (114 GPa).

To use the Rainflow method for fatigue prediction outlined in [109] the peaks and troughs of the motion are identified using simple stress theory. The stress is calculated as a combination of the stress due to torque and that due to vertical displacement. For the simple cylinder studied here the shear stress due to torque is,

$$\tau = \frac{\theta G R}{L} \tag{6.17}$$

where θ is the angle through which the cylinder is turned, R is the maximum distance away from the axis of rotation i.e. r_{out}, and L is the length from the fully fixed root to the point at which the cylinder is rotated through an angle of θ when non-dimensionalised with respect to the semi-chord i.e. the distance from the aerofoil to the fuselage attachment point. The stress due to vertical displacement is calculated as,

$$\sigma_1 = \frac{3E\xi R}{L^2} \tag{6.18}$$

where ξ is the vertical displacement. Using the theory of maximum principal stress [110], the stress is calculated as,

$$\sigma = \frac{1}{2}\sigma_1 + \frac{1}{2}\sqrt{\sigma_1^2 + 4\tau^2} \tag{6.19}$$

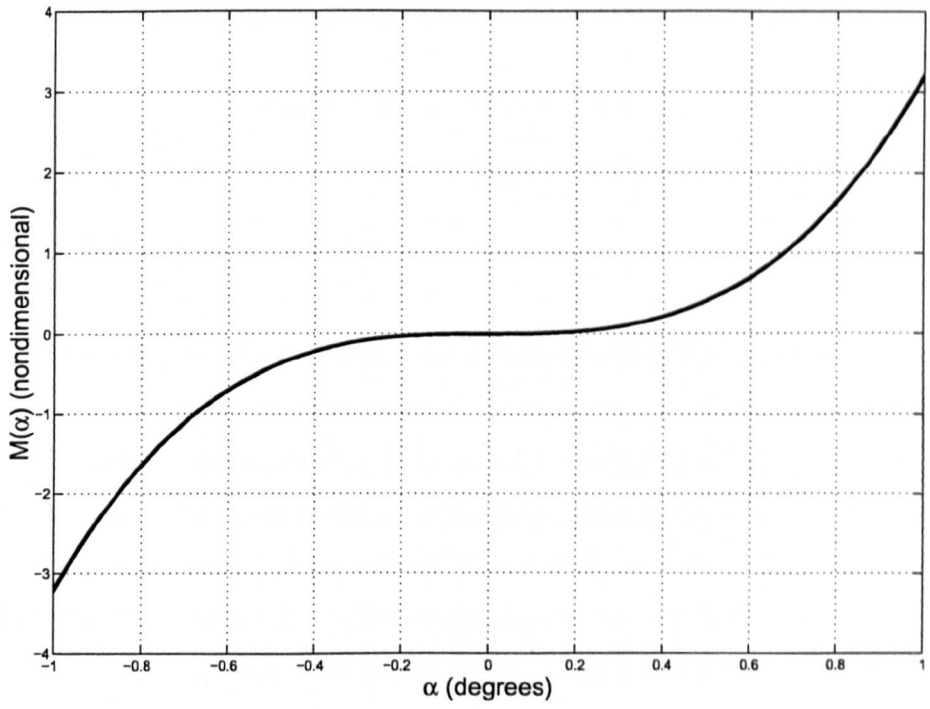

Fig 6.89: Cubic Stiffening Non-Linearity

6.8.3 Testcase

The testcase chosen for this system is that of a polynomial stiffness spring where the non-linearity is of the form,

$$M(\alpha) = \sum_{i=1}^{N} \beta_i \alpha^i \tag{6.20}$$

This is a general case for a non-linearity in the pitch degree-of-freedom. The specific case to be studied is a structural stiffening in the pitch degree-of-freedom. Such stiffening is represented by a cubic equation,

$$M(\alpha) = 6 \times 10^5 \alpha^3 + \alpha \tag{6.21}$$

This non-linearity is quite a strong non-linearity as the system stiffens quickly outside of the central range and can be seen in figure 6.89. The heave degree of freedom is linear and simply represented by,

$$G(\xi) = \xi \tag{6.22}$$

The generalised system parameters to be used in equation 2.77 are,

$$\mu = 100, \quad a_h = -\frac{1}{2}, \quad x_\alpha = \frac{1}{2}$$
$$\zeta_\alpha = \zeta_\xi = 0, \quad r_\alpha = \frac{1}{2}, \quad \overline{\omega} = \frac{1}{5}$$

The dimensions of the aerofoil attachment are,

$$r_{out} = 0.08, r_{in} = 0.06, L = 0.55$$

6.8.4 Results

A simple fatigue analysis was performed for an acceleration from a velocity of 1.0 to 1.753 (non-dimensionalised with respect to the linear systems flutter velocity) and then a deceleration back down again. The reasons for these velocities being selected are that below the level of 1.0 no LCOs occur. To simulate the acceleration process all the velocities within the range selected were taken sequentially upwards and then downward to recreate the acceleration then deceleration. Tests for both a slow (ten cycles at each velocity level) and a fast (one cycle at each velocity level) sequence were performed to assess the impact of a quick acceleration-deceleration compared to that of a gradual acceleration-deceleration process, as shown in figure 6.90 and 6.91 respectively. However, it should be noted that the oscillations seen in these figures are not sinusoidal. Identifying the peaks and troughs from these calculations coupled with the Rainflow technique gave the resultant set of sinusoidal oscillations.

Using the equivalent sinusoids the damage incurred (fraction of the time to failure) was calculated as 8.7512×10^{-4} for the rapid form and 5.3367×10^{-3} for the slow form. Assuming that this motion occurs twice in every flight then this gives a predicted life of 2285 missions if the acceleration was quick or 374 if it was the slow acceleration. The difference in fatigue life is a factor of six and not ten as would be generated by many algorithms. The disparity is because the number of jumps between different oscillatory levels, i.e. different velocities, is still the same and at these junctions much of the fatigue is generated. Additionally, a major contribution to the fatigue is the major cycle, from absolute minimum to absolute maximum, this cycle still only occurs twice i.e. once whilst accelerating once whilst decelerating. This peak loading has the largest alternating stress at $719MPa$, where only 1.03×10^4 cycles are required for a fatigue failure to occur, which, when compared with other stress values that have cycles to failure of the order 10^5 and 10^6, is an order of magnitude worse.

The fatigue example shown here is simplified but demonstrates that it is possible to organise the system so that velocity, mass ratio, inertias and non-linearity can be altered in the numerical continuation. These factors would allow the simulation of changes in speed, changes of altitude, dropping external stores/loss of fuel and realistic inclusion of non-linear stiffnesses.

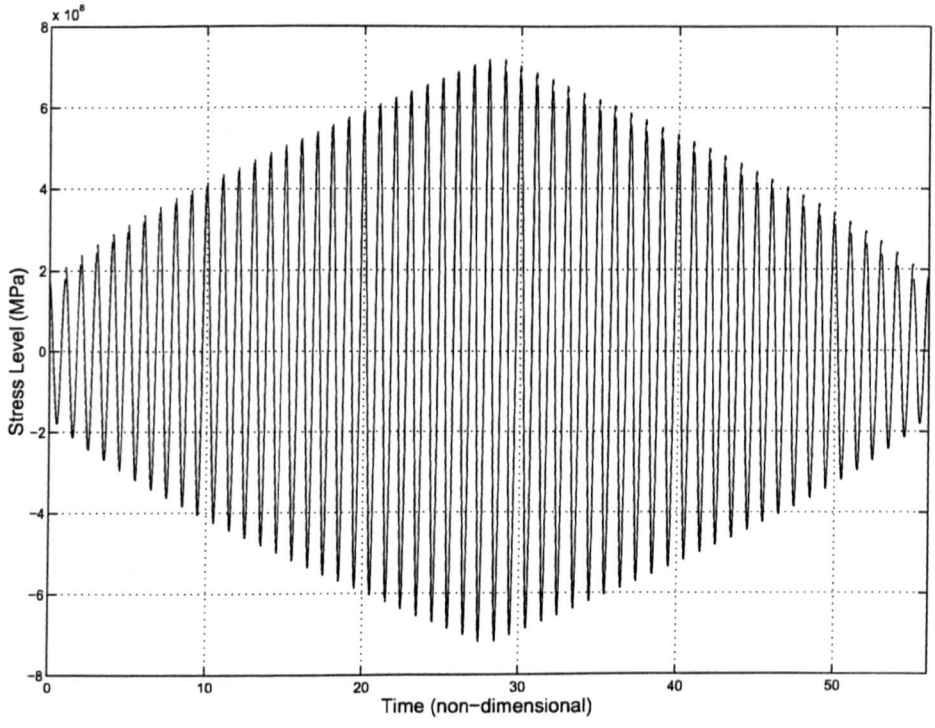

Fig 6.90: Rapid Fatigue Motion

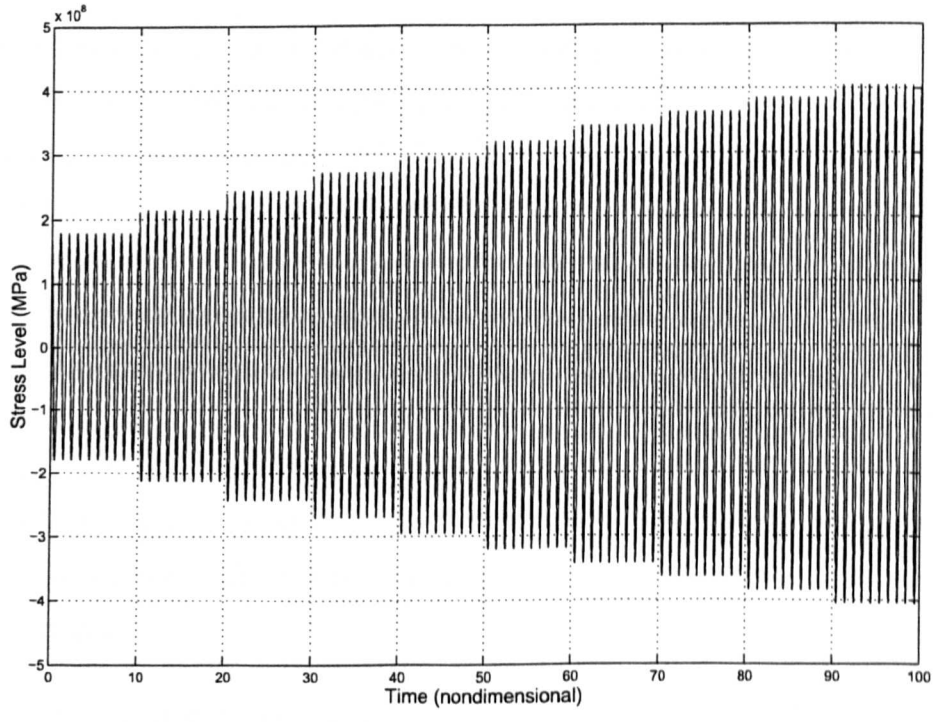

Fig 6.91: A Section of the Slow Fatigue Motion

6.9 Concluding Remarks

This section has demonstrated that analysis of non-linear aeroelastic and aeroservoelastic systems can be performed both rapidly and accurately.

The method of boundary identification proved to be a highly accurate method of analysing piecewise linear forms of non-linearities. The efficiency of the method was good for low-order oscillations e.g. period 1, but, when the oscillations where of more complex forms, e.g. period 2 with harmonics, the solution sequence slowed down considerably. However, most large, dynamic systems tend not to exhibit high-order oscillations due to the presence of structural damping.

Combing numerical continuation with tanh and logarithmic functions representing discrete non-linearities showed to be an efficient way of analysing both piecewise linear and piecewise non-linear systems. The ability to vary a singe parameter to increase the accuracy of the approximations proved to be a particularly useful way of analysing discrete non-linearities when using numerical continuation. Even though the approximations are not exactly the same as the discrete non-linearity it has been shown to be well within engineering tolerances. Using this technique, the speed at which solutions are generated is a markedly better than conventional time integration methods.

The Reduced Order aerodynamic Model (ROM) proved to be an efficient way of capturing the basic dynamics of the transonic airflow around the aerofoils studied. For structurally linear models, the flutter boundaries were calculated accurately and within the differences between other transonic codes. When using the ROM to generate time integration solutions, small differences in the rates of divergence/convergence and frequencies were observed, this error was found to increase when non-linear structures were introduced. For these cases the error was noted to exist within the ROM itself and not the application of continuation as both time integration and continuation methods agreed. The error is attributed to the ROM not capturing all the dominant aerodynamic frequencies and damping values as this would create excessively large matrices. From the studies, the ROM could eventually provide a very useful engineering tool for both conventional linear and non-linear analyses in both normal and modal co-ordinates.

From the analyses performed here it has been shown possible to generate control systems that both attenuate LCOs and delay flutter onset. It was seen that if controllers were optimised for linear systems, they would also be close to being the optimal design for non-linear system controllers. The level to which control of non-linear aeroelastic systems could be studied

was limited within the scope of this thesis and requires further work to obtain an in-depth appreciation of the problem. The optimal controller was found to be the best control law as it proved the best at suppressing LCOs and delaying flutter. The fixed gain controller was found to be very much more *ad hoc* method of generating the required gains. The Minimal Control Synthesis (MCS) adaptive controller was found to be difficult to implement as the gains tended to constantly wind-up. Delay of flutter onset was found to be possible with MCS but care had to be taken of the parameters that determined the rate at which the system adjusted. The control of LCOs was found to be impractical using MCS as the oscillation would never have zero amplitude and, therefore, the gains would never stop increasing. As the gains are constantly changing the application of the numerical continuation techniques was found to be impossible because a steady repeating cycle would never be found. The design of controllers to suppress aeroelastic phenomena requires further investigation as it was found that the controllers could, whilst extending the flutter boundary, destabilise other areas below the flutter boundary.

The impact of non-linearities on the fatigue life was briefly highlighted at the end of this chapter with a simple example given. It is believed that given certain non-linear parameters can be measured throughout a components life and that flight data is logged, better estimates of remaining life can be given. The example showed this in a simplified manner but, in principle, this could be extended to full scale aircraft and detailed structural models.

In summary, the application of numerical continuation to both linear and non-linear aeroelastic problems can both reduce calculation times and increase the accuracy of solution. Using boundary identification as a method of analysing piecewise linear systems was shown to be very accurate and efficient for systems with low periodicity, e.g. period 1, but became inefficient for systems with higher periodicity. Representing discrete non-linearities with approximations and applying numerical continuation was found to deliver both good accuracy and good efficiency of solution. The newly developed Reduced Order Model (ROM) showed much promise with transonic flutter boundaries being found accurately in a fraction of the time that it would take for conventional analysis methods. In analysing non-linear problems, the ROM did show some discrepancies in the amplitude of oscillation that requires further investigation. Control of aeroelastic systems was found to be possible, and the application of numerical continuation to the problem was also seen to be useful except for adaptive controllers where a steady state is never reached. It was found that care must be taken in the design of aeroelastic controllers as they can destabilise the system far below the flutter boundary.

Chapter 7

Summary, Contributions and Future Work

7.1 Summary

The overall goals of the research in this thesis were: the implementation of efficient methods for the analysis of general non-linear systems including piecewise linear and non-linear elements; and the application of these methods to investigate limit-cycle oscillations in the low-speed and transonic regimes both with and without controllers applied.

To date, the main techniques for the analysis of dynamic systems with non-linearities, particularly discrete non-linear elements, have been time integration and harmonic balance schemes. The time integration schemes are slow since a large number of simulations have to be performed not only for different variables e.g. speeds and altitudes, but also for different initial conditions e.g. initial pitch or pitch-rate. This initial condition dependency has to be analysed as the non-linear systems could converge on to different amplitude cycles depending on the initial conditions or perturbation applied to the system. The use of harmonic balance is also commonly used to analyse system with weak forms of non-linearities e.g. cubic non-linearities. However, when analysing piecewise linear sytems the occurence of transient oscillations due to impacting as the system goes through the discontinuous points has meant that the adoption of the harmonic balance is restricted.

Little attention has been given to the development of improved methods for the analysis of challenging non-linear systems with the exception of Wong et al. [7] and associated researchers in Canada [39, 49, 60, 61, 35, 37, 40]. These authors have developed a range of

techniques for analysing aeroelastic systems containing either continuous or piecewise linear elements. Many methods developed to analyse non-linear systems tend to rely on the harmonic balance technique which mandates that the oscillations are made up of either single or multiple harmonics which is not always the case for discrete non-linearities where the impacts excite transients.

The boundary identification technique developed in this work solves the aeroelastic equations exactly for piecewise linear systems. The method splits the system into different linear zones and solves the equations of motion exactly at the boundaries of these zones. Solving the equations exactly at each boundary generates initial conditions for the next linear zone. If, in performing such analyses, all the states at a given boundary are the same as at a previous time at that boundary then a periodic solution has been found. By solving the equations in this way it becomes possible to identify oscillations of different periodicity exactly for different initial conditions and system parameters.

An alternative solution procedure has also been developed and implemented in this research that involves the use of continuous Ordinary Differential Equations (ODEs). To generate continuously differentiable equations the method uses tanh and logarithmic approximations to represent any discrete non-linearities. Using these approximations allows a single parameter to be varied in order to change the accuracy of the approximation, in this way the method lends itself to application within continuation methods, unlike polynomial approximations which require a change in the order of the system to increase their accuracy.

The use of continuous approximations or boundary identification do not in themselves lead to any improvements in the efficiency with which the non-linear aeroelastic phenomenon can be analysed. Efficiency gains for the continuous approximation method arise because the approximations allow analysis with numerical continuation software, which traces branches of results rapidly without the requirement for large numbers of repetitive analyses to be performed as is required when performing analyses using time integration type methods. The boundary identification method, however, uses numerical continuation in a different way and tracks a set of solutions by solving algebraic equations that define an oscillation of a specified periodicity or of a certain number of boundary crossings e.g. period 1 with harmonic. The boundary identification then allows all the solutions to be identified by combining different types of periodic solution and combining them to map the whole domain of interest.

The two new methods developed here have been used to analyse various forms of structural non-linearities including backlash, cubic stiffening, hysteresis and combined backlash/cubic systems. These testcases cover all major forms of non-linearities that could occur within sys-

tems i.e. continuous, piecewise linear and piecewise non-linear. The results generated using boundary identification and numerical continuation have been shown to match exactly with the results generated using more conventional time integration techniques that include boundary capture when discontinuities are present. However, the increased computational efficiency of applying the boundary identification technique compared to time-integration is small if solutions have high periodicity. Applying the continuation techniques to sets of ordinary differential equations and using continuous approximations to represent discrete non-linearities has been shown to reduce the time for calculations considerably when compared to time-integration methods with both the amplitude of the oscillations and the stability of the solution being calculated.

In much of the published literature, the aerodynamic models used for aeroelastic studies are based on low-speed assumptions. The assumptions made in these models enable an aerodynamic model to be generated that is simply a function of the systems states, with the addition of a low number of extra augmented aerodynamic states. As most modern aircraft cruise in the transonic regime such low-speed models are inappropriate for modern analysis. Recent advances in aerodynamic modelling using finite volume schemes has meant that good aerodynamic models can now be generated throughout the flight envelope. However, such models do not lend themselves to application within state space modelling methods because of the large number of states i.e. the unknown velocities and densities at thousands of grid points. To overcome such difficulties, much effort has been applied to the development of Reduced Order aerodynamic Models (ROMs) which have fewer unknowns, but still reproduce the behaviour of the full system of equations with good accuracy. The models used in this work were produced by Gaitonde and Jones [6] and are based on the time-linearised Euler equations. The responses of the linearised Euler equations to a small set of pulse inputs are used to construct ROMs by using the Eigenvalue Realization Algorithm (ERA) as devised by Juang and Pappa [79]. Using ERA, ROMs with a much smaller number of unknowns can be created in a state-space form.

The coupling of the ROM with a linear structural model and numerical continuation has been demonstrated to very rapidly and accurately identify the flutter boundary of the aeroelastic system which would have previously required many time integration solutions of systems with tens of thousands of degrees-of-freedom. Applying the analysis techniques used for low-speed models to transonic structurally non-linear aeroelastic problems has been shown to allow LCOs to be identified within the transonic, coupled system. When comparing the results using the ROM with those generated using the full Euler simulations, the general behaviour of the oscillations have been shown to compare well with the amplitudes and frequencies of the

solutions demonstrated as being in the same region as the actual solutions. It is thought that the loss of accuracy present is due to many of the aerodynamic modes not being included and that some of the eigenvalues are not exactly identified within the ERA. For the identification of flutter boundaries, however, this is not a problem as the boundary is reached when a pair of dominant eigenvalues - that are usually identified and included - cross the imaginary axis.

In this work, three different forms of Flutter Suppression Systems (FSSs) are demonstrated; a fixed gain control system, an optimal control system and an adaptive control system. For aeroelastic models with linear structures, all three algorithms proved successful as a FSS with the largest flutter boundary extension shown by the optimal control system. The basic control system showed good results were obtained when heave and pitch rates where fed back in the three degree-of-freedom system. The selection of the gain levels, however, was somewhat haphazard with gains being "tweaked" by hand to improve the response. The adaptive control system showed good attenuation of oscillations up to approximately 20% beyond the open loop flutter boundary. Beyond this point the rate of departure of the flutter was too fast for the gains to modify without requiring very careful selection of weighting parameters. However, this adaptive system did demonstrate a fast method of generating fixed gains for linear systems as, at a given velocity, the gains rapidly adapted to a fixed value. In real systems this would not occur as system noise and turbulence would introduce gain wind-up. The Linear Quadratic Regulator (LQR) optimal control law showed good suppression, well beyond the flutter boundary, with few limitations on its successful implementation experienced.

In this work it was noted that all the various control systems gave rise to areas of instability at low values of speed index below the linear flutter boundary. From varying the gains by hand the size of the unstable region was found to relate to the amount of pitch or pitch-rate fed back. This demonstrates that when designing systems for flutter suppression the effect upon the whole envelope must be taken in to account. The MCS adaptive control system used was not as promising as first expected. It was anticipated that, due to its adaptive nature, MCS would react rapidly enough to eliminate most oscillations. The requirement for careful selection of some system parameters within the MCS system far above the flutter boundary affected its performance quite dramatically as saturation or divergent oscillations were seen.

The design of controllers to suppress LCOs in non-linear aeroelastic systems is a relatively new field with little literature available. In this work the same control methodologies applied to the linear systems were applied to non-linear testcases. The control laws behaviour was quite similar to that of linear systems with, in general, the controllers that were best for delaying flutter in the linear cases being the best for the suppression of LCOs for the non-linear

cases. When implementing the control laws it was shown that not only could the oscillations be suppressed but the flutter boundary could also be extended by the same amount as the equivalent linear system. This suggests that for both linear and non-linear systems the same modes became oscillatory unstable in the same way.

For both the control of linear and non-linear aeroelastic systems described above, the application of the continuation analysis technique was possible, with the exception of the adaptive control system. This is expected as the gains in the adaptive case would in theory be constantly changing throughout any limit-cycles and as such would be non-repeating. In general, it was found that with the continuation technique adopted results could be generated rapidly in both the linear and non-linear examples.

Beyond the initial aims of this work, further studies have been performed in the simulation of Ground Vibration (or resonance) Tests (GVTs) and the analysis of fatigue. In this thesis, a method to allow mathematical models of the structure to be analysed including any known non-linearities in a way that could be used for comparison with GVTs was described. The aerodynamics of the aeroelastic models were replaced with sinusoidal forces and the system's response examined. This analysis demonstrated that responses could be calculated quickly and accurately analysed without the need for repeating a number of time-responses at different forcing amplitude levels. The non-linear tendencies of the system were highlighted in the results of this work and shown to be very different to results from conventional frequency response analyses of linear models.

A simplified method for the analysis of fatigue due to structural non-linearities has been demonstrated on a very basic low-speed testcase in this work. This system uses the peak values of the oscillations to establish the amount of damage caused. Using the data from such models and information from flight data recorders should allow an estimation of fatigue to be made with possible implications on the costs of aircraft operations and component life extension. The analysis in this work was very basic but shows good potential for improvement when coupled with more realistic aeroelastic and structural models.

7.2 Contributions

All of the aims outlined in section 1.4 at the start of this thesis have been achieved. This section lists the main contributions of this work.

Two new methods have been developed for the analysis of non-linear systems including piece-

wise linear and non-linear systems. These methods reproduce results obtained using existing time-integration techniques that include discontinuity capture. The boundary identification method offers small savings compared to time-integration techniques, whereas the use of continuous approximations and numerical continuation results in major reductions in the computational effort required. This technique is a major advance on existing methods and the methods demonstrated herein could be applied to other situations including general dynamics, electrical engineering, population studies etc.

The technique of arranging transonic coupled aeroelastic systems into state-space forms as is frequently used for low-speed aerodynamic models has been demonstrated by using Reduced Order Models of the flow. This allows the new analysis methods described above to be implemented thus enabling rapid analysis of structurally linear and non-linear systems in higher speed regimes.

It has been demonstrated that control systems can be designed that are capable of suppressing flutter beyond the flutter boundary. However, it is shown that whilst these beneficial effects were achieved the introduction of the control system could lead to regions of instability at low values of speed index away from the flutter boundary. This has demonstrated the need to consider the whole of the flight envelope when designing a flutter suppression control system requiring the possible use of gain scheduling against speed and altitude.

The design of control systems to suppress LCOs in non-linear aeroelastic systems has been shown. It was found that methods that work well for linear systems, in general, work well for the non-linear systems studied. It was demonstrated that LCOs could be suppressed and the flutter boundary extended simultaneously.

A method to allow the rapid and accurate generation of non-linear results for comparison with Ground Vibration Tests (GVTs) has been produced. This method is superior to the more conventional frequency response approach producing more representative results when non-linearities are present.

A fatigue analysis method described in this work has demonstrated that the methods developed in this thesis have applicability beyond the design and test phase of non-linear structures. Although only a basic study was carried out, it showed the potential to generate useful data on the life of structures in a rapid and inexpensive manner.

7.3 Further Work

This work has developed a number of mathematical tools for the analysis of a range of non-linear aeroelastic structures. The software used to perform the analysis was created as a multi purpose tool that can be applied to a number of mathematical problems. In order to take full benefit of the continuation analysis method a more specific tool for the aeroelastic problem should be developed.

A logical extension to the analyses presented in this work is the extension to three-dimensional aeroelastic models incorporating full wings and then full aircraft. Potential computational problems may still exist for the continuation software if higher order systems are analysed as the step sizes used in the predictor-corrector may be restrictively low.

The Reduced Order aerodynamic Model (ROM) has shown great potential in this work with a large decrease in the time required to generate flutter boundaries and LCO information through a large range of Mach numbers. Extending the ROM technique to three-dimensional structures is a logical next step in its development. For such a system, however, impulse responses are not required in every degree-of-freedom of the structure (which could be thousands), instead impulses are required in each of the structural mode shapes that are relevant, these may be generated using modal analysis software available in most FE packages. In theory, for a complete analysis all possible structural modes would be required to be taken but it is thought that taking approximately the first ten to twenty modes would be sufficient to allow a good analysis to be performed. As only a limited number of structural modal responses are required approximately 20 to 40 impulses responses need calculating which would be computationally viable.

A further extension to the ROM is the implementation of an eigenvalue splining routine. Such a routine would allow analyses to be performed between the discrete Mach numbers at which the ROMs are generated. The validity of such a scheme within the highly non-linear transonic dip region, shown in this work, would require further investigation. The use of splining below the transonic regime, down to a Mach number of 0.3, could be very beneficial, however, as the system shows general linearity at these speeds and it is believed that the eigenvalues only vary slightly such that large spacing between ROMs would be valid.

Comparing results of the ROM with those of the full Euler solution showed some differences to exist in amplitude and phase. These differences are thought to be due to the accuracy with which the eigenvalues are identified and the number of aerodynamic modes that are extracted. Therefore, the way in which the ERA functions should be revisited to assess if further im-

provements could be made. Additional errors could be introduced due to the amplitude of the oscillations being beyond the small disturbance approximation of the linearisation. It has therefore been proposed that impulse responses are taken around two or more static positions and splining between the resultant state-space formulations is made such that a better response may be found. The general problem of not enough aerodynamic modes being identified requires further work as it would seem to be a conflicting requirement between accuracy and speed.

In the field of non-linear aeroelasticity, much of the research is concerned with the simulation of the non-linear systems and comparing results with other theoretical testcases. Ideally, comparison should be made between the numerical techniques developed and experimental models. However, modern literature concerned with experimental non-linear aeroelastic structures is severely limited at present and relatively few papers show comparative results. As a result, much more emphasis should be put on the need to perform experimental tests with which the numerical methods could be accurately validated. Such testcases should initially be two dimensional models to prove analysis techniques before three-dimensional cases are considered. Furthermore, such techniques have a great advantage over analysis of flutter in that they are non-divergent so tests can be performed with some confidence that damage will not occur.

A great deal of work is still required in the design of control laws for both linear and non-linear aeroelastic systems. The study in this work showed an overall comparison between aeroelastic controller types with only a small amount of insight gained in to the full nature of the problems that could be encountered. A thorough analysis of the non-linear aeroservoelastic problem is still required with implementation of the various forms of controllers.

The use of the LCO information as a predictive fatigue technique is a further recommendation as only a rudimentary study of the problem has been performed with highly simplified models. If full structural Finite Element (FE) models exist, however, the analysis of the fatigue on such structures due to non-linearities elsewhere in the structure presents an interesting use of the techniques developed in this work.

The application of the continuation method to analyse non-linear structures in the form of sinusoidal forcing is an interesting extension to the analysis problem and allows better comparisons to be made with experimental GVTs. The analysis of such forced systems was found to be very efficient as the aerodynamic complications are removed. Therefore, it is believed that analyses could be performed in times comparable to those used in generating modal methods but with the benefit of incorporating non-linearities. However, non-linear systems would

typically require results to be generated for different forcing amplitudes to capture the full system properties. Comparative experimental analyses could also be performed for non-linear structures as the requirement for a wind-tunnel and the associated expense and complication is removed.

Bibliography

[1] Y.C. Fung. An Introduction to the Theory of Aeroelasticity. New York, 1993. Dover Publications Inc.

[2] J.W. Edwards H. Ashley and J.V. Breakwell. Unsteady Aerodynamic Modeling for Arbitrary Motions. *AIAA Journal*, 17(4):365–374, April 1979.

[3] A.L. Gaitonde and S.P. Fiddes. A Three-Dimensional Moving Mesh Method for the Calculation of Unsteady Transonic Flows. *University of Bristol, Aerospace Engineering Report*, (483), September 1993.

[4] A.L. Gaitonde and D.P. Jones. A Two-Dimensional Linearised Unsteady Euler Scheme for Pulse Response Calculations. *IMechE, Journal of Aerospace Engineering, Part G*, 216:89–104, June 2002.

[5] A.L. Gaitonde and D.P. Jones. The use of Pulse Responses for 2D Unsteady Flows using the Euler Equations. *The Aeronautical Journal*, 106(1063):483–492, Sept 2002.

[6] A.L. Gaitonde and D.P. Jones. Reduced Order State-Space Models from the Pulse Response of a Linearised CFD Scheme. *Accepted for publication, International Journal of Numerical Methods in Fluids*, 2003.

[7] Y.S. Wong L. Liu and B.H.K. Lee. Frequency and Amplitude Prediction of Limit Cycle Oscillations of an Airfoil containing Concentrated Structural Nonlinearities. *AIAA/ASME/ASCE/AHS/ASC Structures, Structural Dynamics and Materials Conference*, Seattle, 2001.

[8] R.L. Bisplinghoff H. Ashley and R.L. Halfman. Aeroelasticity. New York, 1983. Dover Publications Inc.

[9] T. Von Kármán O.H. Ammann and G.B. Woodruff. The Failure of the Tacoma Narrows Bridge. *Report to the Federal Works Agency*, March 1941.

[10] A.E. Davison. Dancing Conductors. *Transactions of the AIEE*, 49:1444–1449, 1930.

[11] J.P. Hartog. Transmission Line Vibration due to Sleet. *Transactions of the AIEE*, 51:1074–1076, 1947.

[12] K-N. Koo. Aeroelastic Charcteristics of Double-Swept Isotropic and Composite Wings. *Journal of Aircraft*, 38(2):343–348, 2001.

[13] E.H. Dowell H.C. Curtiss Jr R.H. Scanlan and F. Sisto. A Modern Course in Aeroelasticity, Second Edition. Kluwer Academic Publishers, 1989.

[14] M. Yamasaki T. Uchida I. Yukimura and K. Isogai. Shock-Stall Flutter of a Two-Dimensional Airfoil. *ICAS 2000 Congress*, Harrogate, UK, 2000.

[15] E.H. Dowell. Flutter of a Buckled Plate as an Example of Chaotic Motion of a Deterministic Autonomous System. *Journal of Sound and Vibration*, 85:333–344, 1982.

[16] W.L. Chen and M.A. Leschziner. Turbulence Modelling of Rotor-Stator Interaction with Linear and Non-Linear Eddy-Viscosity Models. *Proc. 3rd Euro Conf. on Turbomachinery - Fluid Dynamics and Thermodynamics*, pages 259–270, March 1999.

[17] W.A. Silva and D.E. Raveh. Development of Unsteady Aerodynamic State-Space Models from CFD-Based Pulse Responses. *42nd AIAA/ASME/ASCE/AHS/ASC Structures, Structural Dynamics and Materials Conference*, Paper 2001-1213, April 2001.

[18] D. Tang D. Kholodar J-N Juang and E.H. Dowell. System Identification and Proper Orthogonal Decomposition Method Applied to Unsteady Aerodynamics. *AIAA Journal*, 39(8):1569–1576, August 2001.

[19] D.E. Raveh. Reduced-Order Models for Nonlinear Unsteady Aerodynamics. *AIAA Journal*, 39(8):1417–1429, August 2001.

[20] M.R. Turner. Active Flutter Suppression. *Presented at the 40th Meeting of the Structures and Materials Panel of AGARD*, GEN/B55-55/0266, Brussels, Belgium, April 1975.

[21] I. Abel and T.E. Noll. Research and Applications in Aeroservoelasticity at the NASA Langley Research Center. *ICAS 1988*, September 1988.

[22] P.A. Van Gelder. Design of an Integrated Control System for Flutter Margin Augmentation and Gust Load Alleviation, Tested on a Dynamic Wind Tunnel Model. *AIAA Guidance, Navigation and Control Conference*, CP 869, 1986.

[23] R.L. Clark E.H. Dowell and K.D. Frampton. Control of a Three Degree-of-Dreedom Airfoil with Limit-Cycle Behavior. *Journal of Aircraft*, 37(3):533–536, 2000.

[24] C-G Pak. Adaptive Active Flutter Suppression of Wings in Subsonic and Transonic Flight Regimes. *PhD Dissertation, University of California*, 1991.

[25] J.S. Vipperman R.L. Clark M. Conner and E.H. Dowell. Experimental Active Control of a Typical Section Using a Trailing-Edge Flap. *Journal of Aircraft*, 35(2):224–229, Mar-Apr 1998.

[26] D.S. Woolston H.L. Runyan and T.A. Byrdsong. Some Effects of System Nonlinearities in the Problem of Aircraft Flutter. *NACA Technical Note*, 3539, October 1955.

[27] D.S. Woolston H.L. Runyan and R.E. Andrews. An Investigation of Effects of Certain Types of Structural Nonlinearities on Wing and Control Surface Flutter. *24th IAS Meeting*, pages 57–63, January 1956.

[28] S.F. Shen. An Approximate Analysis of Nonlinear Flutter Problems. *Journal of Aerospace Science*, 26:25–32, 1959.

[29] S.F. Shen and C.C. Hsu. Analytical Results of Certain Nonlinear Flutter Problems. *Journal of Aerospace Science*, 25:136–137, 1958.

[30] B.H.K. Lee S.J. Price and Y.S. Wong. Nonlinear Aeroelastic Analysis of Airfoils: Bifurcation and Chaos. *Progress in Aerospace Sciences*, 35:205–334, 1999.

[31] E. Breitbach. Effects of Structural Non-Linearities on Aircraft Vibration and Flutter. Report R-665, AGARD, September 1977.

[32] E. Breitbach. Flutter Analysis of an Airplane with Multiple Structural Nonlinearities in the Control System. TP 1620, NASA, 1980.

[33] E.F. Sheta V.J. Harrand D.E. Thompson and T.W. Strganac. Computational and Experimental Investigation of Limit Cycle Oscillations of Nonlinear Aeroelastic Systems. *Journal of Aircraft*, 39(1):133–141, 2002.

[34] J.J. Stoker. Nonlinear Vibrations. New York, 1950. Interscience Publishers.

[35] B.H.K. Lee L. Gong and Y.S. Wong. Analysis and Computation of Nonlinear Dynamic Response of a Two-Degree-of-Freedom System and its Application in Aeroelasticity. *Journal of Fluids and Structures*, 11:225–246, 1997.

[36] L.N. Virgin. Experimental Aeroelastics. Presentation at The University of Bristol, 2001.

[37] B.H.K. Lee and P. LeBlanc. Flutter Analysis of a Two-Dimensional Airfoil with Cubic Nonlinear Restoring Force. Aeronautical Report LR-618, National Research Council of Canada, 1986.

[38] L.C. Zhao and Z.C. Yang. Chaotic Motions of an Airfoil with Non-Linear Stiffness in Incompressible Flow. *Journal of Sound and Vibration*, 138(2):245–254, April 1990.

[39] L. Liu Y.S. Wong and B.H.K. Lee. Application of the Centre Manifold Theory in Non-Linear Aeroelasticity. *Journal of Sound and Vibration*, 234(4):641–659, 2000.

[40] B.H.K. Lee L.Y. Jiang and Y.S. Wong. Flutter of an Airfoil with a Cubic Nonlinear Restoring Force. *39th AIAA/ASME/ASCE/AHS/ASC Structures, Structural Dynamics and Materials Conference*, April 1998.

[41] A. Sedaghat J.E. Cooper A.Y.T. Leung and J.R. Wright. Linear Flutter Prediction Using Symbolic Programming. *DYMAC99: First International Conference on the Integration of Dynamics, Monitoring and Control*, Manchester, UK, September 1999.

[42] A. Sedaghat J.E. Cooper J.R. Wright and A.Y.T. Leung. Limit Cycle Oscillation Prediction for Non-Linear Aeroelastic Systems. 2000.

[43] W.G. Luber. Flutter Prediction on a Combat Aircraft Involving Backlash on Control Surfaces. *International Modal Analysis Conference (IMAC)*, pages 291–299, 1998.

[44] M.D. Conner D.M. Tang E.H. Dowell and L.N. Virgin. Nonlinear Behavior of a Typical Airfoil Section with Control Surface Freeplay: A Numerical and Experimental Study. *Journal of Fluids and Structures*, 11:89–109, 1997.

[45] S.J. Price B.H.K Lee and H. Alighanbari. Postinstability Behavior of a Two-Dimensional Airfoil with a Structural Nonlinearity. *Journal of Aircraft*, 31(6):1395–, November-December 1994.

[46] Z.C. Yang and L.C. Zhao. Analysis of Limit Cycle Flutter of an Airfoil in Incompressible Flow. *Journal of Sound and Vibration*, 123(1):1–13, 1988.

[47] K. Dutton S. Thompson and B. Barraclough. The Art of Control Engineering. Essex, UK, 1997. Addison Wesley Longman Ltd.

[48] T. Theodorsen. General Theory of Aerodynamic Instability and the Mechanism of Flutter. *NACA Technical Report*, (496):3–23, 1935.

[49] H. Alighanbari and S.J. Price. The Post-Hopf-Bifurcation Response of an Airfoil in Incompressible Two-Dimensional Flow. *Nonlinear Dynamics*, 10:381–400, 1996.

[50] E.J. Doedel A.R. Champneys T.F. Fairgrieve Y.A. Kuznetsov B. Sandstede X. Wang. AUTO 97: Continuation and Bifurcation Software for Ordinary Differential Equations (with HomCont). ftp.cs.concordia.ca pub/doedel/auto, 1998.

[51] M.D. Conner L.N. Virgin and E.H. Dowell. Accurate Numerical Integration of State-Space Models for Aeroelastic Systems with Freeplay. *AIAA Journal*, 34:2202–2205, 1996.

[52] M. Henón. On the Numerical Computation of Poincaré Maps. *Physica 5D*, pages 412–414, 1982.

[53] D. Tang J.K. Henry and E.H. Dowell. Nonlinear Aeroelastic Response of Delta Wing to Periodic Gust. *Journal of Aircraft*, 37(1):155–164, January-February 2000.

[54] D.A. Peters and M.J. Johnson. Finite-State Airloads for Deformable Airfoils on Fixed and Rotating Wings. *Aeroelasticity and Fluid Structure Interaction Problems*, AD-Vol 44, pages 1–28. ASME, 1994.

[55] USA Department of Defense. Military Specification, Airplane Strength and Rigidity, Vibration, Flutter and Divergence. *MIL-A-8870C(AS)*, March 1993.

[56] Defence Procurement Agency. Design and Airwothiness Requirements for Service Aircraft. *DEF-STAN 00-970*.

[57] G. Dimitriadis and J.E. Cooper. Limit Cycle Oscillation Control and Suppression. *The Aeronautical Journal*, (2408):257–263, May 1999.

[58] D. Tang D. Kholdar and E.H. Dowell. Nonlinear Response of Airfoil Section with Control Surface Freeplay to Gust Loads. *AIAA Journal*, 38(9):1543–1557, September 2000.

[59] S.T. Trickey L.N. Virgin and E.H. Dowell. The Stability of Limit Cycle Oscillations in a Nonlinear Aeroelastic System. Submitted to the Royal Society.

[60] L. Liu Y.S. Wong and B.H.K. Lee. Nonlinear Aeroelastic Analysis Using the Point Transformation Method, Part I: Freeplay Models. *submitted to Journal of Sound and Vibration*, 2001.

[61] L. Liu Y.S. Wong and B.H.K. Lee. Nonlinear Aeroelastic Analysis Using the Point Transformation Method, Part II: Hysteresis Models. *submitted to Journal of Sound and Vibration*, 2001.

[62] H. Alighanbari and B.H.K. Lee. Analysis of Nonlinear Aeroelastic Signals. *AIAA/ASME/ASCE/AHS/ASC Structures, Structural Dynamics and Materials Conference*, 1657, Seattle, 2001.

[63] D. De Ferrari L. Chesta O. Sensburg and A. Lotze. Effects of Nonlinearities on Wing-Store Flutter. *AGARD Report*, R-687:15–32, July 1980.

[64] Y. Chan. Numerical Simulation of a Two-Dimensional Airfoil with a Hysteresis Nonlinearity. Project Report IAR-97-1, National Research Council of Canada, 1997.

[65] E.C. Johnson. Sinusoidal Analysis of Feedback-Control Systems containing Nonlinear Elements. *Transactions of the AIEE*, 71:169–81, 1952.

[66] H. Wagner. Uber die Entstehung des dynamischen Aftriebes von Tragflugeln. *Zeitschrift fur Angewandte Mathematik und Mechanik*, 5(1), 1925.

[67] T. von Kármen and W.R. Sears. Airfoil Theory for Non-Uniform Motion. *Journal of Aeronautical Sciences*, 5(10):379–390, 1938.

[68] W.R. Sears. Operational Methods in the Theory of Airfoils in Nonuniform Flow. *Journal of the Franklin Institute*, 230:95–111, 1940.

[69] J.W. Edwards. Unsteady Aerodynamic Modeling and Active Aeroelastic Control. *PhD Dissertation, Stanford University*, 1980.

[70] R.T. Jones. The Unsteady Lift of a Wing of Finite Aspect Ratio. *NACA Report*, (681), 1940.

[71] A.L. Gaitonde. A Dual-Time Method for the Solution of the Unsteady Euler Equations. *The Aeronautical Journal*, pages 283–291, Oct 1994.

[72] A.J. Jameson W. Schmidt and E. Turkel. Numerical Solutions of the Euler Equations by Finite Volume Methods Using Runge-Kutta Time Stepping Schemes. *AIAA Paper*, (81-1259), 1981.

[73] A.J. Jameson. Time Dependant Calculations using Multigrid, with Applications to Unsteady Flows past Airfoils and Wings. *AIAA Paper*, 91-1596, 1991.

[74] L.E. Eriksson. Generation of Boundary Conforming Grids around Wing Body Configurations using Tansfinite Interpolation. *AIAA Journal*, 20(10):1313–1320, 1982.

[75] A.L. Williams and S.P. Fiddes. Moving Grid Generation Using Transfinite Interpolation. *Bristol University Aerospace Engineering Deptartment Report*, 431, 1991.

[76] M. Woodgate J. Anderson K. Badcock and B. Richards. Towards the Direct Prediction of Non-Linear Transonic Flutter Charateristics. *Draft Journal Paper*, 2002.

[77] C.R. Wylie and L.C. Barrett. Advanced Engineering Mathematics. Fifth Edition, 1985.

[78] W.A. Silva and D.E. Raveh. Development of Unsteady Aerodynamic State-Space Models from CFD-Based Pulse Responses. *AIAA Paper*, (2001-1213), 2001.

[79] J-N Juang and R.S. Pappa. An Eigensystem Realization Algorithm for Modal Parameter Identification and Model Reduction. *Journal of Guidance, Control and Dynamics*, 8(5):620–627, 1985.

[80] G. Doetsch. Guide to the Application of the Laplace and Z-transforms (2nd edn). Van Nostrand Reinhold Company, 1971.

[81] C.D. McGillem and G.R. Cooper. Continuous and Discrete Signal and System Analysis. CBS Publishing Japan Ltd., 1984.

[82] J.D. Aplevich. The Essentials of Linear State-Space Systems. Wiley, 2000.

[83] R.R. Craig Jr. Structural Dynamics, An Introduction to Computer Methods. New York, 1981. John Wiley and Sons.

[84] K.J. Bathe. Finite Element Procedure in Engineering Analysis. Englewood Cliffs, New Jersey, 1982. Prentice Hall.

[85] L. Djayapertapa. A Computational Method for Coupled Aerodynamic-Structural Calculations in Unsteady Transonic Flow with Active Control Study. PhD Dissertation, University of Bristol, 2001.

[86] R. Seydel. Practical Bifurcation and Stability Analysis. From Bifurcation to Chaos. Springer-Verlag, 1994.

[87] Y.A. Kuznetsov. Elements of Applied Bifurcation Theory. Applied Mathematical Sciences 112. Springer-Verlag, 1995.

[88] G. James. Modern Engineering Mathematics. Wokingham, UK, 1994. Addison Wesley.

[89] G.H. Golub and C.F. Van Loan. Matrix Computation. Baltimore, Maryland, 1983. John Hopkins University Press.

[90] K.A. Stroud. Further Engineering Mathematics: Programmes and Problems. 1990.

[91] L.E. Kollár G. Stépán and S.J. Hogan. Sampling Delay and Backlash. *Periodica Polytechnica SER. Mechanical Engineering*, 44(1):77–84, 2000.

[92] J.A. Coote and P.L. Denner. Active Flutter Control of a Low Speed Flutter Model: Theoretical Prediction and Comparison with Tunnel Tests. BAe/WBD/D/RD/123, Bristol, UK, 1983.

[93] B.S. Liebst W.L. Garrard and J.A. Farm. Design of a Multivariable Flutter Suppression/Gust Load Alleviation System. *Journal of Guidance and Control*, 11(3), May-June 1988.

[94] V. Mukhopadhyay J.R. Newsom and I. Abel. Reduced-Order Optimal Feedback Control Law Synthesis for Flutter Suppression. *Journal of Guidance, Control and Dynamics*, 5(4), July-August 1982.

[95] P.P. Friedmann D. Guillot and E. Presente. Adaptive Control of Aeroelastic Instabilities in Transonic Flow Using CFD Based Loads. *Journal of Guidance, Control and Dynamics*, 20(6):1190–1199, November-December 1997.

[96] L. Djayapertapa and C.B. Allen. Aeroservoelastic Computations in Unsteady Transonic Flow. *The Aeronautical Journal*, (4226), 2000.

[97] D.P. Stoten and S.P. Hodgson. Comparitive Implementation Studies of the Minimal Control Synthesis Algorithm on a Class 1 Manipulator. *IMechE Part I: Journal of Systems and Control Engineering*, 205(1):23–33, 1991.

[98] D.P. Stoten and H. Benchoubane. The Extended Minimal Control Synthesis. *International Journal of Control*, 56(5):1139–1165, 1992.

[99] D.P. Stoten and H. Benchoubane. The Minimal Control Synthesis Identification Algorithm. *International Journal of Control*, 58(3):685–696, 1993.

[100] D.P. Stoten. Implementation of Minimal Control Synthesis on a Servo-Hydraulic Testing Machine. *IMechE Part I: Journal of Systems and Control Engineering*, 206:189–194, 1992.

[101] D.P. Stoten and S.E.M. Subusang. Gain Bounds in the Minimal Controller Synthesis Algorithm. *Proceedings of the Institute of Mechanical Engineers, Part I, Journal of Systems and Control Engineering*, 212(5):345–360, 1998.

[102] R.E. Mickens. An Introduction to Nonlinear Oscillations. Cambridge University Press, 1981.

[103] N. Kryloff and N. Bogoliuboff. Introduction to Nonlinear Mechanics. Translation by S. Lifschitz, Princeton University Press, 1947.

[104] K. Isogai. On the Transonic-Dip Mechanism of Flutter of a Sewptback Wing. *AIAA Journal*, 17(7):793–795, 1979.

[105] J.J. Alonso and A. Jameson. Fully-Implicit Time-Marching Aeroelastic Simulation. AIAA Paper No, 94-0056, Jan 1994.

[106] K.A. Kousen and O.O. Bendiksen. Limit Cycle Phenomena in Computational Transonic Aeroelasticity. *Journal of Aircraft*, 31(6):1257–1263, Nov-Dec 1994.

[107] S. Schulze. Transonic Aeroelastic Simulation of a Flexible Wing. *AGARD Report*, 822:10.1–11.20, March 1998.

[108] I.J. Polmear. Light Alloys, Metallurgy of the Light Metals (3rd edn). Arnold, Jan 1995.

[109] N.E. Dowling. Fatigue Failure Prediction for Complicated Stress Histories. *Journal of Materials*, 7(1):71–87, 1972.

[110] M.C.Y. Niu. Airframe Stress Analysis and Sizing. Hong Kong Conmilit Press Ltd., 1997.

[111] T. Theodorsen and I.E. Garrick. Nonstationary Flow about a Wing-Aileron-Tab Combination Including Aerodynamic Balance. *NACA Technical Report*, (736):129–138, 1941.

Appendix A

Coefficients used to Generate Aeroforces due to General Pitch/Plunge Motion

This appendix contains the parameters from equation 2.27 as derived by Lee et al. [35].

$$
\begin{aligned}
&c_0 = \frac{1}{\mu}, \quad c_1 = -\frac{a_h}{\mu}, \quad c_2 = \frac{2}{\mu}(1-\psi_1-\psi_2),\\
&c_3 = \frac{1}{\mu}(1+(1-2a_h)(1-\psi_1-\psi_2)), \quad c_4 = \frac{2}{\mu}(\epsilon_1\psi_1+\epsilon_2\psi_2),\\
&c_5 = \frac{2}{\mu}(1-\psi_1-\psi_2+(1/2-a_h)(\epsilon_1\psi_1+\epsilon_2\psi_2)),\\
&c_6 = \frac{2}{\mu}\epsilon_1\psi_1(1-\epsilon_1(1/2-a_h)), \quad c_7 = \frac{2}{\mu}\epsilon_2\psi_2(1-\epsilon_2(1/2-a_h)),\\
&c_8 = -\frac{2}{\mu}\epsilon_1^2\psi_1, \quad c_9 = -\frac{2}{\mu}\epsilon_2^2\psi_2
\end{aligned}
\tag{A.1}
$$

$$
\begin{aligned}
&d_0 = -\frac{a_h}{\mu r_\alpha^2}, \quad d_1 = \frac{1+8a_h^2}{8\mu r_\alpha^2}, \quad d_2 = \frac{1+2a_h}{\mu r_\alpha^2}(1-\psi_1-\psi_2),\\
&d_3 = \frac{1-2a_h}{2\mu r_\alpha^2} - \frac{(1+2a_h)(1-2a_h)(1-\psi_1-\psi_2)}{2\mu r_\alpha^2},\\
&d_4 = -\frac{1+2a_h}{\mu r_\alpha^2}(\epsilon_1\psi_1+\epsilon_2+\psi_2),\\
&d_5 = -\frac{1+2a_h}{\mu r_\alpha^2}(1-\psi_1-\psi_2) - \frac{(1+2a_h)(1-2a_h)(\psi_1\epsilon_1+\psi_2\epsilon_2)}{2\mu r_\alpha^2},\\
&d_6 = -\frac{(1+2a_h)\psi_1\epsilon_1}{\mu r_\alpha^2}(1-\epsilon_1(1/2-a_h)), \quad d_7 = -\frac{(1+2a_h)\psi_2\epsilon_2}{\mu r_\alpha^2}(1-\epsilon_2(1/2-a_h)),\\
&d_8 = \frac{(1+2a_h)\psi_1\epsilon_1^2}{\mu r_\alpha^2}, \quad d_9 = \frac{(1+2a_h)\psi_2\epsilon_2^2}{\mu r_\alpha^2}
\end{aligned}
\tag{A.2}
$$

$$
f(\tau) = \frac{2}{\mu}((1/2-a_h)\alpha(0)+\xi(0))(\psi_1\epsilon_1 e^{-\epsilon_1\tau}+\psi_2\epsilon_2 e^{-\epsilon_2\tau}), \; g(\tau) = -\frac{(1+2a_h)}{2r_\alpha^2}f(\tau) \tag{A.3}
$$

where, from equation 2.17.

$$\psi_1 = 0.165, \quad \psi_2 = 0.335, \quad \epsilon_1 = 0.0455 \quad \text{and } \epsilon_2 = 0.3$$

Appendix B

Aerodynamic Matrices used in the Generation of Aeroelastic ODEs

The matrices from equation 2.33 are given by,

$$\mathbf{M_{nc}} = \begin{bmatrix} -\pi & \pi a_h & T_1 \\ \pi a_h & -\pi(1/8 + a_h^2) & -2T_{13} \\ T_1 & -2T_{13}(1/\pi)T_3 & \end{bmatrix}$$

$$\mathbf{B_{nc}} = \begin{bmatrix} 0 & -\pi & T_4 \\ 0 & -\pi(a_h - 1/2) & -T_{16} \\ 0 & -T_{17} & -(1/\pi)T_{19} \end{bmatrix}$$

$$\mathbf{K_{nc}} = \begin{bmatrix} 0 & 0 & 0 \\ 0 & 0 & -T_{15} \\ 0 & 0 & -(1/\pi)T_{18} \end{bmatrix}$$

$$\boldsymbol{R} = \begin{bmatrix} -2\pi \\ 2\pi(a_h + 1/2) \\ -T_{12} \end{bmatrix}, \quad \boldsymbol{S_1^T} \begin{bmatrix} 0 \\ 1 \\ (1/\pi)T_{10} \end{bmatrix}, \quad \boldsymbol{S_2^T} \begin{bmatrix} 1 \\ (1/2 - a_h) \\ (1/2\pi)T_{11} \end{bmatrix} \tag{B.1}$$

where the constants T_i are defined by Theodorsen [48] and Theodorsen and Garrick [111] as,

$$T_1 = \frac{1}{3}\sqrt{1 - C_\beta^2}(2 + C_\beta^2) + C_\beta \cos^{-1} C_\beta,$$

$$T_2 = (1 - C_\beta^2) - \sqrt{1 - C_\beta^2}(1 + C_\beta^2)\cos^{-1} C_\beta + C_\beta(\cos^{-1} C_\beta)^2,$$

$$T_3 = -\left(\frac{1}{8} + C_\beta^2\right)(\cos^{-1} C_\beta)^2 + \frac{1}{4}C_\beta\sqrt{1 - C_\beta^2}\cos^{-1} C_\beta(7 + 2C_\beta^2) - \frac{1}{8}(1 - C_\beta^2)(5C_\beta^2 + 4),$$

$$T_4 = -\cos^{-1} C_\beta + C_\beta\sqrt{1 - C_\beta^2},$$

$$T_5 = -(1 - C_\beta^2) - (\cos^{-1} C_\beta)^2 + 2C_\beta\sqrt{1 - C_\beta^2}\cos^{-1} C_\beta,$$

$$T_6 = -T_2,$$

$$T_7 = -\left(\frac{1}{8} + C_\beta^2\right)\cos^{-1} C_\beta + \frac{1}{8}C_\beta\sqrt{1 - C_\beta^2}\cos^{-1} C_\beta(7 + 2C_\beta^2),$$

$$T_8 = \frac{1}{3}\sqrt{1 - C_\beta^2}(2C_\beta^2 + 1) + C_\beta\cos^{-1} C_\beta,$$

$$T_9 = \frac{1}{2}\left[\frac{1}{3}(\sqrt{1 - C_\beta^2})^3 + a_h T_4\right],$$

$$T_{10} = \sqrt{1 - C_\beta^2} = \cos^{-1} C_\beta,$$

$$T_{11} = \cos^{-1} C_\beta(1 - 2C_\beta) + \sqrt{1 - C_\beta^2}(2 - C_\beta),$$

$$T_{12} = \sqrt{1 - C_\beta^2}(2 + C_\beta) - \cos^{-1} C_\beta(2C_\beta + 1),$$

$$T_{13} = \frac{1}{2}[-T_7 - (C_\beta - a_h)T_1],$$

$$T_{14} = \frac{1}{16} + \frac{1}{2}a_h C_\beta,$$

$$T_{15} = T_4 + T_{10},$$

$$T_{16} = T_1 - T_8 - (C_\beta - a_h)T_4 + \frac{1}{2}T_{11},$$

$$T_{17} = -2T_9 - T_1 + (a_h - 1/2)T_4,$$

$$T_{18} = T_5 - T_4 T_{10},$$

$$T_{19} = -\frac{1}{2}T_4 T_{11}$$

Additional matrices from equation 2.35 are given by,

$$\boldsymbol{N} = \left[0.006825(U/b)^2 \quad 0.10805(U/b)\right],$$

$$\mathbf{F_p} = \begin{bmatrix} 0 & 1 \\ -0.01365(U/b)^2 & -0.3455(U/b) \end{bmatrix} \tag{B.2}$$

Appendix C

Matrices used in the Derivation of Linearised Euler Equations

The matrices used in the derivation of the linearised Euler equations are given as,

$$(\mathbf{B}^{1})^{-1}_{ij} = \begin{bmatrix} 1 & 0 & 0 & 0 \\ -\overline{u}/\overline{\rho} & 1/\overline{\rho} & 0 & 0 \\ -\overline{v}/\overline{\rho} & 0 & 1/\overline{\rho} & 0 \\ (\gamma-1)\overline{Q} & -(\gamma-1)\overline{u} & -(\gamma-1)\overline{v} & \gamma-1 \end{bmatrix}$$

$$R^{1}_{ij} = \sum_{k=1}^{4} \left\{ \mathbf{B}^{2\mathbf{S}}_{\mathbf{k}} \Delta \overline{\mathbf{y}}_{\mathbf{k}} - \mathbf{B}^{3\mathbf{S}}_{\mathbf{k}} \Delta \overline{\mathbf{x}}_{\mathbf{k}} \right\} \hat{q}_k - \hat{D}_{ij}$$

$$S^{1}_{ij} = \overline{W}_{ij} \frac{d\overline{V}_{ij}}{dt} + \sum_{k=1}^{4} \left\{ \overline{F}_k \Delta \hat{y}_k - \overline{G}_k \Delta \hat{x}_k \right\} - \sum_{k=1}^{4} \overline{W}_k \left\{ x_{t_k} \Delta \overline{y}_k - y_{t_k} \Delta \overline{x}_k \right\} \qquad \text{(C.1)}$$

where,

$$\mathbf{B}^{2\mathbf{S}} = \begin{bmatrix} \overline{u} & \overline{\rho} & 0 & 0 \\ \overline{u}^2 & 2\overline{\rho u} & 0 & 1 \\ \overline{vu} & \overline{\rho v} & \overline{\rho u} & 0 \\ \overline{Q}\overline{u} & (\overline{\rho e}+\overline{p}) + \overline{\rho u}^2 & \overline{\rho v u} & \gamma\overline{u}/\gamma - 1 \end{bmatrix}$$

$$\mathbf{B}^{3\mathbf{S}} = \begin{bmatrix} \overline{v} & 0 & \overline{\rho} & 0 \\ \overline{uv} & \overline{\rho v} & \overline{\rho u} & 0 \\ \overline{v}^2 & 0 & 2\overline{\rho v} & 1 \\ \overline{Q}\overline{v} & \overline{\rho u v} & (\overline{\rho e}+\overline{p}) + \overline{\rho v}^2 & \gamma\overline{v}/(\gamma-1) \end{bmatrix}$$

$$\overline{Q} = \frac{1}{2}(\overline{u}^2 + \overline{v}^2) \qquad \text{(C.2)}$$

The linearised form of the discrete Geometric Conservation Law is given by,

$$\frac{d\widehat{V_{ij}}}{dt} - \sum_{k=1}^{4}\{x_{t_k}\Delta\overline{y}_k - y_{t_k}\Delta\overline{x}_k\} \tag{C.3}$$

This is solved via the same integration scheme used for the physical perturbation equations.

Appendix D

Aeroelastic Coefficients used in the Derivation of Low-Speed Aeroelastic Model

The coefficients for the state-space coupled equations of motions for equation 2.77 are,

$$
\begin{aligned}
&a_{21} = j(-d_5c_0 + c_5d_0), \quad a_{22} = j(-d_3c_0 + c_3d_0), \quad a_{23} = j(-d_4c_0 + c_4d_0) \\
&a_{24} = j(-d_2c_0 + c_2d_0), \quad a_{25} = j(-d_6c_0 + c_6d_0), \quad a_{26} = j(-d_7c_0 + c_7d_0) \\
&a_{27} = j(-d_8c_0 + c_8d_0), \quad a_{28} = j(-d_9c_0 + c_9d_0), \\
&a_{41} = j(d_5c_0 - c_5d_1), \quad a_{42} = j(d_3c_1 - c_3d_1), \quad a_{43} = j(d_4c_1 - c_4d_1) \\
&a_{44} = j(d_2c_0 - c_2d_1), \quad a_{45} = j(d_6c_1 - c_6d_1), \quad a_{46} = j(d_7c_1 - c_7d_1) \\
&a_{47} = j(d_8c_0 - c_8d_1), \quad a_{48} = j(d_9c_1 - c_9d_1)
\end{aligned} \tag{D.1}
$$

where,

$$
j = \frac{1}{c_0d_1 - c_1d_0} \tag{D.2}
$$

c_i and d_i are given in appendix A with the exception of c_0, c_1, d_0 and d_1 that are replaced by,

$$
c_0 = 1 + \frac{1}{\mu}, \quad c_1 = x_\alpha - \frac{a_h}{\mu}, \quad d_0 = \frac{\mu x_\alpha - a_h}{\mu r_\alpha^2} \quad \text{and } d_1 = \frac{1 + 8(\mu r_\alpha^2 + a_h^2)}{8\mu r_\alpha^2} \tag{D.3}
$$